STUDY OF TELEMETRY RECEIVER AND RECORDER PHASE LINEARITY PROBLEMS

August 1966

Ahmad F. Ghais
Eugene J. Ferrari
Charles J. Boardman

DIRECTORATE OF AEROSPACE INSTRUMENTATION
ELECTRONIC SYSTEMS DIVISION
AIR FORCE SYSTEMS COMMAND
UNITED STATES AIR FORCE
L. G. Hanscom Field, Bedford, Massachusetts

(Prepared under Contract No. AF19(628)5655 by ADCOM Inc. 808 Memorial Drive Cambridge, Mass. 02139)

ESD-TR-66-409

Final Report

STUDY OF TELEMETRY RECEIVER AND RECORDER PHASE LINEARITY PROBLEMS

August 1966

Contract No. AF19(628)5655

by

Ahmad F. Ghais
Eugene J. Ferrari
Charles J. Boardman

Prepared for

Electronic Systems Division
Air Force Systems Command
L. G. Hanscom Field
Bedford, Mass.

Approved by Elie J. Baghdady
Elie J. Baghdady
Technical Director

ADCOM, Inc.
808 Memorial Drive
Cambridge, Mass. 02139

G-71-F

FOREWORD

This study was performed by the staff of ADCOM, Inc., 808 Memorial Drive, Cambridge, Mass., under Air Force Contract AF19(628)5655. It was under the technical supervision of Mr. G. Maccarone, ESRIT, Electronic Systems Division, AFSC.

The period of performance for this contract was August 15, 1965 to May 14, 1966, and this final report is submitted on August 14, 1966.

ADCOM, Inc. would like to express its gratitude to the Air Force Eastern Test Range for loan of a complete receiver and converter assembly.

ADCOM, Inc. would also like to express its gratitude to the following manufacturers of telemetry equipment. Their loan of various items of telemetry equipment and their helpful discussions and criticisms greatly facilitated the test-program portion of this study.

AMPEX CORPORATION
Redwood City, California
ASTRO COMMUNICATIONS LABORATORIES, INC.
Gaithersburg, Maryland
DATA CONTROL SYSTEMS, INC.
Danbury, Connecticut

The telemetry equipments employed in this study are not identified explicitly as to manufacturer. They are simply identified as Receivers A, B and C. This was deemed appropriate since the comparison and rating of various products was not one of the project objectives.

C. V. Horrigan

C. V. HORRIGAN
Acting Director
Aerospace Instrumentation

ABSTRACT

The problem of phase nonlinearities in telemetry-receiving systems is studied. The principal data-degrading effect is shown to be intermodulation distortion of FDM telemetry signals. Another form of data degradation, namely, intersymbol interference in TDM telemetry signals, is found not to be related directly to phase nonlinearities, but rather to the transient response of the receiving system.

The noise-loading technique is introduced as an effective means of characterizing, analyzing and measuring intermodulation distortion. Analytical results are established relating the amount of intermodulation distortion to signal and receiving-system parameters. These relationships are verified experimentally using typical telemetry receivers, converters and recorders. Some other sources of data degradation are also identified and evaluated.

The study results are used to establish quantitative tradeoffs between the performance parameters of receiving systems. These tradeoffs are then used in formulating methods of specification for low data degradation. Improvements that can be implemented in existing and future systems are discussed, and it is recommended that study and development efforts should be undertaken to improve data quality.

TABLE OF CONTENTS

TABLE OF CONTENTS (Cont.)

TABLE OF CONTENTS (Cont.)

TABLE OF CONTENTS (Cont.)

LIST OF ILLUSTRATIONS

LIST OF ILLUSTRATIONS (Cont.)

LIST OF ILLUSTRATIONS (Cont.)

LIST OF ILLUSTRATIONS (Cont.)

LIST OF TABLES

LIST OF NOTATIONS

(Arranged in order of appearance in the main text.)

ω	angular-frequency variable
$\Phi(\omega)$	phase characteristic of predetection filter
$T_d(\omega)$	group-delay characteristic of predetection filter
$H(\omega)$	filter transfer function
B	half bandwidth of predetection filter (rad/sec)
$y_n(x)$	Bessel polynomial, order n
a_i	coefficient of Bessel polynomial; coefficient in Taylor series for $H_p(\omega)$
u	normalized frequency variable
$J_n(x)$	spherical Bessel function of the first kind, order n
f_m	modulating frequency in group-delay measurement
V_c	output pulse amplitude in group-delay measurement
V_m	average value of pulse in group-delay measurement
t	time variable
u(t), v(t)	predetection filter input and output waveforms
ω_c	carrier frequency at IF or RF (rad/sec)
A	peak amplitude of u(t)
$\phi(t)$	instantaneous phase modulation on u(t)
x(t)	instantaneous frequency modulation on u(t)
ω_e	rms frequency deviation in FM system (rad/sec)
B(t)	instantaneous amplitude at output of predetection filter
$\theta(t)$	instantaneous phase modulation on v(t)
h(t)	impulse response of predetection filter
$h_p(t)$	cophasal component of h(t)
$h_q(t)$	quadrature component of h(t)
$H_p(\omega)$	Fourier transform of $h_p(t)$, hence symmetric part of lowpass equivalent of $H(\omega)$
$H_q(\omega)$	Fourier transform of $h_q(t)$, hence antisymmetric part of lowpass equivalent of $H(\omega)$
$H_1(\omega)$	positive-frequency part of $H(\omega)$

$H_2(\omega)$	negative-frequency part of $H(\omega)$
$\eta(t)$	quasi-stationary distortion waveform
$\epsilon(t)$	nonquasi-stationary distortion waveform
$R(\omega)$	real part of $H_p(\omega)$
$X(\omega)$	imaginary part of $H_p(\omega)$
$F(t)$	term appearing in expression for $\epsilon(t)$
$G(t)$	term appearing in expression for $\epsilon(t)$
τ	time-shift variable in correlation operations
$R_w(\tau)$	autocorrelation function of any waveform w(t)
c_i	power-series coefficients of $\Phi(\omega)$
h_i	Hermite series coefficients of $\Phi(\omega)$
$H_i(X)$	Hermite-polynomials in any variable x
$\hat{\omega}$	video signal bandwidth rad/sec
ν	normalized angular-frequency variable for video signals, given by $\omega/\hat{\omega}$
$S_w(\nu)$	normalized power spectral density of any waveform w(t)
$I_w(\nu)$	power density spectrum of intermodulation distortion contained in any waveform w(t); a function of frequency within the video band
$S^{(n)}(\nu)$	convolution of $S(\nu)$ with itself (n-1) times
c_i, j	j^{th} Taylor coefficient of i^{th} filter in a cascade
P_1, P_2, P_T	component powers and total power in situation where noise powers arise from two sources
δ	FM modulation index
T_1, T_2	time intervals
α	parameter of gaussian filter
B_{LP}, B_{vid}	bandwidth of a lowpass (or video) filter in a telemetry system
B_{if}	bandwidth of an IF filter in a telemetry system
b	ratio of B_{if} to B_{vid}
B_n	noise bandwidth
T_{imp}	time describing duration of filter impulse response
D	window height in group-delay specification

Section I

INTRODUCTION AND SUMMARY

This section is intended to:

a) describe the study objectives,

b) place the problem of phase nonlinearities in the perspective of overall telemetry data quality,

c) present the essentials of our approach to the problem, and

d) motivate and summarize the contents of the main body of the report.

1.1 Study Objectives

The study objectives are detailed in the work statement of the subject contract. These are reproduced below.

A. The Contractor shall, unless otherwise indicated, supply the necessary personnel, facilities, services and materials to accomplish the following:

Item 1 – Conduct a theoretical investigation and a test program to determine the effects which result from varying degrees of non-linear phase characteristics in telemetry receivers and the predetection record/reproduce process using various telemetry signal formats. All work shall be based on IRIG 106-60 Telemetry Standards (revised 1962), incorporated herein by reference (Ref. 1).

a) The investigation and test program shall include, but not be limited to, the following:

1. Preparation of test procedures to determine and measure receiver and recorder phase characteristics. These test procedures must be prepared in a manner such that they can be easily modified to measure the phase characteristics of any telemetry receiving or recording device.

2. An analysis to determine the causes and effects of non-linear phase characteristics in telemetry receivers and recorders and the degree of distortion and phase non-linearity contributed by each major circuit therein. This analysis shall be supported by mathematical formulae and test data. The supporting test data shall be obtained from tests conducted on a typical telemetry receiver and recorder.

3. Formulation of mathematical interrelationships between phase characteristics, intermodulation, noise level, frequency, carrier and envelope delay, bandwidth, crosstalk, frequency response, harmonic distortion, skirt selectivity, limiter performance, discriminator bandwidth and discriminator

linearity as applied to receivers and recorders. The formulae shall be validated by tests conducted on a typical telemetry receiver and recorder.

4. Formulation of realistic means of stating the phase characteristics of receivers and recorders and establishment of basic phase response criteria. This shall result in minimum signal distortion consistent with other processing requirements and economic considerations. Phase response criteria and characteristics shall be stated in a manner that does not restrict application of the program results, or filter synthesis, to any particular class or configuration of filters. Statements of phase characteristics will describe the phase response or group delay characteristics directly in terms such as range of departure from, or ripple relative to, straight line linear response. Limitations of specific filter designs may be related to the criteria and characteristics.

5. A determination of the limitations imposed upon a telemetry system by receiver and recorder phase characteristics. The limitations and phase characteristics shall be expressed in quantitative as well as qualitative terms. As a part of this, the contractor will determine the improvements that could be expected in a telemetry system resulting from an improvement in receiver and recorder phase characteristics.

6. A comparison of the importance of errors due to phase nonlinearity as compared to other receiver and recorder effects on the multiplexed signal. The comparison shall result in a determination of their relative degrees of severity.

7. Specific recommendations concerning possible changes that could be made to receiver and recorder circuitry to improve their phase characteristics while retaining conformance to IRIG 106-60 (Revised 1962) Standards as specified in Item 1. If there should be a conflict with the Standards, the contractor shall conduct an analysis of trade-off factors. These recommendations shall include modifications that could be made to receiving and recording equipment now on the Air Force Eastern Test Range and information that would be necessary in future receiver and recorder designs. Modifications shall be analyzed in the light of their effect on the characteristics specified in paragraph 3. above. Wherever possible, recommendations shall be of a nature that will remove the cause of the non-linear phase response rather than compensating the existing response. Specific consideration shall be given to the possibility of networks using RC or RLC, plus active element synthesis to avoid the nonlinear phase response introduced in passive band limiting networks.

1.2 Phase Characteristics of Telemetry-Receiving Systems

The need for increased reliability and accuracy in the extraction of telemetry data under adverse conditions has become acute with the increased magnitude and complexity of space missions. It is known that nonlinearities in the phase characteristics of receivers and recorders can degrade the data quality, but until recently very little effort has been devoted to determining the quantitative relationships between phase nonlinearities and data degradation.

Let us begin by identifying the subsystems of the receiving system that contribute to the phase nonlinearities. Now, phase characteristics are meaningful only in the context of linear time-invariant systems (see Ref. 2 Ch. 3 and Ref. 3 Ch. 5). Thus it is the filters in the telemetry-receiving system, irrespective of whether or not they incorporate active elements, that produce the phase nonlinearities.

Consider the typical telemetry-receiving system depicted in Fig. 1. Almost every subsystem shown incorporates filters that may have nonlinear phase characteristics. Since the signals passing through these filters are essentially carriers modulated by the telemetry data, we use the generic term predetection filter to refer to any of these filters.

Figure 2 is a simplified block diagram of the typical telemetry-receiving system which serves to identify the possible locations of predetection filters. The functions of predetection filters can be seen from Fig. 2 to be:

a) to reduce the total additive noise power appearing at the demodulator input,

b) to reject interfering signals from adjacent telemetry bands, and

c) to reject undesired mixer and converter products.

All these functions are best achieved by narrowing the filter bandwidth as far as possible without causing undue degradation of the telemetry data. It is customary to specify the amplitude characteristic of the desired filter, without much regard to the associated phase characteristic. And yet it is well-known that the phase characteristic can exhibit gross nonlinearities, especially at the edges of the passband, resulting in data degradation. It is essential that the telemetry system designer have at his disposal clear and concise information relating the filter characteristics to the resultant data degradation.

Customarily, all but one of the predetection-filtering blocks depicted in Fig. 2 are wideband designs whose function is primarily to reject undesired mixer and spurious components. The remaining block, usually the second IF amplifier, is carefully designed to restrict the bandwidth of the entire receiver, and hence to perform functions a) and b) listed above. Phase nonlinearities over the telemetry signal bandwidth are concentrated in this one block. It is therefore essential to evaluate the data degradation caused by this one block; the results will not be materially changed by the presence of the other predetection filters. Of course, if several predetection filters together restrict the bandwidth of the receiver, then it is necessary to consider the cascade of these filters in determining the data degradation.

We devote Section II to the characterization and measurement of the phase characteristics of telemetry-receiving systems.

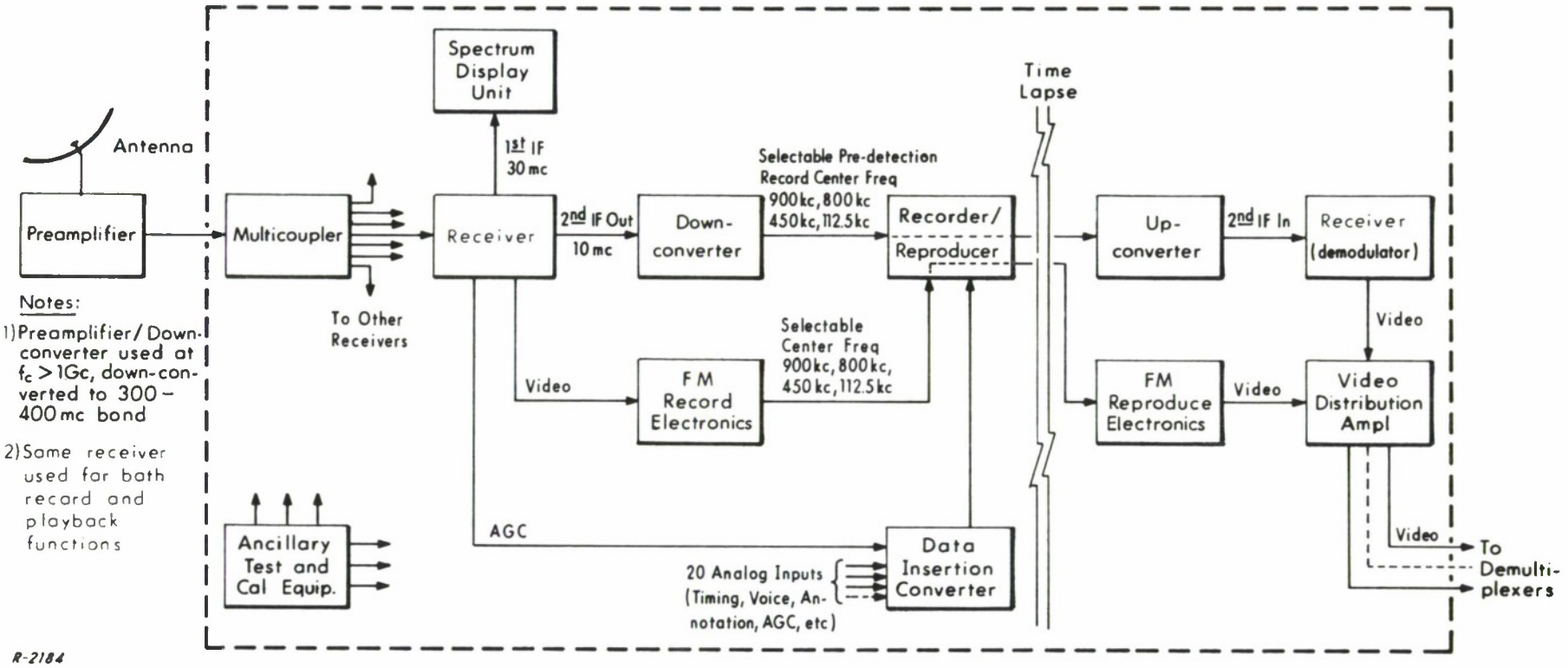

Figure 1 Typical Range Telemetry-Receiving System (System Enclosed Within Dotted Lines is TRKI-12 at Air Force Eastern Test Range).

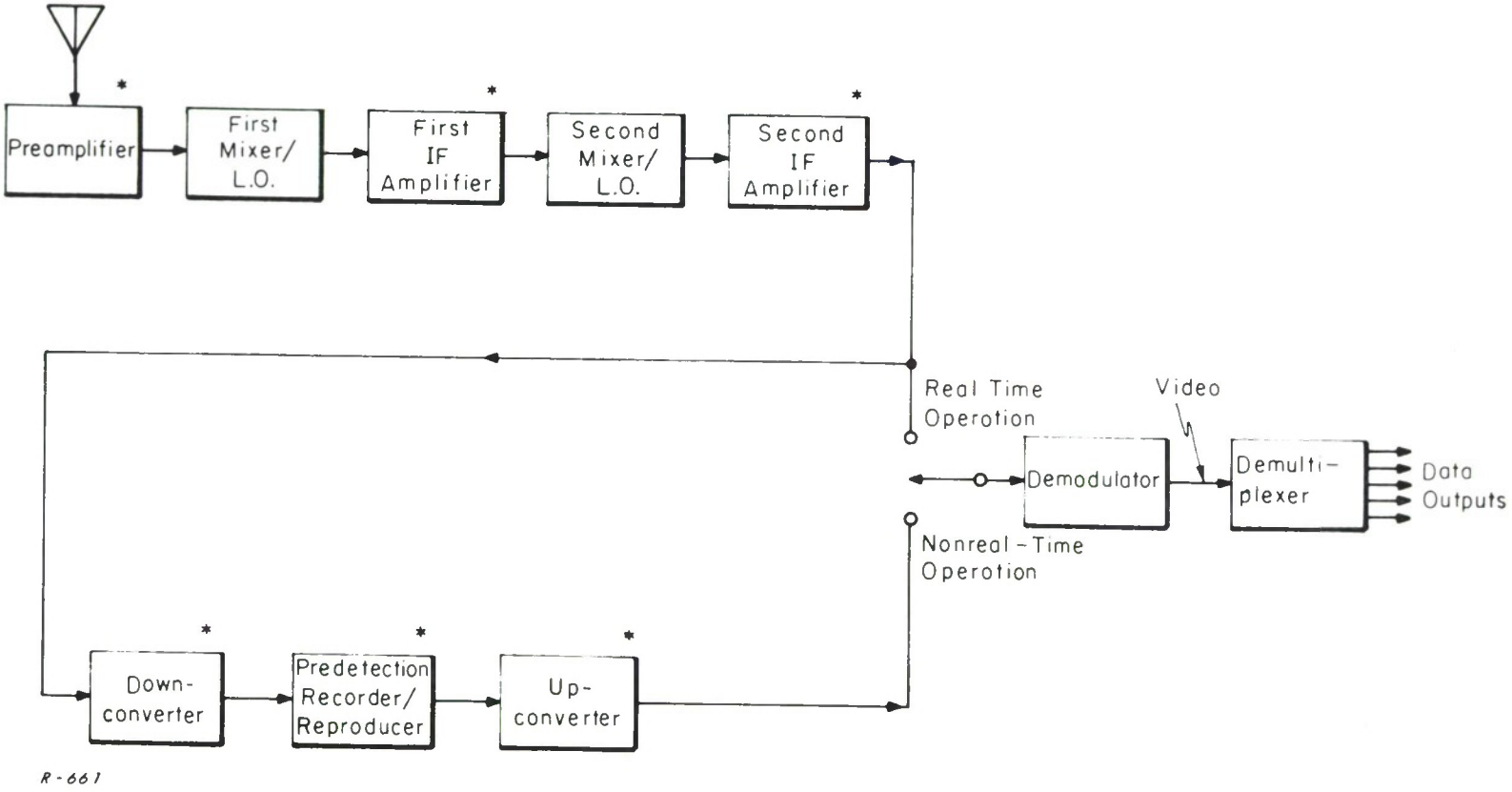

Figure 2 Simplified Block Diagram of Telemetry Receiving System. (* Asterisks Mark Locations of Predetection Filters)

1.3 Telemetry Modulation/Multiplexing Techniques and Data Degradation

The manner in which the phase nonlinearities may degrade the telemetry data depends on the way the data are multiplexed and modulated on the received carrier. All standard telemetry formats employ frequency or phase modulation on the transmitted carrier, and many also have FM or PM subcarriers.

Now, there is no fundamental difference between phase and frequency modulation. Appropriate baseband filtering can convert one type of modulation to the other. Indeed, FM with conventional preemphasis and deemphasis filtering represents an intermediate type of modulation between pure FM and PM. We use the generic term angle modulation to include all these types of modulation, and concentrate the discussion in this document on the degradation of angle-modulated data.

Although amplitude modulation on the transmitted carrier is seldom (if ever) used in space telemetry, we shall include in Subsection 3.3 a brief discussion of the effects of phase nonlinearities on it, because the effects are very similar to those observed on low-deviation angle-modulation signals.

Since telemetry links usually carry more than one data channel, the data are multiplexed by one of the standard techniques and then modulated on the carrier. There are two fundamental classes of multiplex techniques:

a) frequency-division multiplexing (FDM), and

b) time-division multiplexing (TDM)

The data degradation measures appropriate to these classes are different; consequently the analytical techniques employed to relate these degradations to the phase nonlinearities are also different.

We devote Section III to the discussion of the mechanisms by which receiver and recorder phase nonlinearities may degrade the video output of the carrier demodulator, without reference to any specific multiplexing technique. Several cause/effect relationships are established, then the results of Sections II and III are combined and applied in Section IV to the FDM class, and in Section XI to the TDM class. Suitable measures of data degradation for the two classes are formulated and related to signal parameters and receiving-system parameters.

1.4 Sources of Data Degradation in Telemetry Receiving Systems

In this subsection, we briefly review the sources of data degradation in telemetry-receiving systems, in order to:

a) place the problem of data degradation caused by phase nonlinearities in the perspective of overall telemetry data quality, and

b) discuss briefly how this degradation may be observed experimentally, and how it may be masked by other sources of data degradation.

Referring to Figs. 1 and 2, we note that the video output of the receiving system is still in its multiplexed form. In order to extract the telemetry data, the video is fed to the demultiplexer. Now suppose that one of the data channels is kept empty at the transmitter, and all the other channels are fully loaded. In the FDM case this would mean elimination of the appropriate subcarrier, while in the TDM case it would mean that gaps in the video pulse train are left in place of that channel's data pulses. Ideally, the corresponding demultiplexer output remains zero. However, because of practical system imperfections this is not the case. A certain amount of undesired signal (or noise) is always present at the output of the presumably empty channel. Had the channel been loaded, this undesired signal would have degraded the data by superposition.

These undesired signals can be separated into three groups, namely:

a) noise caused by additive noise at the receiver input,

b) interchannel crosstalk, and

c) intermodulation distortion.

a) The noise caused by additive receiver and antenna noise is a well-known phenomenon. Characteristic of this type of output noise is the fact that it is relatively independent of the video signal and will always occur even when all channels are empty. In the following we will assume that the received signal strength is so large that the effects of additive noise can be ignored.

b) Interchannel crosstalk is caused by imperfect filtering, and can be analytically evaluated by applying simple linear system theory. In the case of FDM video signals, interchannel crosstalk in a given channel consists mainly of components from the two adjacent channels which are not sufficiently attenuated by the skirts of the given channel filter.

In the case of TDM video signals, the interchannel crosstalk phenomenon, often named intersymbol interference, is a consequence of pulse stretching and spillover into adjacent time slots. Strictly speaking, intersymbol interference in TDM telemetry can be caused by linear phenomena in video and predetection filters, as well as by nonlinear phenomena in predetection filters. If the causal phenomenon is linear, we may refer to the interference as interchannel crosstalk, whereas if it is nonlinear the resulting interference properly belongs to intermodulation distortion. We shall discuss these distinctions in more detail in Section IX.

The interchannel crosstalk in FDM signals – and that part of it caused by video filters in TDM signals – can be easily observed separately from intermodulation distortion by placing the multiplexer back to back with the demultiplexer and loading only those two channels adjacent to the observed (empty) channel. Intermodulation distortion is negligible under these conditions.

c) Intermodulation distortion is caused by nonlinearities in the telemetry system. By nonlinearity we mean here any operation which creates spectral components in the video output that were absent in the video input. We shall show in Subsection 3.2 that a frequency modulator is inherently nonlinear, even though it may have a perfectly linear voltage-to-frequency characteristic, because it spreads the spectrum of the modulating signal in the process of transferring it to a higher frequency band. We shall also show how, and to what extent, a common RF filter inserted in the receiver between a frequency modulator and a frequency demodulator has a nonlinear effect on the data and produces intermodulation distortion of the video signal. The intermodulation distortion in a channel is very much dependent (in a complicated way) on the signals in all the other channels and will essentially vanish if all other channels are empty.

The following sources of intermodulation distortion may occur in an angle-modulation telemetry system:

a) nonlinearities in baseband and multiplex circuits,

b) FM or PM modulator nonlinearity,

c) predetection filtering at the receiver system,

d) antenna feeder mismatch at the transmitter or receiver,

e) multipath effects in the propagation medium (e.g., frequency-selective fading),

f) FM or PM demodulator nonlinearity,

g) time-base fluctuations in the predetection recorder/reproducer (wow and flutter), and finally,

h) FM-to-AM conversion in predetection filters, followed by AM-to-video conversion by demodulators (incorporating limiters) that are not completely amplitude insensitive.

The fundamental objective of this study is to evaluate the effects of nonlinear phase characteristics in receivers and recorders on telemetry data quality. Thus, of the sources listed in a) to h) above, we are primarily concerned with intermodulation distortion caused by predetection filters.

We have identified in Figs. 1 and 2 the various subsystems incorporating predetection filters. Granted that each of these subsystems performs other functions in addition to filtering, and therefore may incorporate some of the

other data-degrading sources listed above. We must, however, ignore these other sources in our analysis, and we must attempt to identify, separate and "calibrate out" their distortion contributions in the experimental program.

Accordingly, we must assume for analysis purposes that all the converters simply shift the center frequency of the input spectrum, without otherwise modifying it. Similarly, we must view the predetection recorder/reproducer as a simple two-terminal-pair filter, except that the output is delayed by the elapsed time between recording and reproduction.

1.5 Outline of Analytical Approach

The conventional approach to the problem of phase characteristics and their effects on message transmission has been to evaluate the distortion of the RF (or IF) signal, and then to attempt to relate this distortion to data (or message) degradation. We believe that the results of the second step in this approach have been inconclusive, which accounts for the complete lack of design information that relates phase characteristics and data quality. We take a novel approach to the problem, and demonstrate that it yields the desired design information. The novel approach directly relates video signal degradation to phase characteristics, completely bypassing the RF distortion problem.

In Section III we show that the nature of the transfer relation and hence the distortion mechanism in an angle-modulation system depends on the deviation ratio involved. We recognize three distinct cases which correspond to low, high and medium deviation ratios respectively:

Case I: Low-Deviation Angle Modulation

By low-deviation angle modulation (FM or PM) of the carrier is meant the case in which the resulting phase deviation is small compared to one radian. (See Ref. 2, Ch. 19.) An FM deviation ratio much smaller than unity satisfies this condition. We show in Subsection 3.3 that the transmitted signal can then be viewed as the result of a linear modulation operation very similar to amplitude modulation. A predetection filter has a linear-filtering effect on the modulation just like a video filter. Thus, no intermodulation distortion is caused by the predetection filter, irrespective of its phase characteristic. Nevertheless, interchannel crosstalk, i.e., intersymbol interference caused by linear filtering, can result for a TDM video signal.

Case II: The Quasi-Stationary Case

If the message bandwidth is much smaller than the predetection-filter bandwidth, then the instantaneous frequency of the FM signal can be viewed as tracing the static phase characteristic of the predetection filter. This is the case if the FM deviation ratio is much greater than unity. We find in Subsection 3.4 and Appendix I that in this case the intermodulation distortion is determined

only by the filter nonlinear phase characteristic, and not by its amplitude characteristic (assuming that the demodulator is amplitude insensitive, of course). The distortion mechanism is thus memoryless nonlinearity.

Case III: General Angle Modulation

By deriving the transfer relation for a general angle-modulation system, we show in Subsection 3.2 that general angle modulation is fundamentally a nonlinear modulation technique, and that predetection filtering introduces memory in such a system. Thus the distortion mechanism is nonlinearity with memory. We find that the entire transfer function of the filter (i. e., both its amplitude and phase response) is involved in the intermodulation distortion mechanism. The general case is particularly applicable to intermediate values of deviation ratio (in the order of 1 to 3), where the ratio of filter bandwidth to message bandwidth is not much larger than unity.

In Subsection 3.5 and Appendix II we develop a simple approximation to the general transfer relation using a Taylor series technique. We are able to identify two intermodulation distortion terms in the expansion of the demodulated video: a quasi-stationary term identical to the one found in Subsection 3.4, and a nonquasi-stationary term. This paves the way for subsequent evaluation of data degradation in terms of filter characteristics.

1.6 Application to FDM and TDM Video Signals

Sections IV through XI are devoted to the application of the results of Section III to the specific cases of FDM and TDM video signals. In both cases, we begin by selecting a suitable measure of message degradation: in FDM it is the power-density spectrum of the intermodulation distortion, and in TDM it is the amount of intersymbol interference. The objective in Sections IV and XI is to relate the distortion measure to the parameters of the video signal and the predetection filter.

In the FDM case, we choose to model the video signal by a gaussian noise process having a power-density spectrum similar to the message spectrum found in practice. It can be shown that the statistical properties of gaussian noise are very similar to a complex multichannel FDM video signal. Thus, it is meaningful to simulate the video signal by a gaussian noise process.

In addition to being analytically convenient, this so-called noise-loading approach greatly simplifies experimental verification. Intermodulation distortion tests can be standardized and the measurements easily reproduced. In contrast, we believe that the customary method of simulating the video signal by a set of unmodulated subcarriers is inadequate. It is both mathematically intractable (except in the trivial case of one or two subcarriers) and experimentally cumbersome.

The remainder of Section IV is devoted to the computation of the intermodulation-distortion spectrum. The phase characteristic is a sufficient characterization of the filter in the quasi-stationary case discussed in Subsection 4.2. We expand the phase characteristic in a power series, and use a truncated series as an approximation. The distortion spectrum is found to involve multiple convolutions of the input video spectrum (see Eqs. (65) and (67)). The filter characteristic comes in only as constant factors determined by the phase power-series coefficients. Thus, given a video spectrum, we first compute the necessary convolutions (which can often be obtained in closed form), and then by finding the phase power-series coefficients of the predetection filter we can immediately write down the distortion spectrum. Any change of filter characteristic would not necessitate an elaborate recomputation.

A second method of computing the distortion spectrum in the quasi-stationary case is presented in Appendix III. This has certain computational advantages over the power-series method. The phase characteristic is expanded in a series of Hermite polynomials, thus greatly simplifying the form of the final results (see Eqs. (A3.7) and (A3.8)).

The results in Eqs. (65) and (67) are applied in Subsection 4.3 to determine the shapes of the intermodulation-distortion spectra corresponding to a rectangular video spectrum and a parabolically-preemphasized video spectrum. It is found that parabolic preemphasis reduces the distortion at band-edge by 3 dB at the cost of greatly increased distortion at the low-frequency end of the video band.

In Subsection 4.5 we determine the level of the distortion spectrum for several types of predetection filters commonly employed in the telemetry receivers. Thus, we consider double-tuned circuits with various coupling coefficients, Butterworth filters and Bessel filters of various orders. We also consider in Subsection 4.6 the case of cascaded filter stages, showing that the distortion spectrum level increases as the square of the number of identical stages. The computation of the distortion spectrum in the case where the quasi-stationary approximation does not apply is briefly discussed in Subsection 4.7.

In the TDM case covered in Section IX, we point out that intersymbol interference is directly determined by the duration of the transient response of the predetection filter rather than by its phase characteristic. Thus it is neither necessary nor straightforward to relate the intersymbol interference to the phase characteristic. We illustrate this by computing the response of several types of predetection filters to rectangular angle-modulation pulses. We also show that these responses can be adequately approximated by utilizing the lowpass equivalent of the predetection filter. In Subsection 9.4 we demonstrate that the primary source of intersymbol interference in telemetry systems adhering to the IRIG Standards is not the predetection filters but rather the premodulation and postdetection (video) filters.

1.7 The Test Program

The analytical studies were supported and checked by a test program performed on typical telemetry-receiving equipment. The test program was designed to:

a) establish methods of measuring the phase characteristics of receivers and recorders,

b) establish methods of measuring FDM intermodulation distortion spectra,

c) establish methods of measuring intersymbol interference in TDM signals,

d) verify (or disprove) the analytical relationships between signal and filter parameters and the measures of data degradation, and

e) identify other sources of significant data degradation.

Measurement of the phase characteristics of receiving equipment is discussed in Section II. It is experimentally convenient (and more accurate) to measure the group-delay characteristic rather than its phase characteristic. A nonflat group-delay characteristic contains all the data-degrading features of the corresponding nonlinear phase characteristic.

A particularly simple and accurate group-delay measuring setup was developed as described in Subsection 2.3.1. It was used to measure the group-delay characteristics of three types of telemetry receivers and two types of predetection converters. The group-delay characteristic of a predetection recorder/reproducer was measured using a commercial measuring unit. The results of all these measurements are presented and discussed in Subsections 2.6 to 2.8.

A large part of the test program involved the measurement of intermodulation distortion by the noise-loading technique. The test configuration and some preliminary tests are described in Section V. Special attention is directed in Subsections 5.3 and 5.4 to the isolation and correction of residual distortion generated in the measurement equipment. The preliminary tests presented in Subsection 5.5 serve to verify several analytical results obtained in Section IV.

Measurements of intermodulation distortion in three types of telemetry receivers are presented in Section VI. The structure of each receiver is described, and measurements to isolate the primary source of distortion are performed. In every case it is found that the second IF amplifier-filter is the primary source of intermodulation distortion. In addition, the high capture-ratio demodulator incorporated in Receiver A proves to be a source of significant distortion.

The measurements in Section VI are compared with analytical predictions derived on the basis of the results of Section IV. The agreement is generally within a couple of decibels, which may be considered good. In particular, it is found that the quasi-stationary approximation is adequate for the prediction of distortion levels under typical telemetry conditions.

Measurements of intermodulation distortion in two types of predetection converters are presented in Section VII. It is found that the up-converter introduces significant distortion when operated at a low record frequency. The cause of the distortion in this case is insufficient carrier and undesired sideband suppression. This distortion can be eliminated if the up-converter is replaced by a direct demodulator.

Finally, the measurements of intermodulation distortion in the predetection recorder/reproducer are presented in Section VIII. The noise generated internally in the reproduce electronics degraded data quality and interfered with the accurate measurement of distortion. Nevertheless, we are able to confirm that the recorder/reproducer introduces no significant distortion.

The remainder of the test program involved the observation of intersymbol interference in TDM telemetry signals. Tests were conducted on each item of telemetry receiving equipment, and for a variety of parameter choices satisfying IRIG Standards. The observations are presented in the form of oscillograms which clearly show the pulse stretching and spillover. We are able to confirm that, for most telemetry situations conforming to IRIG Standards, the primary sources of intersymbol interference are the premodulation and postdetection filters.

1.8 Tradeoffs, Specifications and Recommendations

The results of the analysis and the test program are brought to bear in Section XI to determine quantitative tradeoffs between various performance parameters. These tradeoffs form the basis for the specification methods introduced in Section XI. Both performance specifications and design specifications are considered.

Two areas where design tradeoffs are not generally understood are identified in Subsections 11.7 and 11.8. Study efforts are recommended in these two areas.

Improvements that could be implemented in telemetry-receiving systems are presented in detail in Section XII. Some of these involve the development of some advanced types of filters for use in telemetry receivers. Others involve fairly simple modifications of existing equipment to improve their data quality. Finally, it is recommended in Section XIII that certain test sets be developed as part of an overall laboratory development program to improve data quality.

Section II

PHASE CHARACTERISTICS OF TELEMETRY-RECEIVING SYSTEMS

2.1 Introduction

This section is devoted to the characterization and measurement of the phase characteristics of telemetry-receiving systems. It has been indicated that a principal source of intermodulation distortion in FDM telemetry is the nonlinear phase characteristics of predetection filters. In order to assess the importance of phase characteristics to data quality it is necessary to establish accurate and convenient methods of measuring these characteristics, and of analytically deriving them from information about the predetection filter design.

Instead of dealing with the phase characteristic $\Phi(\omega)$ directly, it has been found convenient to work with its derivative, the group delay:

$$T_d(\omega) = \frac{d}{d\omega} \Phi(\omega) \tag{1}$$

The group delay is used because it is an easy parameter to measure and it presents the nonlinearities of the phase characteristic in a manner in which they are most evident. A nonflat group-delay characteristic contains all the data-degrading features of the corresponding nonlinear phase characteristic. Measurement of the group delay permits a comparison with the theoretically predicted group-delay characteristics to assess the effects of misalignment, and also enables the computation of the resultant intermodulation distortion.

2.2 Analytical Phase and Group-Delay Characteristics of Predetection Filters

Computations have been made of the group-delay characteristics of various filter types frequently employed as predetection filters in telemetry-receiving systems. Here we present the results, both analytically and graphically, for three general types of filters. We make one simplifying assumption throughout, namely, that the relative bandwidth of the filter is small, so that the familiar lowpass-to-bandpass reactance transformation becomes a simple frequency translation (see Ref. 4, Sec. 11-9).

The first filter type we consider is the Butterworth (or constant-amplitude) filter, which is defined by the maximally-flat amplitude characteristic

$$|H_n(\omega)|^2 = \frac{1}{1 + ((\omega - \omega_c)/B)^{2n}} \tag{2}$$

where 2B is the 3 dB bandwidth, n is the order of the filter, and ω_c is center frequency in radians/sec. The phase and group-delay characteristics of this filter are given (Ref. 5) by

$$\Phi(\omega) = \sum_{m=0}^{\infty} \frac{((\omega - \omega_c)/B)^{2m+1}}{(2m+1)\sin(2m+1)\pi/2n} \quad \text{radians} \tag{3}$$

and

$$T_d(\omega) = \sum_{m=0}^{\infty} \frac{((\omega - \omega_c)/B)^{2m}}{\sin(2m+1)\pi/2n}$$

$$= \frac{1}{1 + ((\omega - \omega_c)/B)^{2n}} \sum_{m=0}^{n-1} \frac{((\omega - \omega_c)/B)^{2m}}{\sin(2m+1)\pi/2n} \quad \text{seconds} \tag{4}$$

The group-delay characteristic is plotted in normalized form in Fig. 3 for orders from 1 to 6.

The second filter type we study is the Bessel (or linear-phase) filter. This filter has the property of a maximally-linear phase characteristic and is defined by the transfer function (Ref. 4, p. 499)

$$H_n(\omega) = \frac{a_o}{y_n(u)} \tag{5}$$

where the y_n are the Bessel polynomials whose coefficients are listed in Table I for n from 1 to 6. A more extensive table of these coefficients is available in Ref. 4, p. 500, or can readily be generated from the recursion formula

$$y_{n+1}(u) = (2n+1)\, y_n(u) + u^2 y_{n-1}(u) \tag{6}$$

The phase and group-delay characteristics corresponding to Eq. (5) can be shown (Refs. 4 & 6) to be

$$\Phi(\omega) = u - \tan^{-1} \frac{J_{n+1/2}(u)}{(-1)^n J_{-n-1/2}(u)} \quad \text{radians} \tag{7}$$

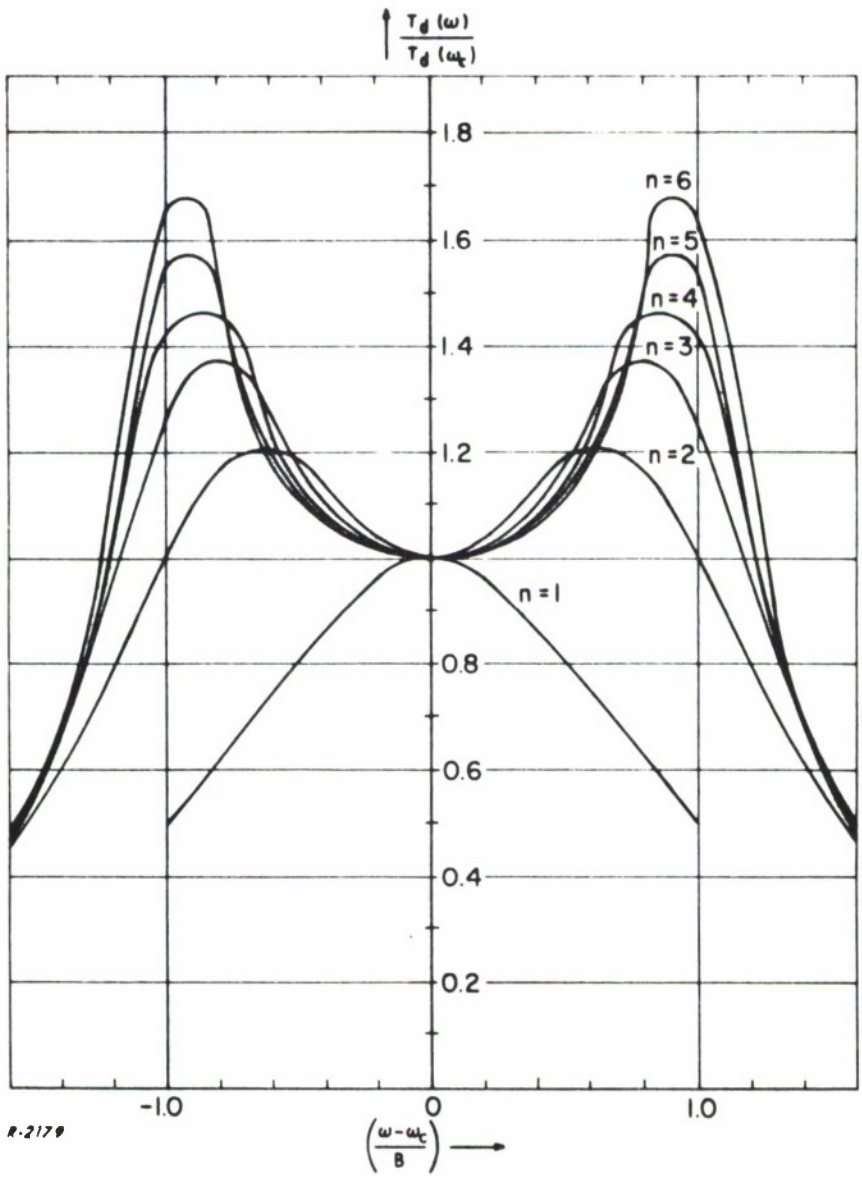

Figure 3 Normalized Group Delay for Butterworth Filters of Various Orders.

Table I

COEFFICIENTS OF THE BESSEL POLYNOMIALS

$$y_n(x) = x^n + a_{n-1}x^{n-1} + \ldots + a_o$$

n	a_o	a_1	a_2	a_3	a_4	a_5
1	1					
2	3	3				
3	15	15	6			
4	105	105	45	10		
5	945	945	420	105	15	
6	10,395	10,395	4,725	1,260	210	21

and

$$T_d(\omega) = T_d(\omega_c)\left(1 - \frac{1}{u^2\left\{\frac{\pi}{2u}\left[J^2_{-n-1/2}(u) + J^2_{n+1/2}(u)\right]\right\}}\right) \text{seconds} \quad (8)$$

where $T_d(\omega_c)$ is the group delay at center frequency and J denotes spherical Bessel functions of the first kind. The argument $u = (\omega - \omega_c)T_d(\omega_c)$ used in Eqs. (5) through (8) is a normalized frequency. It can be converted to the more convenient $(\omega - \omega_c)/B$ using the relationship

$$\frac{\omega - \omega_c}{B} = (\omega - \omega_c)T_d(\omega_c) \times \frac{1}{BT_d(\omega_c)} \quad (9)$$

where the product $BT_d(\omega_c)$ is fixed for a given order of filter and may be found from Table II. (A more extensive table of these time-bandwidth products is available in Ref. 4, p. 502.)

The group-delay characteristics given by Eq. (7) are plotted in normalized form in Fig. 4 with $((\omega - \omega_c)/B)$ as abscissa, for orders n = 1 to 6. It can readily be seen that the Bessel filters give a much flatter group-delay curve than the Butterworth filters of Fig. 3. This, of course, is because the design criterion of the Butterworth's is maximally-flat amplitude rather than maximally-flat group-delay as in the Bessel filters.

The last filter type to be studied is the double-tuned circuit which (near resonance) has the transfer function (Ref. 7, p. 220):

Table II

TIME-BANDWIDTH PRODUCT
FOR BESSEL FILTERS

Order n	$BT_d(\omega_c)$
1	1.00
2	1.36
3	1.75
4	2.13
5	2.42
6	2.70

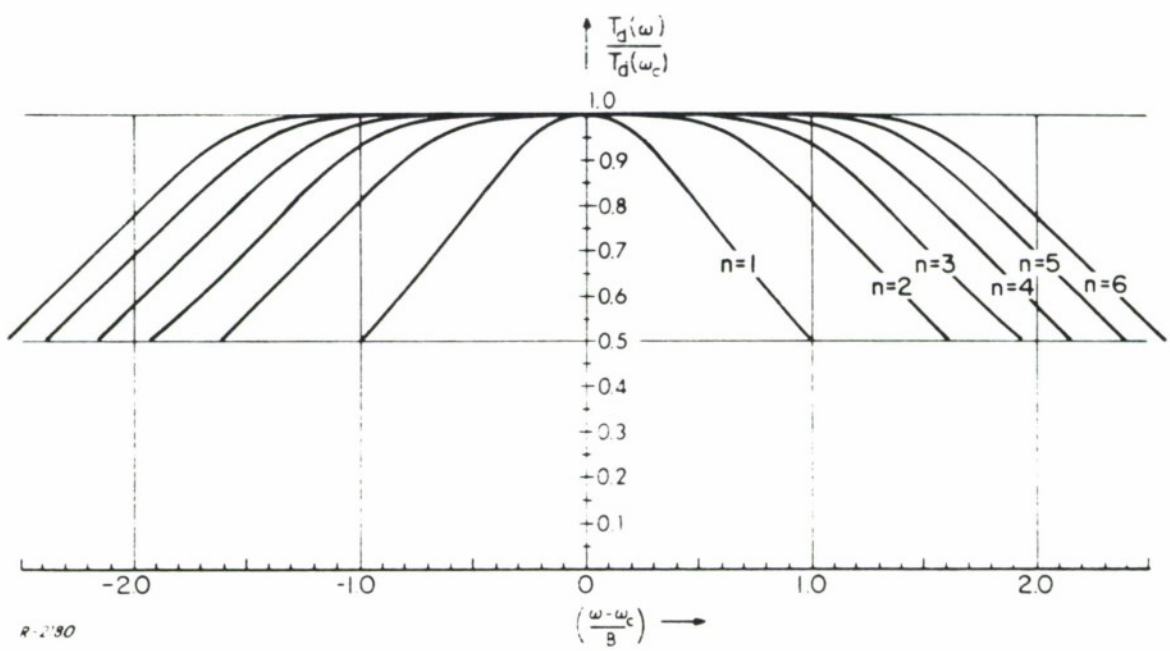

Figure 4 Normalized Group Delay for Bessel Filters of Various Orders.

$$H(\omega) = \frac{1}{1 - \frac{f^2(a)}{1+a^2}\left((\omega - \omega_c)/B\right)^2 + j\frac{2f(a)}{1+a^2}\left((\omega - \omega_c)/B\right)} \tag{10}$$

where

$$f(a) = \frac{2BQ}{\omega_c}\sqrt{a^2 - 1 + \sqrt{2(1+a^4)}} \tag{11}$$

where Q is the "quality factor" of each tuned circuit. The parameter a is the coupling coefficient, such that

$a < 1$ corresponds to undercoupling

$a = 1$ corresponds to critical coupling

$a > 1$ corresponds to overcoupling

The phase characteristic corresponding to Eq. (10) is seen to be

$$\Phi(\omega) = -\tan^{-1}\frac{2f(a)\,(\omega - \omega_c)/B}{f^2(a)\left((\omega - \omega_c)/B\right)^2 - (1+a^2)} \text{ radians} \tag{12}$$

from which we obtained the group delay characteristic

$$T_d(\omega) = \frac{2f(a)}{B}\,\frac{1+a^2 + f^2(a)(\omega - \omega_c/B)^2}{\left[f^2(a)\,(\omega-\omega_c/B)^2 - (1+a^2)\right]^2 + 4f^2(a)(\omega-\omega_c/B)^2} \text{ seconds} \tag{13}$$

This is plotted in normalized form in Fig. 5 for a range of coupling coefficients.

It is now possible with these expressions for the group delay to compare the measured group delay for the predetection filters with the predictions to investigate the alignment accuracy and also to use the predictions to compute the intermodulation distortion anticipated with the various predetection filters.

2.3 Measurement Technique for Group-Delay Characteristics

As indicated previously, the most convenient method for measuring and presenting data about the nonlinearities of the phase characteristics of predetection filters is to measure the group delay. For measurement on receivers and predetection converters, the method of measurement is straightforward. An amplitude-modulated signal is passed through the filter of interest

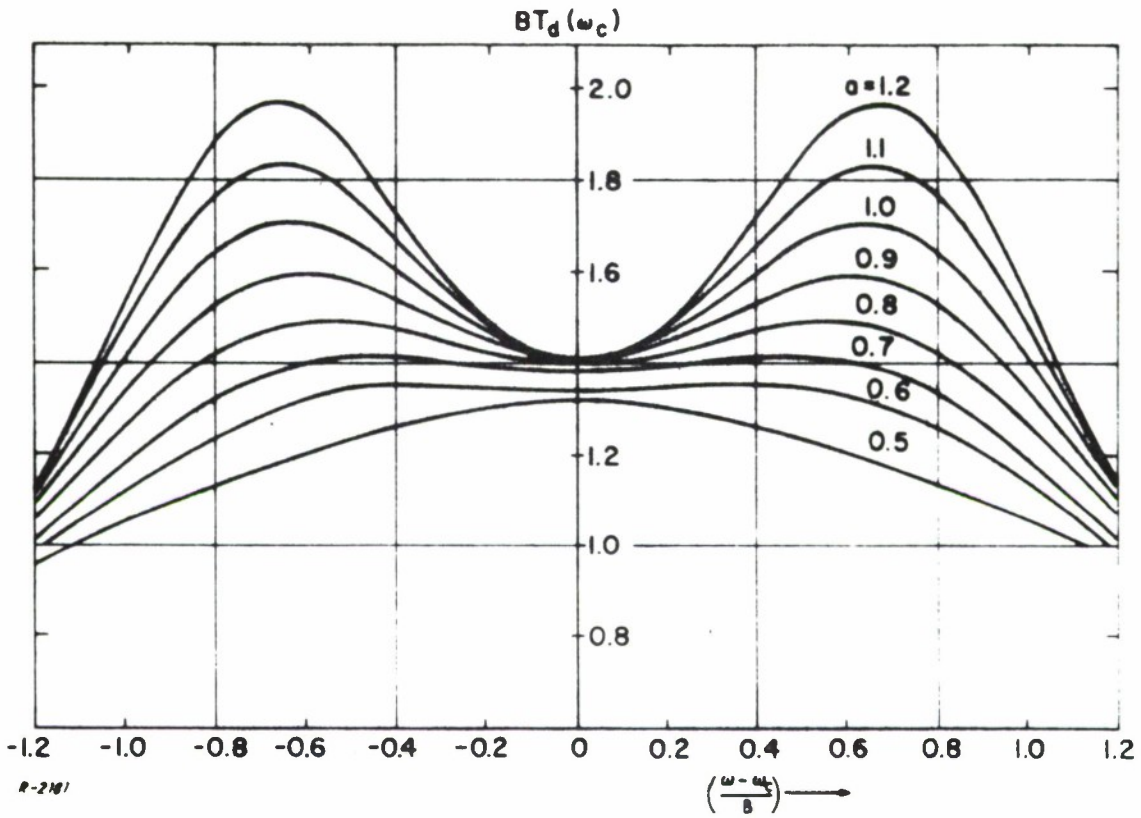

Figure 5 Group Delay for Double-Tuned Circuits with Various Couplings.

and the delay of the detected signal relative to the modulation signal is measured as a function of frequency. The principal concern in implementing this technique is the accuracy of the measurement. Some of the filters in the telemetry receivers tested for this study have linear-phase characteristics which, ideally, correspond to constant group delay in the band of interest. This means that very low values of group-delay variation are to be anticipated with such filters. The resolution of the group-delay measurement technique must be correspondingly high. For this study, it was anticipated that a resolution in the order of 25 nanoseconds would be needed. Since commercial equipment with this accuracy was not readily available, a technique was developed in the ADCOM laboratory for accomplishing it.

The block diagram of the group-delay measurement technique is shown in Fig. 6. The AM generator is modulated with a baseband signal whose frequency f_m is accurately known. The AM signal is passed through the predetection filter thus picking up group delay. After envelope detection, the modulation signal is isolated in a lowpass filter and used to drive a zero-crossing detector.

The zero-crossing detector is a special circuit developed to assist making group-delay measurements. Its schematic is shown in Fig. 7.

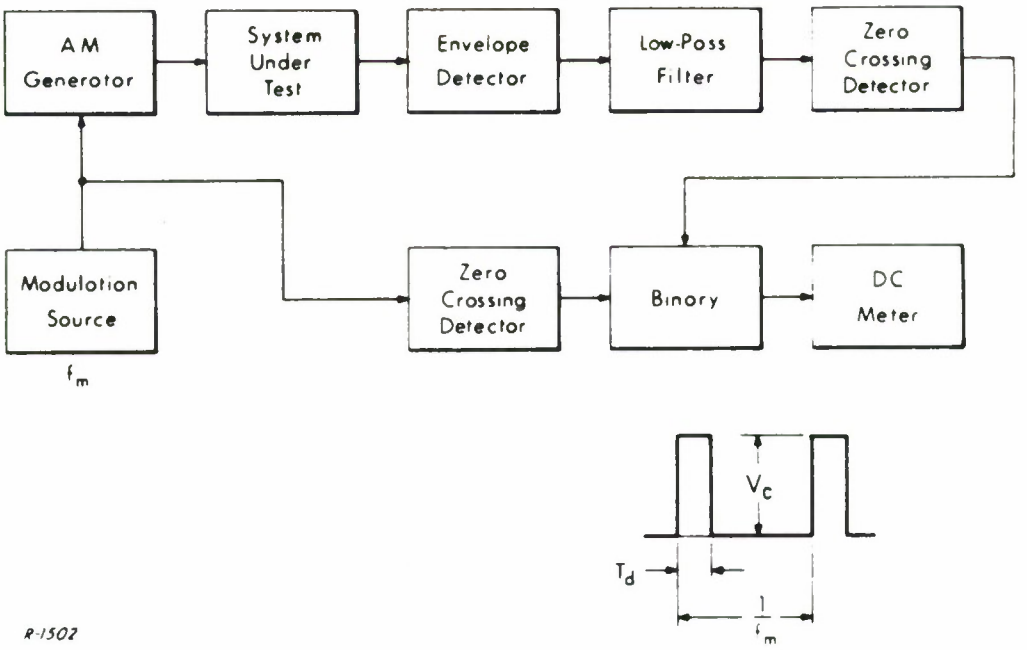

Figure 6 Block Diagram of Group Delay Measurement Technique.

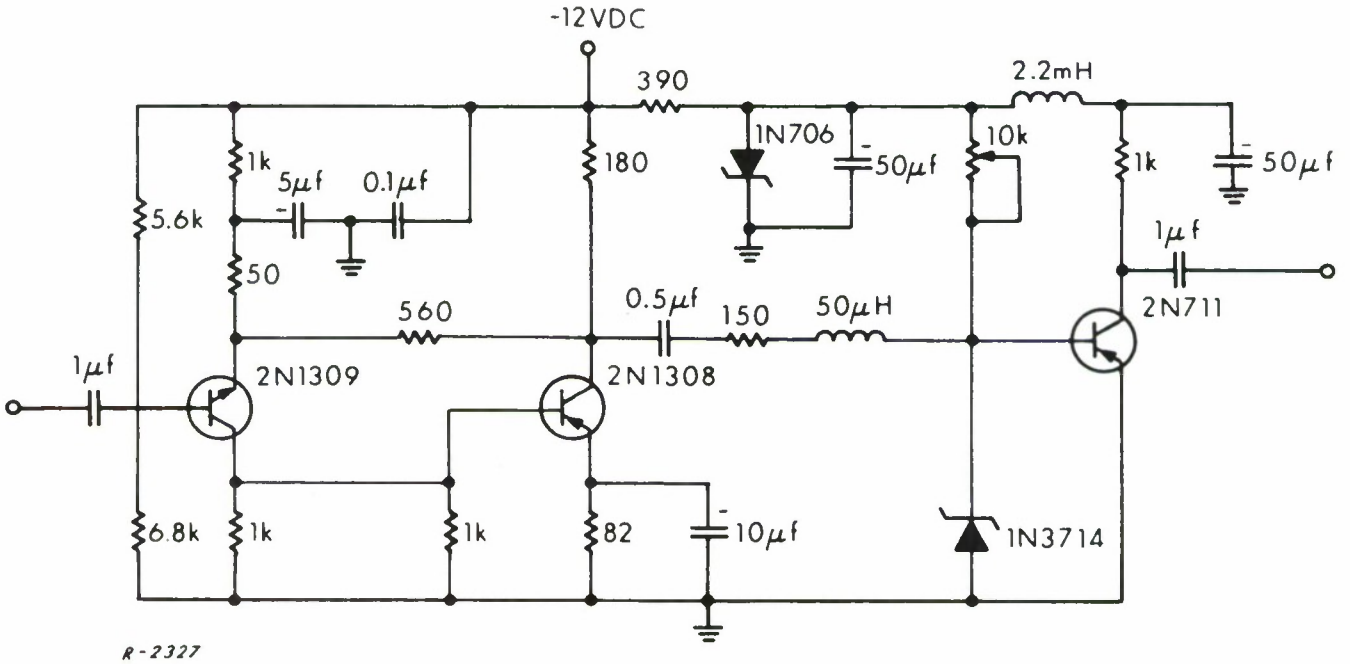

Figure 7 Schematic of Zero-Crossing Detector.

Basically the zero-crossing detector is composed of a low output-impedance amplifier driving a tunnel diode-transistor pair. The tunnel diode is biased such that as the input waveform goes through zero volts, the output transistor changes state between saturation and cutoff. Thus, the output waveform is a square wave having the same zero crossings as the input waveform.

The original modulation is also applied to another zero-crossing detector and the outputs of the two zero-crossing detectors are applied to a bistable multivibrator. The output of the multivibrator is a constant-amplitude variable-duty-cycle pulse. The frequency of the pulse is f_m, the frequency of the modulation signal. The duty cycle or pulse width is determined by the amount of delay picked up by the envelope of the signal passing through the filter. The greater the delay, the longer the pulse. This pulse is then applied to a dc voltmeter which measures the average value of the pulse and hence the group delay. The group delay is found by the formula

$$T_d = \frac{V_M}{V_c f_m} \tag{14}$$

where

T_d = time delay

V_c = output pulse amplitude

V_M = average value of pulse, measured by dc voltmeter

The accuracy of the measured group delay is a function of the accuracy of the voltmeter and the accuracy to which the modulation frequency is known. To find the accuracy of the measurement technique Eq. (14) is differentiated

$$dT_d = \frac{\partial T_d}{\partial V_M} dV_M + \frac{\partial T_d}{\partial f_m} df_m + \frac{\partial T_d}{\partial V_c} dV_c \tag{15}$$

Now evaluating each of the partial derivatives gives

$$\frac{\partial T_d}{\partial V_M} = \frac{\left[\partial (V_M / V_c f_m)\right]}{\partial V_M} = \frac{1}{V_c f_m} \tag{16}$$

$$\frac{\partial T_d}{\partial f_m} = \frac{\left[\partial (V_M / V_c f_m)\right]}{\partial f_m} = -\frac{V_M}{V_c f_m^2} \tag{17}$$

$$\frac{\partial T_d}{\partial V_c} = \frac{[\partial(V_M/V_c f_m)]}{\partial V_c} = -\frac{V_M}{V_c^2 f_m} \tag{18}$$

Substituting Eqs. (16) through (18) into Eq. (15) yields the expression for the error in the group-delay measurement

$$dT_d = \frac{1}{V_c f_m} dV_M - \frac{V_M}{V_c f_m^2} df_m - \frac{V_M}{V_c^2 f_m} dV_c \tag{19}$$

A crystal controlled 10 kHz modulation signal was used whose frequency stability was ±3 parts in 10^8, and the voltmeter was accurate to within ±0.02%. Thus the parameters for Eq. (14) are

$$f_m = 10^4 \text{ Hz}$$

$$V_c = 10 \text{ volts}$$

$$V_M = 2.5 \text{ volts}$$

where V_M is a function of the absolute delay and changes only slightly for the group-delay variations measured here. For example, 1 μsec corresponds to a change of only 0.1 volt. The resulting accuracy of these parameters are seen to be

$$dV_c = \pm 2(10^{-4})\,10 = \pm 2(10^{-3}) \text{ volts}$$
$$dV_M = \pm 2(10^{-4})\,2.5 = \pm 5(10^{-4}) \text{ volts}$$
$$df_m = \pm 3(10^{-8})\,10^4 = \pm 3(10^{-4}) \text{ Hz}$$

Substituting these values into Eq. (19) gives the measurement error for the group-delay test set imposed by the test equipment tolerances

$$dT_d = \pm 25(10^{-9}) \text{ sec.}$$

Some inaccuracy is introduced into the repeatability of the group-delay measurement due to jitter in the zero-crossing detector threshold. This was experimentally found to be ±5 nsec. In addition, some residual group delay is bound to exist in the measurement configuration, but it can readily be accounted for by conducting a test with no filter between the generator and detector. The measurements can thus be corrected for this residual delay to give the actual delay.

As will be demonstrated, the accuracy of the measurement configuration was sufficient to measure all of the receiver IF filters under consideration here, including the linear-phase filters. Measurements made with this configuration compared quite favorably with those taken using a much more complex measurement system, the Wandel u. Goltermann LD-1. It is noteworthy that this technique can be made applicable at any of the frequencies of interest in the telemetry system by appropriate generator selection.

The measurement of group delay in a predetection recorder/reproducer is more difficult than that of measuring group delay in a predetection filter. This is due to the introduction of time translation and jitter inherent in the recording process making comparison with a reference signal as in Fig. 6 impossible. It is, however, possible to combine the reference and test signals and transmit them through the recorder separately and compare them. This technique and its application to measuring the relative group delay of a predetection recorder is described in Ref. 8. Such a technique was available in the Wandel u. Goltermann Group-Delay measuring equipment LD-1. This equipment is capable of measuring relative delay on the recorder/reproducer to within ±1 nanosecond. The LD-1 uses time multiplexing to measure the delay between a reference and test signal. Two carriers are generated and become the reference and test frequencies. They are switched and then modulated with a low-frequency signal. This multiplexed signal is fed through the recorder and applied to the receiver section of the LD-1. Since the recorder displays different delays to each carrier, a phase surge is produced in the envelope of the signal received for each switching point. This surge is reflected, after demodulation, in phase shifts which correspond directly to the relative group delay accumulated in the recorder.

2.4 Measurement Technique for Amplitude Characteristics

The amplitude characteristics of predetection filters in telemetry systems are somewhat easier to measure than the group delay. The block diagram of the test configuration is shown in Fig. 8. The AM generator is modulated and the signal passed through the filter being tested. The output of the filter is envelope-detected and the amplitude of the modulation signal measured in a narrowband filter as a function of carrier frequency. This method provides a convenient and accurate plotting of the amplitude characteristic at greater attenuation than is possible with a direct measurement because of the use of a narrowband filter to restrict the system noise. The accuracy of the measurement is 0.1 dB, and it can be made applicable at any of the frequencies of interest in a telemetry system by changing the AM generator.

2.5 Preliminary Group-Delay Measurements

Prior to performing group-delay measurements on the various predetection filters in the telemetry system, a group-delay measurement

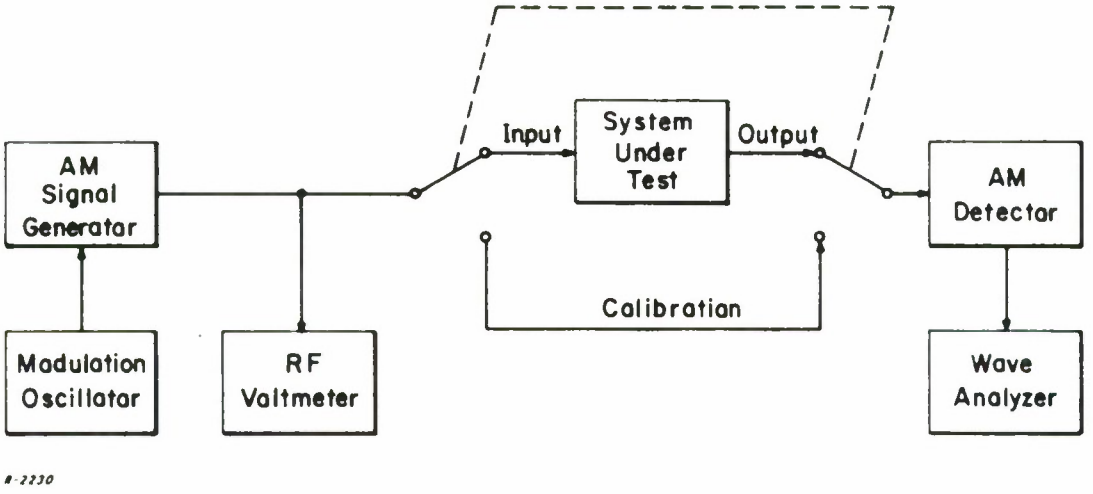

Figure 8 Block Diagram of Measurement Technique for Amplitude Characteristic.

was made on a laboratory filter which closely simulated a receiver second IF filter. This measurement accomplished two ends. First, it permitted evaluation of the group-delay measurement technique by comparing the measurement to a theoretically computed curve of group delay. Second, it provided the measured group-delay characteristic which will be used to predict the intermodulation distortion for this filter which in turn will be measured in a later test.

This filter was a second-order Butterworth design (i. e., critically-coupled double-tuned circuit), with a bandwidth of 425 kHz centered at 10 MHz. The measured group delay is shown in Fig. 9 (dashed curve) along with the theoretical predicted value (solid curve) obtained from Fig. 3. The curve plots the relative group delay, normalized to the delay at the center frequency, as a function of frequency. The relative delay will be used throughout these measurements since the absolute value of delay does not affect the resultant distortion. The distortion results only from group delay variations. It can be seen that prediction and measurement agree to within about 20 nanoseconds which is excellent considering the inherent inaccuracies in filter alignment.

2.6 Measurements of Receiver Characteristics

2.6.1 Measurements on Receiver A

Group-delay measurements on the various receivers tested here were conducted only on the second IF amplifiers, since this is the principal

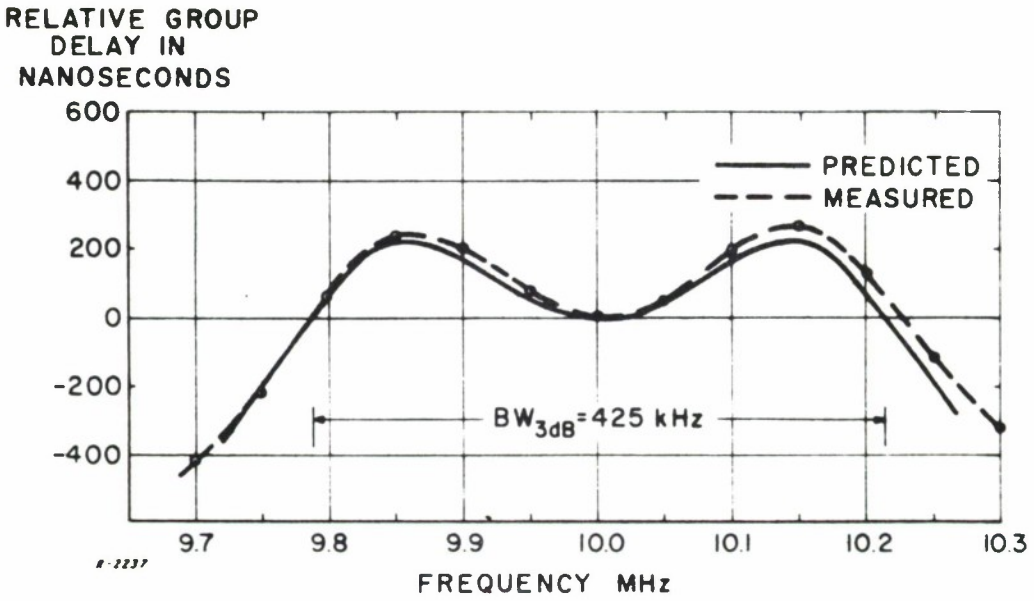

Figure 9 Measured and Predicted Group-Delay Characteristic of Second-Order Butterworth Filter.

bandwidth-limiting component in the receiver. The IF amplifier of Receiver A is composed of a cascade of two fourth-order Butterworth sections having a flat amplitude characteristic and a nominal overall 3 dB bandwidth of 500 kHz. Its measured overall amplitude characteristic, as shown in Fig. 10, is flat to within about 1 dB across most of the band. Its measured group delay is shown in Fig. 11 along with the predicted value from Fig. 3. The experimental agreement is within 0.2 μsec. This sizable discrepancy is due almost entirely to filter misalignment. Note that this misalignment is not readily apparent in the measured amplitude characteristic.

2.6.2 Measurements on Receiver B

Receiver B is equipped with three plug-in IF filters. These consist of a sixth-order Butterworth filter with a nominal 500 kHz 3 dB bandwidth, a sixth-order Bessel with a nominal 500 kHz 3 dB bandwidth, and a sixth-order Bessel with a nominal 300 kHz 3 dB bandwidth.

The amplitude and group delay characteristics of the 500 kHz Butterworth filter are shown in Figs. 12 and 13, respectively. The amplitude is very flat inband but is slightly skewed at the high end. This apparent misalignment is more easily seen by comparing the measured and predicted values of group delay in Fig. 13. Here the shape of the measured and predicted values are similar but the values only agree to within 0.4 μsec, which indicates misalignment of the filter.

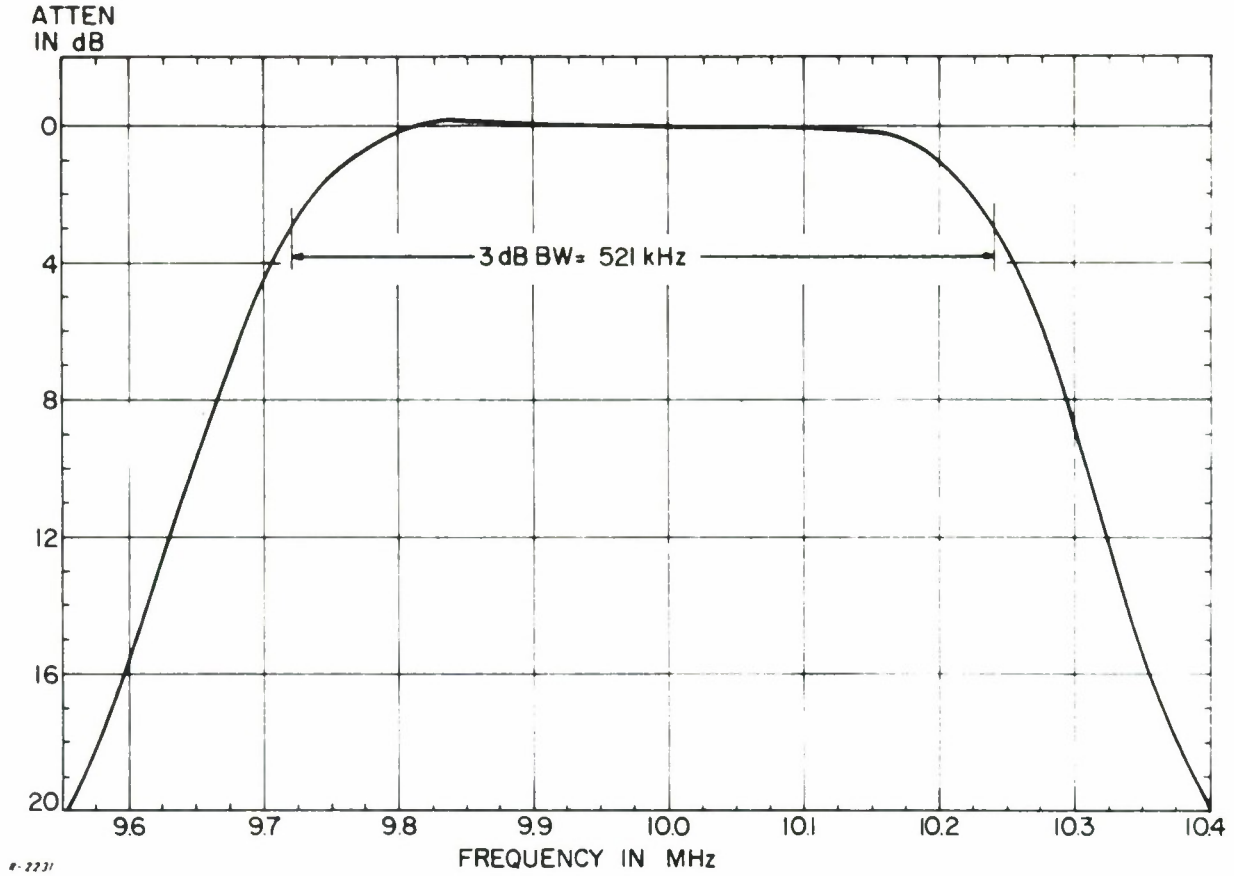

Figure 10 Measured Amplitude Characteristic of Receiver A. 500 kHz Constant-Amplitude IF Amplifier.

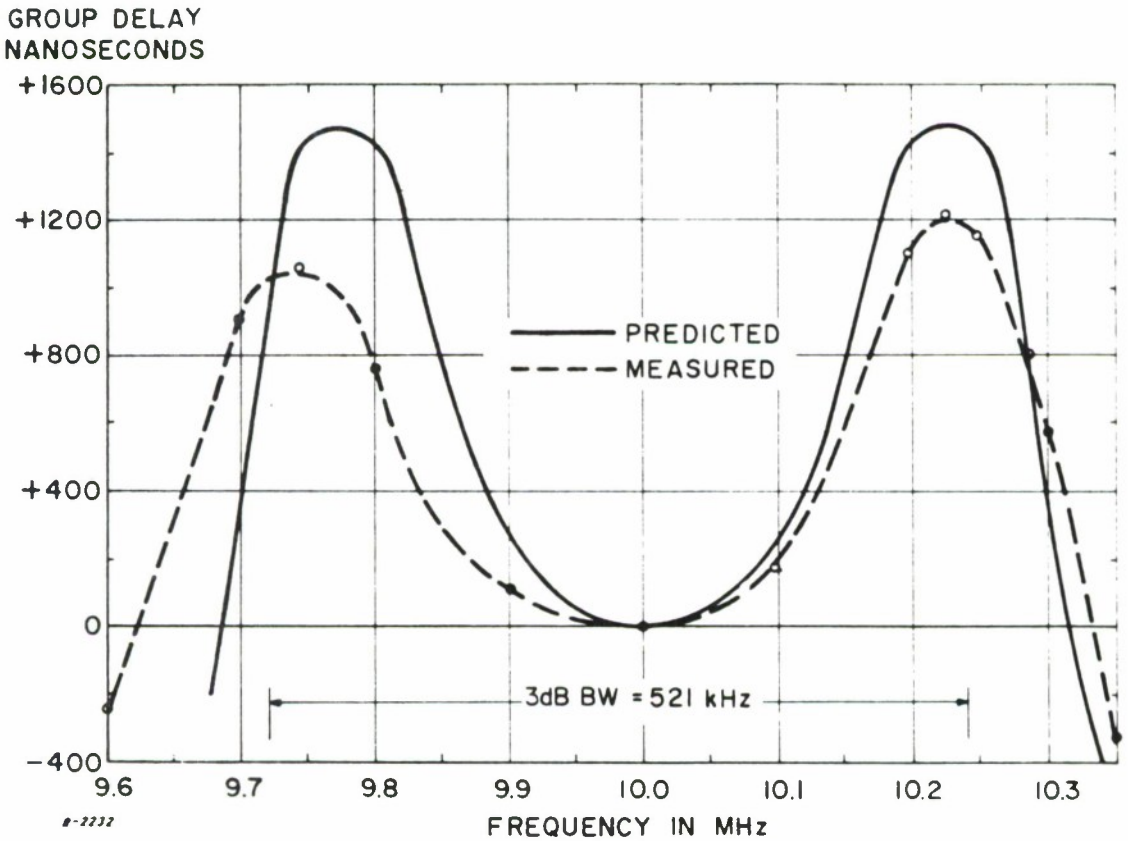

Figure 11 Measured and Predicted Group-Delay Characteristic of 500 kHz Constant Amplitude IF Amplifier of Receiver A.

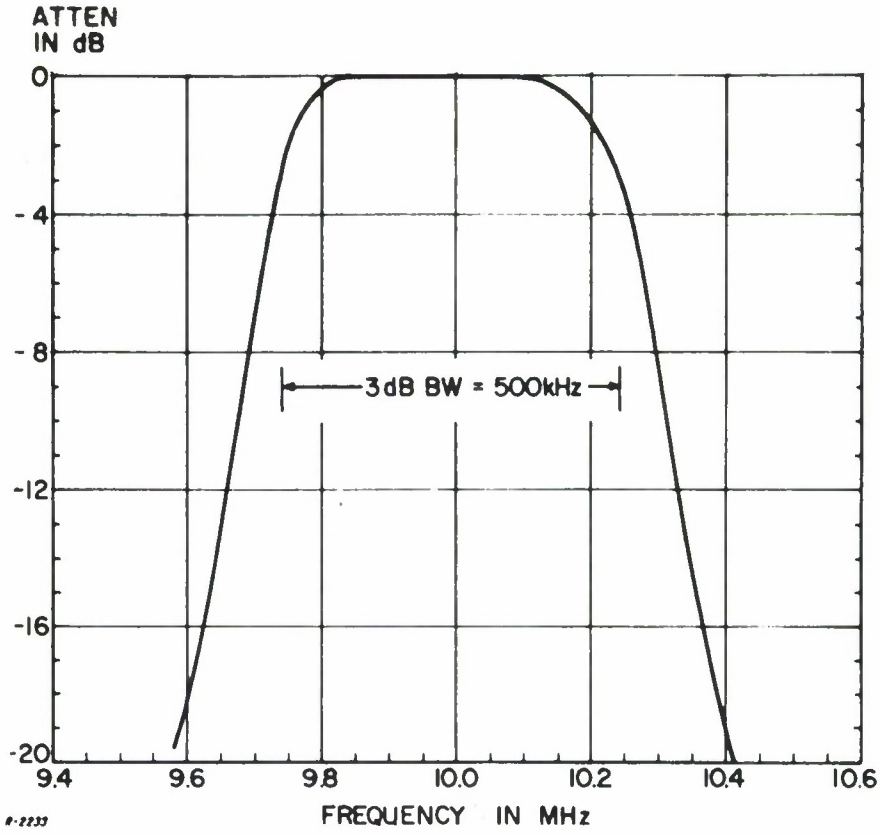

Figure 12 Measured Amplitude Characteristic of Receiver B. 500 kHz Constant Amplitude IF Amplifier.

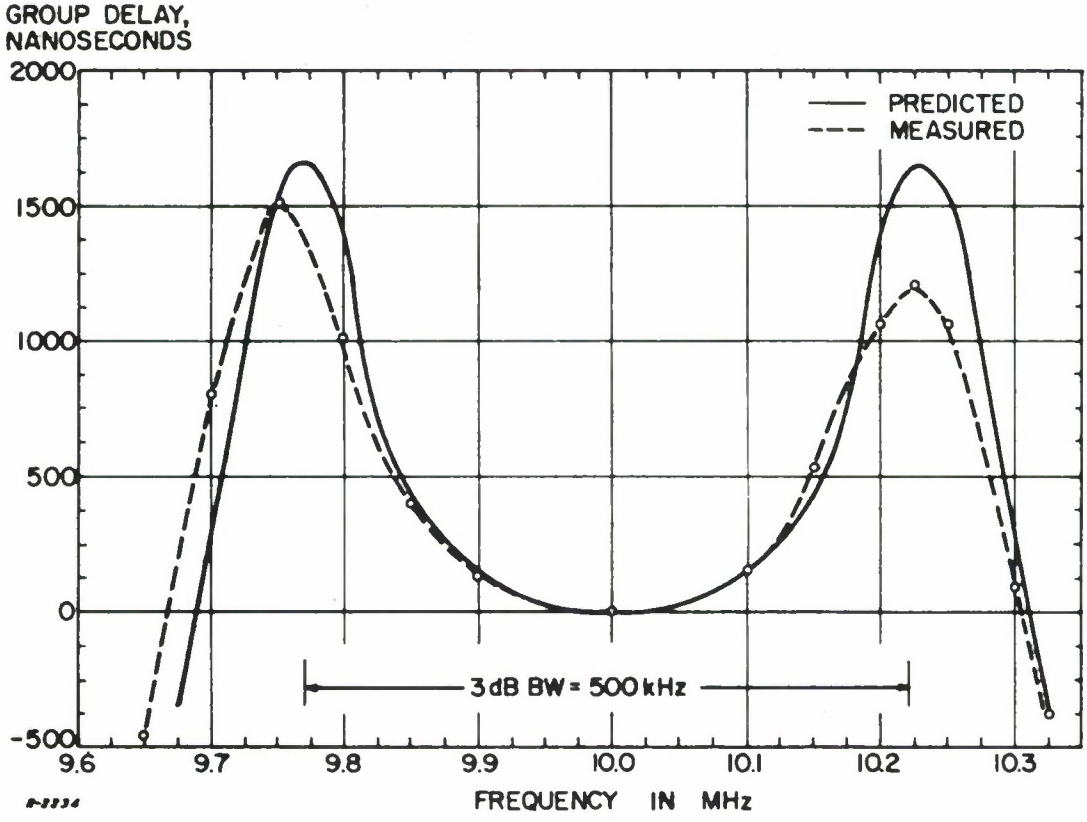

Figure 13 Measured and Predicted Group-Delay Characteristic of 500 kHz Constant Amplitude IF of Receiver B.

The amplitude characteristic of the 500 kHz Bessel filter is shown in Fig. 14. The amplitude characteristic can be seen to be a good approximation of the gaussian characteristic. The measured and predicted values of group delay are plotted in Fig. 15. As can be seen the predicted group delay for the Bessel filter, obtained from Fig. 4 is flat in the band of interest and falls off outside this band. The measured value, however, is seen to have some variation, which is due entirely to filter misalignment.

The amplitude characteristic of the 300 kHz Bessel filter is shown in Fig. 16 and can be seen to approximate a gaussian shape. The measured and predicted group delay curves are illustrated in Fig. 17. The measured values agree fairly well with the prediction in midband, showing some misalignment at the low end and earlier roll-off at both ends.

2.6.3 Measurements on Receiver C

Two of the IF amplifiers of Receiver C were measured for amplitude and group delay. These filters are both composed of a cascade of five slightly overcoupled double-tuned circuits, and have nominal 3 dB bandwidths of 500 kHz and 300 kHz, respectively.

The amplitude characteristic of the 500 kHz IF amplifier shown in Fig. 18 demonstrates that the filter is only very slightly overcoupled having less than a 0.5 dB ripple inband. The measured and predicted values of group delay are plotted in Fig. 19. The predicted value here was obtained from Fig. 5 using a coupling coefficient of 1.0 since the amplitude characteristic was approximately flat. The experimental agreement is quite good within the 3 dB bandwidth.

The amplitude characteristic of the 300 kHz IF amplifier seen in Fig. 20 shows considerably more overcoupling, and also some misalignment which became apparent from detailed measurements on the individual stages. The measured group delay is shown in Fig. 21.

The curves of the group delay for all these filters show different variations. It is obvious, however, that the Bessel filters have considerably lower delay variations than either the Butterworth or overcoupled double-tuned design, and thus presumably will have lower intermodulation distortion. This result is verified later.

2.7 Measurements of Predetection-Converter Characteristics

2.7.1 Measurements with the Down/Up Converter

Amplitude and group-delay measurements were taken on the down/up converter by connecting the down-converter and up-converter back-to-back. This converter was supplied with Receiver C. Several choices of record frequency, i.e., down-converter output frequency, are available with this

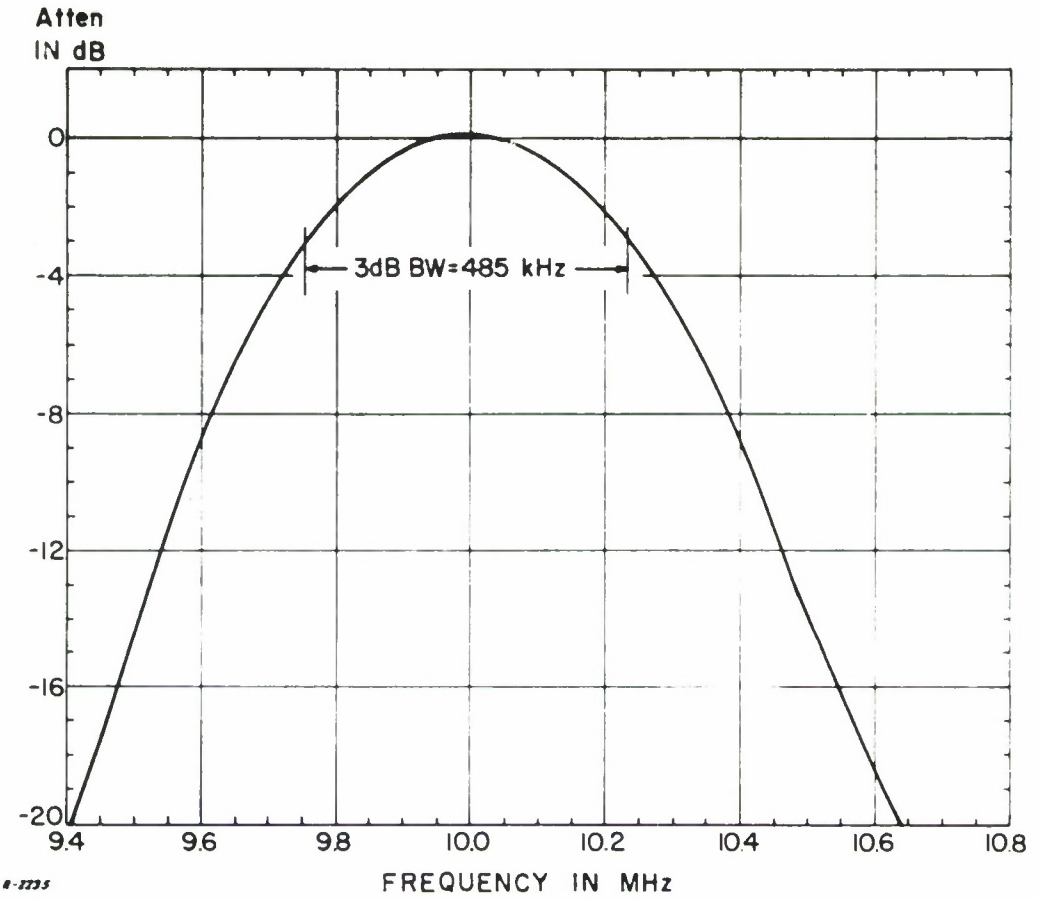

Figure 14 Measured Amplitude Characteristic of Receiver B. 500 kHz Linear Phase IF Amplifier.

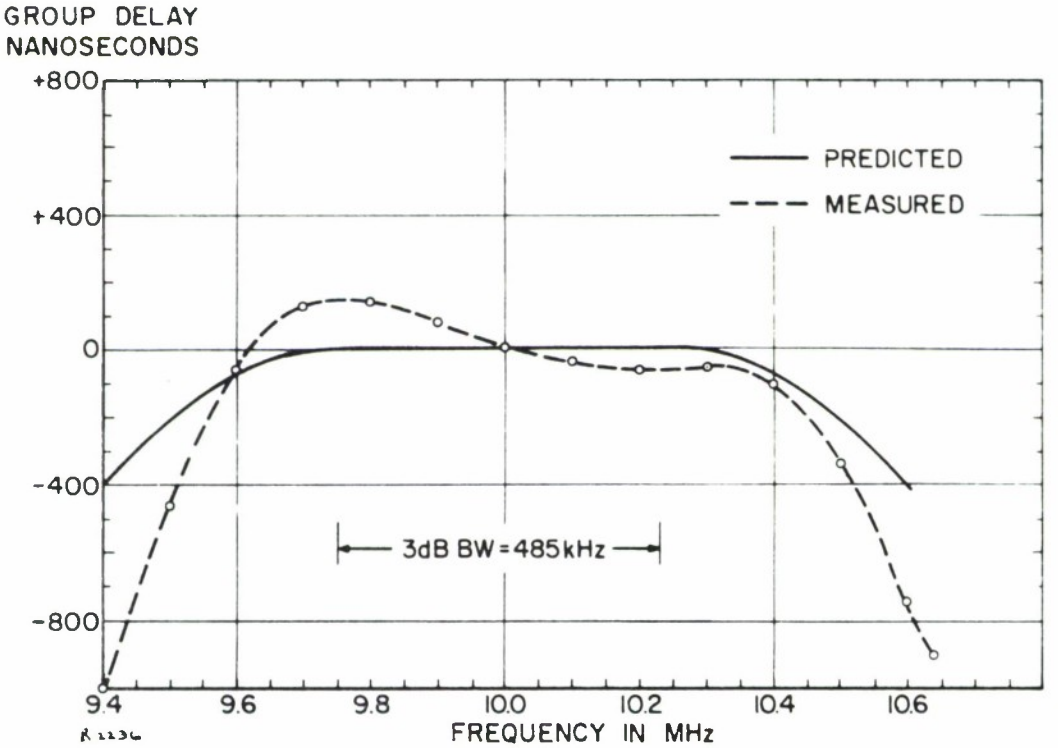

Figure 15 Measured and Predicted Group-Delay Characteristic of 500 kHz Linear Phase IF Amplifier of Receiver B.

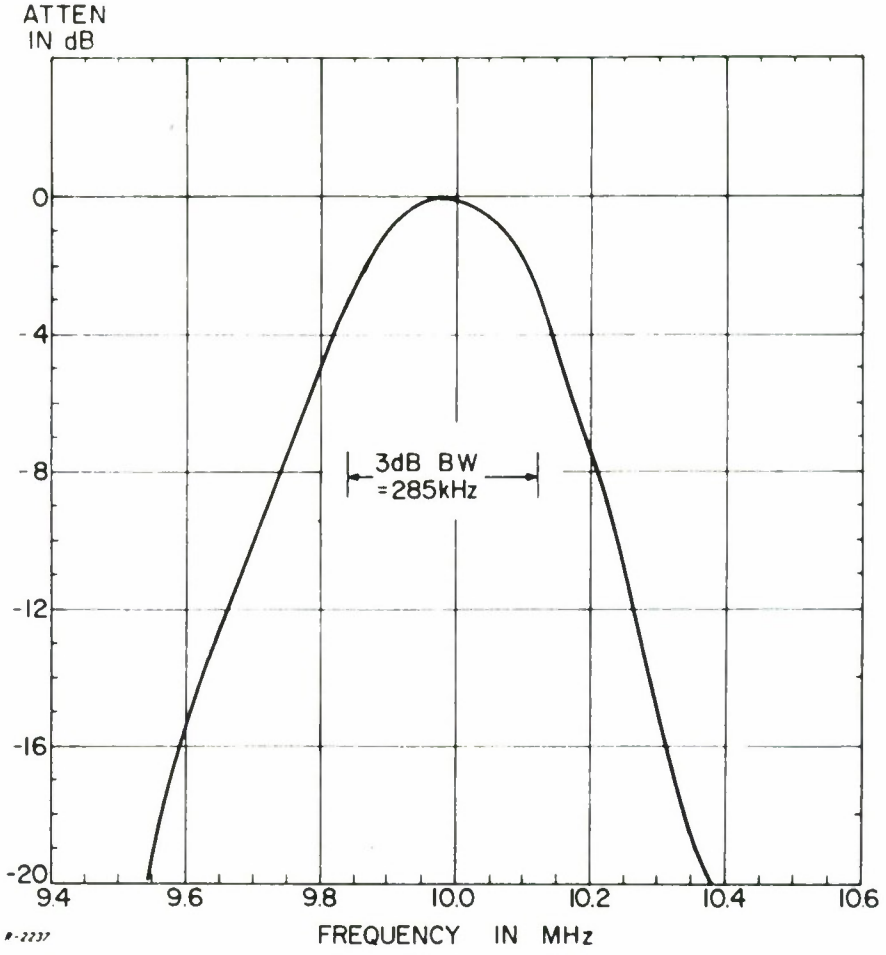

Figure 16 Measured Amplitude Characteristic of Receiver B 300 kHz Linear-Phase IF Amplifier.

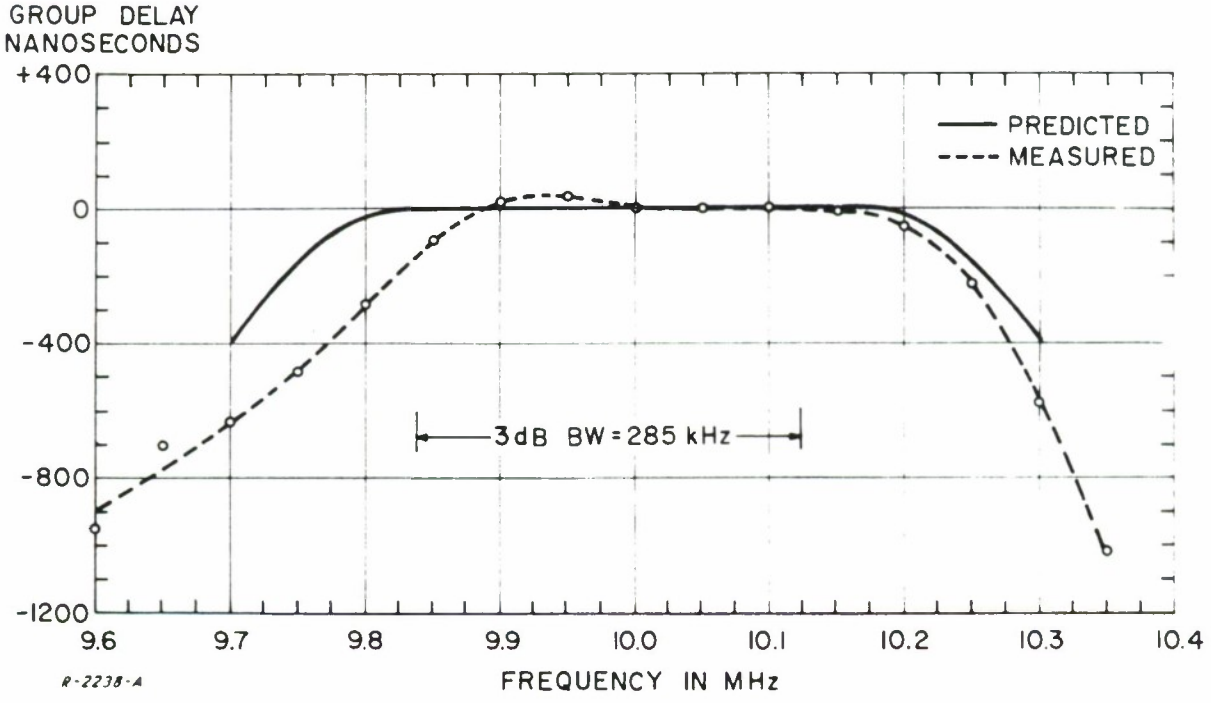

Figure 17 Measured and Predicted Group-Delay Characteristic of 300 kHz Linear-Phase IF Amplifier of Receiver B.

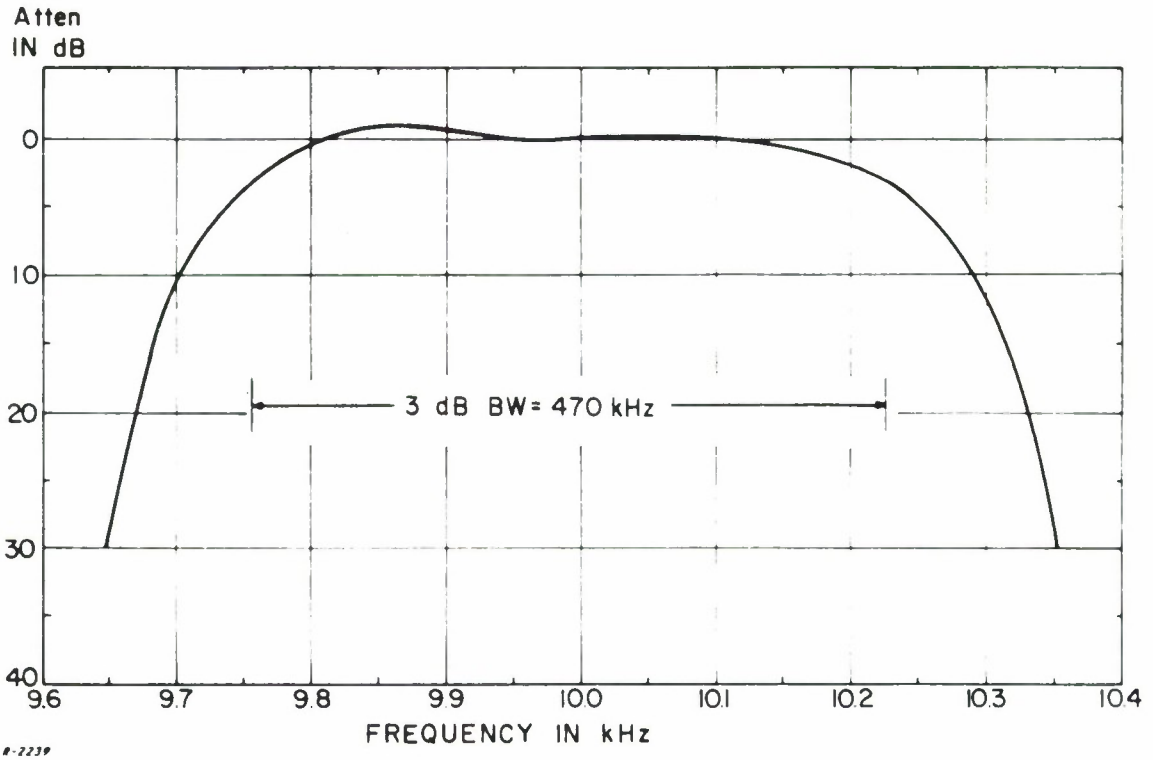

Figure 18 Measured Amplitude Characteristic of 500 kHz IF Amplifier of Receiver C.

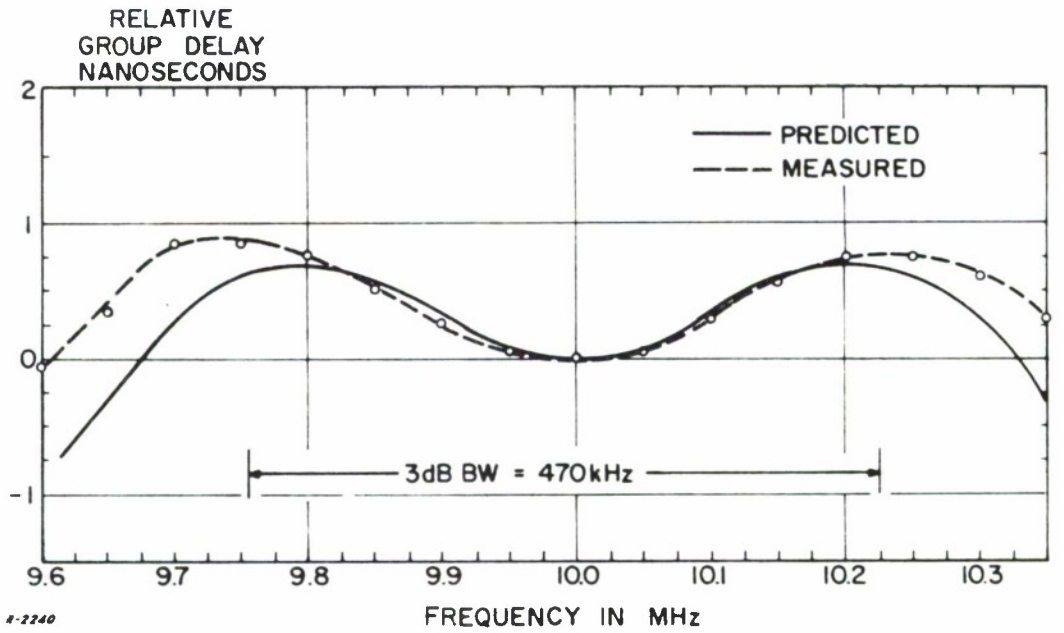

Figure 19 Measured and Predicted Group-Delay Characteristic of 500 kHz IF of Receiver C.

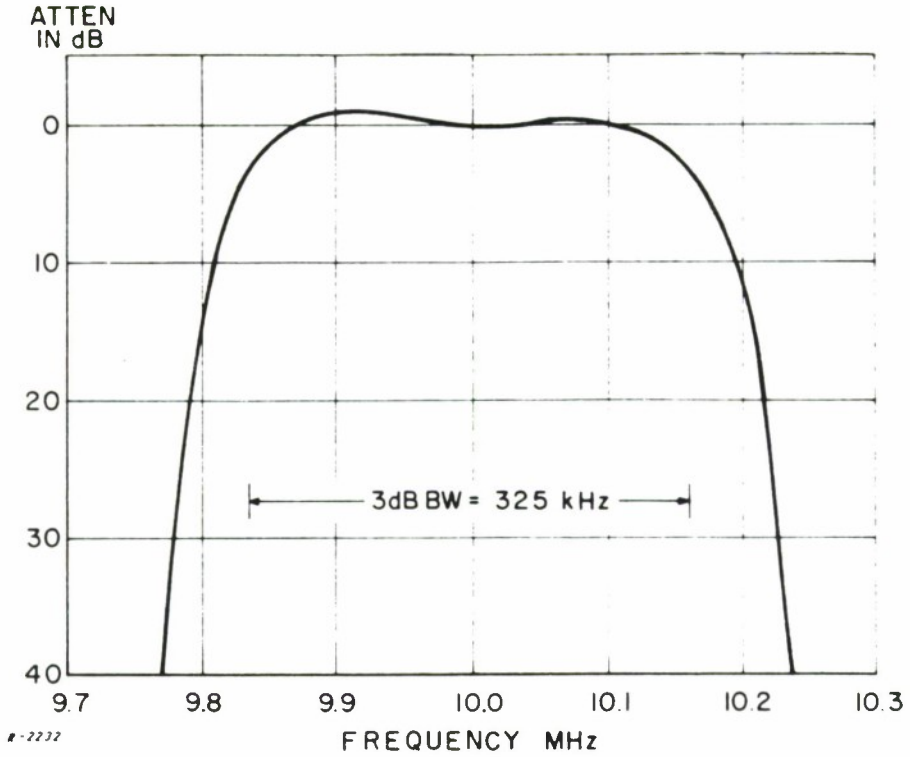

Figure 20 Measured Amplitude Characteristic of 300 kHz IF Amplifier of Receiver C.

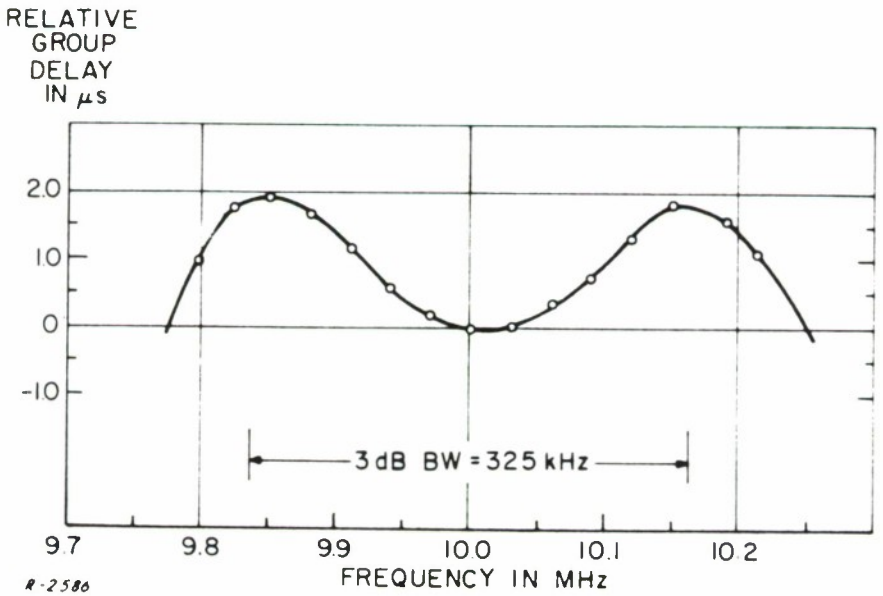

Figure 21 Measured Group-Delay Characteristic of Receiver C 300 kHz IF Amplifier.

converter. For the tests conducted here a record frequency of 450 kHz was selected, since this is the one with which distortion tests were also conducted.

The amplitude characteristic of the down/up converter is shown in Fig. 22. There is approximately 3 dB ripple across the band. The converter is made up of essentially five double-tuned circuits, two in the down-converter and three in the up-converter. The ripple shown here is due to some misalignment in these circuits. The discontinuity in amplitude characteristic at 10.450 MHz is due to a zero beat between the local oscillator in the down-converter and the test signal. In operation this offset (450 kHz) should always be kept greater than half the desired signal bandwidth. Otherwise distortion would be introduced in the form of spectral foldover around zero frequency in the output of the down-converter.

The measured group delay of the down/up converter is plotted in Fig. 23. Here the effect of the discontinuity in the amplitude characteristic is seen as a large variation in the group-delay curve, which covers a wider range of frequency than the amplitude discontinuity. This illustrates one of the benefits of measuring the group-delay characteristic, since it is not always possible to tell the severity of group-delay variations from the amplitude characteristic. In addition to the discontinuity in group delay due to the LO zero beat, the remainder of the curve displays significant nonlinearity, with peaks at each end of the bandpass and a dip in group delay at the center frequency. In all respects this group-delay characteristic reflects quite a bit of phase nonlinearity which will produce intermodulation distortion.

2.7.2 Measurements on Down-Converter/Direct-Demodulator

A second type of predetection-converter unit was available for testing. This converter was supplied with Receiver B. This unit replaces the up-converter in the usual predetection converter with a demodulator, thus obviating the need for translation up to the receiver demodulator. Thus, the unit of interest as far as amplitude and group-delay measurements are concerned is the down-converter. The record frequency used in this test was also 450 kHz and the amplitude and group delay were measured as a function of the down-converter input frequency.

The amplitude characteristic is drawn in Fig. 24, again showing a discontinuity due to the LO and test signal zero beat. The amplitude response is quite flat showing no inband ripple except for the discontinuity. The group delay is shown in Fig. 25. Here again the discontinuity in amplitude corresponds to large variations in group delay. However, except for the discontinuity, the group-delay curve is quite flat indicating that this converter should introduce less distortion than the down/up converter of Section 2.7.1. This expectation is verified by the distortion measurements reported later.

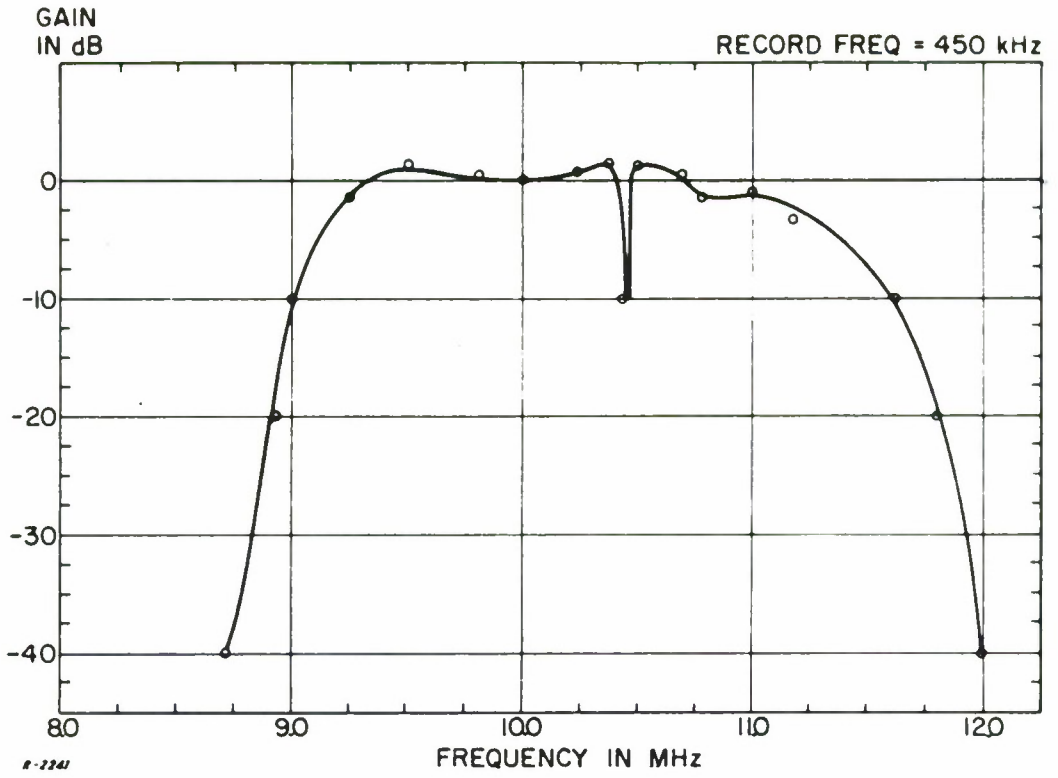

Figure 22 Measured Amplitude Characteristic of Down/Up Converter.

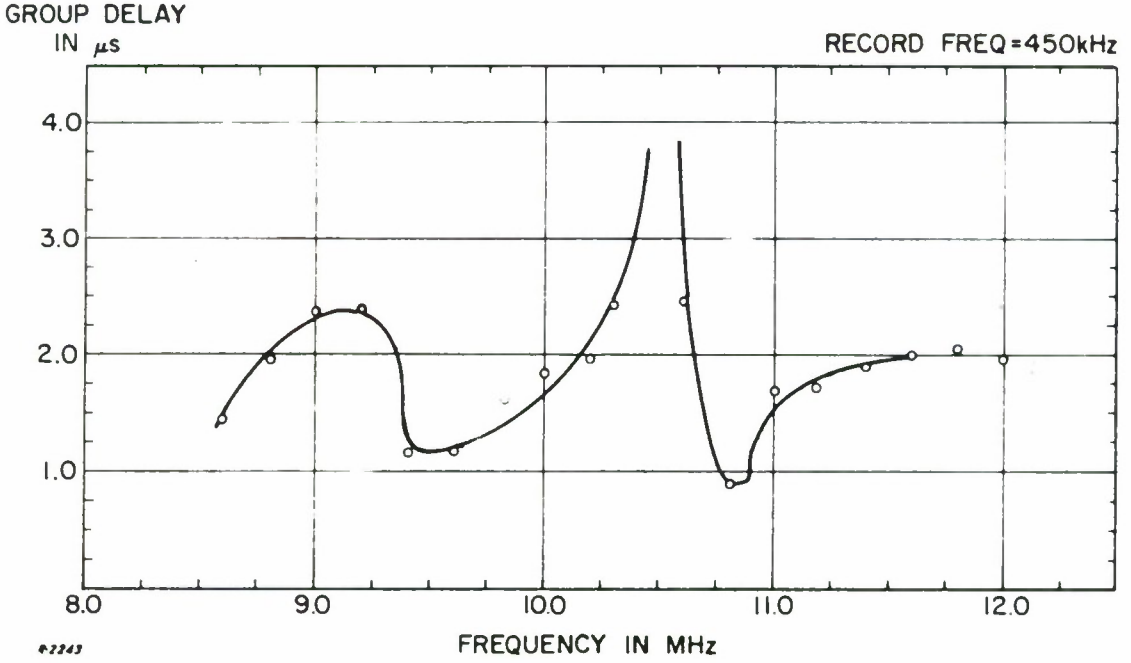

Figure 23 Measured Group-Delay Characteristic of Down/Up Converter.

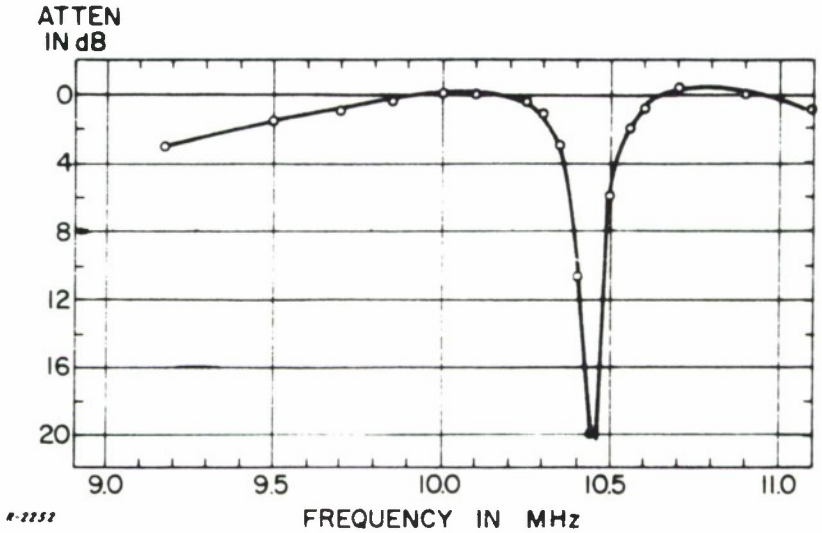

Figure 24 Measured Amplitude Characteristic of Down-Converter/Direct-Demodulator.

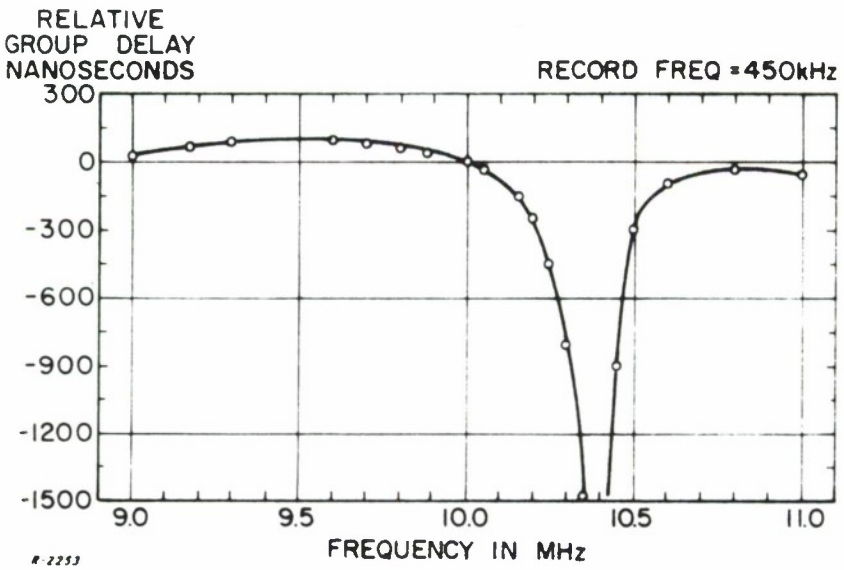

Figure 25 Measured Group-Delay Characteristic of Down-Converter/Direct-Demodulator.

2.8 Measurements of Predetection Recorder/Reproducer Characteristics

The predetection recorder/reproducer on which measurements were conducted is a wideband instrumentation recorder having a 2 MHz 3 dB bandwidth and an equalized phase characteristic to reduce the group-delay variations. The group-delay measurement was made with the Wandel u. Goltermann LD-1 Test Set described in Subsection 2.3. This equipment is limited to a low frequency capability of 100 kHz, hence the lack of measured data below this frequency.

The amplitude and group-delay characteristics for the recorder/reproducer are depicted in Fig. 26. It can be seen that the amplitude characteristic has about 3 dB ripple across the 2 MHz bandwidth. The group delay also has ripple but this is held within about 300 nanoseconds across the band by delay equalization. This delay variation is low compared with some of the other elements in the system and thus should not introduce significant distortion.

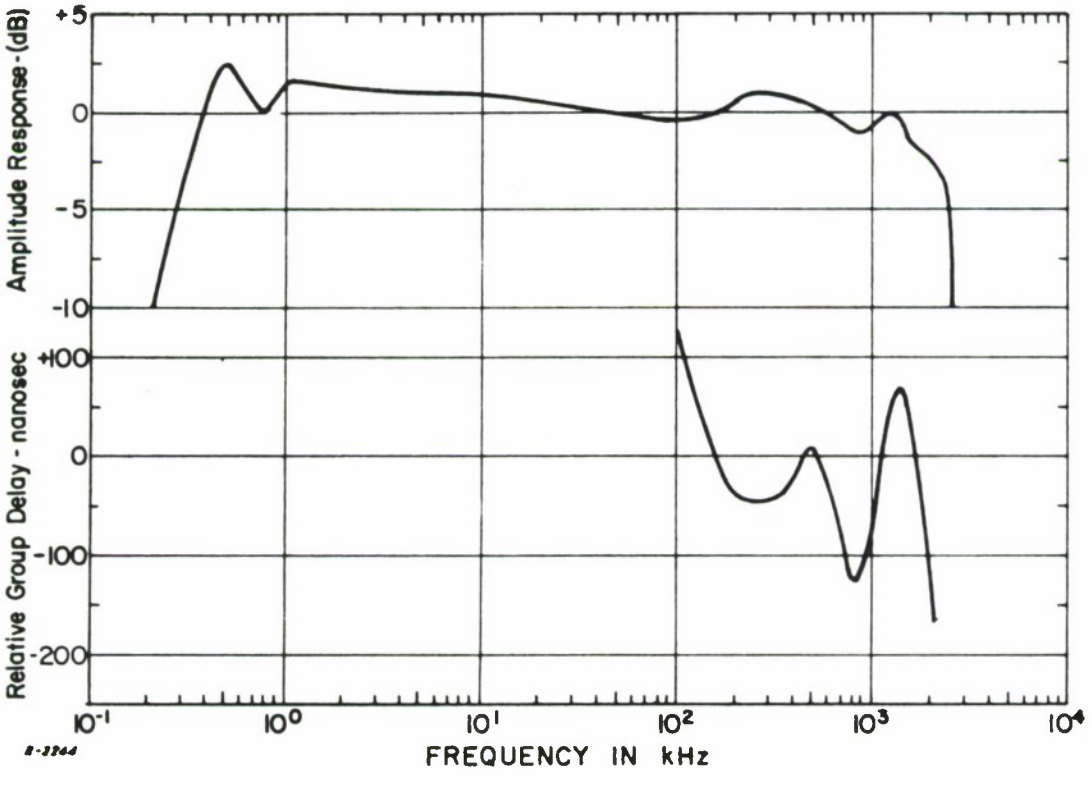

Figure 26 Measured Amplitude and Relative Group-Delay Characteristics of Recorder/Reproducer.

2.9 Conclusions

We have shown that the group-delay characteristic is a convenient and effective method for presenting and investigating the nonlinear phase characteristics in predetection filters of a telemetry system. Theoretical computations of the group delay of several commonly used filter types have been made and a comparison of these indicates that the Bessel filter has the flattest group delay. Measurements have been made of the amplitude and group delay of typical components in a telemetry system including three receivers, two predetection converters and a recorder/reproducer. Theoretical predetections for the group delay of the receiver second IF amplifiers have been compared with the measured values. In most cases, the agreement is quite good, and where discrepancies exist examination of the amplitude characteristic confirms the conclusion that the filters are misaligned.

Confidence has been established in the accuracy of the relatively simple group-delay measuring technique developed for measurements on the receivers and converters. This was accomplished by comparing the measurement using it with the measurement obtained with the Wandel u. Goltermann LD-1 Test Set on the same filter (see Fig. 27). The filter used was the 300 kHz linear phase plug-in for the second IF of Receiver B. This filter had the lowest measured group delay of all those tested and thus should show up any discrepancies in measurement accuracy. The agreement between these two techniques shown in Fig. 27 is excellent with only about 30 nanoseconds discrepancy, indicating that the direct group-delay technique is sufficiently accurate for measuring the group-delay variations anticipated in typical telemetry systems.

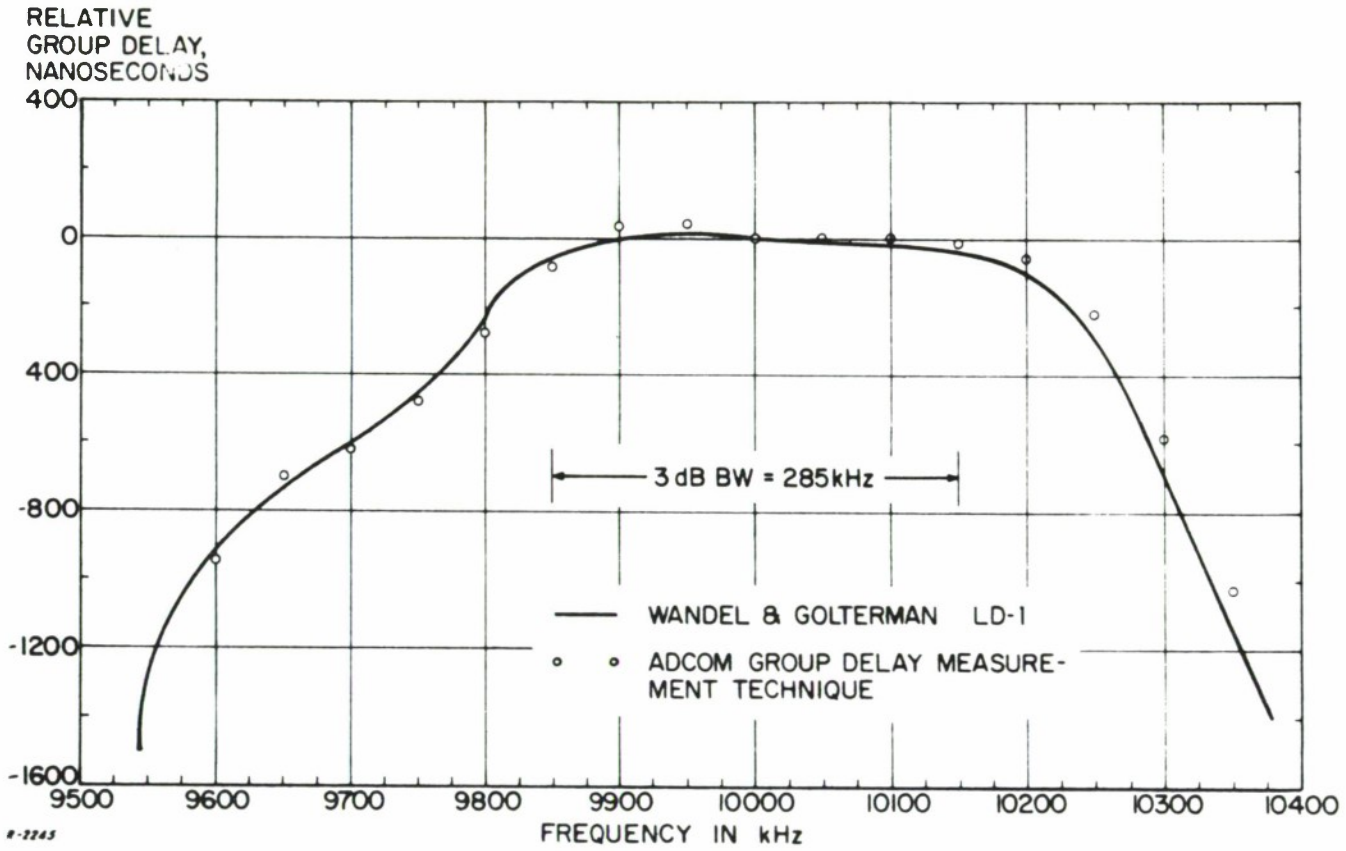

Figure 27 Measured Group-Delay Characteristic of 300 kHz Linear-Phase IF of Receiver B.

Section III

PREDETECTION FILTERING OF ANGLE-MODULATED SIGNALS

3.1 Introduction

An angle-modulation system comprises three main subsystems, as depicted in Fig. 28. Both the angle modulator and demodulator subsystems (which are assumed ideal) perform nonlinear operations. If the filter between these two subsystems is very broadband, then the distortion (or spectrum-spreading) introduced by the angle modulator is perfectly equalized by the FM demodulator. However, if the filter alters the RF signal in any way other than by pure attenuation and/or pure time delay, then the demodulator is no longer a perfect equalizer for the filter output signal, and nonlinear distortion of the demodulated output signal results.

In general, analysis of the properties of a nonlinear system is quite difficult. In the next section an analytic expression is found for the input-output transfer relation of the system of Fig. 28. Unfortunately, this does not permit easy calculation of the desired properties (e. g., intermodulation spectrum in FDM or pulse stretching in TDM). However, Section 3.3 presents a linearized transfer relation which is later shown (Section IX) to be adequate for predicting pulse stretching (as opposed to pulse shaping) in TDM telemetry. Correspondingly, in Section 3.4, the quasi-stationary transfer relation which holds under the conditions of FDM telemetry is derived. In a later section of the report, the quasi-stationary transfer relation is applied to calculate intermodulation spectra. The final subdivision of this section consists of a derivation of a transfer relation which is, in essence, a refinement of the quasi-stationary relation to apply to more general situations. It may be necessary to use this in certain unusual FDM situations.

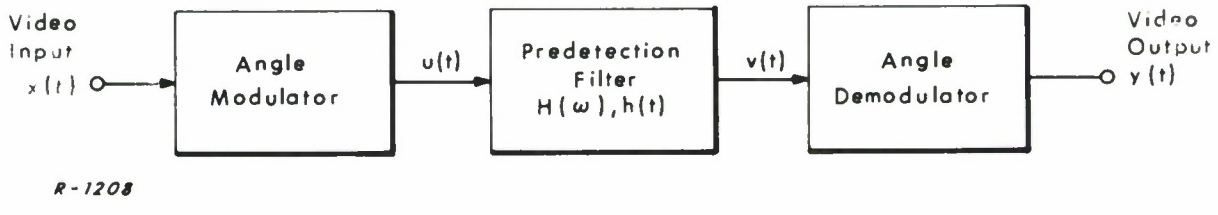

Figure 28 Simplified Block Diagram of an Angle-Modulation System.

3.2 The General Transfer Relation

An angle-modulated signal can be expressed as

$$u(t) = A \sin [\omega_c t + \phi(t)] \tag{20}$$

where A is the amplitude, ω_c is the angular frequency of the carrier and $\phi(t)$ is the instantaneous phase modulation. With an ideal frequency modulator the relation between the input video signal x(t) and the phase $\phi(t)$ is given by

$$\phi(t) = \omega_e \int_{-\infty}^{t} x(\tau)\, d\tau \tag{21}$$

or

$$\frac{d\phi(t)}{dt} = \omega_e x(t) \tag{22}$$

If we normalize the video signal x(t) so that its mean is zero and its mean-square is unity, then ω_e represents the rms frequency deviation. By expanding the sine, Eq. (20) can also be expressed as

$$u(t) = A\{\cos\phi(t) \sin \omega_c t + \sin\phi(t) \cos\omega_c t\} \tag{23}$$

It is clear from Eq. (23) that the frequency modulated signal may be viewed as the result of nonlinear amplitude modulation of two quadrature carriers of identical frequency. The mathematical operations of the frequency modulation process are illustrated in Fig. 29. Here the video signal x(t) is first passed through an integrator after which it is fed to two memoryless nonlinearities having the characteristics $\cos[\cdot]$ and $\sin[\cdot]$. The outputs from these nonlinearities are then multiplied by the two quadrature components of the carrier. Phase modulation differs only in that $\phi(t)$ is the input video signal, and $\theta(t)$ is the output video signal.

The angle-modulated RF signal passes through the predetection filter, whose output can be expressed as

$$v(t) = B(t) \sin [\omega_c t + \theta(t)] \tag{24}$$

where b(t) is the amplitude modulation introduced by the filter and $\theta(t)$ is the instantaneous phase modulation of the RF signal after filtering. In order to express B(t) and $\theta(t)$ in terms of the input to the filter, we first express v(t) in terms of u(t) by the convolution

$$v(t) = \int_{-\infty}^{\infty} h(\tau)\, u(t - \tau)\, d\tau \tag{25}$$

where h(t) is the RF impulse response of the filter. Combining Eqs. (23), (24) and (25) results in

$$v(t) = B(t) \sin [\omega_c t + \theta(t)] =$$

$$A \int_{-\infty}^{\infty} h(\tau) \{ \cos \phi(t-\tau) \sin \omega_c (t-\tau) + \sin \phi(t-\tau) \cos \omega_c (t-\tau) \} \, d\tau \tag{26}$$

The desired transfer relation directly relates the output phase modulation $\theta(t)$ to the input phase modulation $\phi(t)$. To derive such a relation, we need a low-frequency model of the predetection filter. The filter impulse response h(t) can be written in terms of its low-frequency cophasal and quadrature components $h_p(t)$ and $h_q(t)$ in the following manner

$$h(t) = 2h_p(t) \cos \omega_c t + 2h_q(t) \sin \omega_c t \tag{27}$$

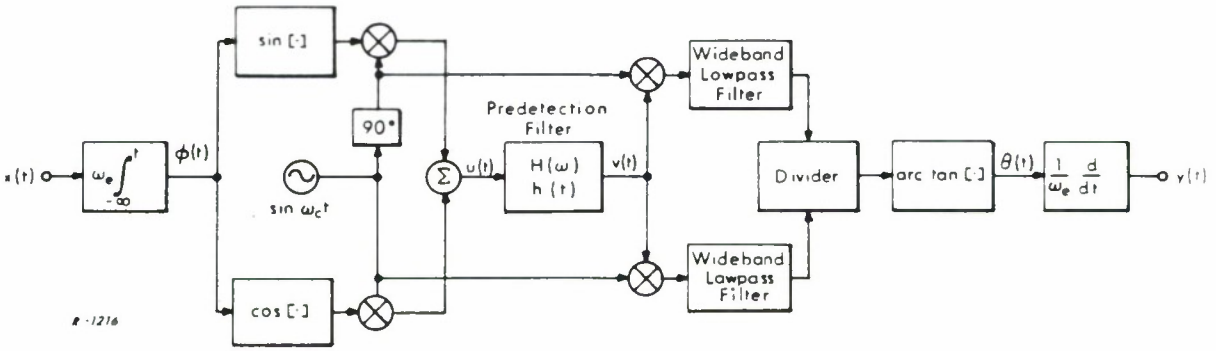

Figure 29 Block Diagram Illustrating the Mathematical Operations in an FM System. (Applied to a PM System if the Integrator and Differentiator Are Eliminated.)

Let the filter transfer function $H(\omega)$ be expressed as

$$H(\omega) = \begin{cases} H_1(\omega) & \text{for } \omega > 0 \\ H_2(\omega) & \text{for } \omega < 0 \end{cases} \tag{28}$$

where $H_1(\omega)$ and $H_2(\omega)$ are the positive- and negative-frequency parts of $H(\omega)$ (see Fig. 30). Then it can be shown (see Ref. 3, p. 131) that the lowpass transfer functions $H_p(\omega)$ and $H_q(\omega)$ corresponding to $h_p(t)$ and $h_q(t)$ are given by

$$H_p(\omega) = \frac{H_1(\omega + \omega_c) + H_2(\omega - \omega_c)}{2} \tag{29}$$

$$H_q(\omega) = \frac{H_2(\omega - \omega_c) - H_1(\omega + \omega_c)}{2j} \tag{30}$$

Figure 30 illustrates how $H_p(\omega)$ and $H_q(\omega)$ are determined by combinations of shifted replicas of $H_1(\omega)$ and $H_2(\omega)$. It is clear from Eq. (30) and Fig. 30 that

$$H_q(0) = \int_{-\infty}^{\infty} h_q(t)\, dt = 0 \tag{31}$$

and that a filter with a perfectly symmetric characteristic about its center frequency will have $H_q(\omega)$ equal to zero everywhere. Thus, $H_p(\omega)$ represents the symmetric part and $H_q(\omega)$ the antisymmetric part of the predetection filter. Moreover, since the video signal is not affected by the absolute gain and phase levels of the predetection filter we may set

$$|H(\omega_c)| = H_p(0) = \int_{-\infty}^{\infty} h_p(t)\, dt = 1 \tag{32}$$

and

$$\underline{/H}(\omega_c) \triangleq \Phi(\omega_c) = 0 \tag{33}$$

without any loss of generality. $\Phi(\omega)$ has been defined in Eq. (33) to be the phase characteristic of the predetection filter.

Combining Eqs. (26) and (27) and realizing that both $H_p(\omega)$ and $H_q(\omega)$ reject double-frequency components at $\omega = 2\omega_c$, we obtain the cophasal and quadrature components of the filter output after some trigonometric manipulations

$$v(t) = B(t) \sin [\omega_c t + \theta(t)] = A \sin \omega_c t \left\{ \int_{-\infty}^{\infty} h_p(\tau) \cos \phi(t - \tau) \right.$$

$$\left. + \int_{-\infty}^{\infty} h_q(\tau) \sin \phi(t - \tau)\, d\tau \right\} + A \cos \omega_c t \left\{ \int_{-\infty}^{\infty} h_p(t) \sin \phi(t - \tau)\, d\tau \right.$$

$$\left. - \int_{-\infty}^{\infty} h_q(\tau) \cos \phi(t - \tau)\, d\tau \right\} \qquad (34)$$

We are now able to express the amplitude modulation B(t) and the phase modulation $\theta(t)$ of the output RF signal in the following forms

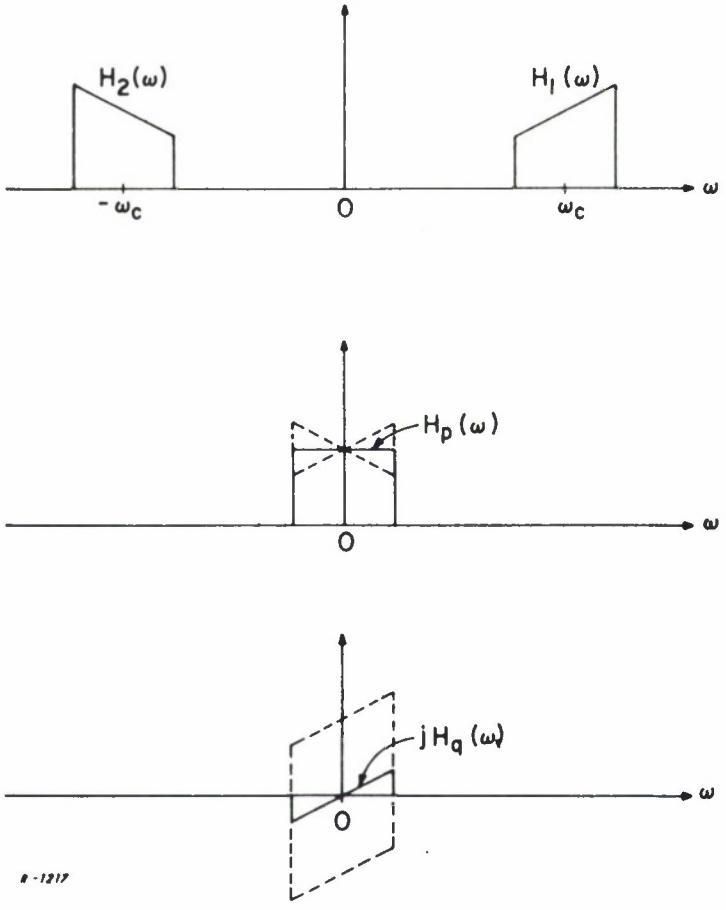

Figure 30 Illustration of the Operations in Eqs. (20) and (21).

$$\frac{B^2(t)}{A^2} = \left\{ \int_{-\infty}^{\infty} h_p(t) \cos\phi(t-\tau)\, d\tau + \int_{-\infty}^{\infty} h_q(\tau) \sin\phi(t-\tau)\, d\tau \right\}^2$$

$$+ \left\{ \int_{-\infty}^{\infty} h_p(t) \sin\phi(t-\tau)\, d\tau - \int_{-\infty}^{\infty} h_q(\tau) \cos\phi(t-\tau)\, d\tau \right\}^2 \quad (35)$$

and

$$\theta(t) = \arctan \frac{\int_{-\infty}^{\infty} h_p(\tau) \sin\phi(t-\tau)\, d\tau - \int_{-\infty}^{\infty} h_q(\tau) \cos\phi(t-\tau)\, d\tau}{\int_{-\infty}^{\infty} h_p(\tau) \cos\phi(t-\tau)\, d\tau + \int_{-\infty}^{\infty} h_q(\tau) \sin\phi(t-\tau)\, d\tau} \quad (36)$$

Equation (35) expresses the PM-to-AM conversion introduced by the predetection filter. If the demodulator is not completely amplitude insensitive (i. e., if the amplitude limiters are not ideal) then some of this AM will appear in the video output as intermodulation distortion. In the present context, however, we can assume that the limiters perform ideally and turn our attention to the desired transfer relation expressed in Eq. (36).

An ideal angle demodulator extracts $\theta(t)$ from the RF signal, then differentiates the output to yield the frequency modulation. The mathematical operations of the angle demodulation process are illustrated in Fig. 29. Here the quadrature components of the filter output are resolved by multipliers, followed by wideband lowpass filters which filter out the $2\omega_c$ components in the multiplier outputs. The ratio of the resulting signals is then formed in a divider and passed through a memoryless nonlinearity having an arctangent characteristic. According to Eq. (36) the output from this nonlinearity is $\theta(t)$, which is the PM video signal. The FM video signal y(t) is obtained by differentiating $\theta(t)$.

At this point it should be noted that no approximations have been used to derive Eq. (36); this equation is perfectly general. Nevertheless, its complexity necessitates finding less complicated approximations to it. As has been discussed in Section 3.1 there exist two cases for which the transfer relation can be simplified considerably. These cases are the low-deviation case and the quasi-stationary case.

3.3 The Transfer Relation in the Low-Deviation Case

Narrowband angle modulation is the case in which the resulting phase deviation is so small compared to one radian that $\cos\phi(t) \approx 1$ and $\sin\phi(t) \approx \phi(t)$, so that Eq. (23) can be written approximately

$$u(t) \approx A[\sin\omega_c t + \phi(t)\cos\omega_c t] \quad (37)$$

The right side of Eq. (37) is identical to the expression for an AM signal, except that the carrier component ($\sin \omega_c t$) is phase shifted by 90^o. The angle-modulated signal can thus be viewed as the result of a linear modulation operation. In particular, FM with deviation ratio much smaller than unity fits into this category.

By following the same analytical procedure as in Section 3.2, we can easily show that the phase modulation at the output of the predetection filter may be expressed as

$$\theta(t) = \int_{-\infty}^{\infty} h_p(\tau)\, \phi(t - \tau)\, d\tau \tag{38}$$

Similarly the FM demodulated output is

$$y(t) = \int_{-\infty}^{\infty} h_p(\tau)\, x(t - \tau)\, d\tau \tag{39}$$

It is clear from Eqs. (38) and (39) that the predetection filter has a linear-filtering effect on the modulation just like a video filter. Thus, no intermodulation distortion is caused by the filter in this case, irrespective of its phase characteristic. The same conclusion holds true for amplitude-modulated signals.

3.4 The Transfer Relation in the Quasi-Stationary Case

The quasi-stationary case is met when the video bandwidth is much smaller than the predetection-filter bandwidth, or equivalently when $\phi(t - \tau)$ changes much more slowly with time than $h_p(\tau)$ or $h_q(\tau)$ in Eq. (36). This is the case if the FM deviation ratio (or the phase deviation) is much greater than unity. We may approximate $\phi(t - \tau)$ by the first two terms of its Taylor series expansion in this case

$$\phi(t - \tau) \approx \phi(t) - \tau \frac{d\phi(t)}{dt} \tag{40}$$

By inserting Eq. (40) in Eq. (36), we show in Appendix I that the output phase modulation is

$$\theta(t) \approx \phi(t) + \Phi[\omega_e x(t) + \omega_c] \tag{41}$$

or the output frequency modulation is

$$y(t) \approx x(t) + \frac{1}{\omega_e} \frac{d}{dt} \{\Phi[\omega_e x(t) + \omega_c]\} \tag{42}$$

where $\Phi(\omega)$ is the phase characteristic of the predetection filter. The instantaneous frequency of the FM signal may be viewed as tracing the phase characteristic of the predetection filter. The distortion is represented by the second terms in Eqs. (41) and (42), and is entirely determined by the (memoryless) nonlinearities in the filter phase characteristic $\Phi(\omega)$. It is not affected by the filter amplitude characteristic.

3.5 Extension of the Quasi-Stationary Transfer Relation to the General Case

In the preceding subsection we found the following transfer relation for the quasi-stationary case (Eq. (41))

$$\theta(t) \approx \phi(t) + \Phi[\omega_e x(t) + \omega_c] \tag{43}$$

For convenience we define a new time function to represent the quasi-stationary distortion waveform in this transfer relation

$$\eta(t) \triangleq \Phi[\omega_e x(t) + \omega_c] \tag{44}$$

Thus the quasi-stationary case corresponds to the transfer relation

$$\theta(t) \approx \phi(t) + \eta(t) \tag{45}$$

In the general case we may represent the exact transfer relation as

$$\theta(t) = \phi(t) + \eta(t) + \epsilon(t) \tag{46}$$

The added term $\epsilon(t)$ represents the complete nonquasi-stationary distortion waveform. In this subsection we will derive an approximate expression for $\epsilon(t)$. The only assumption will be that the filter transfer function is symmetric.

With the assumption of symmetry $h_q(t)$ is zero and the exact transfer relation of Eq. (36) becomes

$$\theta(t) = \tan^{-1} \frac{h_p(t) \boxtimes \sin \phi(t)}{h_p(t) \boxtimes \cos \phi(t)} \tag{47}$$

where $\boxtimes$ indicates convolution. We make use of a Taylor series expansion for the lowpass transfer function

$$H_p(\omega) = a_o + a_1 \left(\frac{j\omega}{B}\right) + a_2 \left(\frac{j\omega}{B}\right)^2 + a_3 \left(\frac{j\omega}{B}\right)^3 + \ldots \tag{48}$$

From the properties of Fourier transforms we can show that Eq. (48) implies that when we convolve $h_p(t)$ with any time function the result is

$$h_p(t) \otimes f(t) = a_o f(t) + \frac{a_1}{B} f'(t) + \frac{a_2}{B^2} f''(t) + \frac{a_3}{B^3} f'''(t) + \ldots \tag{49}$$

where the number of primes denotes the number of differentiations with respect to time. We now define the real and imaginary parts of Eq. (48) as $R(\omega)$ and $X(\omega)$ respectively, and define two additional time functions as

$$F(t) = \frac{a_2}{B^2} \phi'' + \frac{a_3}{B^3} \phi^{(3)} + \frac{a_4}{B^4}\left(\phi^{(4)} - 6\phi'^2\phi''\right) + \frac{a_5}{B^5}\left(\phi^{(5)} - 15\phi'\phi''^2 - 10\phi'^2\phi^{(3)}\right) + \ldots \tag{50}$$

$$G(t) = -3\frac{a_3}{B^3} \phi'\phi'' - \frac{a_4}{B^4}\left(4\phi'\phi^{(3)} + 3\phi''^2\right) - 5\frac{a_5}{B^5}\left(-2\phi'^3\phi'' + \phi'\phi^{(4)} + 2\phi''\phi^{(3)}\right) + \ldots \tag{51}$$

Using these definitions and Eq. (49) we show in Appendix II that we may write

$$\theta(t) \approx \tan^{-1} \frac{\tan\phi + \dfrac{X[\phi'(t)] + F(t)}{R[\phi'(t)] + G(t)}}{1 - \dfrac{X[\phi'(t)] + F(t)}{R[\phi'(t)] + G(t)} \tan\phi(t)} \tag{52}$$

Applying the trigonometric identity for the tangent of a sum, we reduce Eq. (52) to

$$\theta(t) \approx \phi(t) + \tan^{-1} \frac{X + F}{R + G} \tag{53}$$

If we recognize that an alternate expression for the quasi-stationary distortion waveform is

$$\eta(t) = \tan^{-1} \frac{X[\phi'(t)]}{R[\phi'(t)]} \tag{54}$$

we may apply the identity for the tangent of a sum again to Eq. (53), with the result

$$\theta(t) \approx \phi(t) + \eta(t) + \tan^{-1} \frac{\dfrac{X+F}{R+G} - \dfrac{X}{R}}{1 + \dfrac{X+F}{R+G} \cdot \dfrac{X}{R}} \tag{55}$$

This equation is of the same form as Eq. (46), from which we readily identify the nonquasi-stationary term $\epsilon(t)$ with the last term in Eq. (55).

The argument of the arctangent in Eq. (55) is readily simplified to the following form

$$\epsilon(t) \approx \tan^{-1} \frac{R[\phi'(t)]\ F(t) - X[\phi'(t)]\ G(t)}{\left|H_p[\phi'(t)]\right|^2 + R[\phi'(t)]\ G(t) + X[\phi'(t)]\ F(t)} \tag{56}$$

This is the desired result for the nonquasi-stationary distortion term. In Subsection 4.7 we will discuss how this result may be used to obtain a better estimate of the distortion spectrum than that obtained under the quasi-stationary approximation.

Section IV

INTERMODULATION DISTORTION IN FDM TELEMETRY

4.1 Spectral Characterization of Intermodulation Distortion

The obvious way to measure overall intermodulation distortion in a telemetry system is to connect the output of the transmitter via an attenuator to the input of the receiver. (This, of course, will not take into account the distortion caused by the antenna feeders and the propagation medium.) Then all but one of the data channels are fed with appropriate signals and the output power of the empty channel is measured. Since the output from the empty channel is only intermodulation distortion (assuming negligible interchannel crosstalk), one can compute an intermodulation noise-to-signal power ratio (I/S ratio) for the particular data channel by dividing the measurement obtained in the unloaded channel by the signal power measured when the particular data channel is fully loaded. From the measurements of the I/S ratio for each channel a bar graph can be plotted showing the I/S ratio versus the frequency location of the channel in the video spectrum.

In order to simplify and standardize the measurement of intermodulation noise, the video signal at the input to the FM modulator is conveniently simulated by a gaussian noise process covering the bandwidth of the video signal. It can be shown that the statistical properties of gaussian noise are very similar to a complex multichannel (FDM) video signal. Thus it is meaningful to simulate the video signal in a telemetry system by a gaussian process. When this noise-loading technique is used, it is necessary to shape the power-density spectrum of the applied noise signal with a filter so that the resulting signal has approximately the same power-density spectrum as the actual video signal.

Figure 31 shows a block diagram of the noise-loading technique. In order that the intermodulation distortion noise at the demodulator output be measured, an "empty channel" has to be simulated in the input spectrum by a narrowband reject filter (see Fig. 32). The power measured in a corresponding narrow bandpass filter at the output constitutes the intermodulation distortion noise power. By switching out the reject filter it is possible to measure the signal power in the bandpass filter and compute the I/S ratio. If this measurement is performed for different video frequencies a curve of I/S density ratio vs video frequency can be constructed as shown in Fig. 33. This curve exhibits the increased intermodulation noise with video frequency commonly encountered in FM systems.

In addition to being analytically convenient, the noise-loading approach greatly simplifies experimental verification. Intermodulation distortion tests can be standardized and the measurements easily reproduced. In contrast,

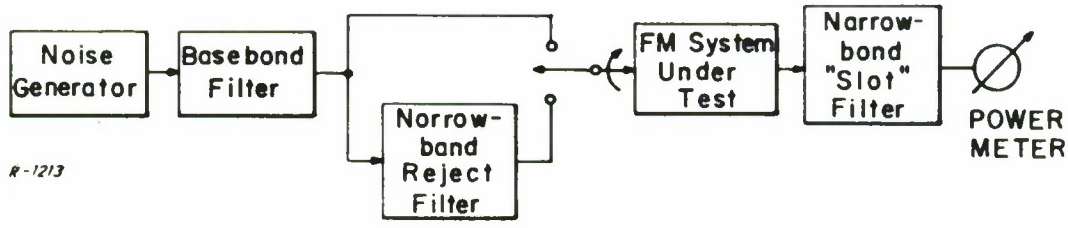

Figure 31 Noise-Loading Technique for Measurement of Intermodulation Distortion.

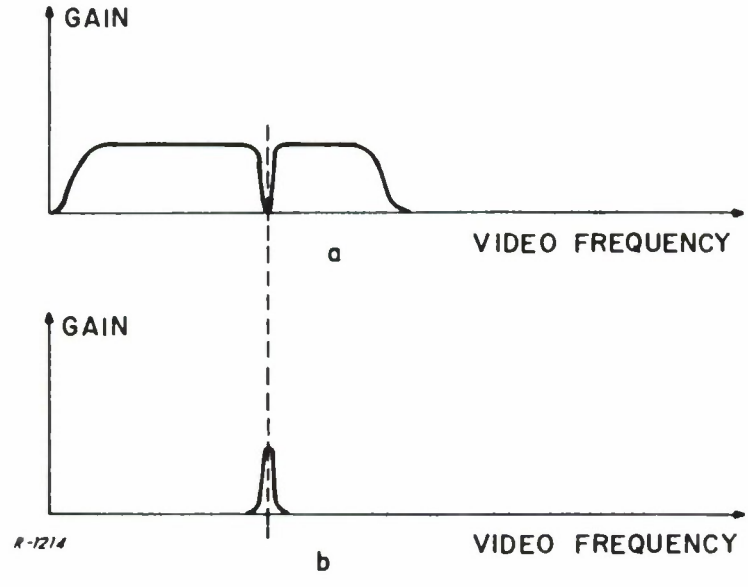

Figure 32 a) Amplitude Characteristic of Spectral-Shaping Filter for the Noise-Loading Technique.

b) Amplitude Characteristic of Narrowband "Slot" Filter.

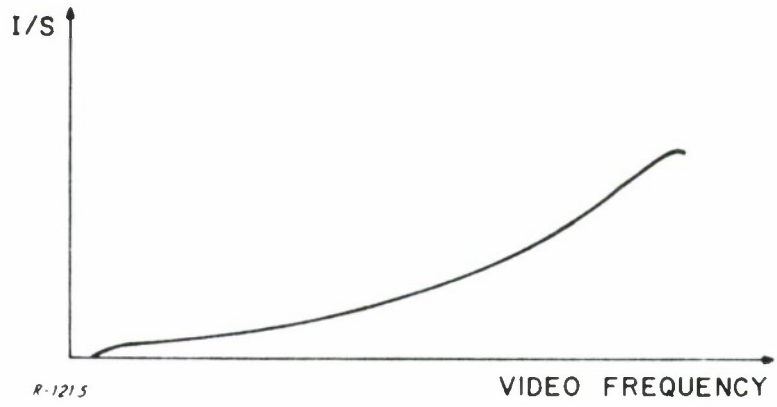

Figure 33 Typical Curve of Intermodulation Noise-to-Signal Ratio vs Video Frequency.

we believe that the customary method of simulating the video signal by a set of unmodulated subcarriers is inadequate. It is both mathematically intractable (except in the trivial case of one or two subcarriers) and experimentally cumbersome.

Because of the relative simplicity of the noise-loading test it is very common to specify intermodulation distortion in terms of a gaussian noise input signal (as, for example, in FDM/FM telephony). It would be very useful to be able to predict the amount of intermodulation distortion in a given system caused by a given phase nonlinearity, so that the susceptibility of the design to this type of distortion could be determined prior to the construction of the equipment. In the remainder of this section we present effective analytical techniques for evaluating the intermodulation distortion spectrum in the quasi-stationary case, in terms of the parameters of the filter and the video signal.

4.2 Distortion Spectrum in the Quasi-Stationary Case

We wish to compute the power-density spectrum of the intermodulation distortion represented by the second term of Eq. (42). It is convenient to begin by computing the power-density spectrum of the PM distortion term of Eq. (41). The procedure is to represent this term by a power series in x(t), then find its autocorrelation function $R_\theta(\tau)$ in terms of the autocorrelation function $R_x(\tau)$ of the input FM video signal and the coefficients of the power series. Fourier transformation of $R_\theta(\tau)$ yields the power-density spectrum I_θ of the PM distortion. Finally, the PM distortion term is simply related to the FM distortion term by scaling and differentiation (see Eq. (22)); consequently their power-density spectra are also simply related by

$$I_y = \left(\frac{\omega}{\omega_e}\right)^2 I_\theta \tag{57}$$

This yields the desired distortion spectrum, which when divided by the input video spectrum S_x yields the I/S ratio.

We begin by expanding the phase characteristic $\Phi(\omega)$ in a power series:

$$\Phi(\omega) = \sum_{i=0}^{\infty} c_i \left(\frac{\omega - \omega_c}{B}\right)^i \tag{58}$$

where we define B as half the bandwidth of the predetection filter, and c_i as the power-series coefficients. Now, the first term c_o represents the carrier phase shift which we have already set to zero in Eq. (33). Moreover, the second term $c_1(\omega - \omega_c)/B$ represents overall group delay which does not produce distortion, so we may set c_1 to zero without loss of generality. One familiar power series which takes the form of Eq. (58) is the Taylor series. In this case the c_i's are the Taylor coefficients given by

$$c_i = \frac{1}{i!} \left.\frac{d^i \Phi(\omega)}{d(\omega/B)^i}\right|_{\omega = \omega_c} \tag{59}$$

Combining Eq. (58) with the PM distortion term of Eq. (41) we have

$$\Phi[\omega_e x(t) + \omega_c] = \sum_{i=0}^{\infty} c_i \left[\frac{\omega_e}{B} x(t)\right]^i \tag{60}$$

Now, Thomson (Ref. 9) has shown that for gaussian inputs

$$R_\theta(\tau) = \sum_{n=0}^{\infty} n!\, R_x^n(\tau) \left[\sum_{k=0}^{\infty} \frac{(n+2k)!}{2^k k!\, n!}\, c_{n+2k} \left(\frac{\omega_e}{B}\right)^{n+2k}\right]^2 \tag{61}$$

The zero-order term (n=0) represents the dc component of the output which is of no practical interest and may be dropped. The first-order term n=1 is a linear undistorted component, so we drop it in computing the distortion spectrum.

In what follows we will use a normalized Fourier transformation to obtain the power-density spectrum

$$S(\nu) = \frac{\hat{\omega}}{2\pi} \int_{-\infty}^{\infty} R(\tau) \cos \hat{\omega} \nu \tau \, d\tau \tag{62}$$

This is convenient because the normalized video frequency $\nu = \omega/\hat{\omega}$ (range (0,1)) takes the place of the actual video frequency ω (range $(0, \hat{\omega})$). Our definition also differs from the normal one by a factor of $\hat{\omega}/(2\pi)$; this is to preserve the property that the spectrum of a process with unity mean-square value will have an area of one in the (S, ν) plane. This will not affect the magnitude of our results because we will be interested in the ratio of intermodulation spectrum to signal spectrum.

Applying Eq. (62) to Eq. (61) yields the PM distortion spectrum

$$I_\theta(\nu) = \sum_{n=2}^{\infty} n! \, S_x^{(n)}(\nu) \left[\sum_{k=0}^{\infty} \frac{(n+2k)!}{2^k k! n!} \, c_{n+2k} \left(\frac{\omega_e}{B} \right)^{n+2k} \right]^2 \tag{63}$$

where

$$S_x^{(n)}(\nu) \triangleq \underbrace{S_x(\nu) \boxtimes S_x(\nu) \boxtimes \ldots \boxtimes S_x(\nu)}_{n \text{ terms}} \tag{64}$$

denotes the $(n-1)^{th}$ convolution of $S_x(\nu)$ with itself.

Finally, we use Eq. (57) and divide by $S_x(\nu)$ to obtain the desired I/S ratio as a function of normalized video frequency.

$$\frac{I_y(\nu)}{S_x(\nu)} = \left(\frac{\hat{\omega}\nu}{\omega_e} \right)^2 \sum_{n=2}^{\infty} n! \, \frac{S_x^{(n)}(\nu)}{S_x(\nu)} \left[\sum_{k=0}^{\infty} \frac{(n+2k)!}{2^k k! n!} \, c_{n+2k} \left(\frac{\omega_e}{B} \right)^{n+2k} \right]^2 \tag{65}$$

4.3 Discussion of the General Result on Distortion Spectrum

It is instructive to write out a few distortion terms from the general result of Eq. (65)

$$I_y(\nu) = 2!\,(\frac{\hat{\omega}}{B})^2\,(\frac{\omega_e}{B})^2\nu^2\,S_x^{(2)}(\nu)\,[\,c_2 + 6\,c_4(\frac{\omega_e}{B})^2 + 45\,c_6(\frac{\omega_e}{B})^4 + \ldots]^2$$

$$+ 3!\,(\frac{\hat{\omega}}{B})^2\,(\frac{\omega_e}{B})^4\nu^2\,S_x^{(3)}(\nu)\,[\,c_3 + 10\,c_5\,(\frac{\omega_e}{B})^2 + 105\,c_7(\frac{\omega_e}{B})^4 + \ldots]^2$$

$$+ 4!\,(\frac{\hat{\omega}}{B})^2\,(\frac{\omega_e}{B})^6\nu^2\,S_x^{(4)}(\nu)\,[\,c_4 + 15\,c_6\,(\frac{\omega_e}{B})^2 + \ldots\,]^2$$

$$+ 5!\,(\frac{\hat{\omega}}{B})^2\,(\frac{\omega_e}{B})^8\nu^2\,S_x^{(5)}(\nu)\,[\,c_5 + 21\,c_7\,(\frac{\omega_e}{B})^2 + \ldots\,]^2$$

$$+ \ldots . \qquad (66)$$

The first line of Eq. (66) represents second-order distortion, the second line represents third-order distortion, etc. It can be seen that an even-power coefficient (c_i) contributes only to all even-ordered distortion up to order i, while an odd-power coefficient (c_j) contributes only to all odd-ordered distortion up to order j. Now, a symmetric filter has an anti-symmetric phase characteristic $\Phi(\omega)$, so that all its even-order coefficients vanish. Consequently a symmetric filter will introduce only odd-ordered distortion. Comparing the various odd-order terms we see that successive terms are reduced in magnitude by the factor $(\omega_e/B)^4$. Thus the third-order term will usually predominate over the fifth- and higher-order terms. Therefore the I/S ratio for symmetric filters is given approximately by

$$\frac{I_y(\nu)}{S_x(\nu)} \approx 3!\left(\frac{\hat{\omega}}{B}\right)^2\left(\frac{\omega_e}{B}\right)^4 \frac{\nu^2 S_x^{(3)}(\nu)}{S_x(\nu)} \left[c_3 + 10\,c_5\left(\frac{\omega_e}{B}\right)^2 + 105\,c_7\left(\frac{\omega_e}{B}\right)^4 + \ldots\right]^2 \qquad (67)$$

In Appendix III the result of Eq. (66) is obtained in a different form involving Hermite polynomials, which may be more useful when making predictions from experimental data.

We now have in Eq. (67) a general result relating the intermodulation distortion spectrum to the parameters of the filter and the video signal. The spectrum of the input video signal appears only in the form of a double convolution. The factor in which this appears

$$\frac{\nu^2 S_x^{(3)}(\nu)}{S_x(\nu)} \qquad (68)$$

completely determines the shape of the distortion spectrum. The effect of input spectral shape on distortion spectral shape is discussed in the next subsection. The magnitude of the distortion is determined in part by the factor

$$3!\left(\frac{\hat{\omega}}{B}\right)^2\left(\frac{\omega_e}{B}\right)^4 \tag{69}$$

which involves only the normalized video bandwidth ($\hat{\omega}/B$) and the normalized rms deviation (ω_e/B). The other factor determining the magnitude is

$$\left[c_3 + 10\,c_5\left(\frac{\omega_e}{B}\right)^2 + 105\,c_7\left(\frac{\omega_e}{B}\right)^4 + \ldots\right]^2 \tag{70}$$

which involves the filter phase coefficients in conjunction with the normalized rms deviation. The type of filter influences the magnitude of the distortion spectrum solely through this factor. Section 4.5 presents the coefficients for the various filter types encountered in this study, while Section 4.6 discusses the manner in which distortion accumulates in a cascade of filter stages.

The three factors identified above (Eqs. (68) through (70)) may be obtained readily in dB's and added to obtain the I/S ratio. The first factor (Eq. (68)) can be taken directly from Fig. 34 for any desired value of ν. The second factor (Eq. (69)) requires only a rapid calculation and conversion to dB's. The third factor (Eq. (70)) is tabulated in Section XI for various filter types and for selected values of (ω_e/B). Interpolation may give sufficient accuracy for intermediate values of (ω_e/B); if not, the coefficients c_i are available for direct calculation in Subsection 4.5.

4.4 The Effect of Video-Spectrum Shape on the Distortion Spectrum

In the preceding section we identified the factor

$$\frac{\nu^2 S_x^{(3)}(\nu)}{S_x(\nu)} \tag{71}$$

which determines the shape of the I/S curve. In this section we consider two possible input spectra and calculate the shape of the resulting I/S curves. The two input spectra are shown in Fig. 35. The rectangular spectrum results when a rectangular video spectrum is applied directly to the FM transmitter. The parabolic spectrum results when a rectangular video spectrum is passed through an ideal preemphasis network before FM modulation. (Alternately, it represents applying a rectangular video spectrum directly to a PM modulator.) As mentioned earlier, both spectra are normalized to have unit area in the (S, ν) plane. For these two spectra, the double convolutions in Eq. (71) are given in the range of interest by:

Rectangular Spectrum:

$$S_x^{(3)}(\nu) = S_x(\nu) \boxtimes S_x(\nu) \boxtimes S_x(\nu) = \frac{1}{8}(3 - \nu^2) \qquad |\nu| < 1 \tag{72}$$

Parabolic Spectrum:

$$S_x^{(3)}(\nu) = S_x(\nu) \boxtimes S_x(\nu) \boxtimes S_x(\nu) = \frac{27}{8}\left(\frac{1}{40} + \frac{\nu^2}{3} - \frac{\nu^4}{4} + \frac{\nu^8}{840}\right) \qquad |\nu| < 1 \tag{73}$$

Substitution of these results into Eq. (71) gives the curves shown in Fig. 34 for the two cases. It can be seen that ideal preemphasis has reduced distortion at the upper end of the video band by a few dB. This may be significant when a peak I/S criterion is to be met. However, this has been at the cost of somewhat higher distortion at the lower video frequencies. The crossover point where the two spectra give equal distortion is about $\nu = 0.7$.

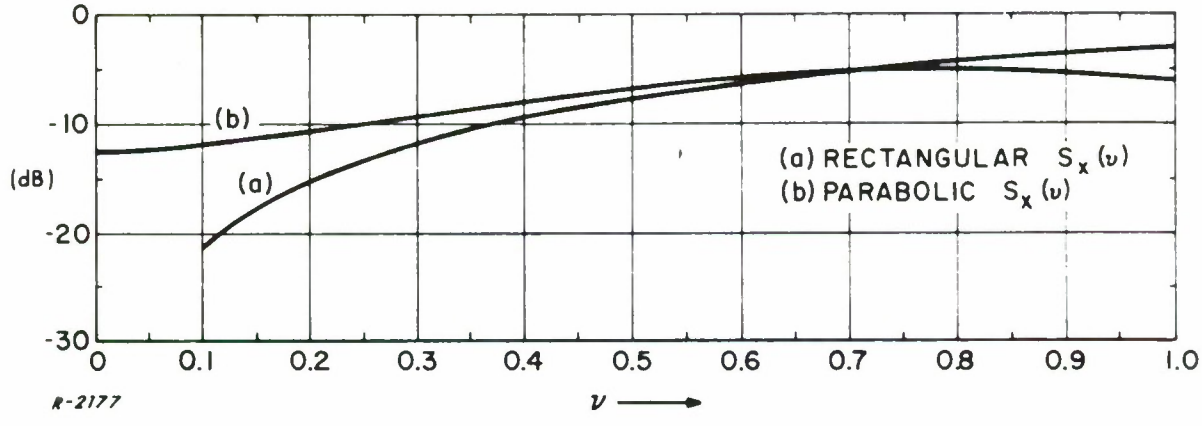

Figure 34 $\dfrac{\nu^2 S_x^{(3)}(\nu)}{S_x(\nu)}$ vs ν for Different Input Spectra.

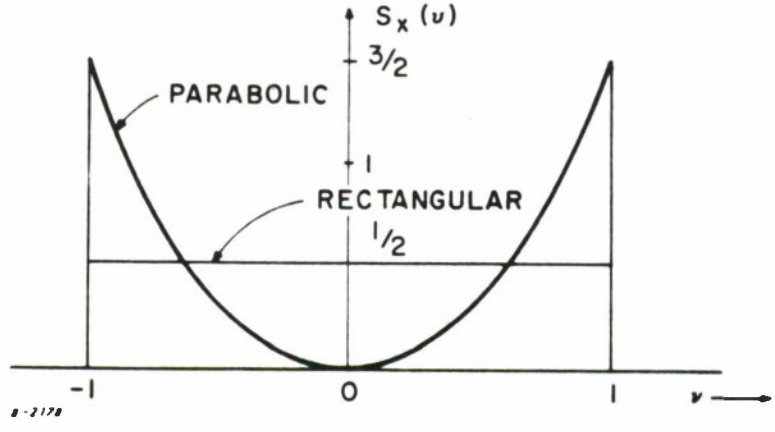

Figure 35 Rectangular and Parabolic Input Spectra.

More complicated preemphasis schemes are frequently employed in telemetry systems. It is difficult to evaluate the resulting distortion spectra in closed form; but results can readily be obtained by performing the double convolutions on a digital computer. Nevertheless, results obtained for a rectangular spectrum should be considered representative for most practical situations.

4.5 The Effect of Filter Type on the Distortion Spectrum

In this section we tabulate phase coefficients c_i defined by the series representation

$$\Phi(\omega) = \sum_{i=0}^{\infty} c_i \left(\frac{\omega - \omega_c}{B}\right)^i \tag{74}$$

where 2B is the 3 dB bandwidth of the filter in question. These coefficients depend upon the type (e. g., Butterworth) and order of the filter. Table III lists the coefficients for Butterworth filters of order n. The general expression is readily found from Eq. (3) to be

$$c_{(2i+1)} = \frac{1}{(2i+1)\sin\frac{(2i+1)\pi}{2n}} \qquad i = 0, 1, 2, \ldots \tag{75}$$

Table IV lists the coefficients for Bessel filters of order n. Since the Bessel filters have maximally-linear phase characteristics, the first nonzero coefficient after c_1 is c_{2n+1}. c_1 is given by (Ref. 5)

$$c_1 = B\,T_d(\omega_c) \tag{76}$$

while the three succeeding nonzero coefficients are (Ref. 5)

$$c_{2n+1} = -\frac{(B\,T_d(\omega_c))^{2n+1}}{(2n+1)\,a_o^2} \tag{77}$$

$$c_{2n+3} = \frac{(B\,T_d(\omega_c))^{2n+3}}{(2n+3)(2n-1)\,a_o^2} \tag{78}$$

$$c_{2n+5} = - \frac{2(n-2)\,(B T_d(\omega_c))^{2n+5}}{(2n-1)^2\,(2n-3)\,(2n+5)\,a_o^2} \tag{79}$$

where the values of $B T_d(\omega_c)$ are listed in Table (II), and those for a_o are listed in Table (I). Formulas for higher-order coefficients c_i have not been obtained because of the computational complexity involved.

Finally, Table V shows the coefficients for double-tuned circuits with various values of coupling coefficients. The general formulas for these coefficients have been computed from Eq. (12) to be

$$c_1 = \frac{2}{1+a^2} f(a) \tag{80}$$

$$c_3 = \frac{2}{(1+a^2)^2} \left(f(a)\right)^3 \left[1 - \frac{4}{3(1+a^2)}\right] \tag{81}$$

$$c_5 = \frac{2}{(1+a^2)^3} \left(f(a)\right)^5 \left[1 - \frac{4}{1+a^2} + \frac{16}{5(1+a^2)^2}\right] \tag{82}$$

$$c_7 = \frac{2}{(1+a^2)^4} \left(f(a)\right)^7 \left[1 - \frac{8}{1+a^2} + \frac{16}{(1+a^2)^2} - \frac{64}{7(1+a^2)^3}\right] \tag{83}$$

$$c_9 = \frac{2}{(1+a^2)^5} \left(f(a)\right)^9 \left[1 - \frac{40}{3(1+a^2)} + \frac{48}{(1+a^2)^2} - \frac{64}{(1+a^2)^3} + \frac{256}{9(1+a^2)^4}\right] \tag{84}$$

$$c_{11} = \frac{2}{(1+a^2)^6} \left(f(a)\right)^{11} \left[1 - \frac{20}{1+a^2} + \frac{112}{(1+a^2)^2} - \frac{256}{(1+a^2)^3} + \frac{256}{(1+a^2)^4} - \frac{1024}{11(1+a^2)^5}\right] \tag{85}$$

where f(a) is given in Eq. (11).

4.6 Accumulation of Distortion in Cascaded Filter Stages

When a receiver contains a single predetection filter it is a simple matter to look up the appropriate coefficients in Table III, IV or V and insert them into Eq. (70). However, frequently two or more filters are used in cascade; in this case obtaining suitable phase coefficients is not so straightforward. In this section we consider two approaches: the first is completely general and the second simplifies the calculation when the cascade consists of identical filters.

Table III

PHASE COEFFICIENTS OF BUTTERWORTH FILTERS OF VARIOUS ORDERS

	n=1	n=2	n=3	n=4	n=5	n=6
c_1	1.00	1.414	2.00	2.61	3.24	3.86
c_3	-0.333	0.471	0.333	0.361	0.412	0.471
c_5	0.200	-0.283	0.400	0.216	0.200	0.207
c_7	-0.143	-0.202	-0.286	0.373	0.177	0.552
c_9	0.111	0.157	-0.111	-0.283	0.360	0.157
c_{11}	-0.0909	0.129	-0.182	-0.0984	-0.294	0.351

Table IV

PHASE COEFFICIENTS OF BESSEL FILTERS OF VARIOUS ORDERS

	n=1	n=2	n=3	n=4	n=5	n=6
c_1	1.00	1.36	1.75	2.13	2.42	2.72
c_3	-0.333	0	0	0	0	0
c_5	0.200	-0.103	0	0	0	0
c_7	-0.143	0.0455	-0.0319	0	0	0
c_9		0	0.0152	-9.05×10^{-3}	0	0
c_{11}			-5.08×10^{-3}	4.82×10^{-3}	-1.70×10^{-3}	0
c_{13}				-2.12×10^{-3}	9.34×10^{-4}	-2.88×10^{-4}
c_{15}					-4.17×10^{-4}	1.66×10^{-4}
c_{17}						-8.61×10^{-5}

Table V

PHASE COEFFICIENTS OF DOUBLE-TUNED CIRCUITS
WITH VARIOUS COUPLING COEFFICIENTS

	a=0.5	a=0.6	a=0.7	a=0.8	a=0.9	a=1.0	a=1.1	a=1.2	a=1.3	a=1.4
c_1	1.346	1.366	1.385	1.401	1.411	1.414	1.411	1.401	1.384	1.363
c_3	-0.0508	-0.0170	0.104	0.211	0.335	0.471	0.615	0.760	0.900	1.031
c_5	-0.0656	-0.116	-0.172	-0.226	-0.267	-0.283	-0.264	-0.204	-0.103	0.036
c_7	0.039	0.0466	0.0373	-0.00144	-0.0803	-0.202	-0.358	-0.529	-0.689	-0.813
c_9	-0.00883	0.00433	0.0346	0.0816	0.132	0.157	0.119	-0.0152	-0.259	-0.602
c_{11}	-0.00301	-0.0141	-0.0260	-0.0297	0.021	0.129	0.296	0.477	0.588	0.540

Consider a cascade of filters having phase characteristics Φ_1, Φ_2, etc. which are expressed as series

$$\Phi_1(\omega) = \sum_{i=1}^{\infty} c_{1,i}\left(\frac{\omega - \omega_c}{B_1}\right)^i$$

$$\Phi_2(\omega) = \sum_{i=1}^{\infty} c_{2,i}\left(\frac{\omega - \omega_c}{B_2}\right)^i$$

$$\vdots \qquad (86)$$

where B_1, B_2, etc. are the half-bandwidths of the individual stages. The cascade will have a phase characteristic $\Phi(\omega)$ equal to the sum of the individual phases

$$\Phi(\omega) = \Phi_1(\omega) + \Phi_2(\omega) + \ldots \qquad (87)$$

We can express $\Phi(\omega)$ as a series

$$\Phi(\omega) = \sum_{i=1}^{\infty} c_i\left(\frac{\omega - \omega_c}{B}\right)^i \qquad (88)$$

where B is the overall half-bandwidth of the cascade. Substitution of Eqs.(86) and (88) into (87) gives the coefficients of the cascade in terms of the coefficients of the stages

$$c_1 = c_{1,1}\left(\frac{B}{B_1}\right) + c_{2,1}\left(\frac{B}{B_2}\right) + \ldots$$

$$c_3 = c_{1,3}\left(\frac{B}{B_1}\right)^3 + c_{2,3}\left(\frac{B}{B_2}\right)^3 + \ldots$$

$$\vdots \qquad (89)$$

Therefore to compute the I/S ratio we may consider the cascade as a single filter of bandwidth B having the coefficients c_1, c_3, etc. (given by Eq. (89)) and substitute these values directly into Eq. (70). Note that in order to compute the coefficients it is necessary to know the coefficients and bandwidths of each individual stage as well as the resulting overall bandwidth.

As might be expected, these calculations can be simplified considerably in the case where all stages are identical. If the result of Eq. (89) is simplified to the case of k filters with identical coefficients and equal bandwidths, substitution into Eq. (70) gives the result that the overall I/S ratio is k^2 times the I/S ratio which would be calculated for an individual stage. In other words, we make the calculation assuming one of the individual stages is present and then multiply by k^2. This result is easily verified by noting that the distortion waveforms produced by each stage are identical. These waveforms add in voltage so that the overall distortion waveform is k times that produced by one stage. Therefore the overall distortion power is k^2 times the individual distortion power.

Overall bandwidths of a cascade may be obtained by simple formulae in certain simple cases. In particular, if the cascade consists of k identical stages, each of which is an n^{th} order Butterworth, it can be shown that the overall half-bandwidth is given by

$$B_k = \sqrt{2^{n/k} - 1}\ B \tag{90}$$

where B is the half-bandwidth of an individual stage.

Another situation where the bandwidth of a cascade may be found from an explicit equation is the case of k identical double-tuned stages, each having coupling coefficient a. We have computed the overall half-bandwidth to be

$$B_k = \frac{\omega_c}{2Q} \sqrt{a^2 - 1 + \sqrt{2^{1/k}(1+a^2)^2 - 4a^2}} \tag{91}$$

Equation (91) is plotted in Fig. 36. The overall half-bandwidth of a single stage is given in terms of the resonant angular frequency ω_c and "quality factor" Q by

$$B = \frac{\omega_c}{2Q} \sqrt{a^2 - 1 + \sqrt{2(1+a^4)}} \tag{92}$$

Equation (92) is, of course, simply a special case of Eq. (91).

Finally we consider the case of a cascade of k Bessel filters of order n. It is well-known that, for sufficiently large n, the amplitude of a Bessel filter approaches the gaussian shape. In this limit it is easy to show that the bandwidth of a cascade is $1/\sqrt{k}$ times the bandwidth of an individual stage. This result is adequate if $n \geq 4$; the exact results for lower values of n have been calculated and are shown in Table VI.

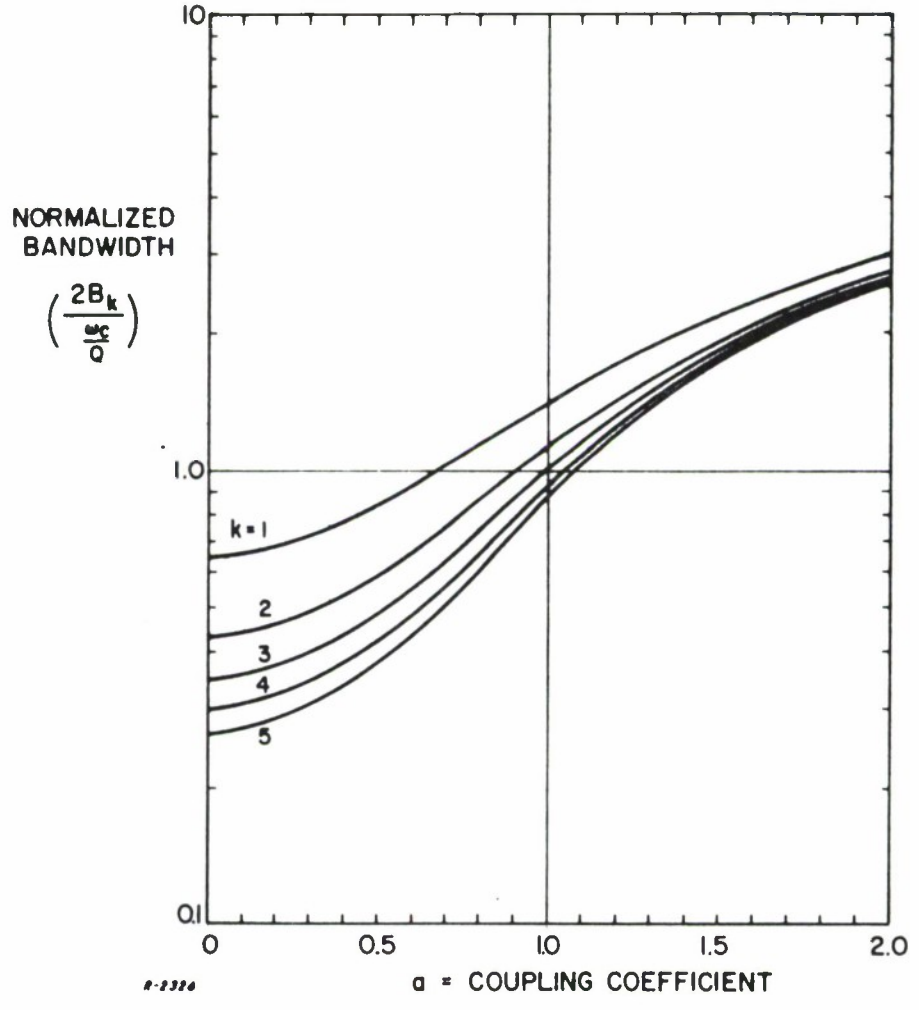

Figure 36 Bandwidth of k Identical Cascaded Double-Tuned Circuits as a Function of Coupling Coefficient.

4.7 Distortion Spectrum for Nonquasi-Stationary Cases

The quasi-stationary approach we have presented has proved to be adequate in all the situations we encountered in FDM telemetry. (See Sections V and VI.) However, it is interesting from the theoretical point of view to consider the situation where nonquasi-stationary effects become important. This problem may be approached by utilizing the extension of the quasi-stationary transfer relation derived in Subsection 3.5.

Table VI

BANDWIDTH OF A CASCADE OF k IDENTICAL n^{th}-ORDER BESSEL FILTERS

Order of Filter n	B_k/B					
	k=1	k=2	k=3	k=4	k=5	k=6
1	1	0.643	0.510	0.435	0.384	0.350
2	1	0.71	0.59	0.51	0.47	0.42
3	1	0.74	0.60	0.52	0.48	0.43
4	1	0.72	0.59	0.51	0.46	0.42
limit as $n \to \infty$	1	0.707	0.577	0.500	0.447	0.408

We showed in Subsection 3.5 that, in general, the distortion waveform is the sum of a quasi-stationary term $\eta(t)$ and a nonquasi-stationary term $\epsilon(t)$. We obtained an approximate expression for $\epsilon(t)$ in Eq. (56). Now, if we use the same procedure as that of Subsection 4.2 to obtain the overall distortion spectrum, we first find that the autocorrelation function of the distortion is given by

$$R_\theta(\tau) = R_\eta(\tau) + 2R_{\eta\epsilon}(\tau) + R_\epsilon(\tau) \tag{93}$$

The term $R_\eta(\tau)$ is the autocorrelation function of the quasi-stationary distortion alone, which was previously found to be the right-hand side of Eq. (61). The term $R_\epsilon(\tau)$ is the autocorrelation function of the nonquasi-stationary distortion alone, which can be computed in detail starting with Eq. (56). Finally, the middle term $R_{\eta\epsilon}(\tau)$ represents the crosscorrelation function between the quasi-stationary and nonquasi-stationary distortion terms. It can be computed in detail starting with Eqs. (44) and (56).

Applying the Fourier transformation of Eq. (62) to Eq. (93) yields the distortion spectrum

$$I_\theta(\nu) = I_\eta(\nu) + 2I_{\eta\epsilon}(\nu) + I_\epsilon(\nu) \tag{94}$$

Here again, the term $I_\eta(\nu)$ is power-density spectrum of the quasi-stationary distortion alone, which was previously found to be the right-hand side of Eq. (63). The term $I_\epsilon(\tau)$ is the power-density spectrum of the nonquasi-stationary distortion alone, and hence is a positive function of ν. Finally, the middle term $I_{\eta\epsilon}(\nu)$ represents the cross-power-density spectrum between the quasi-stationary and nonquasi-stationary distortion terms. Note that $I_{\eta\epsilon}(\nu)$, being a cross-power density, is not constrained to be a positive function.

It is interesting to note that, while $I_\eta(\nu)$ involves only the phase coefficients c_i of the predetection filter, Eq. (63), $\epsilon(t)$ in fact contains coefficients of both the phase and amplitude of the filter transfer function. Therefore the complete distortion spectrum of Eq. (94) would depend on both the phase and amplitude characteristics of the predetection filter, as to be expected.

We attempted to carry out the detailed analysis described above in order to obtain the two terms $I_\epsilon(\nu)$ and $I_{\eta\epsilon}(\nu)$ in terms of the filter parameters and signal parameters. However, we were hampered by a great deal of algebraic complexity and by uncertainty about the degree of approximation involved in Eq. (56) for $\epsilon(t)$. Furthermore, all the experimental measurements were adequately interpretable in terms of the quasi-stationary results, so we had no experimental evidence by which to test any nonquasi-stationary results.

A worthwhile conjecture can be made at this point. There is reason to believe that, whenever nonquasi-stationary phenomena occur, the magnitude of the cross term $I_{\eta\epsilon}$ will be negligible in comparison with I_ϵ. It would follow from Eq. (94) that the quasi-stationary term I_η represents a lowerbound on the overall distortion spectrum level, i. e., that the overall distortion level is always equal to or greater than the quasi-stationary part.

Section V

MEASUREMENT OF INTERMODULATION DISTORTION IN FDM TELEMETRY

5.1 Description of Measurement Configuration

The technique used to measure intermodulation distortion in telemetry receivers is the noise-loading technique introduced in Section 4.1. Distortion is measured by simulating a fully loaded telemetry video signal by a noise spectrum having a rectangular shape. This video spectrum contains a notch simulating an empty channel in which the intermodulation distortion is measured after processing through the telemetry system under test.

The block diagram of the intermodulation distortion measurement configuration is shown in Fig. 37. The white noise generator output is passed through a lowpass filter which shapes the noise to simulate the video spectrum used with telemetry systems. The video spectrum is passed through an amplifier for gain and isolation, then through a notch filter which places a narrow, deep notch in the video spectrum. Figure 38 illustrates the shape of the resultant video spectrum using various notches. The video filter has a flat response with a 3 dB bandwidth at 85 kHz and an 18 dB per octave roll-off as specified in the IRIG Telemetry Standards (Ref. 1). Four different notch filters are used, centered at 10 kHz, 30 kHz, 50 kHz, and 80 kHz which permit measurement of the distortion at four points in the video band.

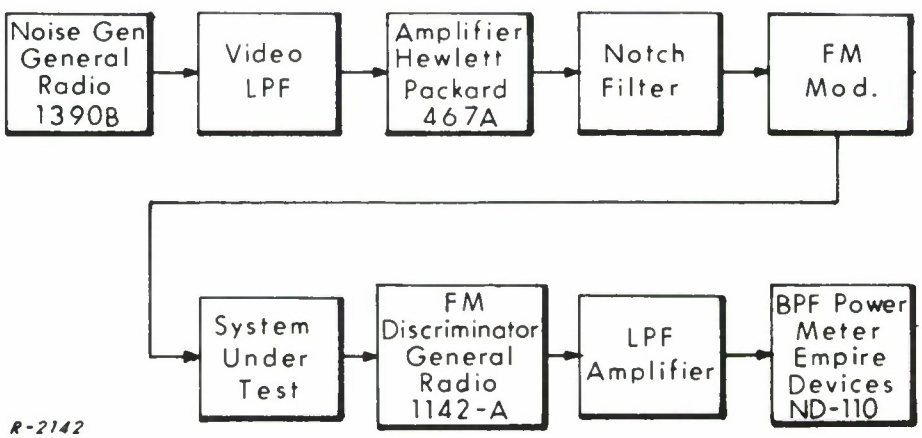

Figure 37 Block Diagram of Intermodulation Measurement Configuration.

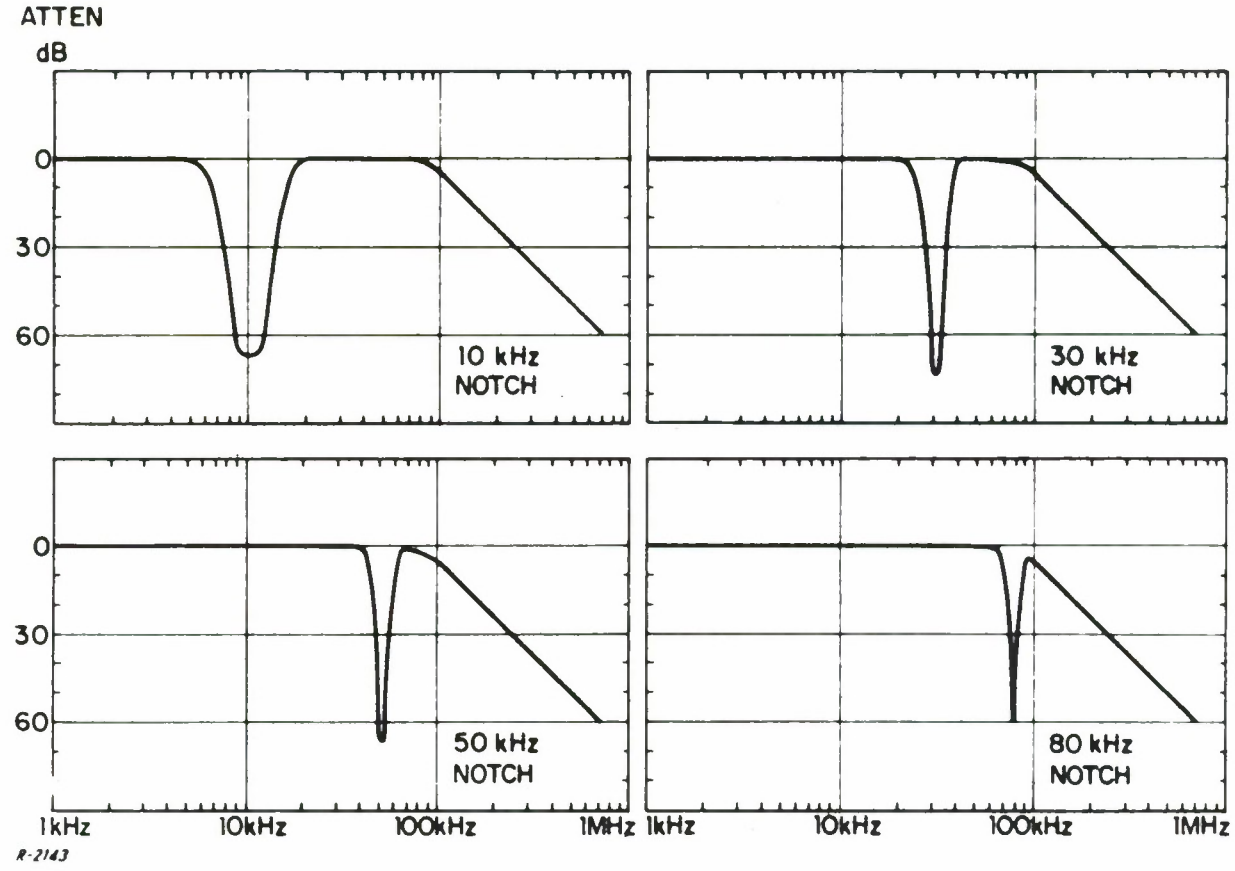

Figure 38 Simulated Video Spectrum with Empty Channel.

The shaped video signal is then applied as the modulation signal to an FM modulator and the resulting FM signal processed through the predetection filter of the receiver under test. Intermodulation distortion results from the nonlinear action of the predetection filter on the video signal. The FM signal is then demodulated in a very linear pulse-averaging discriminator whose output contains the baseband signal with the distortion introduced in the receiver. It is important that both the FM modulator and the demodulator (hereafter referred to as modems) have very linear modulation and demodulation characteristics so as to minimize their contribution to distortion. The detected signal is passed through a lowpass filter-amplifier to attenuate any RF signals at the discriminator output, then it is applied to a tunable bandpass filter, tuned to the notch-filter center frequency and having a somewhat narrower bandwidth than the notch. The output of the bandpass filter is applied to a power meter which then measures the amount of distortion power in the notch. This meter can be read to ±0.5 dB and measurement is accurate to ±1 dB.

If the notch filter at the input is bypassed or, equivalently, if the bandpass filter is tuned to a point where the input spectrum is flat, then a measurement of signal power at the location of the notch can be taken and a ratio of intermodulation distortion power to signal power (I/S) can be formed. This ratio is used throughout this report to represent the relative distortion levels.

5.2 Description of Special Test Equipment

Much of the equipment needed for distortion measurements is standard laboratory equipment. These are indicated in Fig. 37 by manufacturer and model number. Several of the needed functions were either not commercially available or were more conveniently built. The lowpass filter used to shape the baseband spectrum is the 3-pole Butterworth filter shown in Fig. 39.

Notch filters with the necessary specifications were not readily available, so a passive 7-pole Butterworth filter was designed and built. Since it was desired to measure the I/S as a function of the position of the notch, four of these filters were constructed. They are all of the same form with different element values (see Fig. 40) and have approximately the same notch shapes. As can be seen from Fig. 41 the 50kHz filter is very narrow and deep, having a 60 dB bandwidth of 4 kHz and being approximately 70 dB deep. The depth of the notch filter sets the lower limit to the measurement of distortion since any distortions less than -70 dB would be indistinguishable from noise passed by the notch filter. For the measurements performed here attenuations of 70 dB were adequate since the distortions measured were above -70 dB.

The FM modulator employed in most of the tests is a voltage-controlled oscillator centered at 10 MHz. This is a reasonably simple yet vital circuit, and is essentially a free-running multivibrator whose period of oscillation is controlled by the voltage at its input. The importance of this

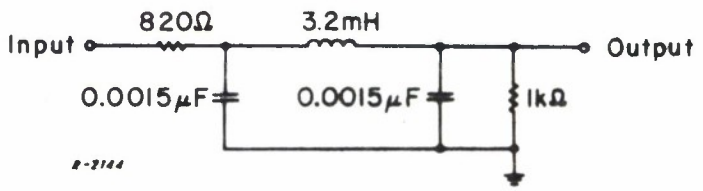

Figure 39 Schematic of 85 kHz Lowpass Filter.

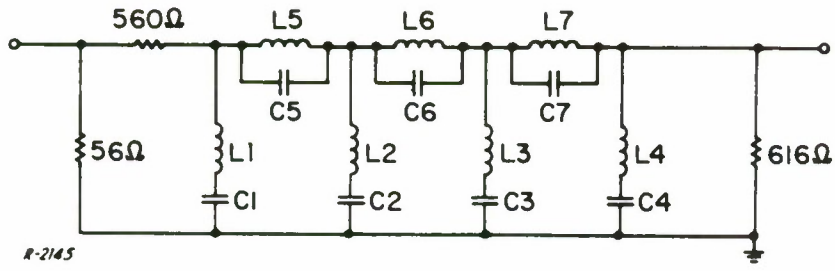

Filter Element Values

Notch Filter Center Freq	L1	C1	L2	C2	L3	C3	L4	C4	L5	C5	L6	C6	L7	C7
10 kHz	22mH	0.012μF	5.4mH	0.047μF	5.4mH	0.047μF	22mH	0.012μF	12.2mH	0.021μF	19.7mH	0.013μF	12.2mH	0.021μF
30 kHz	22	1275pF	5.4	5170pF	5.4	5170pF	22	1275pF	1.4	0.021	2.2	0.013	1.4	0.021
50 kHz	22	460	5.4	1870	5.4	1870	22	460	0.49	0.021	0.79	0.013	0.49	0.021
80 kHz	22	205	5.4	830	5.4	830	22	205	0.22	0.021	0.35	0.013	0.22	0.021

Figure 40 Schematic and Table of Element Values for Notch Filters.

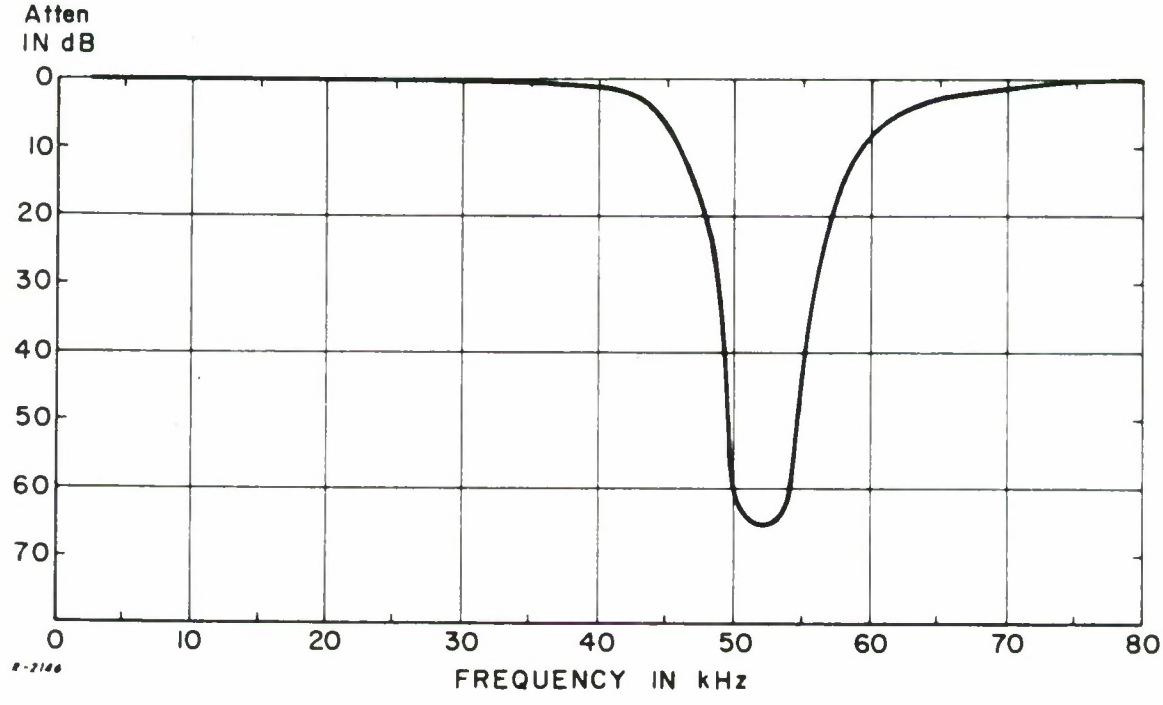

Figure 41 Amplitude Response of 50 kHz Notch Filter.

circuit is in the linearity of its modulation characteristic, which keeps the intermodulation distortion of the FM generator within acceptable bounds. Nonlinearities in the modulator could severely restrict the usefulness of this technique by introducing more distortion than that to be measured in the predetection filters. A comparison of the linearities of the VCO and a standard FM generator is given later in Fig. 48, showing that the commercial FM generator introduces much more distortion than the VCO.

The lowpass filter-amplifier which follows the pulse-count discriminator is used only to eliminate the carrier component which is present at the output of the discriminator. The filter has a 3 dB cutoff frequency of 200 kHz and hence will not affect the baseband spectrum. Its schematic is shown in Fig. 42.

The tunable-bandpass noise meter is a special test unit containing a crystal filter and a true-power meter. The filter bandwidth is 4.8 kHz at -80 dB points, which is slightly narrower than the notch filter so that only distortion and no signal is measured when tuned to the notch frequency. This bandpass filter is tunable over the range 5 kHz to 100 kHz by mixing the baseband frequency up to the crystal filter with a local oscillator. A block diagram of the bandpass noise meter and its amplitude characteristics is shown in Figs. 43 and 44.

5.3 Accumulation of Distortion in the Measurement Configuration

The mechanism for the accumulation of distortion in various parts of the receiver and measurement configuration is of central interest. In Section III it was indicated that when the modulated signal passes through identical cascaded filters, the distortions were highly correlated and added as voltages. In the case where the distortions are not introduced by identical operations, such as with a cascade of a modem and a filter, the individual distortions are uncorrelated and add as powers. A proof of this statement is given in Appendix IV.

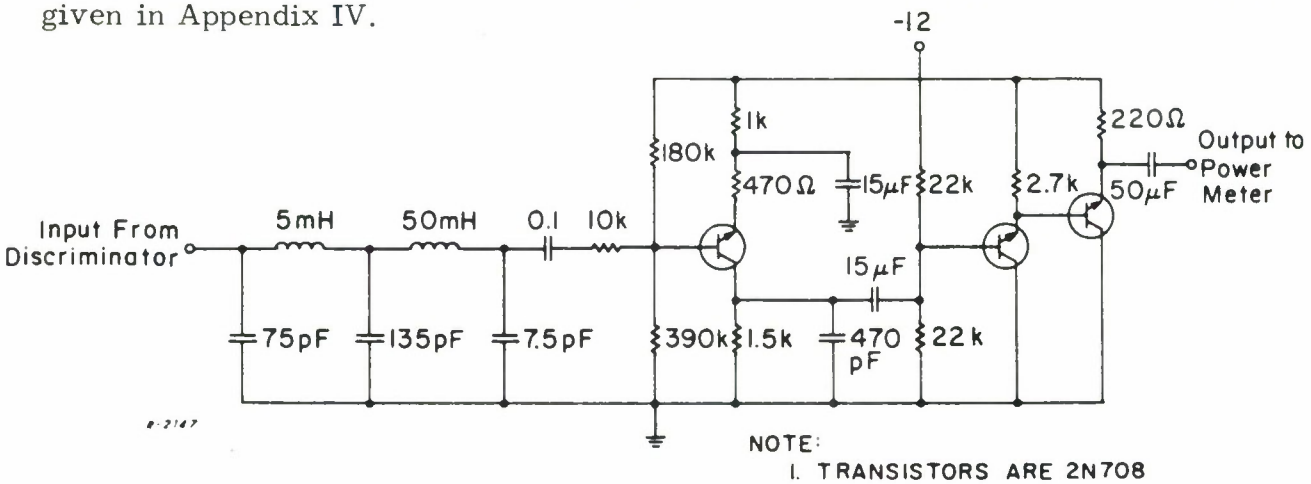

Figure 42 Schematic of Filter-Amplifier for Output of Discriminator in Noise-Loading Configuration.

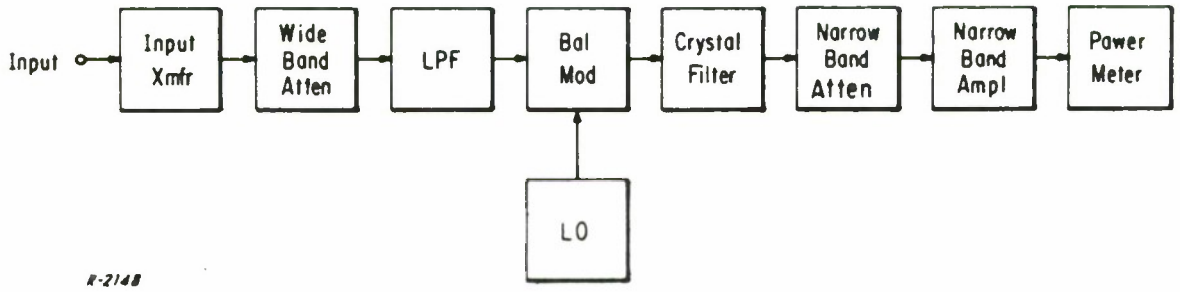

Figure 43 Block Diagram of Empire Devices Bandpass Noise Meter.

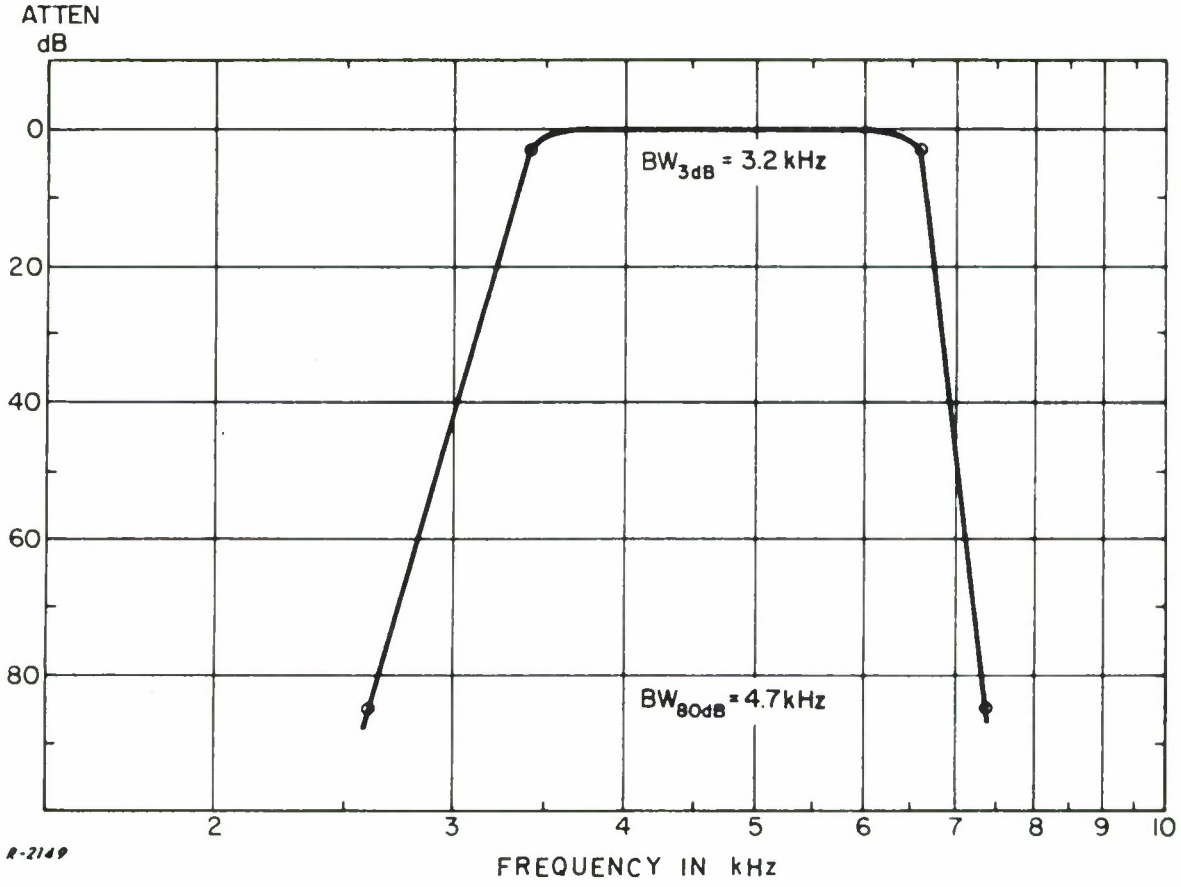

Figure 44 Amplitude Characteristic of Bandpass Filter.

A nomograph which facilitates the computation of distortion accumulation is shown in Fig. 45 for both voltage and power addition. This curve relates the distortion power, in dB, from each of two sources to the total distortion from both sources combined. It permits computation of one of the three distortions involved; i. e., either of the two individual, or the total distortion.

For example, consider the case of the cascade of a predetection filter and modem. The distortion in dB from the modem alone can be measured by removing the filter from the measurement configuration, but the filter distortion can only be measured in combination with the modem. Thus, two measurements are necessary in order to isolate the individual contributions. First, the distortion in dB using only the modem is measured and then the distortion in dB using both the modem and filter. The distortion introduced by the filter can then be found by using Fig. 45. Since the distortions are uncorrelated, curve a is applicable. The distortion in dB with the modem (P_1) is subtracted from the total distortion (P_T) and this difference ($P_T - P_1$) is used to enter the ordinate of Fig. 45. The intercept of this difference with curve a gives a point on the abscissa which corresponds to the difference in dB between the individual distortions of the modem and filter ($P_2 - P_1$). If now the distortion with the modem (P_1) is added to this difference, the distortion in dB of the filter alone (P_2) is obtained. The difference ($P_2 - P_1$) can be either positive or negative decibels depending upon whether the difference between the measurements ($P_T - P_1$) is greater than or less than 3 dB. This causes no difficulties. Similar computations can be made for a cascade of identical filters using curve b.

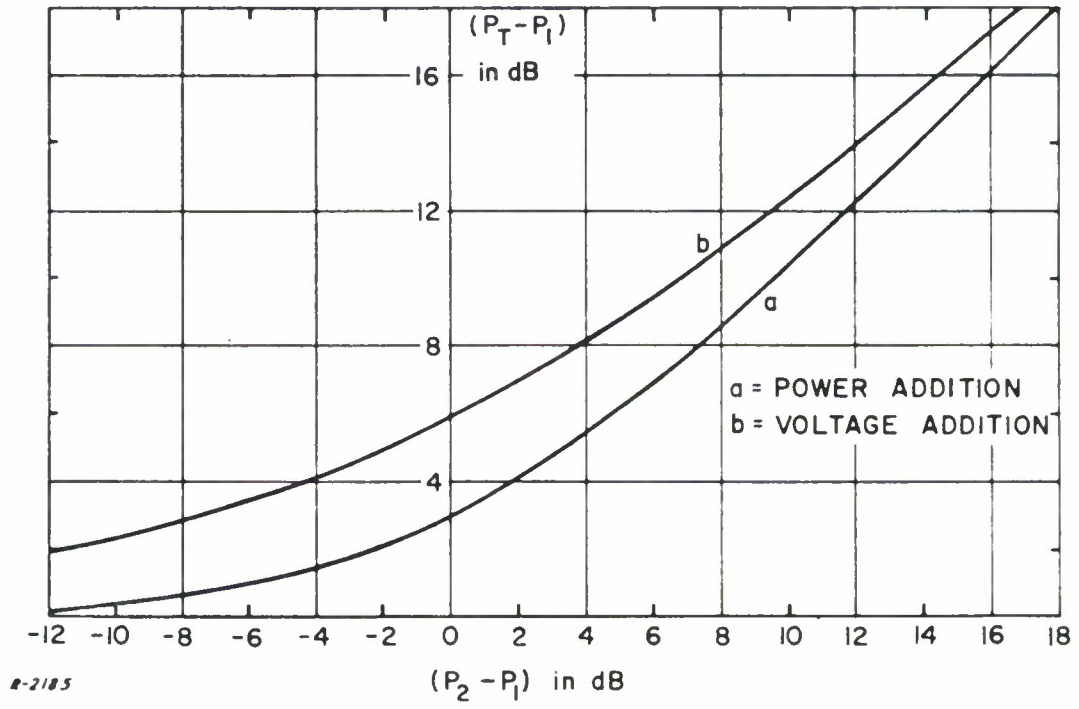

Figure 45 Nomograph for Accumulation of Distortion.

5.4 Measurement Limitations

Limitations to the measurement of distortion in predetection filters arise from the masking of this distortion by other disturbances in the measurement configuration. Masking can occur in two ways. The first occurs when the notch filter is too shallow so that noise passing through the notch adds to the distortion generated in the predetection filter. This limitation was negligible in the measurements described here because the notch depth (-70 dB) was well below the anticpated predetection filter distortions. The second occurs because the FM modulator and discriminator are not perfectly linear and as a result introduce intermodulation distortion of their own. As long as this distortion does not overwhelm the distortion from the predetection filters no significant problem exists, because we can use the nomograph of Fig. 45 to isolate filter distortion from the overall distortion measurement.

Before proceeding with the actual measurement of distortion in predetection filters, it is necessary to measure the residual distortion introduced in the measurement configuration in order to establish its noise floor, i. e., the lower limit to I/S distortion. Figure 46 shows the test setup for each of four noise-floor measurements. Part A of Fig. 46 shows the equipment arrangement for measuring the residual distortion caused by the notch filter and baseband shaping circuits. For this test with each of the four notch filters, I/S of at least -60 dB were measured.

In Part B, the spectrum-shaping circuits plus the amplifier-filter following the discriminator are evaluated. The noise floor here was at least -56 dB. This small increase is due to unavoidable noise generated in the amplifier. Both of these noise floors are quite acceptable since much greater distortions were anticipated in the telemetry receivers to be tested.

Part C of Fig. 46 shows the measurement of the noise floor for the entire test system using an 80 kHz notch filter. This filter will give the highest distortion readings since it is at the high end of the video spectrum. The noise floor in this case was measured as a function of rms deviation of the VCO, and the results plotted in Fig. 47.

In order to maintain a constant level into the power meter an attenuator was inserted between the amplifier-filter and the bandpass filter-power meter. As the deviation was changed, this attenuator was changed keeping the level at the power meter constant. The lower curve in Fig. 47 shows the effect of the attenuator setting on the noise floor with no baseband modulation on the VCO. In effect this curve plots the noise level measured at the power meter resulting from decreasing the attenuation of this noise. The noise measured here is generated in the discriminator and amplifier-filter. As is to be expected, it is highest at the low attenuator settings, corresponding to

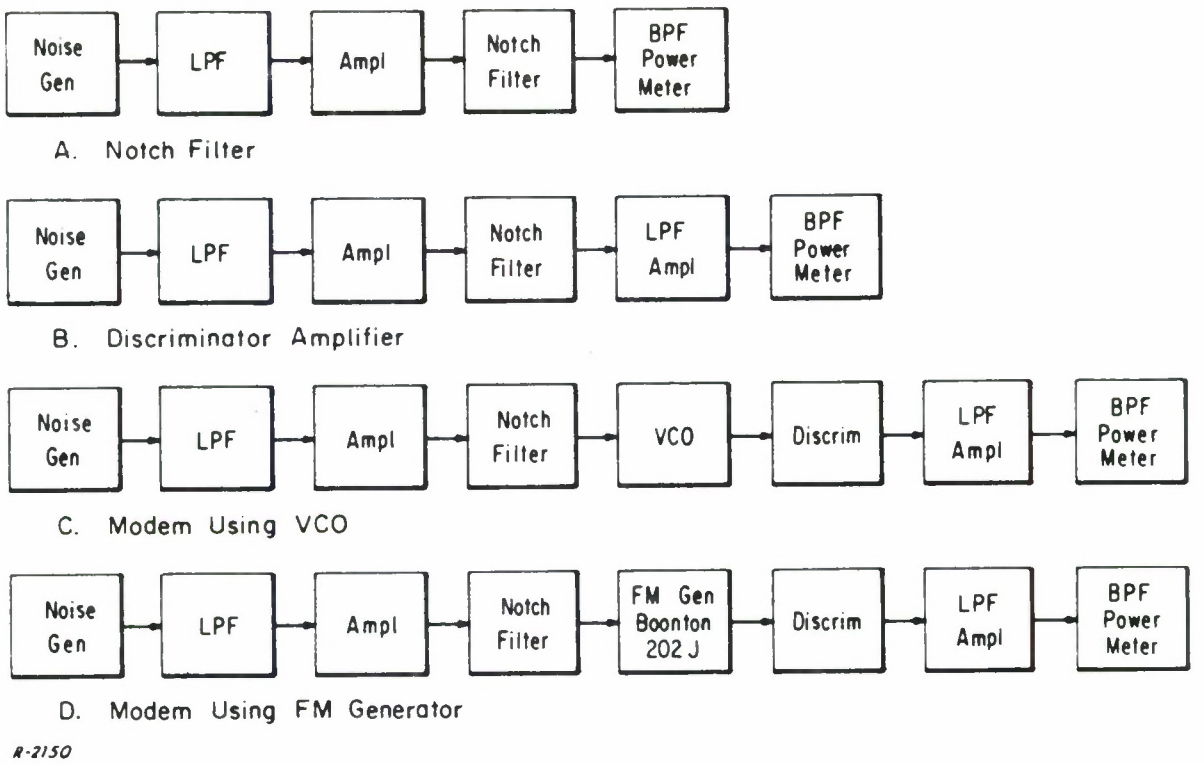

Figure 46 Test for Identifying Contributions to the Residual Distortion.

the low deviations and may place some limitations in measuring wideband predetection filters with very low deviations since the distortion from the filter would be low. In this case the noise floor of -49 dB at 20 kHz deviation still permitted measurement of the I/S of the filters.

The upper curve is a plot of actual noise floor as a function of deviation. Here the noise floor decreases as the deviation decreases. This kind of performance is to be expected since the distortion which is principally caused by the VCO-discriminator combination is directly related to modulator characteristic nonlinearities which are necessarily worse at large deviations.

It should be observed that an rms deviation of 53.3 kHz corresponds to a reading of 125 kHz peak deviation on the telemetry receiver deviation meter which is the recommended peak deviation for telemetry operation in the IRIG telemetry standards. This deviation will be used in most of the tests conducted on the telemetry system. At 53.3 kHz deviation the system noise floor was -47 dB. This means distortions much less than -47 dB cannot be measured. However, as the following data show, this floor was quite sufficient to permit measurement of the I/S in predetection filters. This noise floor can be reduced even further by utilizing a more linear VCO or discriminator characteristic.

Part D of Fig. 46 is the setup using a standard FM generator rather than the VCO. This generator has a nonlinearity specification of less than 1.5%

deviation from a straight line. With this generator the noise floor is considerably increased to -39 dB, which demonstrates the need for good linearity in the VCO. Figure 48 is a comparison of the VCO and FM generator modulation characteristics. The superior linearity of the VCO is obvious and is reflected in lower distortion measurements.

In conclusion, the noise-floor tests establish the minimum I/S which can be measured and indicate areas, particularly VCO and discriminator, in which the distortion in the measurement configuration can be improved and the noise-loading technique extended in usefulness.

5.5 Preliminary Measurements With Cascaded Identical Filters

Before performing I/S tests on typical telemetry systems, a test was performed using two identical cascaded bandpass filters to verify the analysis outlined in Section IV concerning the accumulation of distortion in identical

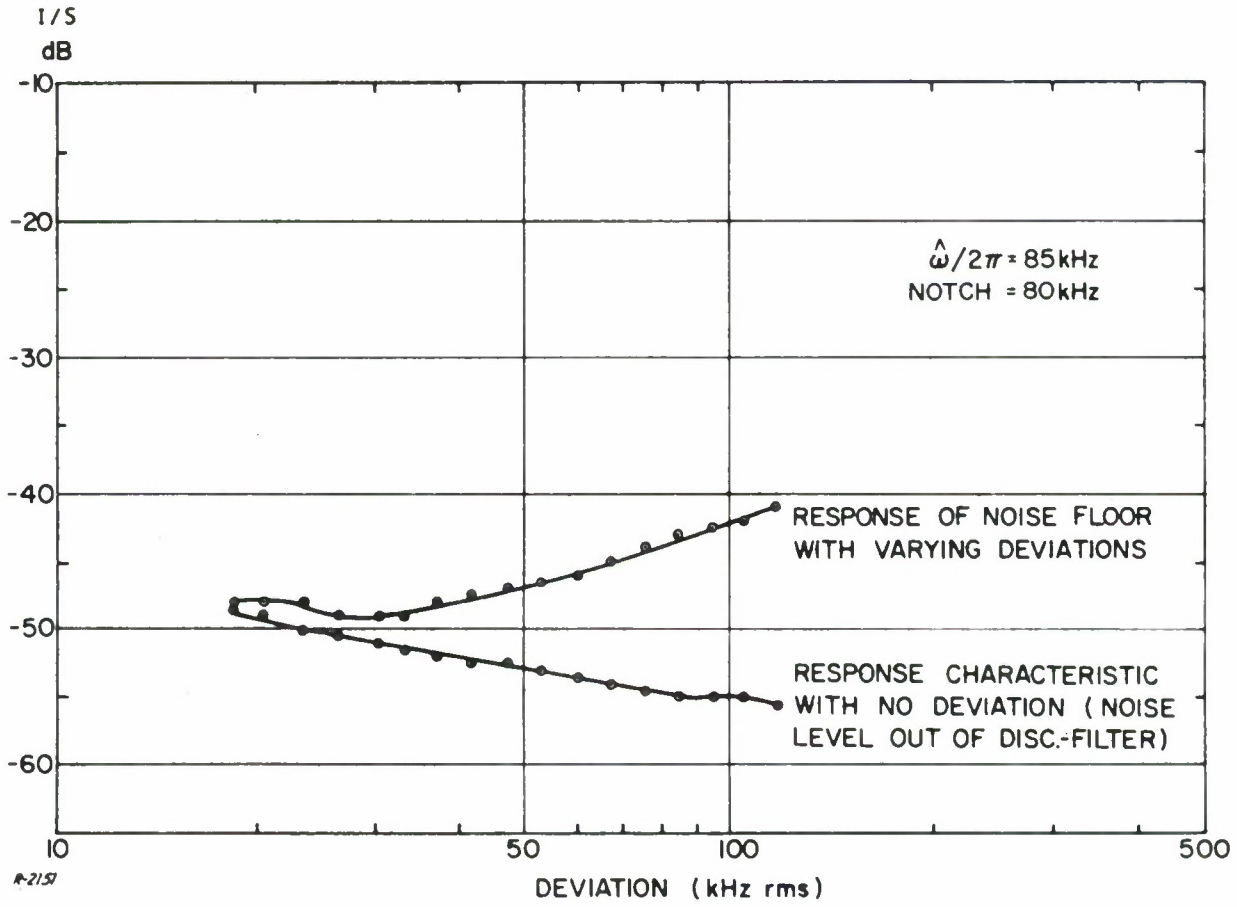

Figure 47 Noise Floor vs Deviation.

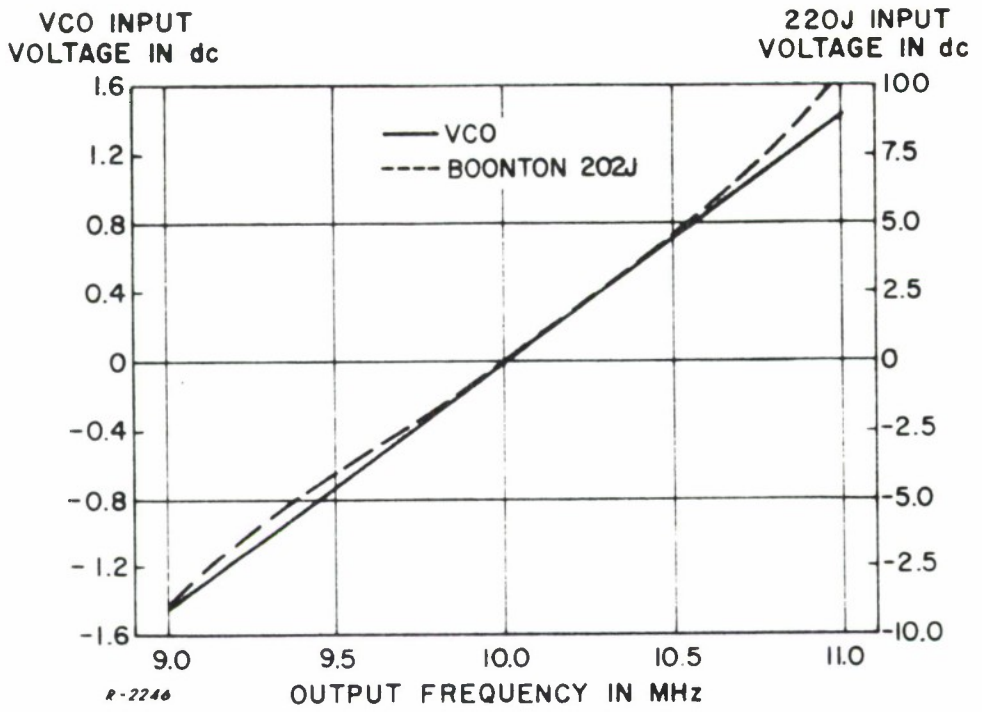

Figure 48 Modulation Characteristics of VCO and Boonton 202 J Generator.

filters, and in Appendix IV dealing with noise-floor correction. The experimental setup is shown in Fig. 49. The bandpass filters were identical 2-pole Butterworth designs with 3 dB bandwidths of 400 kHz each, centered at 10 MHz. This design closely simulates that of a receiver IF but permits measurement of individual as well as overall distortions, and hence verification of the theory of accumulation of distortion.

The first test was performed using only one filter to demonstrate the method of removal of the residual equipment distortion (noise floor) which, as indicated previously, is primarily introduced by modem nonlinearities. Table VII lists the measurements using both a 50 kHz and 80 kHz notch filter, and an rms deviation of 53.3 kHz. The first line shows the residual distortion of the test configuration. The second line is then the measured distortion of the filter and modem combined. Correcting this measurement for power addition as outlined in Subsection 5.3 gives in line three the measured distortion of the filter alone.

The analytical predictions of the distortion for this filter are computed as outlined in Section IV and listed in line four. The shape of the curve across the video band is given by Eq. (68) and plotted in Fig. 34. It will be seen that the shape of the distortion prediction for all the predetection filters included in this study is identical provided the filters are aligned to be symmetrical; only the level changes. The level of the distortion for this filter is given by

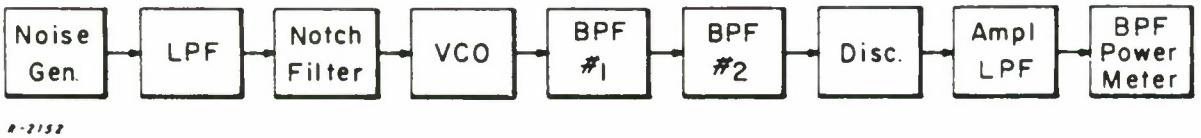

Figure 49 Test Setup for Measurements on Cascaded Identical Filters.

two factors as defined in Eqs. (69) and (70). Equation (69) permits a simple calculation involving the modulation deviation and bandwidth and the filter bandwidth. In this case Eq. (69) yields -22.6 dB. The effect of the filter phase characteristic is accounted for in Eq. (70). The filter coefficients are obtained from Table III and combined with the deviation and bandwidth to give in this case a distortion term of -12.8 dB. The universal curve of Fig. 34 is 3 dB down at the bandedge. Adding these three factors together yields a distortion of -38.4 dB at the bandedge. This then gives one point through which the universal curve can be drawn resulting in the single filter distortion prediction curve shown in Fig. 50. The predictions for the 50 kHz and 80 kHz notches are then obtained by entering the curve at $\nu = 0.6$ and 0.94 respectively. These predictions are listed on line four. Comparison of the distortion measurement and prediction (lines three and four) shows excellent agreement.

The second test was performed with both 50 kHz and 80 kHz notch filters and an rms deviation of 53.3 kHz for each filter separately and then for the cascade of the two filters. The results of the experiment are listed in Table VIII. Again it is necessary to correct each of the measurements of filter distortion by removing the contribution in the measurement due to the noise floor (VCO-discriminator). The second and third lines show the measurement and correction for the individual filters. Line four shows the measurement and correction of the cascade of both filters. Line five is the computation of the total distortion of two filters from individual measurements of lines two and three. Lines four and five thus verify the theory of accumulation of distortion in voltage. Line six lists the theoretical predictions for the cascade of two identical filters obtained by adding +6 dB to the single filter distortion curve just computed. Lines four and six thus compare the measured and predicted distortion for the cascade of two filters showing agreement within 1.4 dB. Figure 50 summarizes the comparison of theoretical and experimental results of the test. The distortion is plotted as a function of ν, the position of the notch in the video spectrum. The solid line is the prediction and the circled points are the corrected measurements. The agreement between the predictions and measurements is seen to be excellent.

Table VII

DISTORTION MEASUREMENTS ON 2nd ORDER BUTTERWORTH FILTER (BW 3 dB = 400 kHz)

	Notch Location	
	50 kHz	80 kHz
1. Noise Floor	-46 dB	-47 dB
2. Measured I/S	-40 dB	-37.5 dB
3. Corrected I/S	-41.3 dB	-38.0 dB
4. Predicted I/S	-41.5 dB	-38.5 dB

Table VIII

TEST RESULTS FOR CASCADED IDENTICAL FILTERS

FILTER	I/S MEASUREMENTS			
	50 kHz Notch Filter		80 kHz Notch Filter	
	Measured	Corrected	Measured	Corrected
1. Noise Floor	-46 dB		-47 dB	
2. BPF #1	-40 dB	-41.3 dB	-36 dB	-36.4 dB
3. BPF #2	-39 dB	-40.0 dB	-37.5 dB	-38 dB
4. BPF 1+2	-34.5 dB	-34.7 dB	-31 dB	-31.1 dB
5. Computation Adding 1 + 2		-34.6 dB		-31.2 dB
6. Prediction		-35.5 dB		-32.5 dB

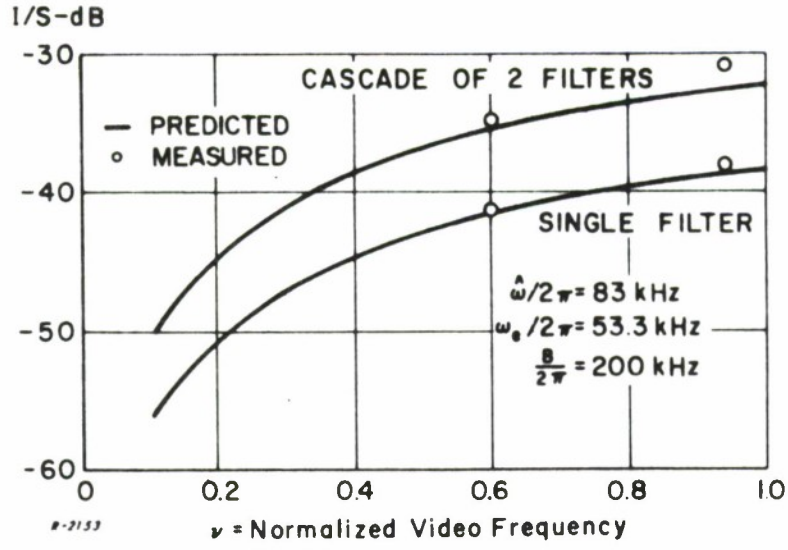

Figure 50 Measured and Predicted Distortion for a Cascade of a Cascade of Two Second-Order Butterworth Filters.

The filter used in the preceding test was also used to further verify the prediction of I/S given by Eq. (66). Of primary interest here was the dependence of distortion on the rms deviation ω_e and the video spectrum bandwidth $\hat{\omega}$. Equation (66) shows that, assuming the third-order distortion term to predominate, the distortion increases with ω_e^4. That is for a factor of two increase in ω_e, I/S should increase by 12 dB, (i. e., 12 dB/octave). This dependence was measured experimentally using a 400 kHz bandwidth second-order Butterworth filter. The results of the test are shown in Fig. 51. The lower curve is a plot of the residual distortion in the test configuration as a function of deviation. The top solid curve is a plot of the measured distortion, while the dashed curve is the measurements corrected for noise floor. The slope of the corrected curve is found to be approximately 12 dB/octave which verifies the prediction and indicates that the principal distortion term is of third order.

Equation (66) also predicts a dependence of I/S on the video spectrum bandwidth $\hat{\omega}$. In this case the third-order prediction depends on $\hat{\omega}^2$, which is 6 dB/octave. This was tested by measuring the distortion as a function of $\hat{\omega}$ as shown in Fig. 52. The experimental results and prediction are plotted as a function of the notch location for three values of $\hat{\omega}$. The solid curves are the predictions obtained from Eq. (66) and the circled points are the measurements. Two results are evident. First, the experimental results agree quite closely with the predictions, demonstrating the 6 dB/octave dependence on $\hat{\omega}$. Secondly, this agreement continues even for the very large values of $\hat{\omega}$. As indicated in Section III, the quasi-stationary approximation of the distortion is expected to break down as $\hat{\omega}/B$ becomes large. It is shown here that even

for $\hat{\omega}/B$ approaching unity the quasi-stationary approximation still holds. Since it is extremely unlikely in any telemetry system that $\hat{\omega}$ will ever be greater than B, it follows that the quasi-stationary approximation is particularly applicable to dealing with telemetry systems.

5.6 Conclusions

Initial measurements conducted with the noise-loading test configuration have produced the following significant results:

a) Established the feasibility of the noise-loading technique as applied to telemetry in general, and ADCOM's adaptation of this technique to the measurement of intermodulation distortion produced by predetection filters.

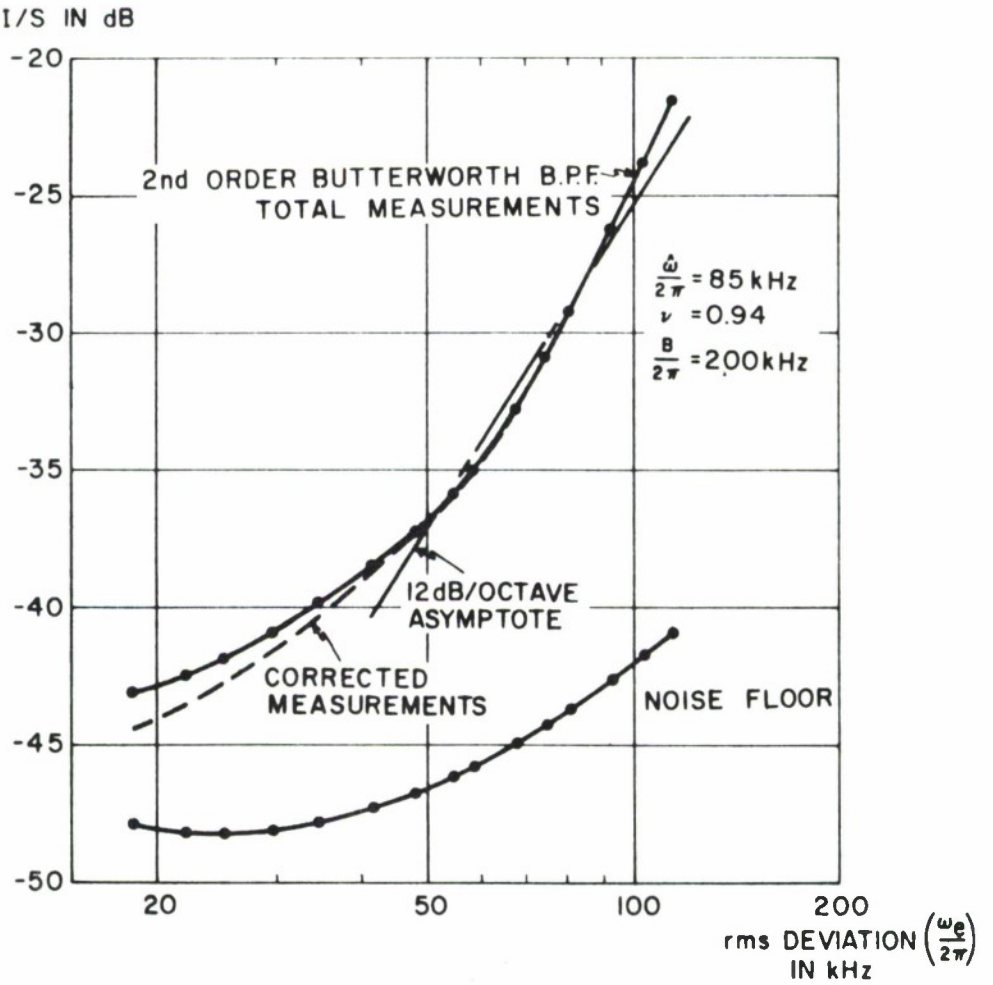

Figure 51 Effect of Deviation on Measured Distortion, Second-Order Butterworth Filters.

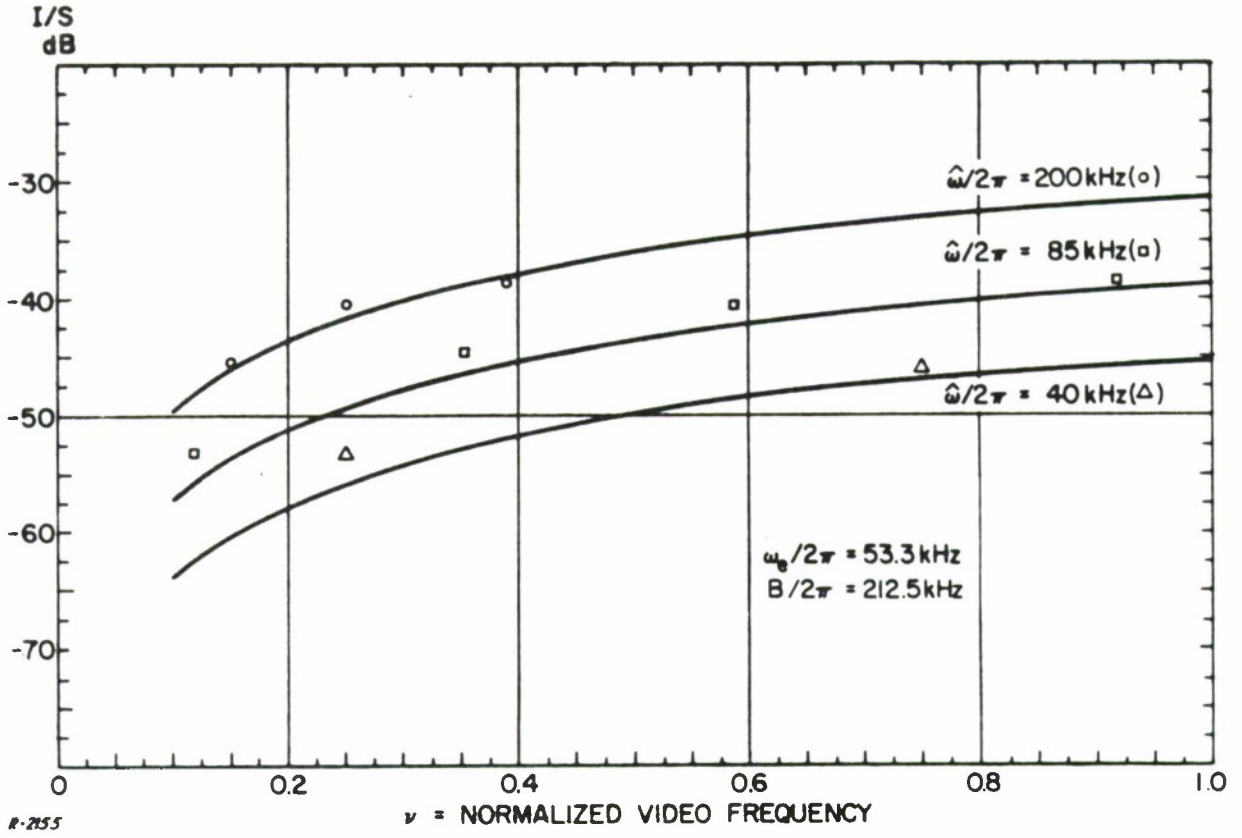

Figure 52 Measured and Predicted Distortion for Different Maximum Video Frequencies, Second-Order Butterworth Filters.

b) Verified the procedure for the correction of measurements to account for the residual distortion generated by the measurement equipment.

c) Verified the analytical results on the accumulation of distortion in cascaded identical filter stages.

d) Verified the quasi-stationary theory of intermodulation distortion based on the filter phase characteristic, at least for the types of filters and the ranges of parameters used in the tests.

e) As a consequence of d) above, showed that nonquasi-stationary distortion levels are negligible, at least for the types of filters and the ranges of parameters used in the test.

Section VI

MEASUREMENT OF INTERMODULATION DISTORTION IN TELEMETRY RECEIVERS

6.1 Measurements on Receiver A

6.1.1 Description of Receiver A

The block diagram of Receiver A is shown in Fig. 53. This receiver is completely solid state and is equipped with two RF plug-in modules, a VHF and UHF (S-Band) head, a plug-in IF amplifier and a high-capture-ratio discriminator.

The RF and first IF filters are double-tuned circuits with bandwidths of 4 MHz each. The 500 kHz IF amplifier plug-in consists of two cascaded fourth-order Butterworth filters. The second IF in this receiver is centered at 10 MHz, and the 500 kHz bandwidth identifying the IF amplifier is the 3 dB bandwidth.

The high-capture-ratio discriminator contains three narrowband limiter stages which serve to suppress undesired signals in a multi-signal environment. For best capture performance, the bandwidth of the filters in the discriminator should be equal to that of the IF amplifier.

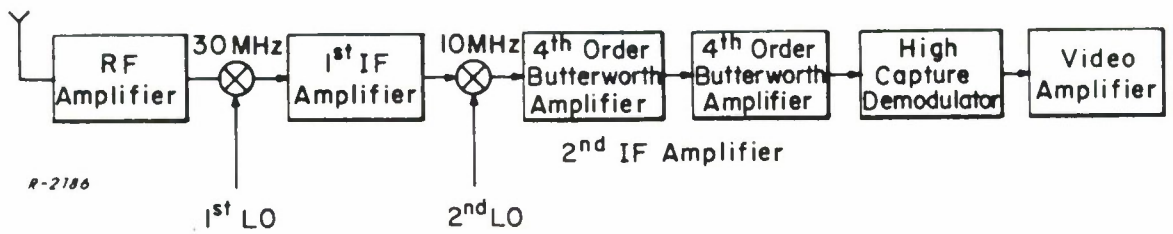

Figure 53 Block Diagram of Receiver A.

6.1.2 Distortion Measurements on the Receiver Second IF Amplifier

As indicated earlier in this report, the principal source of distortion in telemetry systems, under the quasi-stationary approximation, is the nonlinearity of the predetection-filter phase characteristic. In addition, it was indicated that most of the nonlinearity occurs in the second IF filter, which is usually the principal band-limiting device in the receiver. The philosophy in all tests conducted here will be to measure the distortion of the second IF alone, and as many other parts of the telemetry system as convenient and then measure each in combination with the second IF. Thus it will be possible to isolate and compare the distortion in the various sections of the system and identify the major sources of distortion.

To make distortion measurements on the second IF amplifier, the 10 MHz VCO was used as an FM modulator and its output fed into the second IF input of the receiver. The input amplitude was adjusted to simulate normal operating conditions of frequency deviation. The predetection output of the receiver which is the second IF output was then fed to the FM discriminator in the I/S measurement configuration of Fig. 37.

Distortion tests were conducted on the 500 kHz IF for $\hat{\omega}/2\pi = 85$ kHz and $\omega_e/2\pi = 53.3$ kHz at four different notch locations in the video spectrum. The 500 kHz IF is composed of two fourth-order Butterworth filters whose individual 3dB bandwidths were found by direct measurement to be 558 kHz.

Tests were first conducted with all four notches without the second IF in the measurement configuration. This permitted establishment of the test system noise floor which could then be subtracted out of the measurements on the second IF. Figure 54 shows the results of this test. The equipment noise floor is plotted as the circled points. The measurements with the second IF are plotted by the x points. Since the distortion can be measured to ± 0.5 dB it can be seen that the difference between these two is large enough to give good accuracy when the correction is made. The dashed curve shows the distortion due to the second IF obtained by correcting the overall measurements for the noise floor. Finally the solid curve shows the theoretically obtained prediction for these test conditions. The agreement between prediction and measurement is within 2 dB which is quite acceptable.

6.1.3 Measurements With High-Capture-Ratio Demodulator

Receiver A is equipped with a high-capture-ratio demodulator to enhance its multi-signal-environment operation. The high capture performance is obtained by using the well-known technique of narrowband limiting which spreads the spectrum of the resultant of the desired and undesired signals and filters this spectrum. The mechanism is such that sizable portions of the interference spectrum are thus excluded without substantially affecting the strong signal spectrum. For optimum performance

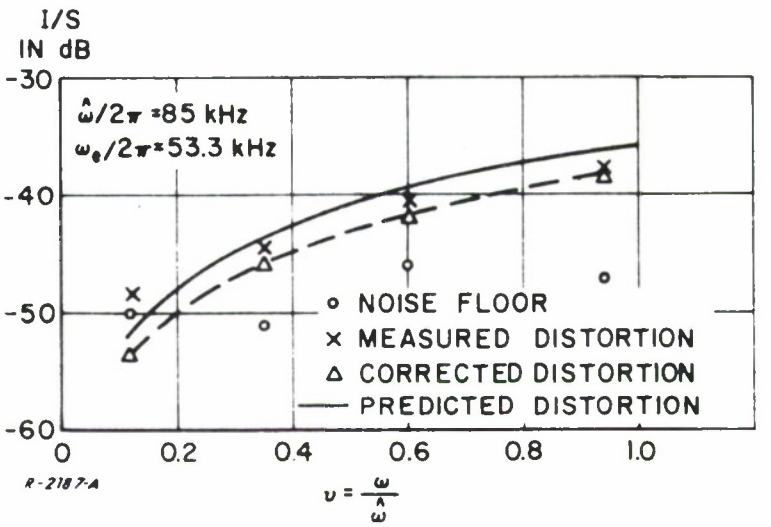

Figure 54 Noise Floor and Distortion Measurements on Second IF Amplifier of Receiver A.

the bandwidth of the narrowband limiter should be equal to that of the desired signal. Since this bandwidth is not always known, the best compromise is to have the narrowband limiter bandwidth equal the second IF bandwidth. Thus, when using the 500 kHz IF amplifier in this receiver, a 500 kHz bandwidth demodulator is also used.

Distortion tests were conducted on this demodulator alone to permit comparison of its distortion to that of the second IF amplifier and also to other receiver demodulators and to the laboratory demodulator used in the I/S measurement configuration. In the test, the FM output of the VCO was fed directly into the high-capture-ratio demodulator, replacing the pulse-count discriminator in the I/S measurement configuration. The value of $\hat{\omega}/2\pi$ and $\omega_e/2\pi$ were maintained at 85 kHz and 53.3 kHz and tests with the four notch filters were conducted. Figure 55 displays the experimental results using the high-capture demodulator (solid curve) and the laboratory demodulator (broken line). It can be seen that the high-capture demodulator introduces significantly more distortion than the pulse-averaging demodulator. As will be shown later, it also introduces more distortion than a receiver demodulator without the high-capture-ratio capability.

The relative distortion levels introduced by the high-capture demodulator and the receiver IF amplifier can be seen in Fig. 56. Here the distortion with the 500 kHz second IF taken using the pulse-count

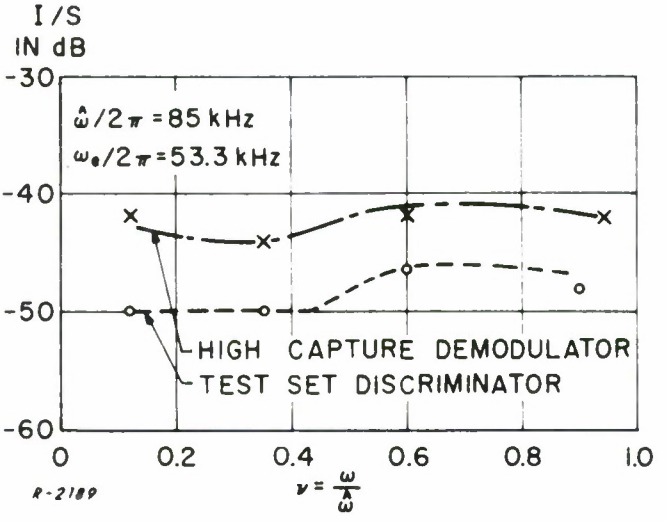

Figure 55 Measured Distortion of High-Capture-Ratio Demodulator of Receiver A.

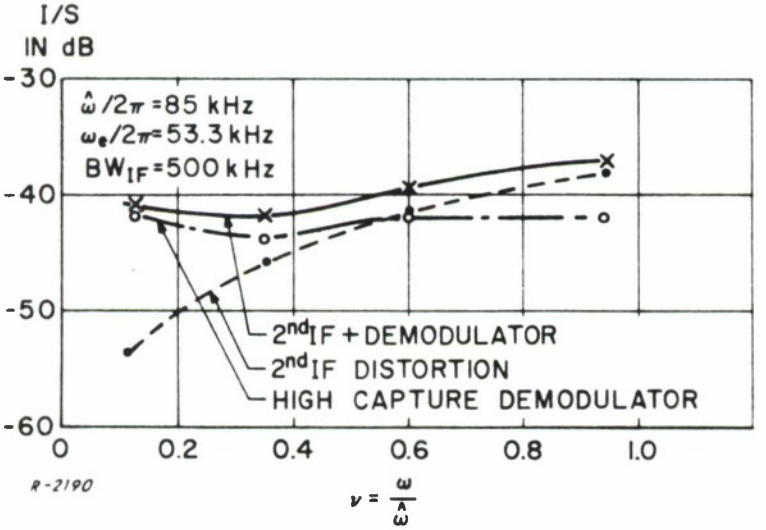

Figure 56 Measured Distortion with 2nd IF Amplifier and High-Capture Demodulator of Receiver A.

discriminator and corrected for noise floor is plotted as a dashed curve. The distortion using the high-capture demodulator alone is shown by the broken curve, and the distortion taken cascading the second IF and high-capture demodulator is the solid curve. It can be seen that the demodulator distortion and the second IF distortion are of the same order. This is to be expected since their bandwidths are the same and the form of the filters are similar. This results in the distortion of the cascade being significantly higher than that of the second IF alone. These results indicate that a compromise exists between improvement in data quality in a multi-signal environment obtained with the high-capture demodulator, and inherent high distortion of such a demodulator.

6.1.4 Measurements With the RF Sections

Two RF plug-ins were provided with Receiver A; the standard VHF head with a 216 MHz to 260 MHz tuning range and a new UHF head with tuning range of 2200 MHz to 2300 MHz. Both heads were broadband, having a 3 dB bandwidth of 4 MHz. Tests were conducted only in conjunction with the second IF of the receiver since it would have otherwise been impossible to get sufficient signal level, without external amplification, to detect the FM.

For tests with the VHF head, a Boonton 202J Telemetry Band Generator was used as the FM source in the block diagram of the I/S measurement configuration of Fig. 37. Tests were taken using this generator with the pulse-count discriminator alone and second IF to measure the noise floor and account for any changes in distortion readings with the second IF. In general, tests with this generator gave higher distortions because of its more nonlinear modulation characteristic as discussed in Subsection 5.4. However, when the noise floor was subtracted out, the distortion of the second IF amplifier was the same as obtained using the VCO in the preceding section.

Distortion was also measured using the entire receiver, i. e., VHF, second IF and high-capture demodulator. Figure 57 illustrates these three measurements with $\hat{\omega}/2\pi$ and $\omega_e/2\pi$ still 85 kHz and 53.3 kHz respectively. The lower two curves compare the distortion with the second IF alone (dashed curve) and the VHF head cascaded with the second IF (broken curve). As is to be expected, the RF section introduces very little additional distortion (less than 3 dB). This is because of the wide bandwidth and hence low phase nonlinearity of the front-end filters. The solid curves show the distortion using the entire receiver simulating actual field operation. Again, the addition of the high-capture demodulator has increased the distortion significantly.

For the test using the UHF front-end no S-Band FM generator was readily available so the technique of Fig. 58 was used. The 10 MHz VCO was modulated as before with the video spectrum and was then mixed up to

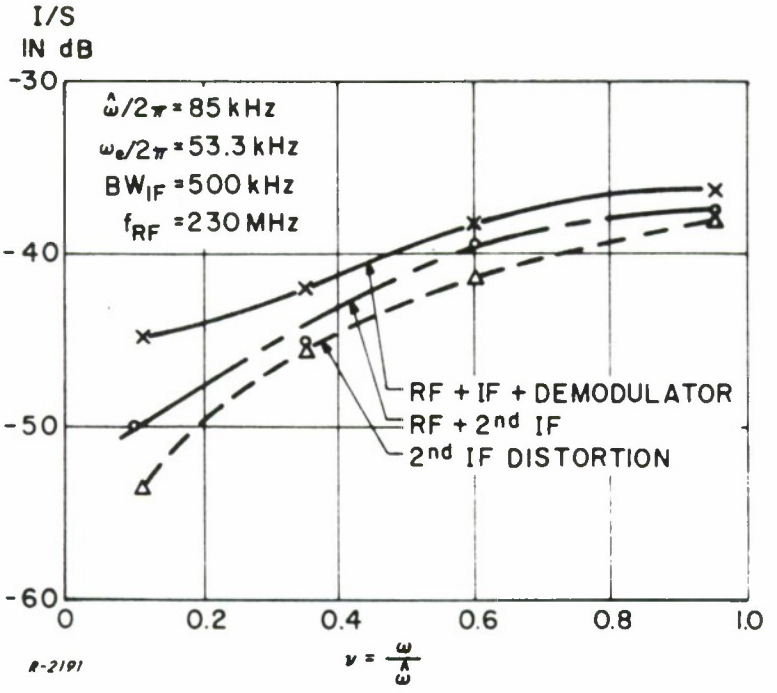

Figure 57 Measured Distortion with VHF Receiver A.

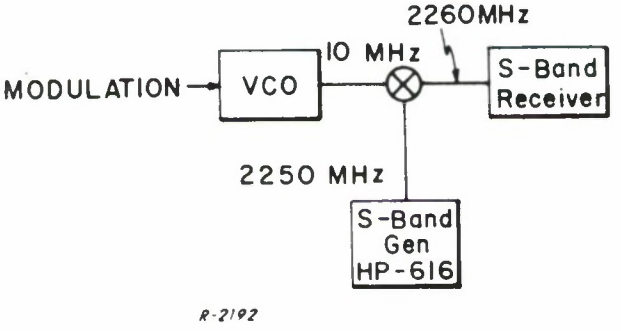

Figure 58 Technique for Generating S-Band FM Signal.

2260 MHz in a microwave mixer using a S-Band generator as the LO. The mixer output was coupled to the receiver RF input and the receiver was used to select one of the sidebands. The 20 MHz separation between sidebands was sufficient for the receiver to reject both the carrier and undesired sideband. The test was conducted maintaining $\hat{\omega}/2\pi$ and $\omega_e/2\pi$ at 85 kHz and 53.3 kHz respectively. Figure 59 compares the distortion with the second IF alone to that of the entire receiver with the UHF and VHF head. The results are almost exactly the same as those obtained using the VHF head and shows no significant distortion introduced by the UHF front-end.

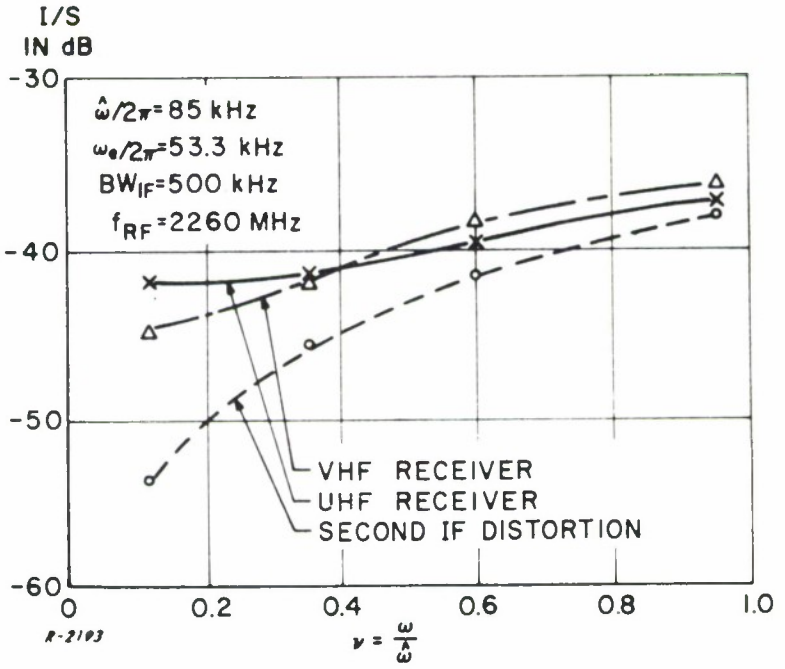

Figure 59 Measured Distortion with UHF Receiver A.

Some difficulties were encountered in taking measurements with the S-Band head. These were related to proper line lengths and terminations between the mixer output and receiver RF input. It was discovered that as the line length was changed, setting up standing waves at the RF input, the intermodulation distortion was increased significantly, by as much as 5 dB. This result indicates that echo distortion resulting from the standing waves acts to degrade the data quality in much the same way as predetection filtering. An interesting side result of this test is that such echo distortion effects can be measured with the noise-loading technique. It is to be emphasized that, with proper matching, the UHF head introduced no significant distortion above that of the second IF amplifier.

The results of tests on Receiver A can be summarized as follows:

a) The computation of distortion on the basis of the second IF amplifier phase characteristic has again been demonstrated to be an accurate prediction of the distortion.

b) Although much of the distortion in the receiver is generated in the second IF amplifier, high-capture demodulators also contribute significant distortion. Thus, a tradeoff between performance in a multi-signal environment and inherent distortion exists.

c) No significant distortion is introduced by the VHF or UHF front-ends. However, the UHF head was found to be susceptible to echo distortion caused by mismatched transmission lines.

6.2 Measurements on Receiver B

6.2.1 Description of Receiver B

The block diagram of Receiver B is shown in Fig. 60. This receiver is completely solid state and is equipped with a VHF RF section, three plug-in second IF filters and a wideband FM demodulator.

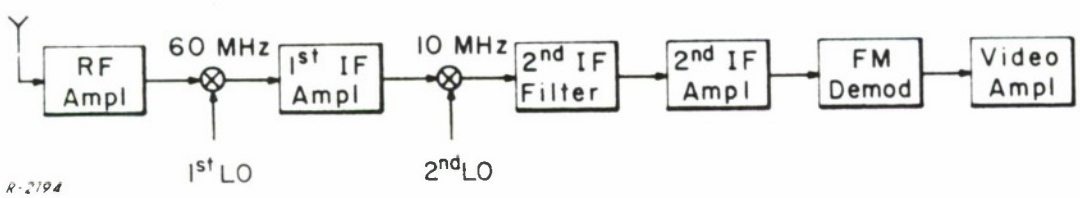

Figure 60 Block Diagram of Receiver B.

The RF and first IF sections of this receiver have a 5 MHz bandwidth. The second IF amplifier is centered at 10 MHz and has a bandwidth of 3 MHz with a response shape of a three-pole Bessel (linear-phase) filter. The second IF bandwidth is controlled by plug-in filter modules which are isolated from the IF amplifier, thus permitting changes in bandwidth without affecting other receiver characteristics. The three plug-ins were all sixth-order filters with a

500 kHz constant amplitude (Butterworth design), a 500 kHz linear phase (Bessel design), and a 300 kHz linear phase. The FM demodulator in the receiver is a wideband Foster-Seely type having a bandwidth of 3 MHz.

6.2.2 Distortion Measurements on the Receiver Second IF Amplifier

Using the same test technique discussed in conjunction with tests on the second IF of Receiver A, distortion measurements were conducted on the second IF amplifier and filter of Receiver B. The measurement configuration was the same as shown in Fig. 37 with the VCO output feeding the second IF and its output in turn feeding the pulse-count discriminator. Prior to testing the filters, residual distortion measurements were again made on the test configuration. In this case it was possible to have the second IF amplifier of the receiver in the test configuration and simply switch out all filters. The noise floor measured with this test configuration was essentially the same as that in the test with Receiver A. Tests on all three filters in this receiver were taken with $\hat{\omega}/2\pi = 85$ kHz and $\omega_e/2\pi = 53.3$ kHz.

The results of the test with the 500 kHz constant-amplitude filter are shown in Fig. 61. The solid curve is the theoretical prediction calculated on the basis of the filter phase characteristic. The circled points are experimental measurements corrected for noise floor which agree with the prediction

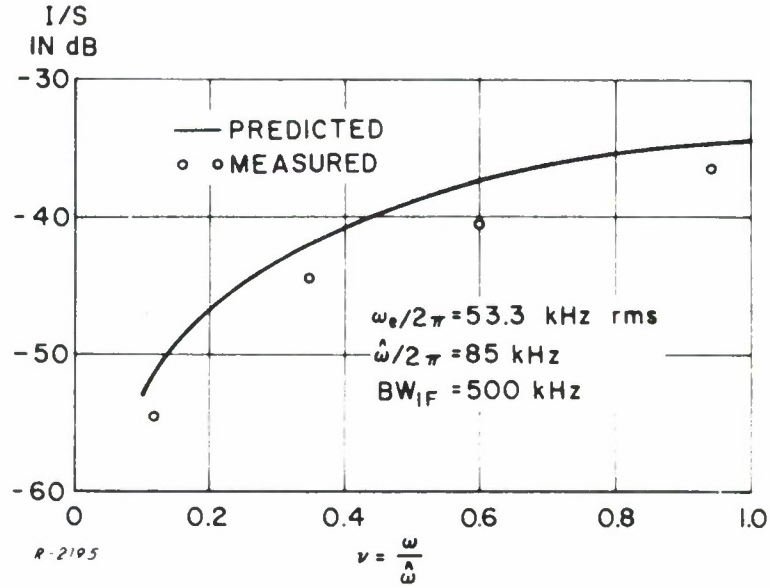

Figure 61 Measured and Predicted Distortion of 500 kHz Constant Amplitude IF of Receiver B.

to within about 2 dB. The fact that the measured distortion is lower than the predicted distortion is in agreement with the measurements of the group-delay characteristic. In Fig. 12 the measured group delay showed lower nonlinearity at the center frequency than the theoretical delay. This is caused by slight misalignment of the filter. It would then be expected that the predicted distortion would be higher than the measured distortion as is the case.

Similar tests were conducted using the 500 kHz and 300 kHz linear-phase filters. The measured results and theoretical predictions are plotted in Figs. 62 and 63, respectively. Here the agreement between experiment and prediction is not as good as it was with the Butterworth filters. The reason for this is connected with the nature of the Bessel filter phase characteristics.

It can be seen from Fig. 4 that properly-aligned Bessel filters are capable of highly linear-phase characteristics. The corresponding low-order phase coefficients vanish (see Table IV), resulting in extremely low I/S ratios (see Table XI). However, slight misalignment can result in the reappearance of some of the low-order phase coefficients, and hence, in greatly increased I/S ratios. Thus, the low-distortion capabilities of Bessel filters are strongly dependent on accurate alignment.

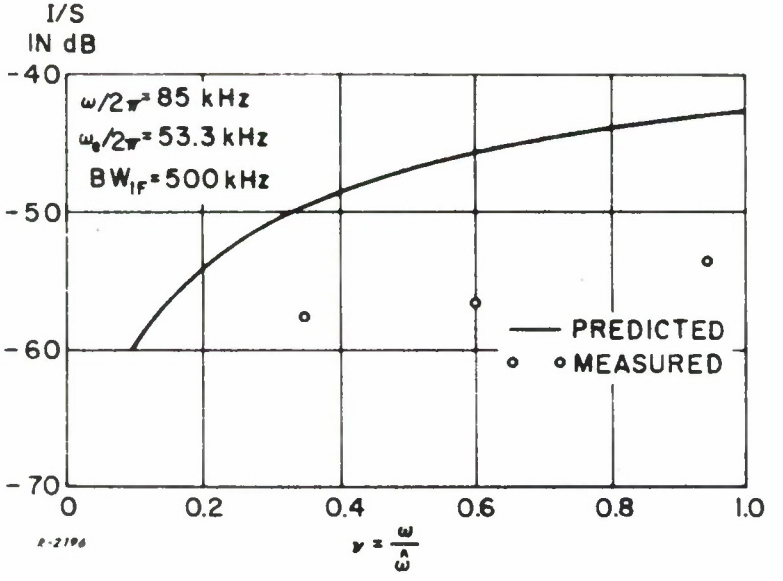

Figure 62 Measured and Predicted Distortion on 500 kHz Linear Phase IF of Receiver B.

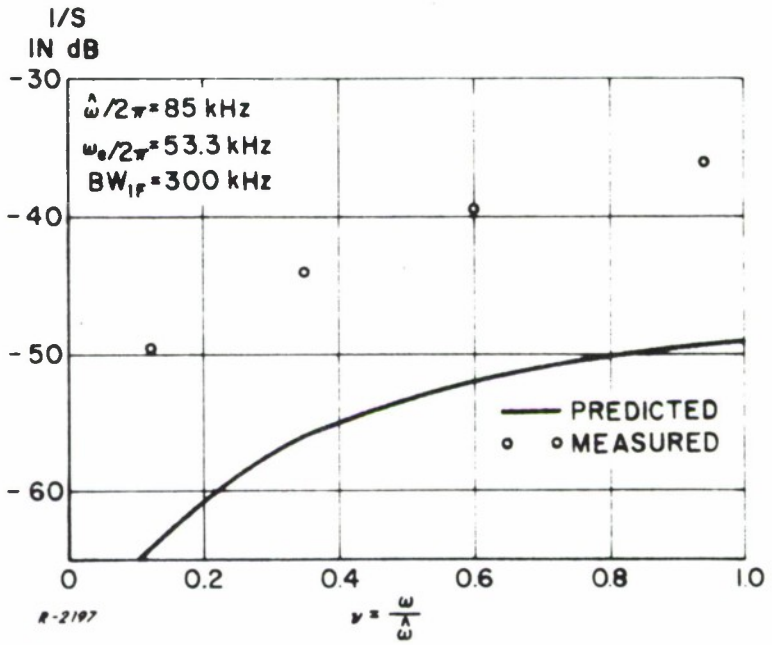

Figure 63 Measured and Predicted Distortion on 300 kHz Linear Phase IF of Receiver B.

The measured group delays of the linear-phase filters (Figs. 64 and 65) show significant misalignment, which accounts for their failure to achieve the very low I/S ratios indicated by Tables IV and XI. In particular, both curves have a pronounced slope at the origin. This indicates that the phase coefficient c_2 is nonzero, since the two are related by

$$\text{slope at origin} \quad \left(\text{sec}^2/\text{rad}\right) = \frac{2c_2}{B^2}$$

The value of c_2 was estimated in both cases by fitting a straight line (shown on Figs. 64 and 65) tangent to the group-delay curve at the origin. The corresponding values of slope and c_2 are also shown on the figures. The predictions shown in Figs. 62 and 63 are obtained by inserting these values of c_2 into the second-order term of Eq. (66).

In the case of the 500 kHz linear-phase filter the prediction in Fig. 62 is about 10 dB too high. This corresponds to a change in the slope of the group delay characteristic by a factor of 3. Examination of the group delay shows that the slope is ambiguous, and indicates the need for a better attempt at extracting the coefficients from the group-delay curve, such as using higher-order coefficients.

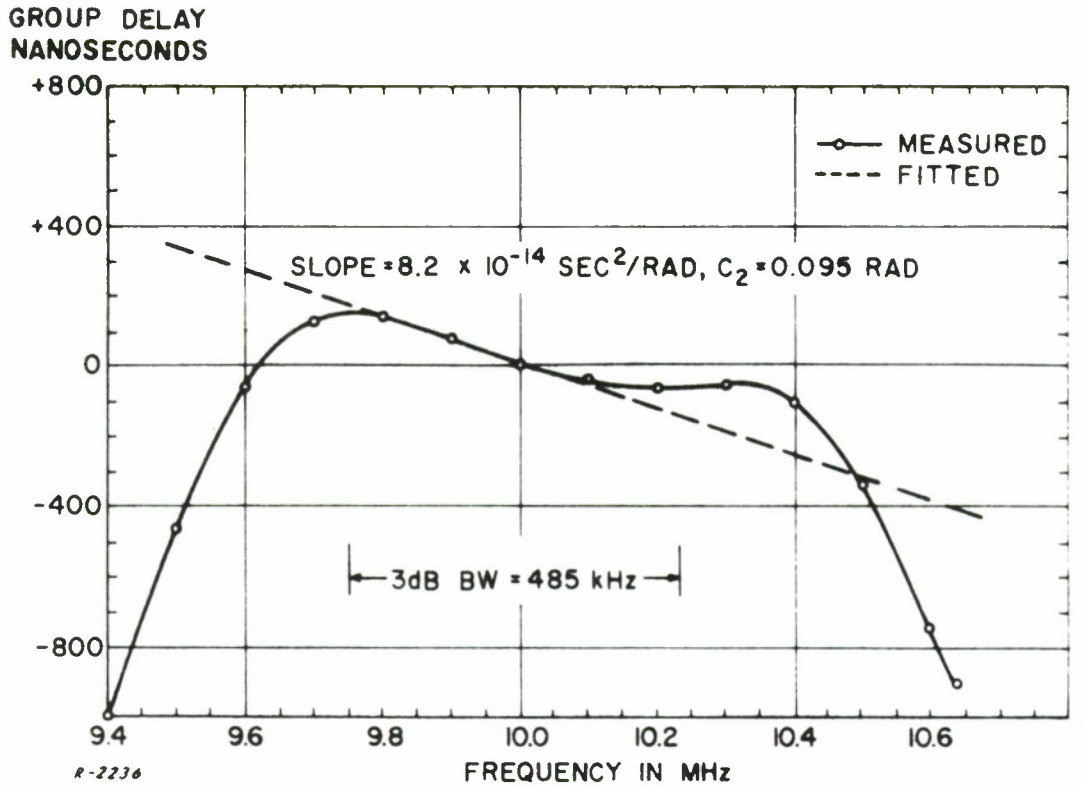

Figure 64 Measured Group Delay and Fitted Tangent, 500 kHz Linear Phase Filter.

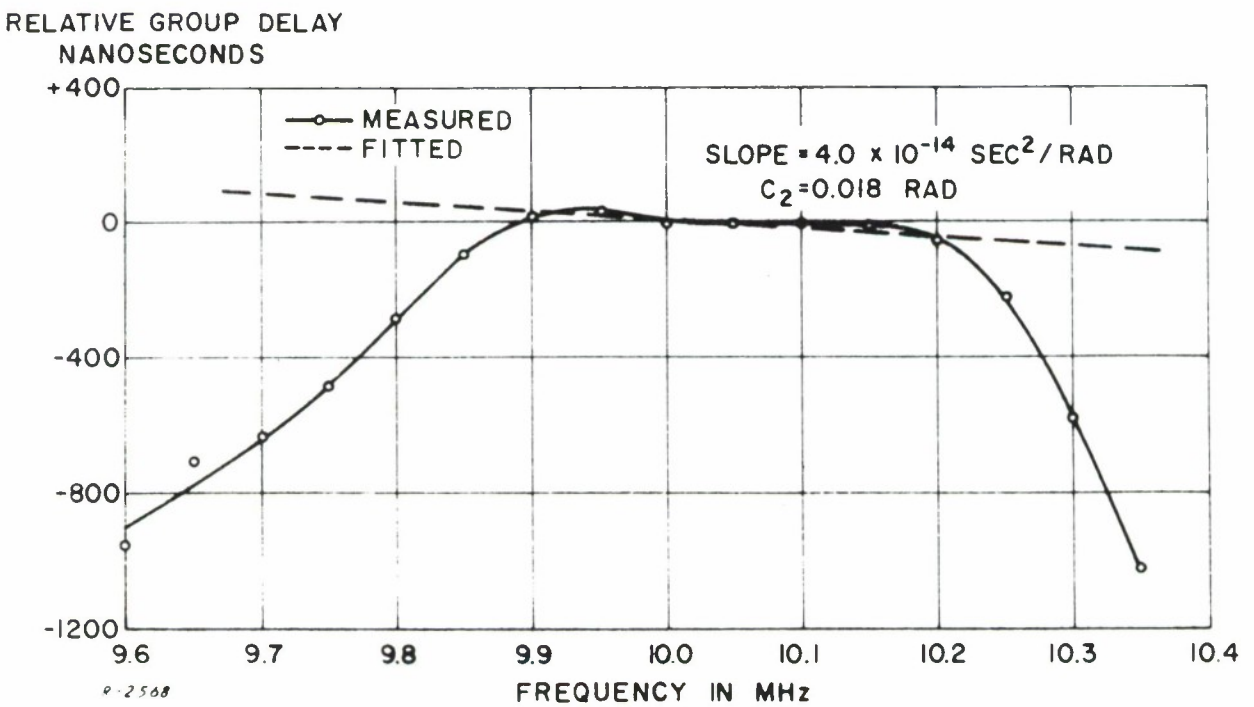

Figure 65 Measured Group Delay and Fitted Tangent, 300 kHz Linear Phase Filter.

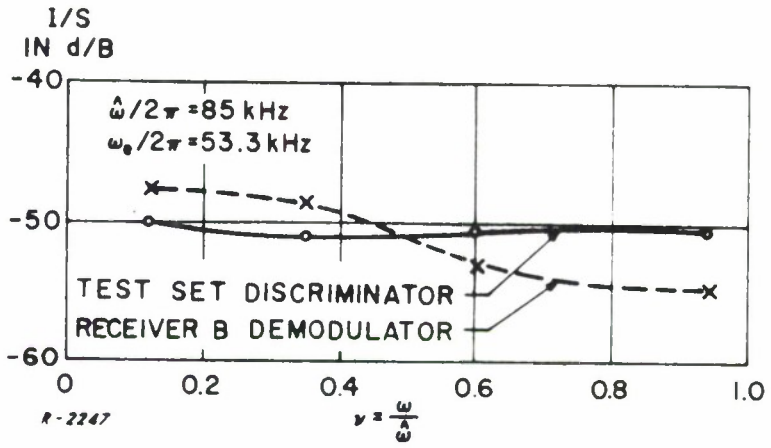

Figure 66 Measured Distortion of Receiver B Demodulator.

In the case of the 300 kHz filter, the prediction is further off, being 12 dB too low. The problem here, as with the 500 kHz filter, is the accuracy necessary in drawing the tangents for such low group-delay variations. Higher-order coefficients could be derived by fitting a more complicated curve to the measured distortion and the prediction of distortion should agree more closely with the measurement. On the other hand, this problem lends itself particularly to the Hermite Polynomial Technique for predicting the distortion spectrum, as outlined in Appendix III. The procedure would be to compute the coefficients h_2 and h_3 using Eq. (A3.4) and the measured points in Figs. 15 and 17. A digital computer would be required to perform the numerical integration.

An interesting comparison can be made between the 500 kHz constant-amplitude and 300 kHz linear-phase filters. Examining their measured distortion levels from Figs. 61 and 63 shows that they are approximately equal. This is an interesting and important result from two points of view. First, as can be seen by comparison of the amplitude characteristics in Figs. 12 and 16, the out-of-band amplitude characteristic of the 300 kHz Bessel filter falls within that of the 500 kHz Butterworth indicating at least the same amount of attenuation to spurious and adjacent channel signals. Second, the distortion of the narrower filter, 300 kHz Bessel, is no more than that of the wider filter, 500 kHz Butterworth. This is directly attributable to the relative linearities of their phase characteristics. The importance of the phase linearity is even more striking when the distortion of the 500 kHz linear-phase and constant-amplitude

filters are compared. Here, although they have the same 3 dB bandwidths, the linear-phase filter has far less distortion than the Butterworth filter. Had the Bessel filters been more accurately aligned, they would have achieved more spectacular performance.

6.2.3 Measurements With the Receiver Demodulator

As indicated earlier the demodulator supplied with Receiver B is a wideband Foster-Seely type having a 3 MHz bandwidth. Tests were conducted using this demodulator in place of the pulse-count discriminator of the I/S measurement configuration of Fig. 37 to evaluate its contribution to distortion. Since the demodulator is wideband the contribution to distortion would arise from nonlinearities in the demodulation characteristic.

Tests conducted on this demodulator indicate that its distortion is as low as and sometimes lower than that of the pulse-count discriminator in the I/S test configuration. Figure 66 illustrates this. A comparison of Figs. 66 and 55 illustrates the compromise in intermodulation distortion incurred by having a demodulator with a high-capture-ratio property. The distortion level with the wideband demodulator of Receiver B is 6 to 10 dB lower than that of the high-capture demodulator. This result must be considered when contemplating the use of a high-capture demodulator depending on narrowband limiters for its performance.

Figures 67 and 68 illustrate the relative levels of distortion introduced by the demodulator of Receiver B and the 500 kHz and 300 kHz linear-phase IF filters. Figure 67 represents the situation when the second IF distortion is very low resulting in the distortion of the demodulator becoming significant. The broken curve is the distortion of the demodulator alone and

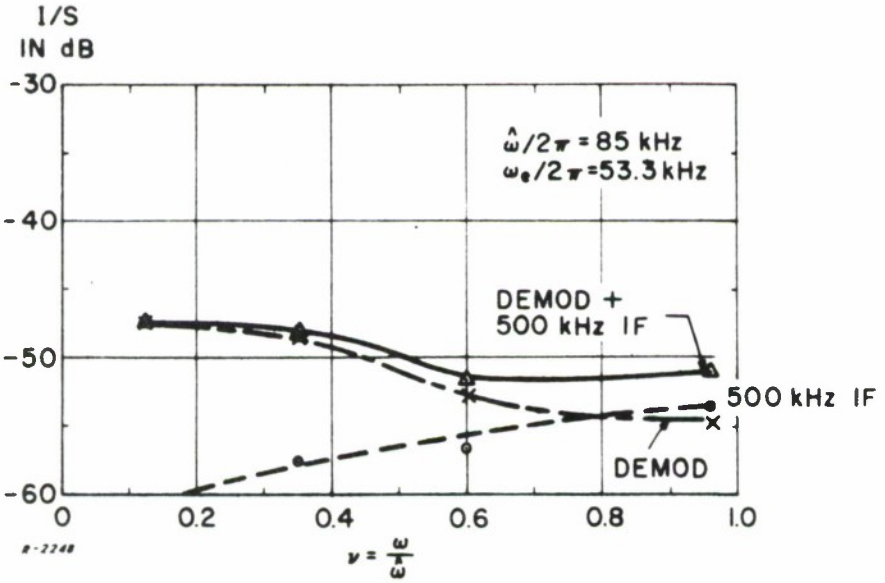

Figure 67 Measured Distortion with 500 kHz Linear-Phase IF Amplifier and Demodulator of Receiver B.

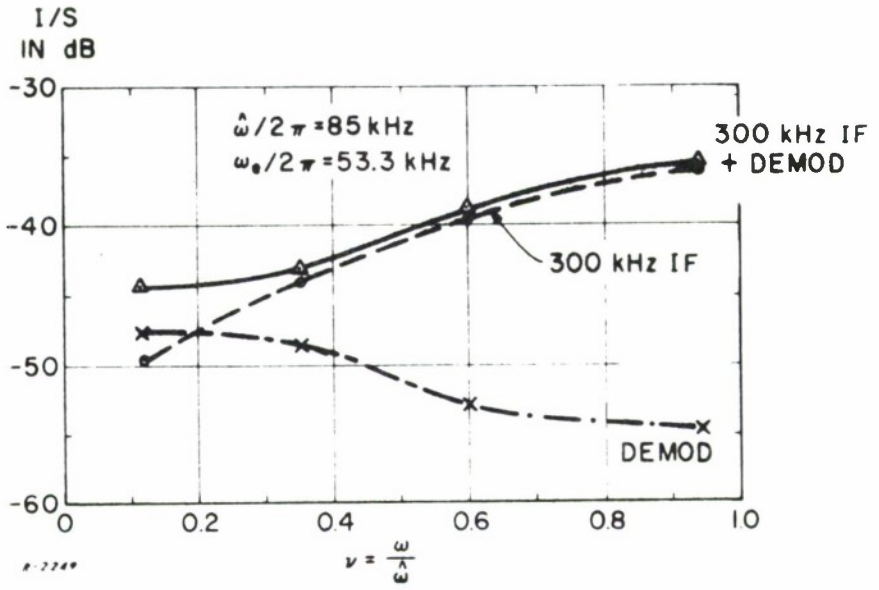

Figure 68 Measured Distortion with 300 kHz Linear-Phase IF Amplifier and Demodulator of Receiver B.

the dashed curve the distortion of the 500 kHz linear phase IF alone. The solid line is the distortion of the cascade. Figure 68 shows that for the second IF filter with the higher distortion level, the demodulator distortion is insignificant. Here again the broken line is the demodulator alone, the dashed line is the second IF distortion and the solid curve is the distortion of the cascade. Clearly the distortion of the cascade is approximately the same as that of the second IF alone.

6.2.4 Measurements With VHF RF Section

Receiver B is equipped with a VHF head with a tuning range of 216 MHz to 260 MHz. Once again tests were conducted only in conjunction with the second IF amplifier of the receiver. However, since this receiver had the facility of removing all IF filters and using only the wideband second IF amplifier, it was possible to get a measure of the distortion of the RF section alone.

The tests were conducted using the Boonton 202J Generator, which as mentioned previously, has higher inherent distortion. All tests were conducted with $\hat{\omega}/2\pi = 85$ kHz and $\omega_e/2\pi = 53.3$ kHz and with signal levels which simulated normal operating conditions. The first test was conducted using the RF and wideband IF of the receiver in the measurement configuration of Fig. 37. This measurement included the residual noise of the FM generator in addition to that of the receiver RF and wideband IF. An attempt was made to subtract out the effects of the generator by using it at a 10 MHz output and

measuring the equipment noise floor with the second IF amplifier. The measurements in both cases were nearly identical, indicating that the FM generator was introducing most of the distortion in this test.

In addition tests were conducted by cascading the 500 kHz constant-amplitude second IF filter and the receiver demodulator with the RF section. These tests simulate the actual field operation of Receiver B. Figure 69 illustrates these test results. The dashed curve is the distortion of the second IF alone. The solid curve is the distortion of the entire receiver. It is clear in this case that distortion in the RF and demodulator sections is insignificant compared to that of the second IF.

The results of the tests conducted with Receiver B may be summarized as follows:

a) The principal source of distortion is the second IF filter.

b) The Bessel filter gives considerably lower distortion than the Butterworth with the same bandwidth and number of poles. This is directly attributable to the better phase linearity of the Bessel filter.

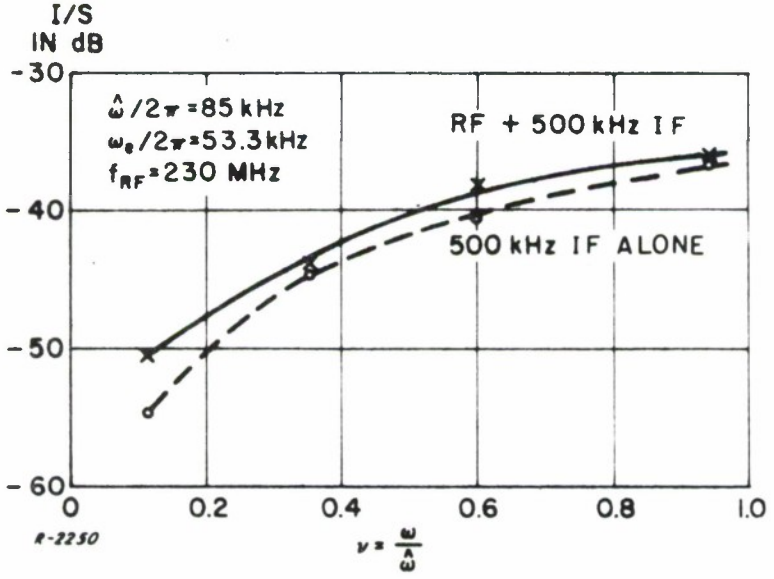

Figure 69 Measured Distortion with VHF and IF of Receiver B.

c) The 300 kHz Bessel filter and 500 kHz Butterworth filter have approximately the same measured distortion and skirt selectivity, indicating that the flatness of the amplitude characteristic is of only secondary importance when considering intermodulation distortion.

6.3 Measurements on Receiver C

6.3.1 Description of Receiver C

The block diagram of Receiver C is shown in Fig. 70. It is composed of both vacuum-tube and transistor amplifiers and is equipped with a VHF RF unit, an IF amplifier and demodulator unit having several plug-in IF amplifiers, two of which were tested, and three plug-in demodulators, and a video amplifier unit.

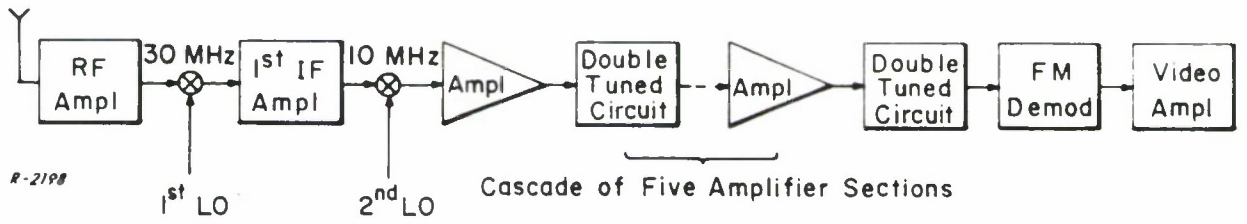

Figure 70 Block Diagram of Receiver C.

The RF and first IF filters are composed of cascaded double-tuned circuits with an overall bandwidth of 4 MHz. Each second IF plug-in amplifier is composed of a cascade of five double-tuned circuits, each slightly over-coupled and isolated by amplifier stages. Two IF's, the 500 kHz and 300 kHz amplifiers, were tested extensively. The three demodulators are Foster-Seely types with different bandwidths. The narrowband demodulator is composed of two single-tuned circuits and has an 80 kHz bandwidth. The intermediate demodulator also has two single-tuned circuits and has a bandwidth of 1 MHz. The wideband demodulator has two double-tuned circuits with a 5 MHz bandwidth.

6.3.2 Distortion Measurements on Second IF Amplifiers

The distortion tests at IF were conducted using the 10 MHz VCO and the laboratory discriminator of the I/S test configuration in Fig. 37. Measurements were again made with $\hat{\omega}/2\pi = 85$ kHz and $\omega_e/2\pi = 53.3$ kHz at four different notch locations in the video spectrum and at normal operational signal levels.

The distortion measurements for the 500 kHz IF amplifier are shown in Fig. 71 along with the theoretical predictions. As was indicated previously, the IF amplifiers are made up of five cascaded double-tuned circuits. From the measurements of the amplitude and group delay on this amplifier presented in Figs. 18 and 19, it can be seen that this amplifier was approximately critically coupled (i. e., flat amplitude characteristic). The prediction shown in Fig. 71 (solid curve) was made under the assumption that the amplifier is a cascade of five critically-coupled equal bandwidth stages. It can be seen that the experimental agreement is within 2 dB which is quite acceptable.

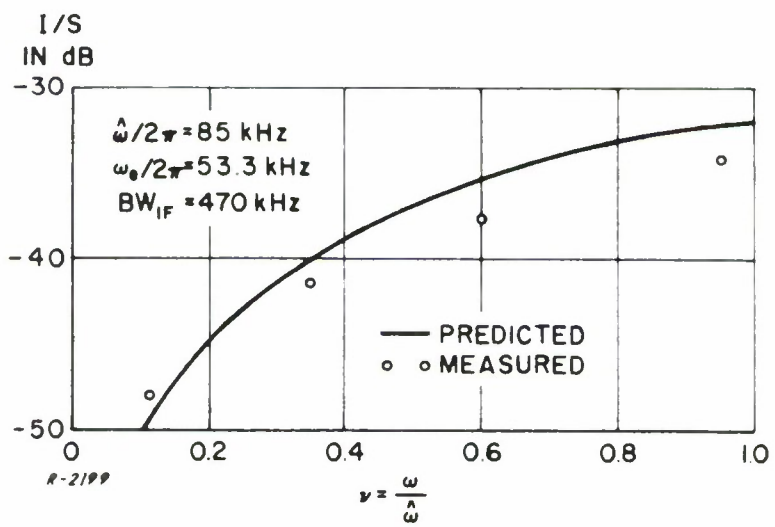

Figure 71 Measured and Predicted Distortion of 500 kHz IF of Receiver C.

The distortion measurements for the 300 kHz IF amplifier are shown in Fig. 72. Our first effort at obtaining distortion predictions proceeded as follows. The amplitude characteristic of each of the five stages was measured. Large differences were noticed between the various stages, indicating misalignment. From the amplitude characteristics, bandwidth and coupling coefficients were estimated for each stage. These two parameters completely describe a double-tuned circuit. Next, the phase coefficients for each stage were obtained from Eqs. (80) to (85), and combined using Eq. (89) to find overall coefficients for the cascade. When these coefficients were used to calculate the I/S ratio, the results differed significantly from the experimental results. As a check on self-consistency, overall group delay was plotted for the particular cascade of filters assumed in these calculations. This calculated curve was quite different from the experimental curve obtained from the real filter. The conclusion drawn from this disagreement is that use of the amplitude characteristics of the double-tuned stages to estimate their parameters did not produce a satisfactory agreement with the phase characteristic, resulting in the disagreement between I/S prediction and measurement.

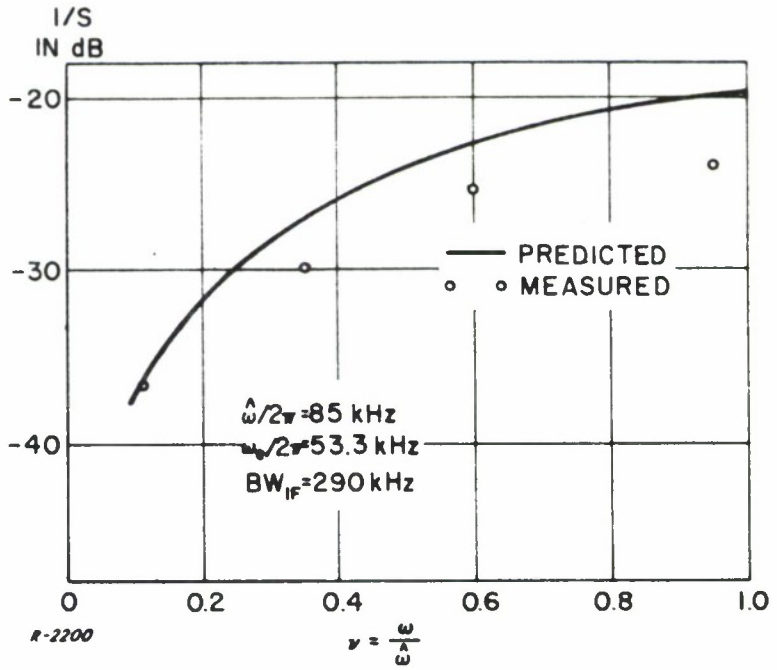

Figure 72 Measured and Predicted Distortion with 300 kHz IF of Receiver C.

In view of the above difficulties a more direct approach was used to obtain I/S predictions. A parabola was fitted to the measured group-delay curve as shown in Fig. 73. Assuming the truncated series for the phase

$$\Phi(\omega) = c_1\left(\frac{\omega - \omega_c}{B}\right) + c_3\left(\frac{\omega - \omega_c}{B}\right)^3$$

results in the parabolic form for the group delay

$$T_d(\omega) = \frac{c_1}{B} + \frac{3c_3}{B^3}\left(\frac{\omega - \omega_c}{B}\right)^2$$

The value of c_3, corresponding to this parabola ($c_3 = 0.89$) was used to make the I/S prediction shown in Fig. 72. (In Figs. 109 and 110 nomographs are presented which facilitate this procedure.) With this method the agreement between theory and prediction is within 4 dB. By a closer approximation to the experimental curve, i.e., deriving higher-order coefficients in the expansion, the agreement would be even better. This method of computing the distortion on the basis of the experimentally derived group-delay characteristic is particularly promising since it is computationally simple and provides a direct relationship between the distortion and group-delay variations. This is particularly encouraging in the light of the apparent difficulty as demonstrated here of accurately computing the group delay and hence distortion from the amplitude characteristic of the filters involved.

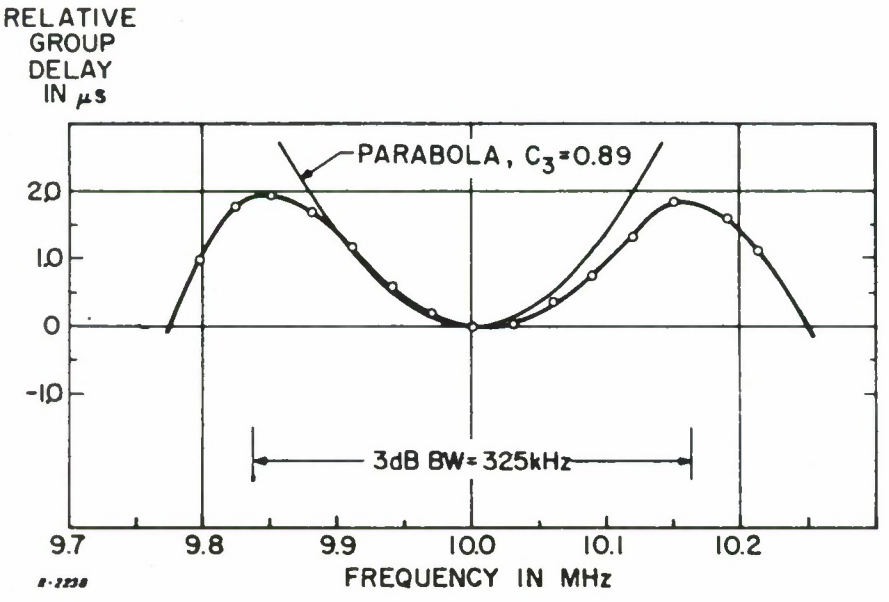

Figure 73 Measured Group-Delay Characteristic of Receiver C 300kHz IF Amplifier and Fitted Parabola.

6.3.3 Distortion Measurements With Demodulators

Tests were conducted to compare the distortion introduced by the laboratory discriminator and the wideband and intermediate bandwidth demodulators of Receiver C. As indicated previously, each of the receiver demodulators have filters preceding the discriminator which limit the bandwidth. The results of the test are shown in Fig. 74. The solid curve is the distortion using the laboratory discriminator. The dashed curve is obtained by using the wideband receiver demodulator and is seen to have as low distortion as the laboratory discriminator. The broken curve shows that the intermediate bandwidth discriminator introduces much more distortion. This result is directly attributable to the nonlinear phase characteristic of the filter preceding the discriminator. In the wideband demodulator, this filter is wide enough so that the phase characteristic is essentially linear in the region of signal occupancy. This is no longer true in the intermediate demodulator.

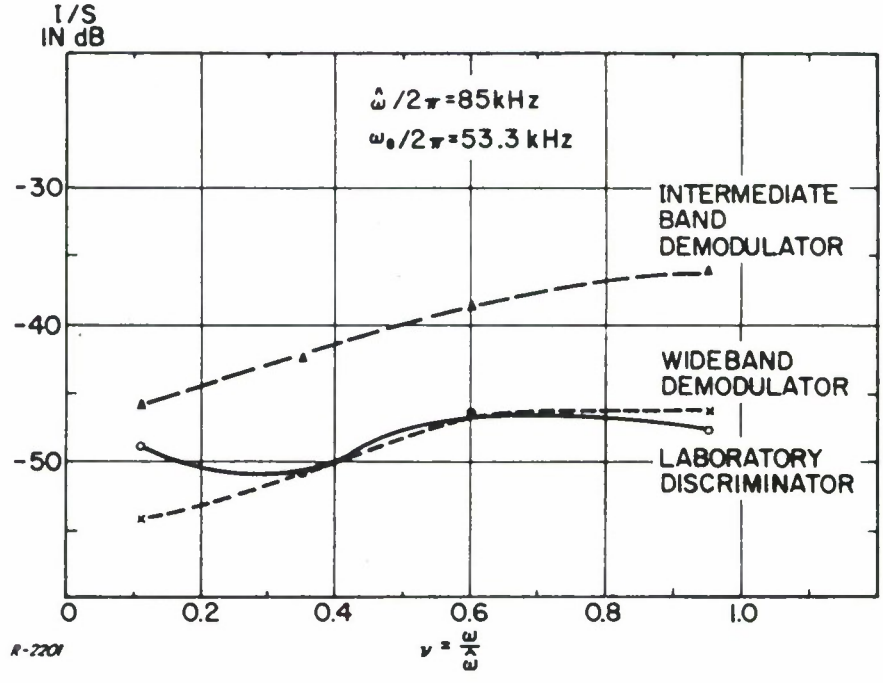

Figure 74 Measured Distortion with Receiver C Demodulators.

Thus, as was the case with the high-capture demodulator of Receiver A, narrowing the demodulator bandwidth introduces more distortion. This effect must be taken into account when considering demodulator bandwidth changes in adverse signal environments.

6.3.4 Distortion Measurements With the RF Section

With Receiver C as with Receiver A, it was impossible to make distortion measurements on the RF alone without introducing an external IF amplifier. Thus, tests were conducted in conjunction with the second IF. The Boonton 202J was again used as the FM generator. The curves of Fig. 75 compare the distortion due to the 500 kHz second IF amplifier (dashed curve) with the distortion using the entire receiver (solid curve). The VHF head was tuned to 230 MHz and the receiver's wideband demodulator was used. Figure 75 indicates that, for the high notch locations, the RF head and demodulator add little distortion to that introduced by the second IF amplifier. At the lower notch location there is a difference between the second IF and total receiver distortion. This however is due almost entirely to the inherent distortion in the 202J FM generator as discussed previously. Thus, the principal source of distortion in Receiver C is the second IF amplifier.

The results of the tests conducted with Receiver C indicate the following:

a) The principal source of intermodulation distortion is the second IF amplifier.

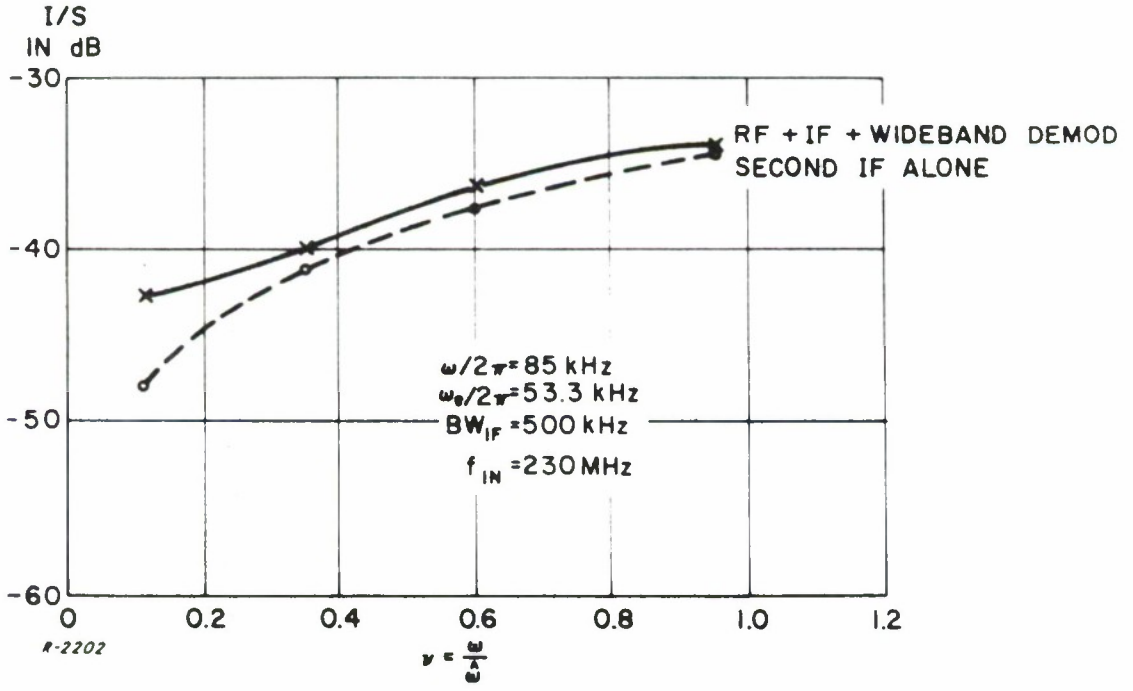

Figure 75 Measured Distortion with VHF Receiver C.

b) Narrowband FM demodulators are sources of significant distortion.

c) When the critical predetection filter consists of multiple cascades of misaligned filters, distortion prediction is more reliable on the basis of the overall group delay of the filter than those based on the amplitude characteristic.

6.4 Conclusions

The test results obtained from the intermodulation distortion measurements demonstrate that the noise-loading technique is an accurate and useful tool for measuring distortion in FDM telemetry receivers. The method is easy to implement and use, and results obtained with it have been highly meaningful. With this method the prediction of intermodulation distortion on the basis of predetection filter phase characteristics have been verified. Thus the phase characteristic alone has been demonstrated to be the principal mechanism by which intermodulation distortion occurs in the typical telemetry conditions simulated in these tests.

Within the telemetry receiving system, the second IF filter has been isolated and identified as the principal distortion-generating element. It has further been demonstrated that the highly linear-phase filters, such as the Bessel filter, cause less distortion than other types whose phase characteristics are not controlled. In addition, it has been shown that high-capture-ratio demodulators are a source of significant distortion due to the narrow bandwidths inherent in such devices. Also, echo effects due to mismatching in the S-Band tuner can be a source of distortion.

Section VII

MEASUREMENT OF INTERMODULATION DISTORTION IN PREDETECTION CONVERTERS

7.1 Measurements with the Down/Up Converter

7.1.1 Description of the Down/Up Converter

Predetection converters are used to translate the FM signal from the output of the receiver second IF to the record frequency of the recorder, and also to retranslate the reproducer output to the second IF frequency for playback purposes. The block diagram of the down/up converter used here is shown in Fig. 76. This converter was supplied with Receiver C. The down-conversion is accomplished by mixing the second IF output with a local oscillator whose frequency determines the input record frequency. The difference frequency between these two is selected and applied to the recorder input. For playback of the recorded predetection signal the reproducer output is mixed with a local oscillator of the same frequency as used in the down-converter.

Because this mixing process normally generates two sidebands with the desired signal information and with relatively small frequency separation, it is necessary to reject one of the sidebands (and the LO) before attempting demodulation of the desired sideband. This can be accomplished by any of several methods of single-sideband filtering. The method used in this up-converter is the phase-shift method. The reproducer output signal is applied to two-phasing networks whose output signals have a constant 90 degree phase difference. The local oscillator is also split and phase shifted to give two LO signals with 90 degree phase differences. The in-phase shifted reproducer signal and LO are then mixed in a balanced modulator giving the sum and difference frequencies of these two at the modulator output. The 90 degree phase-shifted reproducer signal and LO are also mixed in a balanced modulator again giving the sum and difference frequencies. In this case, however, because of the 90 degree phase shift in both signals, the sum frequency has a 180 degree phase shift and the difference frequency a 0 degree phase shift. Thus, when the output of the two balanced modulators are added, the amplitudes of the sum frequency cancel (opposite phase) while those of the difference frequency add. This procedure enables the suppression of the unwanted sideband and the carrier and provides the desired signal at the up-converter output. This signal is then generally applied to the playback input of the receiver and processed through the second IF and demodulator of the receiver.

There are several predetection filters in the down/up converter whose phase characteristics can contribute to intermodulation distortion. In the down-converter, the input amplifier has two double-tuned filters and the video amplifier has a lowpass filter. The bandwidth of the down-converter is 2 MHz. The up-converter, in addition to the phase-shift networks which

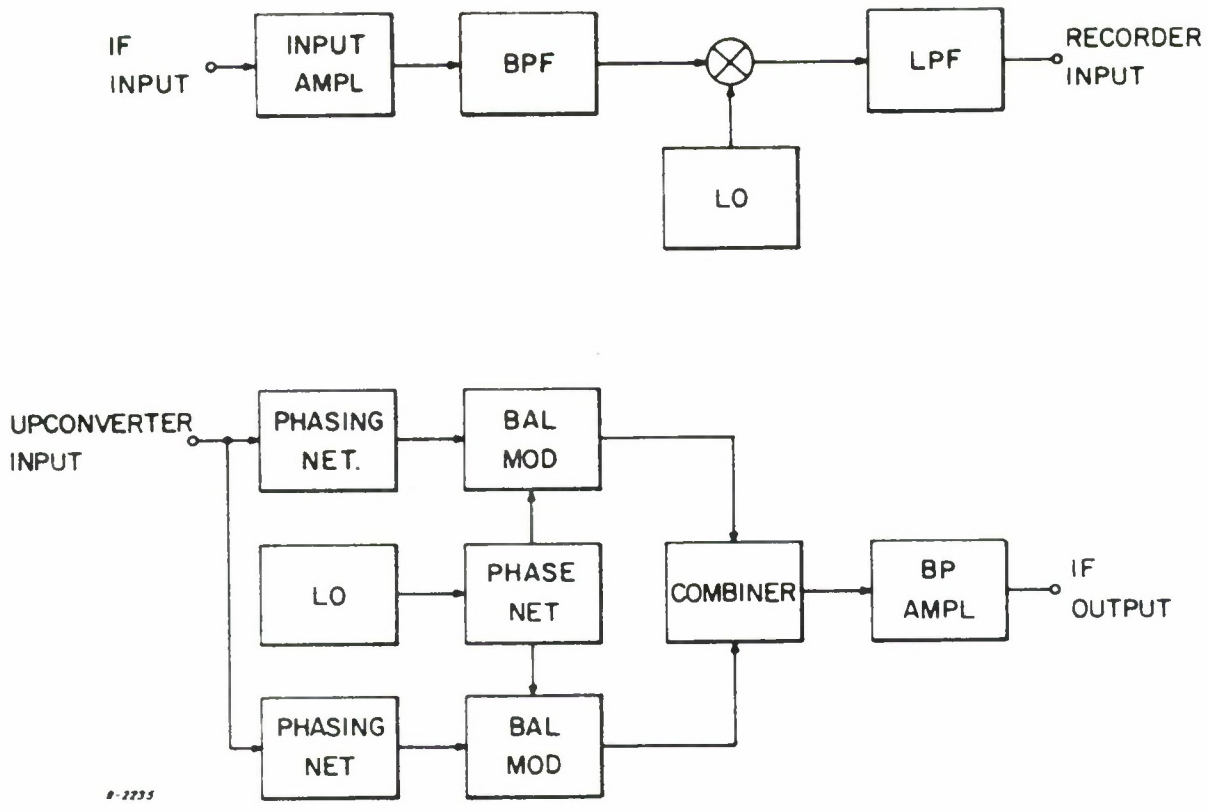

Figure 76 Block Diagram of Down/Up Converter.

have some nonlinearity, has three double-tuned filters in the output amplifier. The up-converter bandwidth is approximately 3 MHz.

7.1.2 Distortion Measurements With the Predetection Down/Up Converter

Distortion tests were conducted on the predetection converter alone. The converter was inserted between the VCO and pulse count discriminator of the I/S measurement configuration of Fig. 37. The signal from the VCO, which simulates that out of the receiver second IF, was applied to the down-converter whose output frequency was a parameter of the test. The down-converter output was supplied directly to the up-converter input, thus bypassing what would normally be the record process. The up-converter output was then applied to the FM discriminator of the test set for demodulation and I/S measurement. The bandwidth and deviation were maintained at the values used for the receiver tests, $\hat{\omega}/2\pi$ = 85 kHz and $\omega_e/2\pi$ = 53.3 kHz. The signal amplitude was adjusted to simulate actual operational conditions.

The results of the distortion measurements on the down/up converter are shown in Fig. 77. The distortion is plotted for four notch locations as a function of the record frequency which is selected by changing the LO frequency of the converter. The distortion measurements shown have all been corrected for noise floor. The curves indicate that the distortion of the converter is heavily dependent on the choice of record frequency, increasing as the record frequency is lowered. The reason for this can be readily seen by referring to the measured group delay of the down/up converter presented in Fig. 23. Here it can be seen that the group delay has a large variation near the location of the converter LO. This discontinuity results from the zero beat between the LO and the input signal. As the record frequency is reduced, the LO offset becomes smaller, causing more of the signal to traverse this nonlinearity and resulting in higher distortion.

In addition, some residual amount of carrier and unwanted sideband exists due to imperfections in the modulators. These were measured to be attenuated about -30 dB relative to the desired sideband. These residual components also introduce distortion by beating with the desired signal and with each other. The choice of record frequency is thus a significant parameter in this converter. It is limited on the low end by phase nonlinearities and distortion due to spectral folding which occurs when the record center frequency is less than half the signal bandwidth. It is restricted on the high end by the maximum frequency which can be accepted by predetection recorders.

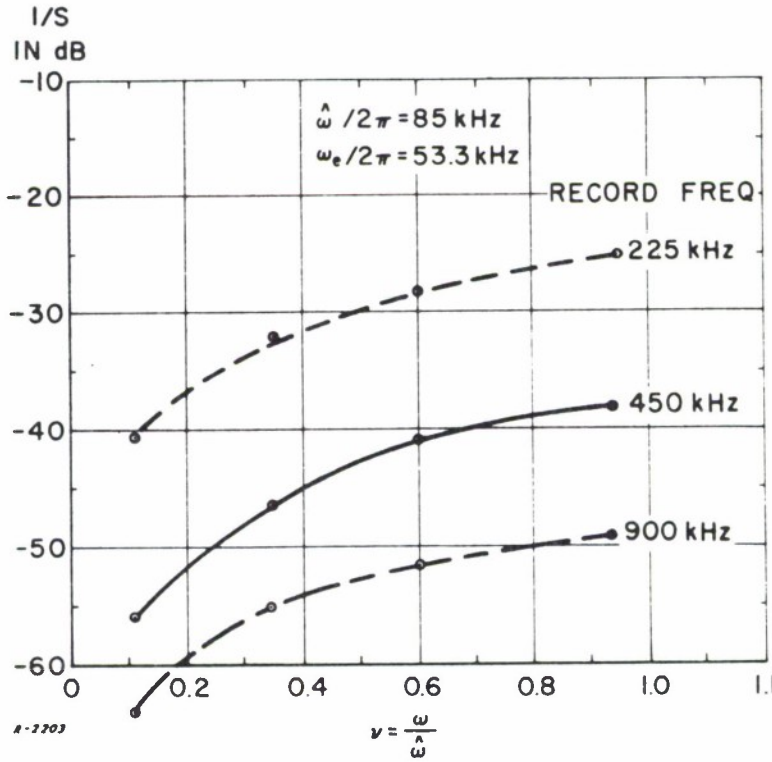

Figure 77 Distortion Measurements with Up/ Down Converter.

The distortion in the down/up converter is then seen to result from three sources:

1. the nonlinearity of the phase characteristics of the filters in both the down- and up-converter,
2. the discontinuity in the phase characteristic due to LO and signal zero beat, and
3. the residual carrier and sideband in the up-converter.

7.1.3 Measurements of Down/Up Converter and Receiver

The relative contribution of the converter to the distortion of the overall telemetry system was measured by performing a distortion test on the cascade of the receiver second IF amplifier and the down/up converter. For this test the I/S measurement configuration of Fig. 37 was again used with the VCO signal applied to the second IF of Receiver C, which in turn fed the down/up converter whose output was demodulated in the FM discriminator. The signal parameters were again $\hat{\omega}/2\pi = 85$ kHz and $\omega_e/2\pi = 53.3$ kHz.

The results of the test are plotted in Fig. 78 and compared with the individual distortions of the receiver second IF amplifier and the converter. The broken curve plots the distortion of the down/up converter alone for a record frequency of 450 kHz. The dashed curve is the distortion of the 500 kHz second IF of Receiver C. The solid line is the distortion of the receiver second IF and converter in cascade. It can be seen that the converter at a record frequency of 450 kHz does contribute some distortion to the overall measurement. The major contribution, however, is still in the second IF of the receiver.

The dashed line of Fig. 78 does not completely represent the distortion incurred in the operational use of the receiver and converter. In normal use, the signal is processed through the receiver to the input of the down-converter then through the down/up converter to the playback input of the receiver. The distortion incurred thus far is that shown by the curve in Fig. 78. However, the playback input reprocesses the playback signal through the second IF before demodulation. Now, if the operating procedure calls for utilizing the same IF amplifier to filter the reproduced signal as was used to filter the signal prior to recording, then another distortion contribution, whose level is given by the solid curve, is incurred. This accumulates coherently with the distortion given by the dashed curve, thus raising it by almost 6 dB.

If, on the other hand, the operating procedure is to record through a wideband IF amplifier and then play back through a narrowband IF amplifier, then use of the wideband second IF does not introduce much distortion, and the total accumulated distortion is given essentially by the dashed curve. In conclusion, it should be emphasized that preceding and following the predetection record process by equal bandwidth IF amplifiers unnecessarily adds 6 dB to the overall distortion on the signal, and thus should be avoided wherever possible.

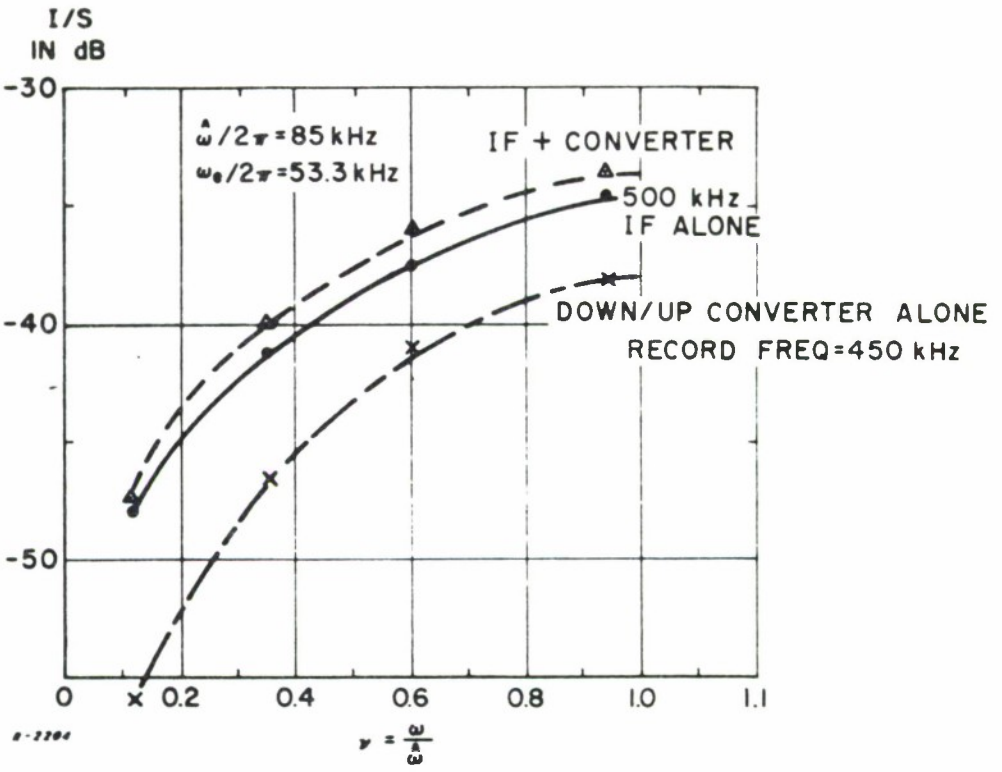

Figure 78 Distortion Measurement with Receiver A Predetection Second IF Amplifier and Down/Up Converter.

7.2 Tests with the Down-Converter/Direct-Demodulator

7.2.1 Description of the Down-Converter/Direct-Demodulator

One way of avoiding the distortion produced by the phase nonlinearities of the up-converter is to demodulate the signal directly at the reproducer output. This technique is referred to here as direct demodulation. The block diagram of the unit tested is shown in Fig. 79. This converter/demodulator unit was supplied with Receiver B. The down-converter is of the same form as that used in the preceding test. The output of the second IF amplifier is mixed with a local oscillator to translate the signal to the record frequency. The reproducer output, however, is applied directly to a demodulator rather than up-converting to the second IF amplifier.

There are two predetection filters in this unit, a bandpass filter at the down-converter input and a video filter in the down-converter output. The down-converter bandwidth is 2 MHz. The direct demodulator is a pulse-averaging discriminator with no input filter which is able to operate with the typical signal level out of the reproducer. Its bandwidth limitation is imposed by deviation linearity rather than by a filter.

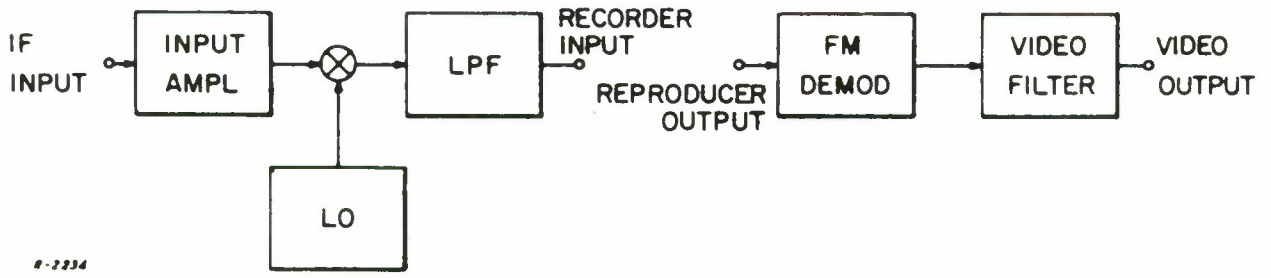

Figure 79 Block Diagram of Down-Converter/Direct-Demodulator.

7.2.2 Distortion Measurements with Down-Converter/Direct-Demodulator

The tests conducted with the down-converter/direct-demodulator were set up with the down-converter following the VCO as in the I/S measurement configuration of Fig. 37 and its output going directly into the direct demodulator which then functioned in place of the laboratory discriminator in Fig. 37. Because of the way in which this test is set up it is not possible to separate the distortion due to the down-converter from that due to the demodulator. Thus, no noise floor corrections can be made. The direct demodulator used here was limited in that it could be used only at one record frequency, 450 kHz. This did not interfere with making measurements on it or with the receiver or recorder, but did limit the flexibility of those tests, inasmuch as measurements could not be made as a function of the record frequency.

The signal parameters for the tests with the down-converter/direct-demodulator were maintained at $\hat{\omega}/2\pi$ = 85 kHz and $\omega_e/2\pi$ = 53.3 kHz. Figure 80 compares the noise floor of the standard measurement configuration of Fig. 37 (dashed curve) with the distortion using the down-converter/direct-demodulator (solid curve). It is clear that the down-converter/direct-demodulator has about as low a residual distortion as the discriminator in the I/S test configuration. This result was anticipated from the flatness of the group-delay measurement on this down-converter which was presented in Fig. 25.

7.2.3 Measurements with Receiver and Down-Converter/Direct-Demodulator

The measurements made on the cascade of the down-converter/direct-demodulator and the receiver second IF amplifier were conducted using Receiver B. The VCO output of the I/S measurement configuration of Fig. 37 was applied to the receiver record IF input. The output of the second IF was

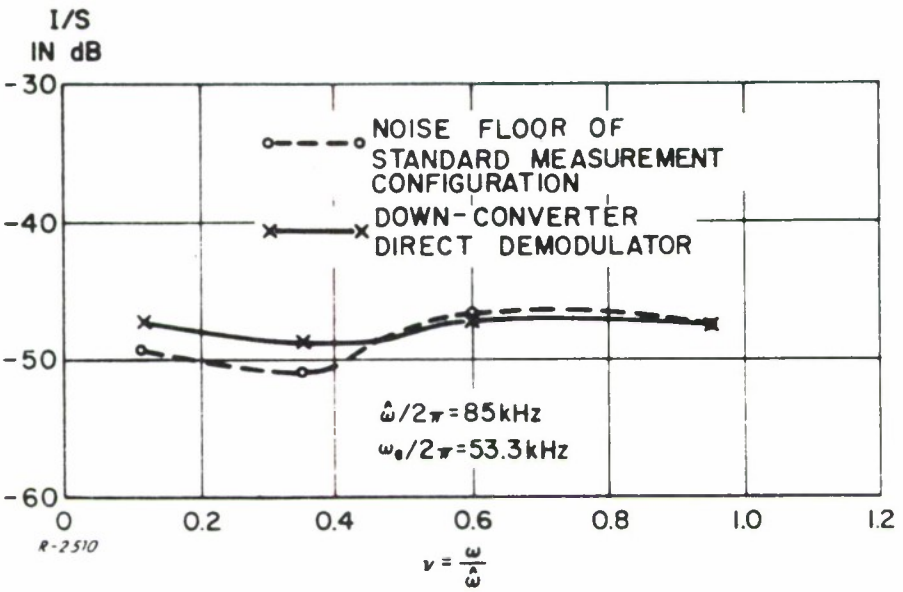

Figure 80 Residual Distortion Measurement of Down-Converter/Direct-Demodulator.

supplied to the down-converter which translated the signal down to the input of the direct demodulator. It will be remembered that Receiver B has the facility of switching out all second IF filters leaving only the wideband second IF amplifier in the circuit. Tests were conducted using $\hat{\omega}/2\pi$ = 85 kHz and $\omega_e/2\pi$ = 53.3 kHz with both the wideband second IF of Receiver B and the 500 kHz constant amplitude filter.

Figure 81 presents the results of this test. The top solid curve is the distortion measured with the receiver 500 kHz constant amplitude second IF amplifier and down-converter/direct-demodulator cascaded. The second curve is the distortion of the second IF filter alone. The difference between these curves is very small, indicating that the receiver second IF filter contributes most of the distortion.

The lower two curves in Fig. 81 show a very interesting result. The second from the bottom (dashed) curve is the residual distortion of the down-converter/direct-demodulator. When this was cascaded with the wideband second IF of Receiver B, the measured distortion was actually reduced. This was a surprising result. It was hypothesized that the only way in which the distortion of a cascade of two units could be lower than that of either was if the overall group delay of the cascade was flatter than that of either component. Subsequently, the group delay of the down-converter alone was measured and compared to the group delay of the cascade of the wideband second IF and down-converter. The results shown in Fig. 82 indicate that indeed the

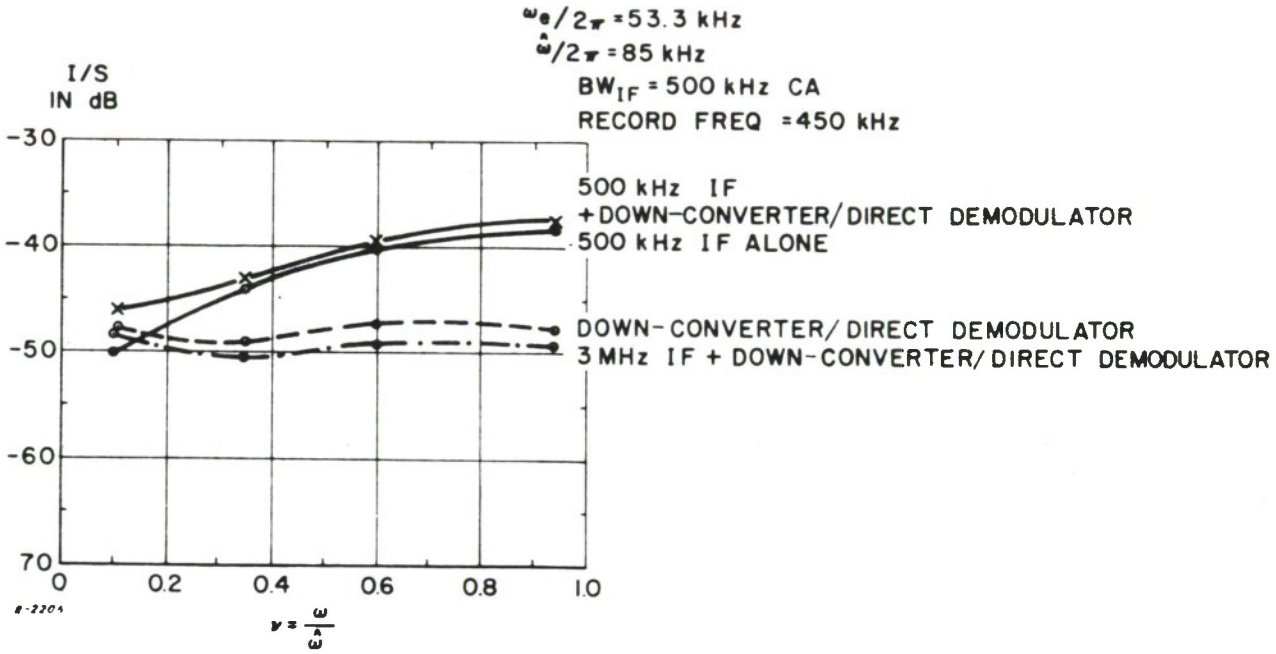

Figure 81 Measurement of Distortion with Receiver B and Down-Converter/Direct-Demodulator.

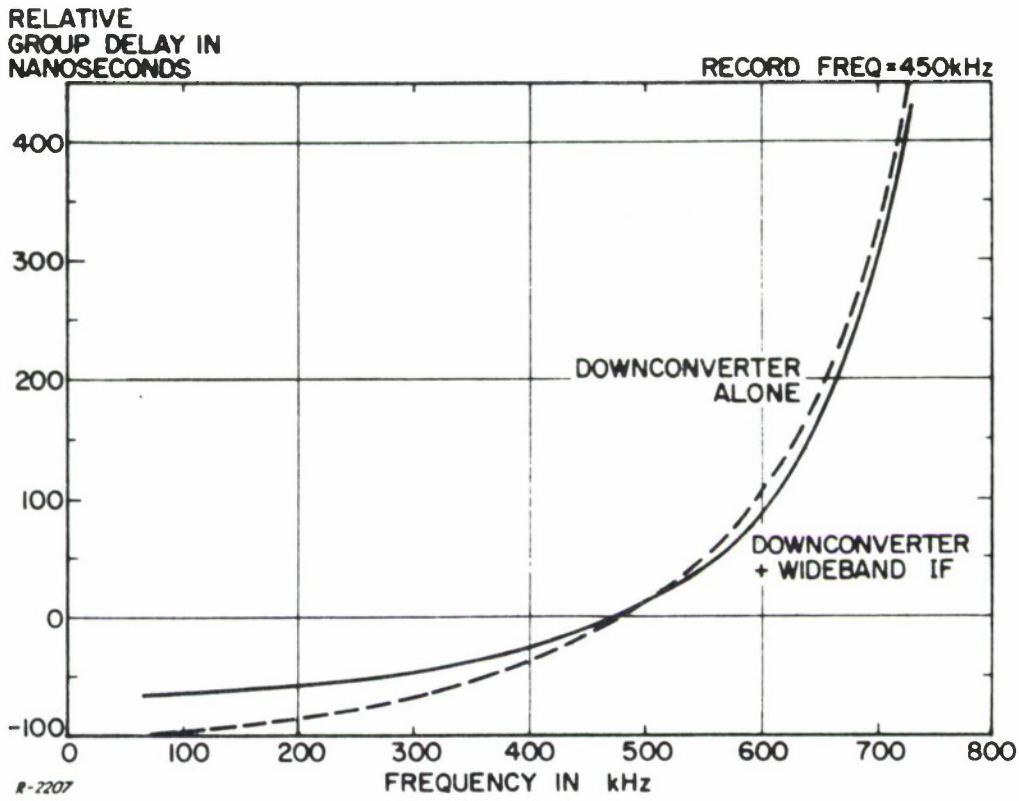

Figure 82 Measured Group Delay of Receiver and Down-converter.

group delay of the cascade is flatter than that of the down-converter alone. These results mean that the possibility exists that the phase characteristics of two non-identical cascaded units could add in such a complementary way as to reduce to overall nonlinearity over a portion of the band, thereby reducing the distortion incurred.

It should be noted that the method of prediction of the distortion of a cascade of non-identical filters on the basis of the addition of the prediction of each is not invalidated since it serves as an upper bound to the resultant distortion. In addition, the actual distortion of the cascade can be readily predicted by computation from the overall group-delay characteristic.

7.3 Conclusions: Comparison of Predetection Converters

It is useful to compare the two techniques of predetection conversion in the light of the test results. Because the direct demodulator could operate at only one record frequency, namely 450 kHz, we can compare the performance of the two techniques at only this frequency. This is no great restriction, however, since this frequency is the one most frequently used in practice.

Figure 83 illustrates the distortion using these two techniques. The distortion with the down/up converter is the solid curve and has been corrected for the noise floor of the test configuration. The dashed curve is the

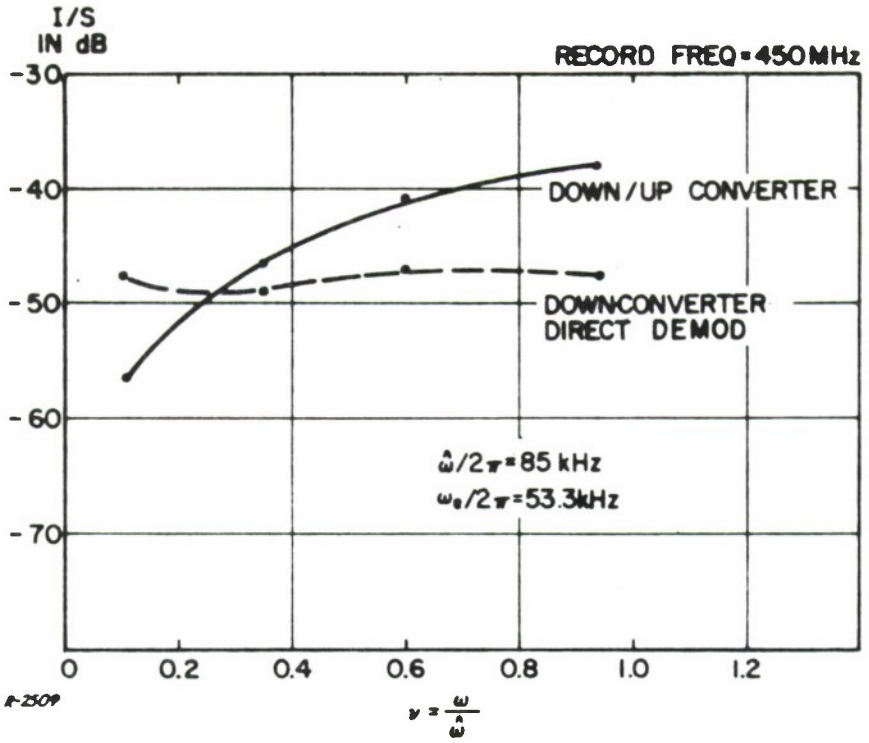

Figure 83 Comparison of Distortions for Up-Conversion and Direct Demodulation.

distortion with the down-converter/direct-demodulator which cannot be corrected for noise floor. It can be seen that, at the record frequency of 450 kHz, the direct demodulation technique yields lower distortion than the up-converter.

The up-converter introduces more distortion through two mechanisms:

a) because it has insufficient LO and unwanted-sideband suppression, and

b) because its group delay has a sharp nonlinearity near the LO frequency.

These two mechanisms become less important as the record frequency is increased, thus accounting for the reduced distortion at higher record frequencies.

The direct demodulator eliminates the distortion due to LO and unwanted sideband intermodulation by dispensing with the up-converter, and greatly reduces the distortion due to the delay discontinuity by using linear phase filters. The reduced distortion is achieved at a possible cost of increased equipment, depending on whether predetection-bandwidth selection is implemented before or after recording. This point bears elaboration.

Consider the case where the predetection bandwidth is set by selecting the appropriate second IF bandwidth prior to recording. Then no predetection filtering is required after tape playback, and the reproduced signal can be applied to a broadband highly-linear direct demodulator. Low distortion can be achieved in this manner. The direct demodulator can be implemented with switchable center frequency to accommodate the various record frequencies employed. Alternatively, the direct demodulator can be implemented as an extremely broadband pulse-count discriminator, thereby eliminating the need for switchable center frequency and still achieving low distortion.

Now consider the other case where it is desired to select the final predetection bandwidth after playback. This appears to be the procedure preferred by range-instrumentation engineers. The first consideration is that the second IF bandwidth used prior to recording must be selected in conjunction with the record frequency so that no noise folding takes place at the down-converter output.

Next, by building some special predetection filters to be cascaded with the direct demodulator, it is still possible to utilize the low-distortion capabilities of direct demodulators. Here again, the direct demodulator can be implemented with switchable center frequency, or it can be designed as an extremely broadband pulse-count discriminator.

The special predetection filters constitute the extra equipment that must be added to the telemetry receiving facility. Yet they offer some intriguing possibilities for improvements in data quality. Since the reproduced signal occupies the low end of the spectrum almost down to dc, the special predetection filters can be implemented as lowpass filters. This offers the possibility of very flat group-delay characteristics and hence low distortion, especially if the advanced active filter designs (discussed in Section XII) are used. Various predetection bandwidths and record frequencies can be accommodated by switchable lowpass-filter bandwidths. In addition, implementation of these lowpass filters is easily accomplished because of the low Q requirement.

Section VIII

MEASUREMENT OF INTERMODULATION DISTORTION IN PREDETECTION RECORDER/REPRODUCER

8.1 Description of Measurement Configuration

Tests were conducted on a predetection recorder/reproducer in conjunction with a predetection converter and a receiver to evaluate the relative contribution of each to the distortion in a telemetry system. The equipment setup for the composite system measurement is shown in Fig. 84. The simulated video spectrum is used to modulate the VCO which supplies the FM signal to the second IF amplifier of Receiver B. The output of the second IF is translated in the down-converter to the recorder input where the signal is recorded. The reproducer output is applied to the direct demodulator where the signal is detected and an I/S measurement performed.

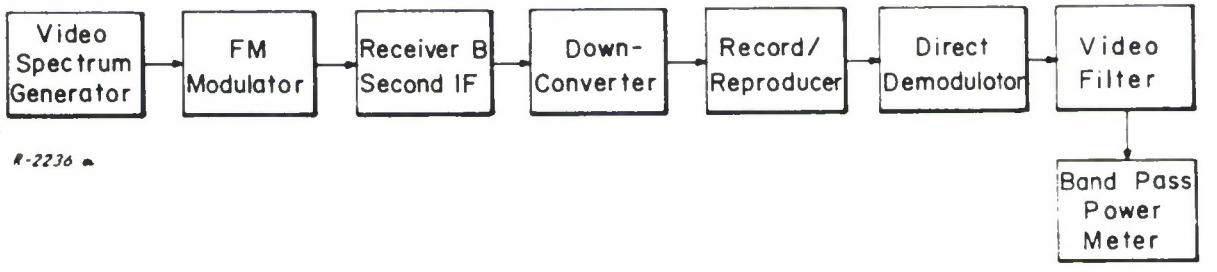

Figure 84 Implementation of Intermodulation Distortion Test with Recorder/Reproducer.

Receiver B and the down-converter/direct-demodulator were used here to make up the telemetry system. Because of this the record frequency used was 450 kHz. The signal modulations were $\hat{\omega}/2\pi = 85$ kHz and $\omega_c/2\pi = 53.3$ kHz for all tests.

The block diagram of the recorder/reproducer used in these tests is illustrated in Fig. 85. This recorder is a broadband predetection recorder with a 3 dB bandwidth of 800 Hz to 2 MHz. It has a controlled group-delay characteristic which is flat within ±300 nanoseconds, and a record speed capability of 120 in/s. The input record amplifier is very broadband,

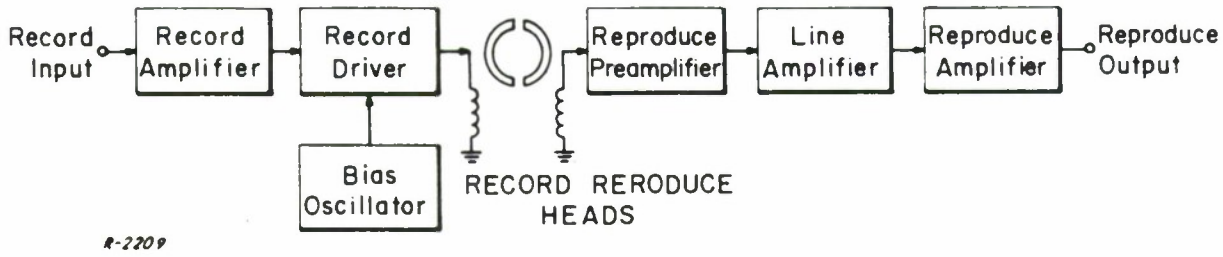

Figure 85 Block Diagram of Recorder/Reproducer.

having a 3 dB bandwidth of about 40 MHz. The principal frequency-sensitive elements are the record and reproduce heads. These heads have the well-known amplitude characteristic shown in Fig. 86. In order to increase the useful frequency range, amplitude compensation circuits are added in the reproducer electronics. This amplitude compensation in turn introduces undesirable phase nonlinearities which are themselves compensated for in delay-equalizer networks. The amplitude and group-delay equalization are included in the reproduce amplifier.

8.2 Measurement Limitations

Initial distortion measurements were made using only the down-converter, recorder and direct demodulator in the measurement configuration of Fig. 84. In order to isolate the distortion due to the recorder alone, a noise-floor test similar to that described in Section 5.3 was performed on the down-converter/direct-demodulator. The first test conducted with the recorder gave much higher distortion than was expected. This was quickly identified to be a function of the signal-to-noise ratio (SNR) out of the recorder. The SNR specification for this recorder was 21 dB through a filter of 800 Hz to 2 MHz at the reproducer output.

Since the effect of interest here was the distortion due to the nonlinear phase characteristics, the relative effects of SNR and phase nonlinearity distortion were investigated. First, the source of the noise out of the reproducer was identified. By measuring the noise power output

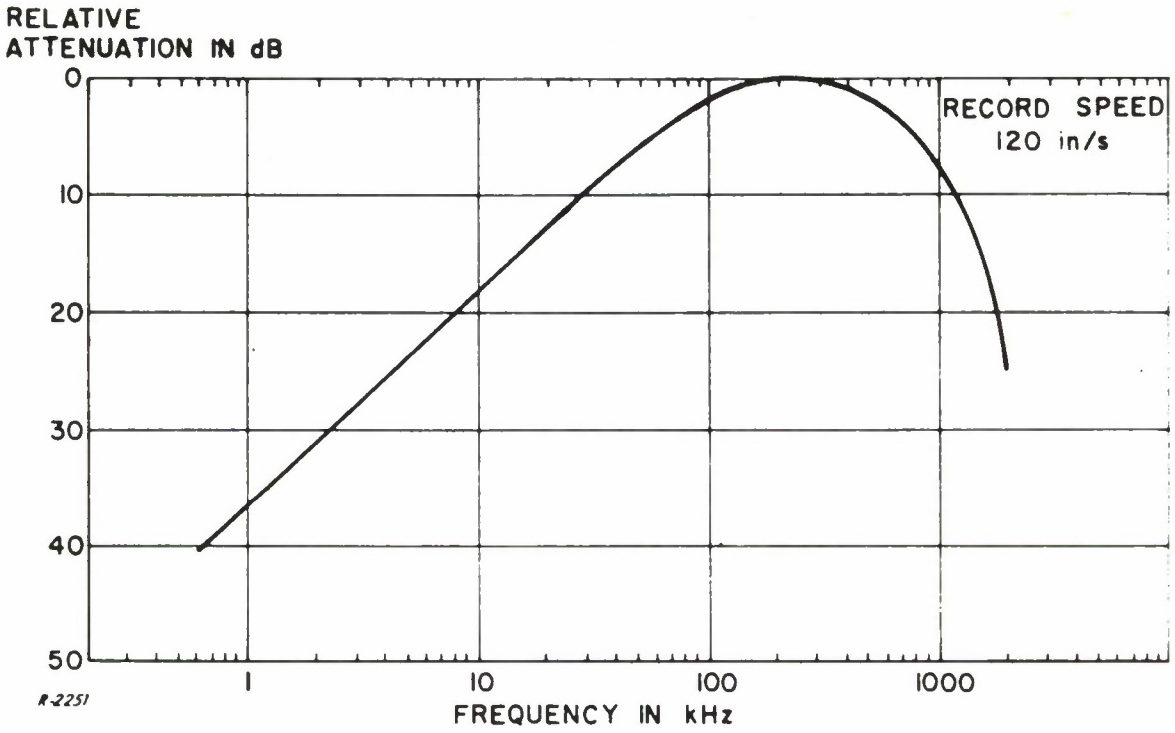

Figure 86 Recorder/Reproducer Head Characteristic.

with the recorder on and tape running (no signal into recorder) and comparing this to the noise output without the tape running, it was found that most of the noise was contributed by the reproduce electronics. In fact, the noise measurement under these conditions changed by less than 1 dB. In addition, tests conducted on the reproduce head indicated that it was at least 20 dB down from the reproduce electronics noise. This identified the reproduce electronics as the principal source of the noise at the output. Further verification of this was obtained by comparing the amplitude response of the reproduce electronics to the spectral density of the noise at the reproducer output. This is shown in Fig. 87. Since the noise spectral density is almost exactly the same form as the reproduce electronics amplitude response, the source is identified as white, thermal noise generated in the input of the reproduce electronics.

Having identified the source of the noise it was possible to improve the SNR by various methods. For example, the input signal amplitude to the recorder could be increased or the bandwidth at the output could be reduced. The latter was particularly effective since, as seen in Fig. 87, most of the noise power is at the edges of the band. This reduction in bandwidth was accomplished by inserting a variable bandwidth bandpass filter between the reproducer output and the direct demodulator.

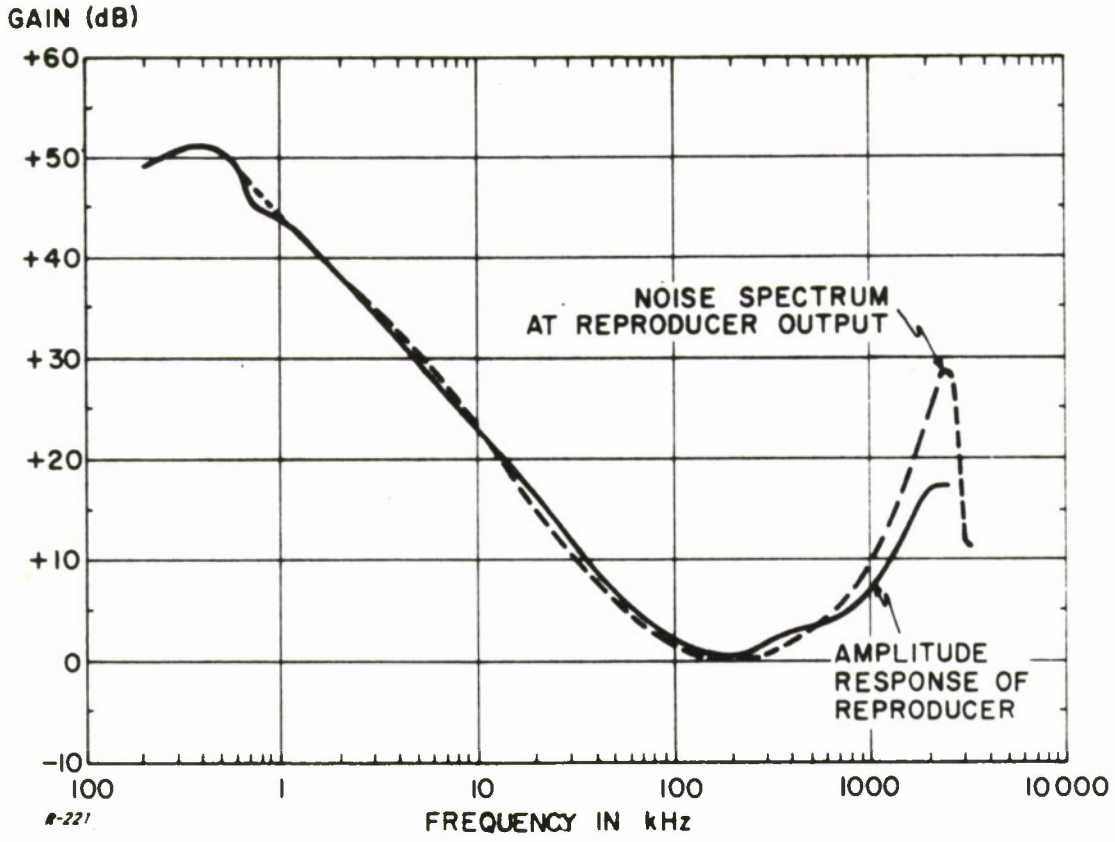

Figure 87 Comparison of Amplitude Response and Noise Spectrum of Reproducer.

The relationship between the input and output SNR of an FM demodulator is well known as

$$SNR_{out} = 3\delta^2 (SNR)_{in}$$

where

$$\delta = \frac{\Delta f}{f_m}$$

Δf = peak deviation

f_m = modulation rate

In this case the output SNR with no filter was 16 dB; after the processing through the direct demodulator the I/S was -31 dB. Thus, if no distortion due to phase nonlinearities is assumed the SNR improvement is 15 dB. Computing the improvement as above yields an improvement of 13 dB. The 2 dB difference is

readily accounted for by the lackof flatness of the spectral density at the reproducer output.

To isolate the effects of reproducer SNR and distortion due to nonlinear phase characteristics a measure of the distortion at the demodulator output was taken as a function of SNR out of the reproducer for two conditions of FM test signal. The results of this test are shown in Fig. 88. First, the VCO in the test set was not modulated so that just a CW carrier was recorded and applied to the demodulator. The SNR at the reproduce output was then varied by changing the bandpass filter bandwidth and the I/S out of the demodulator was measured. Clearly, since no modulation was present on the FM carrier, no intermodulation distortion due to nonlinear phase characteristics was incurred. Thus, all of the distortion measured at the output was due to the noise generated in the reproduce electronics. The dashed curve of Fig. 88 plots this result.

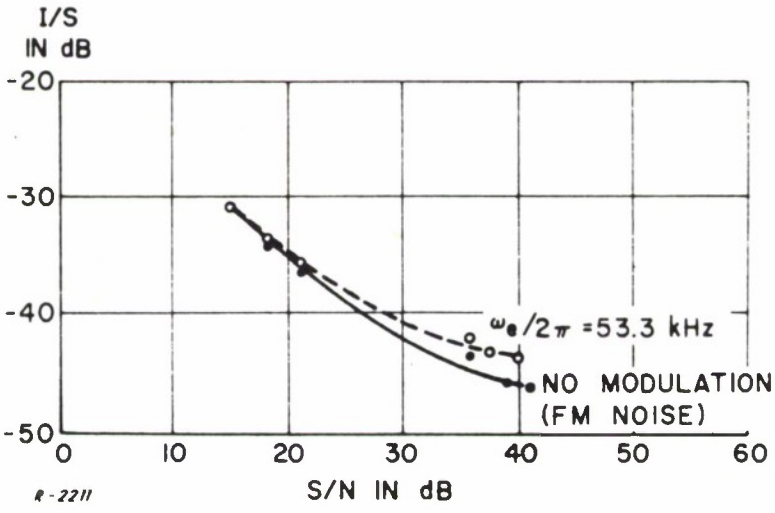

Figure 88 Measurement of Down-Converter and Recorder Distortion vs Reproduce Output S/N.

This test was repeated with the normal modulation of the VCO so that the distortion measured out of the demodulator is a combination of both phase-nonlinearity distortion and reproducer noise. The solid line of Fig. 88 plots this result. It is clear that only at the very high SNR out of the reproducer (40 dB) is there a noticeable contribution to distortion by the nonlinear phase characteristics. Hence, it can be concluded that the intermodulation distortion due to nonlinear phase characteristics in recorders is acceptably low. However, these test results demonstrate that the SNR of the recorder is an important parameter that must be controlled since the noise introduced at the demodulator output acts just like front-end noise of a receiver to corrupt the data quality.

For the remainder of the tests conducted with the recorder, the SNR was maintained at 40 dB. This was accomplished by reducing the bandwidth of the bandpass filter at the reproducer output to a 3 dB bandwidth of 10 kHz to 1 MHz, and by increasing the input signal level 5 dB above the normal level. The reduction in bandwidth did not otherwise affect the performance since the record input was at 450 kHz and a check of the group delay indicated that it remained within the specified range. The increase in amplitude also brought no adverse effects since the recorder was linear up to this point.

Another important recorder specification is flutter. This is basically a low-frequency disturbance introduced by irregularities in tape speed due to eccentricities in the recorder mechanism and tape fluctuations. This introduces low-frequency noise out of the demodulator. The standard method for measuring flutter, which is measuring the noise through a lowpass filter after the demodulator, was employed and the measurement was found to meet both the manufacturer's and IRIG specifications. It should be pointed out in passing that this flutter measurement is ambiguous because the actual flutter effects are inseparable from the low-frequency noise contributed by the SNR at the reproducer output. For the measurements of interest here, the flutter was not a critical factor.

8.3 Measurements of Intermodulation Distortion With the Recorder/Reproducer and Receiver

The distortion due to phase nonlinearities was measured on the recorder with the reproducer SNR = 40 dB. The FM signal with $\hat{\omega}/2\pi = 85$ kHz and $\omega_e/2\pi = 53.3$ kHz was supplied from the VCO in Fig. 84 to the down-converter input. The output of the down-converter at 450 kHz was applied to the recorder and the reproducer output demodulated directly and an I/S measurement made. The signal was recorded and played back at 120 in/s. The measured distortion was corrected for the noise floor of the down-converter/direct-demodulator and plotted in Fig. 89 as the broken curve.

The distortion was also measured on the composite receiver down-converter and recorder/reproducer by including the second IF of Receiver B between the VCO and down-converter. The 500 kHz constant amplitude second IF filter of Receiver B was used. The corrected measurements on the receiver second IF alone (dashed curve) and receiver cascaded with recorder (solid curve) are also plotted in Fig. 89. These curves demonstrate that the recorder/reproducer adds very little distortion to that of the receiver second IF.

A final test was conducted on the recorder/reproducer which measured the effect of crosstalk on intermodulation distortion. Since crosstalk between channels is similar to introducing additive noise on the desired signal, it should raise the apparent distortion level. To test for this, one channel of the recorder was used to prerecord the standard telemetry test signal without using a notch in the video spectrum. The standard distortion

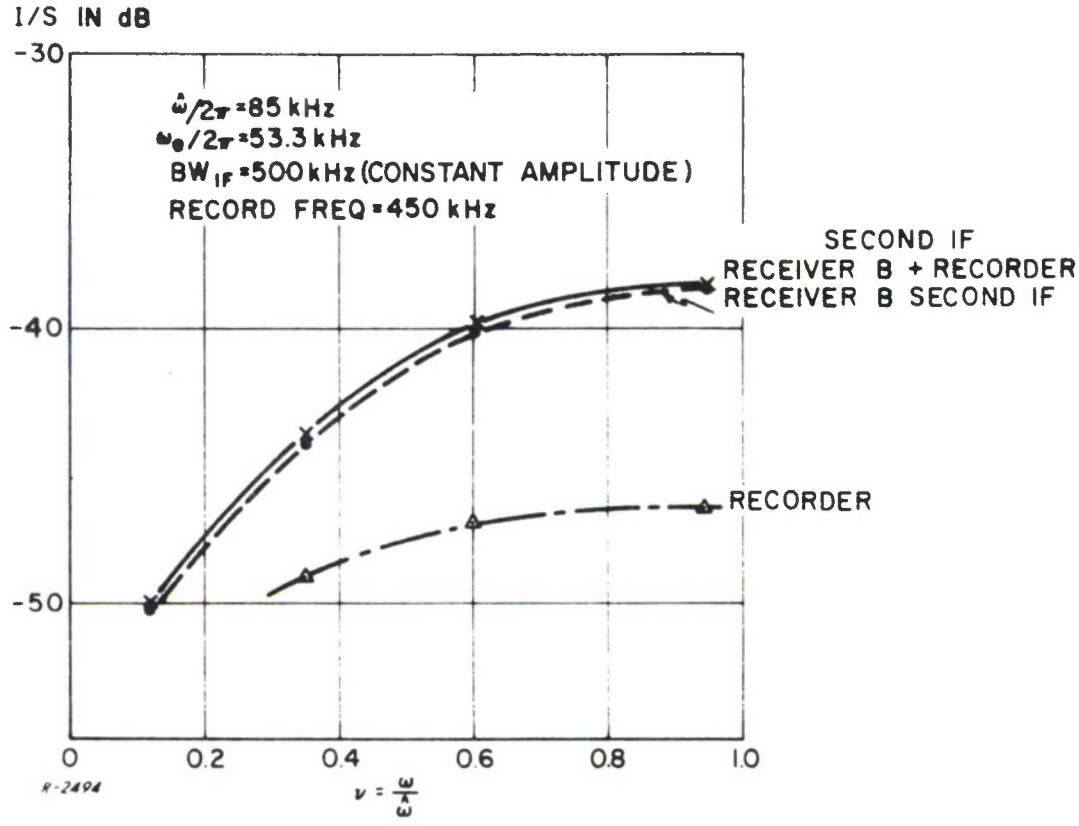

Figure 89 Distortion Measurement with Receiver, Down-Converter and Recorder.

test with the 80 kHz notch in the video was then conducted using an adjacent channel with and without the signal present on the first channel. There was no measurable difference between the two distortion measurements, indicating that crosstalk did not contribute significant distortion.

8.4 Conclusions

Tests with a typical predetection recorder have shown that the intermodulation distortion due to phase nonlinearities is insignificant compared to those produced in the receiver second IF amplifier. This is a direct result of the delay equalization used in this recorder to maintain low delay variations across its bandwidth.

The signal-to-noise ratio out of the recorder has been found to be a significant source of data degradation. The noise bandwidth and particularly the high and low portions of the reproducer spectrum must be controlled in order to prevent corruption of the data by recorder noise. This can be accomplished by including a bandpass filter at the reproducer output and adjusting the filter to the desired signal bandwidth, thus optimizing the signal-to-noise ratio and reducing its contribution to data degradation.

Finally, the effects of interchannel crosstalk on data distortion were measured and found to be insignificant. In general, the recorder with a controlled SNR was not found to introduce significant amounts of distortion.

Section IX

INTERSYMBOL INTERFERENCE IN TDM TELEMETRY

9.1 Introduction

The previous sections (IV through VIII) have been concerned with a video signal consisting of frequency-division multiplexed (FDM) subcarriers. Under those conditions it was appropriate to assume that the video signal was equivalent to a gaussian signal. In this section we consider a video signal consisting of a sequence of pulses constructed by time-division multiplex (TDM) of data channels. The pulses, which may be of varying shape, amplitude and width, are applied as direct carrier modulation in the form of PM or FM. Included in this category are video signals such as PCM, PAM, PDM and PACM. The last named is a combination of pulse-code modulation and an additional analog amplitude modulation on each PCM pulse. Direct carrier frequency-shift keying (FSK) and phase-shift keying (PSK) are considered special cases of PCM/FM and PCM/PM respectively, where the PCM pulses are chosen to be rectangular.

We must distinguish between two forms of pulse-distortion which can be produced in TDM telemetry systems by the predetection or video filters in the system. The first, called "self-distortion", refers to any deterministic distortion of the video pulse shape observable within the nominal time-slot of the pulse. It is well-known that the phase characteristics of the filters, whether predetection or video, can contribute significantly to the self-distortion. On the other hand, all techniques for the extraction of information from pulses rely either on the area of the pulse, or on the magnitude of the pulse at a given instant within the pulse duration. Thus the effects of self-distortion on the output information waveforms can be readily corrected by appropriate calibration of the pulse detection circuits.

The second form of distortion, called "intersymbol interference", refers to any distortion of the video pulse shape caused by spillover (or crosstalk) from the preceding pulse or pulses. In contrast to self-distortion, intersymbol interference effects are not deterministic because they depend on the pulse sequence preceding the given pulse, and hence cannot be corrected by simple calibration. We identify intersymbol interference as the primary mechanism by which predetection filters may degrade TDM telemetry data. In the next two subsections we study the problem in more detail. In Subsection 9.4 we discuss the intersymbol interference introduced by the video filter, and discuss the relative degradation due to the two types of filtering.

9.2 Duration of Pulse Spillover

In this section we consider the problem of estimating the pulse duration or spillover from a linear model of the predetection filter, and compare the results with those obtained from the exact model. In Section 3.2 we found the general (exact) transfer relation (Eq. (36)) to be

$$\theta(t) = \arctan \frac{\int_{-\infty}^{\infty} h_p(\tau) \sin \phi(t-\tau)\, d\tau - \int_{-\infty}^{\infty} h_q(\tau) \cos \phi(t-\tau)\, d\tau}{\int_{-\infty}^{\infty} h_p(\tau) \cos \phi(t-\tau)\, d\tau + \int_{-\infty}^{\infty} h_q(\tau) \sin \phi(t-\tau)\, d\tau} \tag{95}$$

In Section 3.3 we found that a linear approximation to this relation is given by Eq. (38)

$$\theta(t) = \int_{-\infty}^{\infty} h_p(\tau)\, \phi(t-\tau)\, d\tau \tag{96}$$

From Eq. (96) it is clear that, for a given pulse duration, it is the duration of the impulse response $h_p(t)$ which governs the duration of the linearly-derived output pulse. To be more explicit, suppose that

$$\phi(t) = 0 \qquad \text{for } t > T_1 \tag{97}$$

and

$$h_p(\tau) = 0 \qquad \text{for } t > T_2 \tag{98}$$

Then we see from Eq. (96) that

$$\theta(t) = 0 \qquad \text{for } t > (T_1 + T_2) \tag{99}$$

To demonstrate that this property also holds true for the total (exact) output, $\theta(t)$, consider Eq. (95). Assuming that the predetection filter is symmetric ($h_q(t) = 0$) only the leading integrals in the numerator and denominator are nonzero. Using Eq. (98), we may change the upper limits of both integrals to T_2. Then, because of Eq. (97), $\phi(t-\tau)$ will be zero for $t > (T_1 + T_2)$. Since the sine of zero is zero while the cosine is unity, the ratio of the two integrals will be zero for $t > (T_1 + T_2)$ and so will $\theta(t)$. Therefore, by limiting the duration of the lowpass equivalent impulse response, we not only limit the duration of the linear term, but also the duration of the complete (exact) response. Because of this, filter design to prevent intersymbol interference can be performed conceptually at lowpass rather than at bandpass. Before proceeding to an example we note that in Appendix V we prove the above property holds for a lowpass model known as the "lowpass prototype" as well as the "lowpass equivalent" considered above. Also, the above considerations were presented in terms of a phase input and output, but they can be readily modified to the case of frequency input and output by differentiating the transfer relations. The same conclusions hold in that case.

As an example, we consider a predetection filter which has a lowpass equivalent (or, as shown in Appendix V, lowpass prototype) with a gaussian impulse response:*

$$h_p(t) = \frac{1}{2\sqrt{\pi\alpha}}\, e^{-(t-t_o)^2/4\alpha} \tag{100}$$

where t_o is the overall time delay, and α is related to the bandwidth and has the dimensiona of time-squared. Choice of this example is motivated by the fact that this gaussina filter has a linear-phase characteristic, as seen from the frequency response:

$$H_p(j\omega) = e^{-\alpha\omega^2}\, e^{-j\omega t} \tag{101}$$

As an input pulse waveform, we choose a simple rectangular pulse of height a radians phase-modulating the carrier:

$$\phi(t) = a[u(t) - u(t-T_1)] \tag{102}$$

where u(t) is the unit step located at t = 0. It is straightforward to show by direct substitution into Eq. (95) (assuming $h_q(t) = 0$) that the exact response is given by

$$\theta(t) = \tan^{-1}\left\{\frac{\sin a\left[\Phi\left(\frac{t-t_o}{\sqrt{2\alpha}}\right) - \Phi\left(\frac{t-t_o-T_1}{\sqrt{2\alpha}}\right)\right]}{1-(1-\cos a)\left[\Phi\left(\frac{t-t_o}{\sqrt{2\alpha}}\right) - \Phi\left(\frac{t-t_o-T_1}{\sqrt{2\alpha}}\right)\right]}\right\} \tag{103}$$

where $\Phi(x)$ denotes the tabulated cumulative gaussian function. For purposes of comparison, the linear term is given by

$$\theta_1(t) = a\left[\Phi\left(\frac{t-t_o}{\sqrt{2\alpha}}\right) - \Phi\left(\frac{t-t_o-T_1}{\sqrt{2\alpha}}\right)\right] \tag{104}$$

---

* Strictly speaking, this impulse response is unrealizable because it has nonzero response for $t < 0$. However, by choosing a large enough delay t_o we may eliminate this difficulty. Bessel filters are designed as approximations to the gaussian filter.

In Fig. 90, we have plotted the exact response and the linear approximation for an input pulse with

$$a = 1 \text{ radian and } \frac{T_1}{\sqrt{2\alpha}} = 1 \tag{105}$$

Another case of an input pulse with larger amplitude and duration is shown in Fig. 91. The discrepancy between the exact response and the linear approximation represents nonlinear distortion. As expected, more nonlinear distortion is present in the second case with the larger phase deviation. However, in both cases the duration predicted by the linear model agrees closely with the exact duration from the nonlinear model. It is also clear that despite the linear phase characteristic of the gaussian filter, the pulse waveform has been distorted considerably from its original rectangular form. Thus it is not the phase characteristic that determines the distortion or lack of it produced by a filter. Rather, the impulse response directly determines the response of the filter to an input pulse.

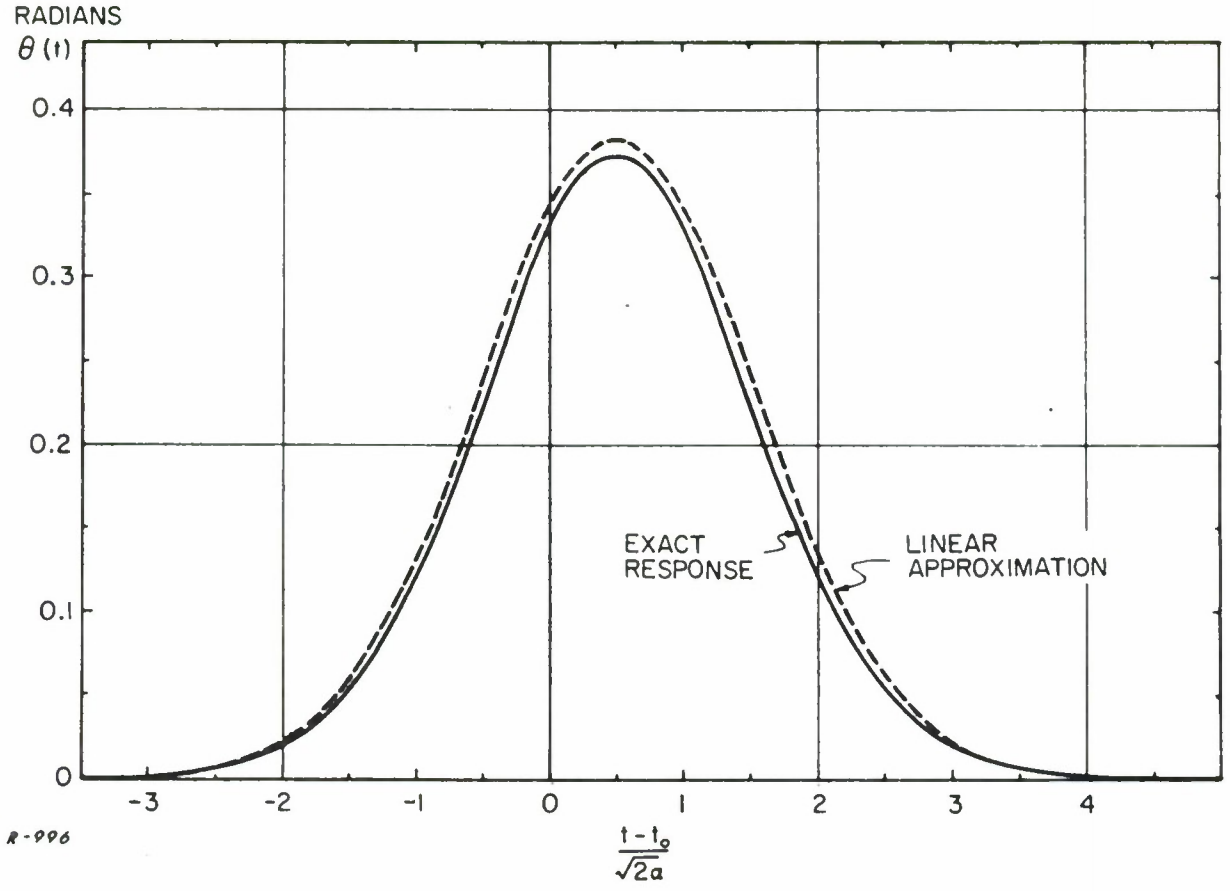

Figure 90 Exact Response and Linear Approximation $a = 1$ radian $\frac{T_1}{\sqrt{2\alpha}} = 1$.

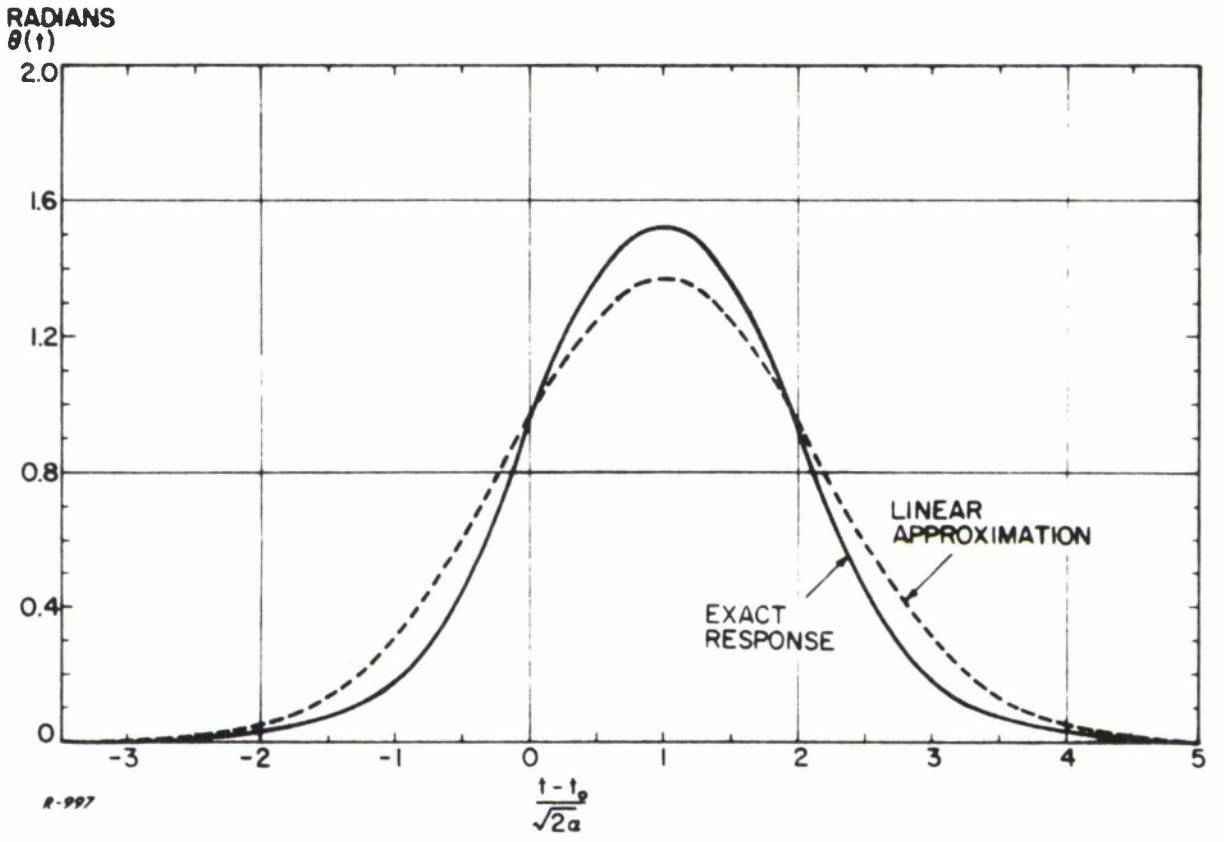

Figure 91 Exact Response and Linear Approximation a = 2 radians $\frac{T_1}{\sqrt{2\alpha}} = 2.$

9.3 Computation of Pulse Spillover Using the Linear Model

In the preceding section we have justified using the lowpass impulse response of a predetection filter as a design criterion in TDM situations. To implement this criterion it is convenient to have the impulse responses plotted for various filter forms considered in this report. Figure 92 shows the impulse response and step response for lowpass Butterworth filters; the time axis is normalized to the 3 dB bandwidth 2B. Figure 93 gives the Bessel filter responses with the time axis normalized to the center frequency group delay $T_d(\omega_c)$. This axis may be converted to tB for each curve separately by obtaining the value of $BT_d(\omega_c)$ from Table II. Finally, Fig. 94 gives the impulse response for double-tuned circuits with various coupling coefficients. The time axis is again normalized to the 3 dB bandwidth B.

9.4 Effect of the Video Filter on Intersymbol Interference

In common TDM telemetry systems it is likely that the contribution to intersymbol interference due to predetection filtering is negligible compared to that of premodulation and post-detection filtering. In fact, the IRIG Telemetry Standards (Ref. 1) for PCM make this quite clear. It is specified that that receiver

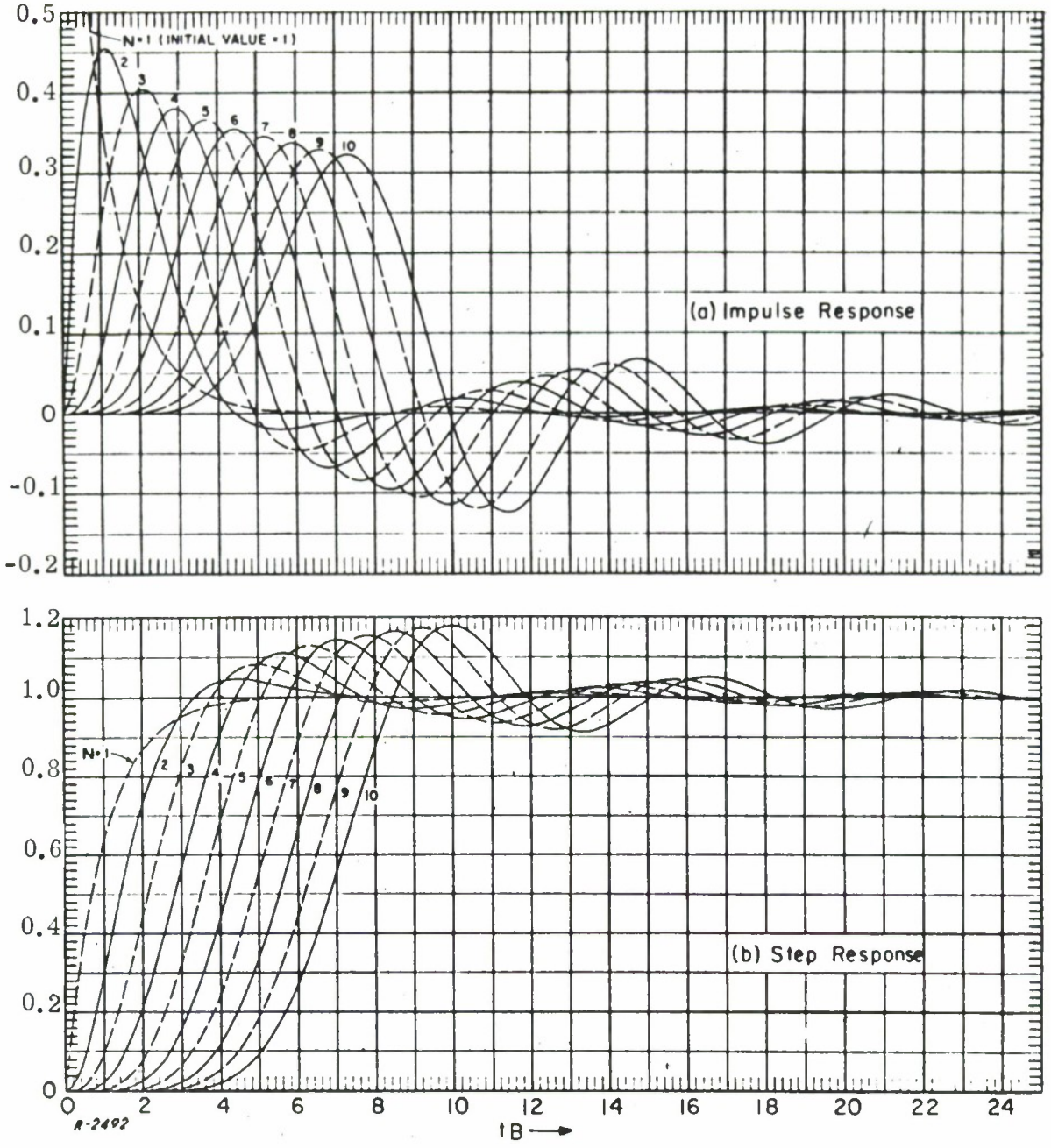

Figure 92 Transient Response of Butterworth Filters of Order N (Extracted from Ref. 9).

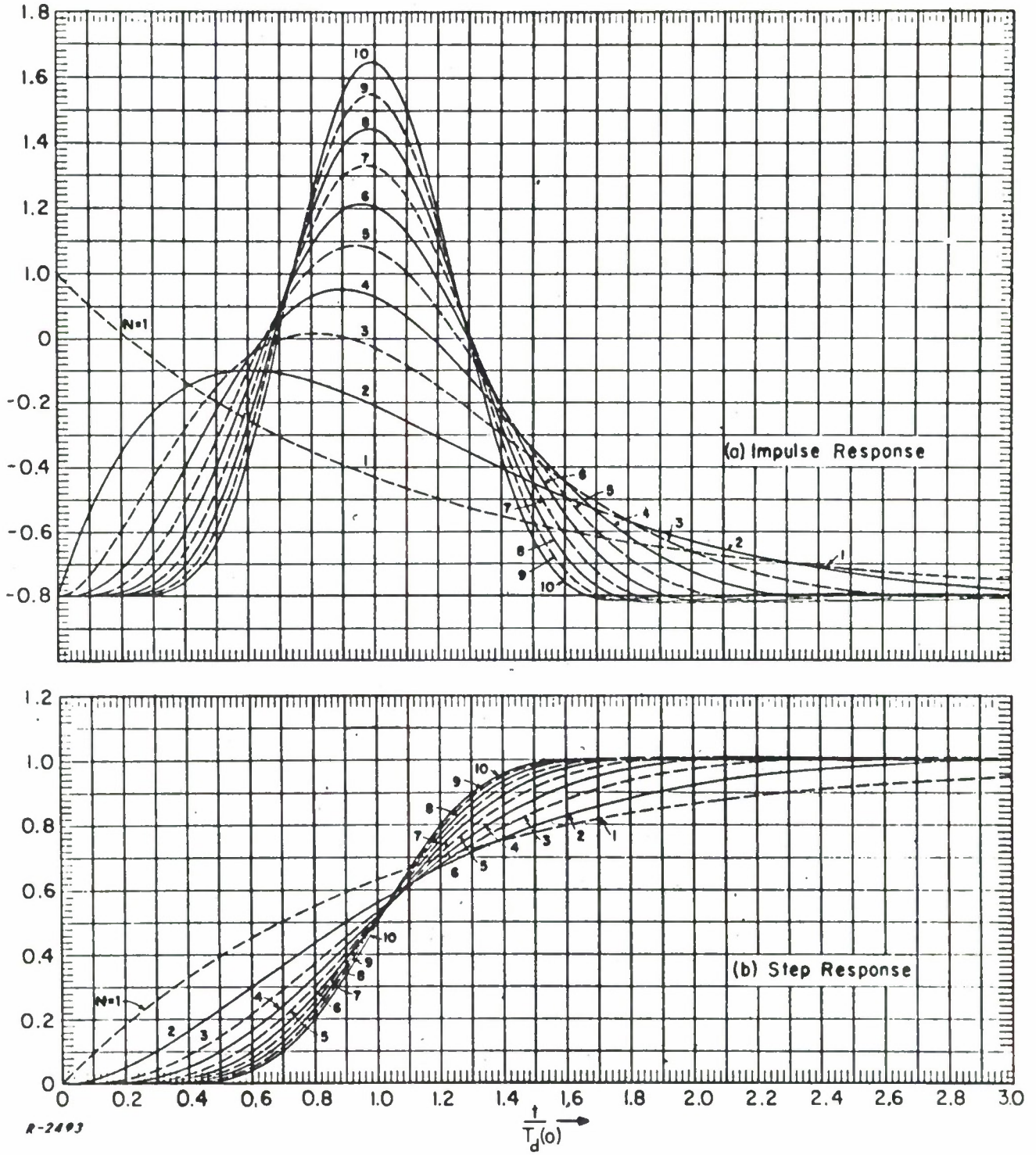

Figure 93 Transient Response of Bessel Filters of Order N (Extracted from Ref. 9).

IF bandwidth (3 dB points) be between 1.5 times and 3.3 times the bit rate. Furthermore, it is recommended that a premodulation lowpass filter with cut-off frequency (3 dB) equal to the bit rate be used. Combining these two requirements, we have the following relationship between the IF bandwidth (B_{if}) and the premodulation filter bandwidth (B_{LP}):

$$1.5\ B_{LP} \leq B_{if} \leq 3.3\ B_{LP}$$

Since the duration of the impulse response of a filter is given roughly by the reciprocal of its bandwidth, and since we have shown that the duration of the impulse response directly determines the degree of pulse spillover, we conclude that the principal cause of intersymbol interference in PCM telemetry is the premodulation filter.

The IRIG Telemetry Standards are much less specific about bandwidth requirements for PAM signals. It is specified that the receiver IF bandwidth lie between three times and 23 times the bit rate. No premodulation filter bandwidth is specified, but if we use the reasonable assumption that it is chosen to be equal to the bit rate, we arrive at the relationship

$$3\ B_{LP} \leq B_{if} \leq 23\ B_{LP}$$

Our earlier conclusion is again valid in this case.

In the next section we present the result of our experimental investigation of TDM which confirms the above conclusions.

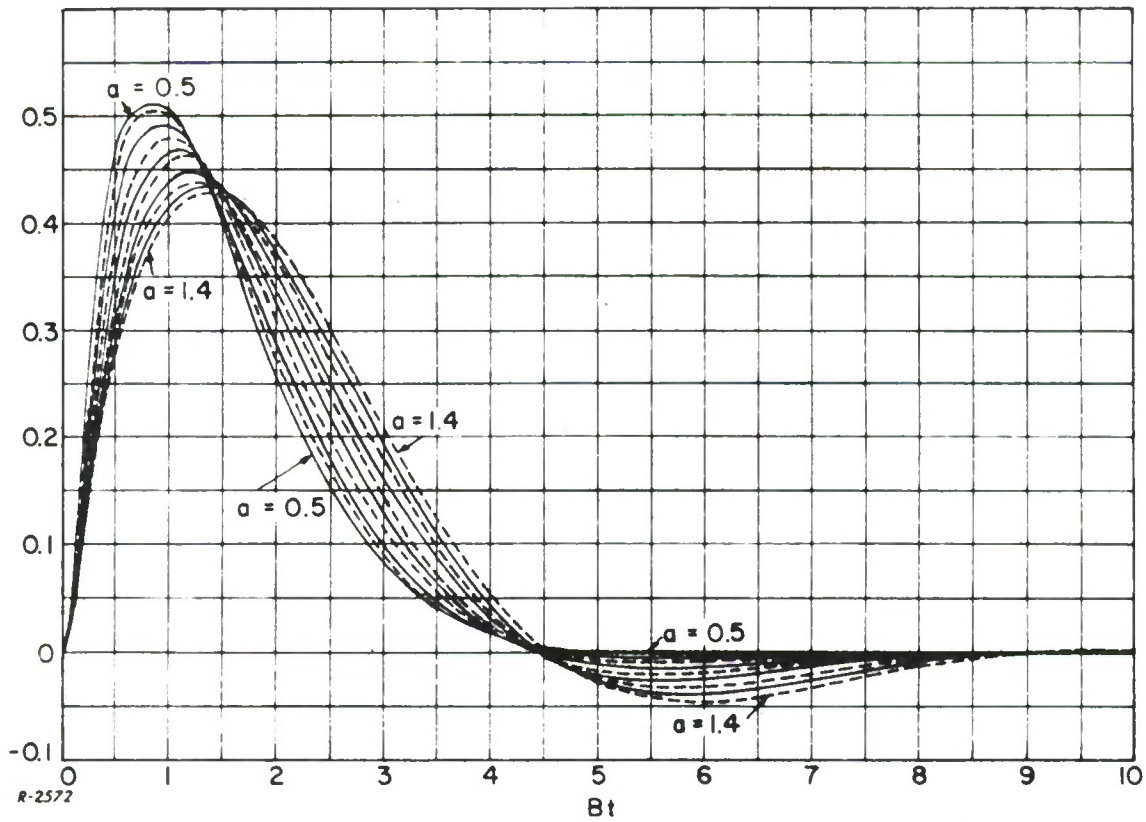

Figure 94 Impulse Response of Double-Tuned Circuits (For Various Coupling Coefficients at Increments of 0.1).

Section X

MEASUREMENT OF INTERSYMBOL INTERFERENCE IN TDM TELEMETRY

10.1 Test Configuration

The block diagram of Fig. 95 illustrates the test method used here to measure intersymbol interference. Basically an FM generator is modulated with pulses to form a simulated PCM signal such as is commonly encountered in TDM telemetry. This signal is then processed through a predetection filter which introduces distortion in the signal in the form of pulse spillover. The signal is then demodulated and the resulting pulses examined for the amount of stretching into the next pulse location. In order to facilitate identification of this spillover, a low duty cycle pulse waveform is used. This can be visualized as removing from the pulse waveform several succeeding pulses. The tail of each remaining pulse is then examined for its degree of spillover into what would be the next time slot. Because the bit rate of an actual signal is proportional to the reciprocal of the pulse duration and this duration is maintained constant, omission of several pulses does not change any of the pertinent test parameters.

The output of the demodulator is passed through a video filter prior to examination of the output pulse waveform. This simulates the premodulation filter which is present at the transmitter of all TDM telemetry systems. The premodulation filter is used to restrict the bandwidth of the pulse waveform before modulation so that a control is maintained on the RF bandwidth of the signal. Since this filter operates on the video pulse waveform, its effect can be simulated by a video filter following the demodulator. This filter location was chosen for these tests because of the availability of the video filters in the telemetry receivers.

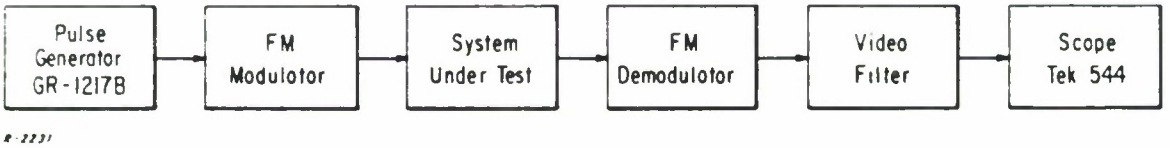

Figure 95 Block Diagram of TDM Test Configuration.

The output pulse waveform from the video filter is then examined on an oscilloscope where the degree of pulse stretching can be accurately determined. Test results are presented in the form of oscillographs of the input and output pulse waveforms. In order to experimentally determine the relative contributions to intersymbol interference of various sections of the TDM telemetry system, we investigate the pulse spillover introduced by each section of the system separately.

10.2 Selection of Test Parameters

The parameters of the modulation waveform and receiver bandwidth used for the tests conducted here are derived from the IRIG Telemetry Standards (Ref. 1) and are summarized in Table IX. The specification of peak deviation determines the pulse amplitude of the modulation waveform, which was maintained at 125 kHz peak for all tests. The relationship between the receiver IF bandwidth, premodulation or video bandwidth

Table IX

SELECTION OF TDM TEST PARAMETERS

Modulation Parameters

Maximum Peak Deviation = ±125 kHz
Maximum RF Signal Bandwidth = 500 kHz

Receiver Bandwidth and Bit Rate

IF Bandwidth = (1.5→3.3) Bit Rate $b = \frac{BW_{if}}{BW_{vid}} \begin{cases} > 1.5 \\ < 3.3 \end{cases}$

Premodulation Bandwidth = Bit Rate

Pulse Duration

Return to Zero (RZ)

$$T_1 = \frac{1}{2\,(\text{Bit Rate})}$$

Nonreturn to Zero (NRZ)

$$T_1 = \frac{1}{(\text{Bit Rate})}$$

and bit rate is completely specified by the standards. The premodulation bandwidth (B_{vid}) is made equal to the bit rate resulting in the IF bandwidth (B_{if}) being restricted to the range

$$1.5\ B_{vid} \leq B_{if} \leq 3.3\ B_{vid} \tag{106}$$

Thus the bandwidth ratio factor $b = B_{if}/B_{vid}$ constrains the IF bandwidth to be at least 1.5 times the video bandwidth. Since the IF bandwidth is equal to twice the equivalent lowpass filter bandwidth B_{LP}, this implies that

$$0.75\ B_{vid} \leq B_{LP} \leq 1.65\ B_{vid} \tag{107}$$

Specification of the bit rate also determines the duration τ of the pulses in the modulation waveform. There are two forms of pulse modulation in current use, return-to-zero (RZ), in which the pulses return to zero for 50 per cent of the bit time, and nonreturn-to-zero (NRZ) in which the pulses occupy the complete bit time. For the same bit rate the duration for RZ is equal to one-half that for NRZ. This provides a guardband in the case of RZ which tends to reduce the effects of spillover, at the expense of increased RF bandwidth. The IRIG standards do not specify one of these forms explicitly, but Section 5.8.2 of Ref. 1 implies NRZ. The TDM tests performed for this study have been conducted for both RZ and NRZ. However, for brevity the bulk of the reported results will deal with only NRZ.

10.3 Measurements With Modem and Video Filters

A preliminary test was conducted using the configuration of Fig. 95 and bypassing the system under test, to establish the amount of pulse stretching introduced by the modem and the video filter. The FM modulator for these tests was the 10 MHz VCO which has been described previously in conjunction with the intermodulation distortion tests. The demodulator used was the FM demodulator in the Receiver B. The results of this test are shown in Fig. 96. The fourth trace in the photograph is the input pulse modulation. The amplitude is adjusted to give 125 kHz peak deviation on the VCO. The duty-cycle is 1/10 to permit examination of the pulse stretching. The third trace is obtained by passing the input pulse through the video filter directly without going through the modem. The video bandwidth and pulse duration are related as described in Table IX. This trace shows clearly that some pulse stretching occurs in a properly chosen video filter. The second trace shows the effect of the modem on pulse stretching. This trace was taken by applying the pulse input to the modems and measuring the output of the demodulator without passing through the video filter. Here some pulse stretching is observed but not as much as with the video filter. This stretching occurs in the modem because its modulation characteristic has a finite impulse response time which acts like that of a filter to introduce pulse stretching. The top trace shows the pulse stretching incurred by passing

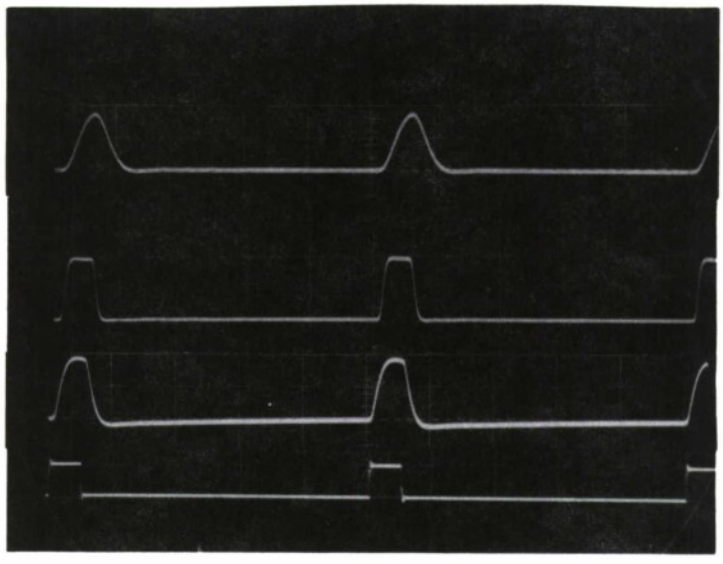

R-2517

1. Through Modem and 200 kHz Video Filter.
2. Through Modem Alone.
3. Through 200 kHz Video Filter.
4. Pulse Input (T_1 = 2.5 μs, PRF = 40 kHz, RZ).

Figure 96 Effects of Video Filter and Modem of Receiver B on Pulse Stretching.

the pulse through the modem and video filter. The pulse stretching here is then the resultant of that contributed by the modem and video filter and is seen to be significant. This set of curves was taken for the modulation condition of RZ which, as indicated earlier, can tolerate more pulse stretching than NRZ.

A comparison of the pulse stretching effects RZ and NRZ of the modem and video filter is shown in Fig. 97. As indicated previously, for the same bit rate, and hence video filter bandwidth, RZ pulse waveforms have one-half the duration of NRZ waveforms. Since the duration is smaller in RZ, pulse stretching would be expected to be more noticeable. Figure 97 demonstrates this. The fourth trace is the pulse input for NRZ. The third trace is the output of the modem and video filter for NRZ. The top two traces are input and output waveforms for RZ. Note the change in time scale for the two sets of traces. Comparison of trace one and three verifies that RZ waveforms do indeed incur more pulse stretching than NRZ. Again, it should be noted that RZ waveforms have an inherent guardband which offsets the effects of this stretching. Note also that for either RZ or NRZ waveforms significant pulse stretching is introduced by a properly chosen video filter.

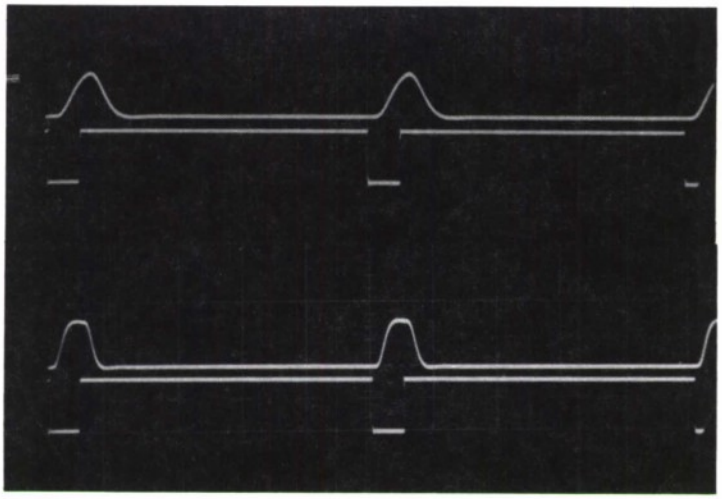

R-2574

1. Through Modem and 200 kHz Video Filter. } RZ
2. Pulse Input (T_1 = 2.5 μs, PRF = 40 kHz). }
3. Through Modem and 200 kHz Video Filter. } NRZ
4. Pulse Input (T_1 = 5 μs, PRF = 20 kHz). }

Figure 97 Comparison of RZ and NRZ Pulse Stretching.

The effects of chosing the video-filter bandwidth greater than the bit rate is shown in Fig. 98. Trace four is the input pulse (NRZ) which in this case is simply passed through the video filter. The first trace shows the effect of a video filter whose bandwidth equals the bit rate, indicating some pulse stretching. For trace two and three this bandwidth is increased and the pulse stretching correspondingly reduced. It should be noted that the video bandwidth is chosen equal to the bit rate in order to conserve RF bandwidth. Thus some pulse stretching and hence intersymbol interference is accepted in order to reduce the RF bandwidth requirements.

A comparison of different video filter designs was also possible. Receiver A has a six-pole Butterworth video filter while Receiver B has a six-pole Bessel video filter. Figure 99 compares the pulse stretching using the video filters alone for NRZ waveforms and shows that the Bessel design has much less pulse stretching than the Butterworth. The duration and bandwidth were again chosen to conform with Table IX. The absence of any ringing at the end of the pulse using the Bessel filter is a characteristic which makes it particularly desirable for pulse waveforms.

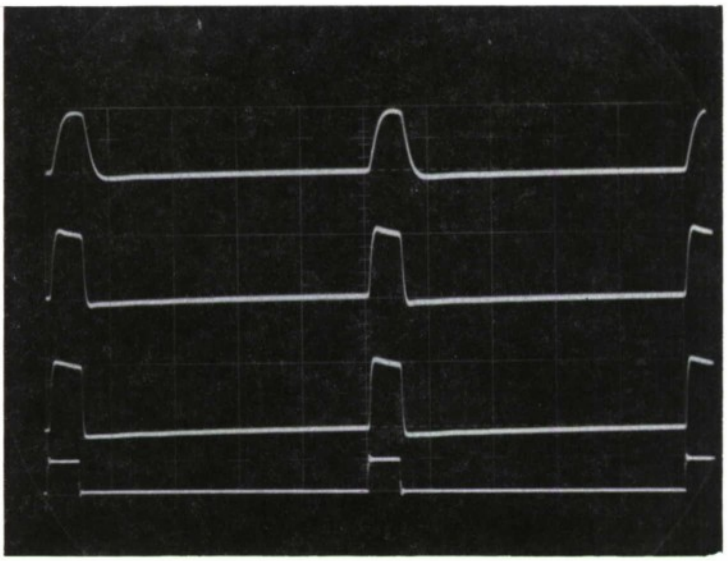

R-2519

1. Through 200 kHz Video.
2. Through 500 kHz Video.
3. Through 1 MHz Video.
4. Pulse Input (T_1 = 2.5 μs, PRF = 40 kHz, NRZ).

Figure 98 Effect of Video Bandwidth of Receiver B on Pulse Stretching.

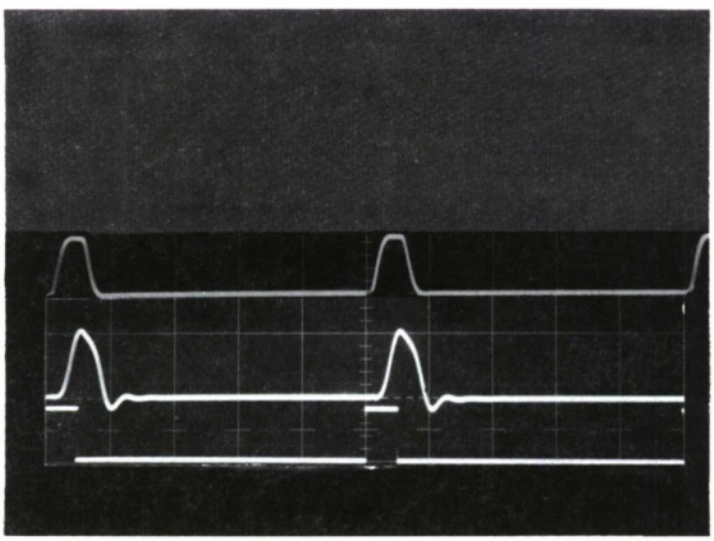

1. Through 100 kHz Bessel Filter.
2. Through 100 kHz Butterworth Filter.
3. Pulse Input (T_1 = 10 μs, PRF = 10 kHz, NRZ).

Figure 99 Comparison of Pulse Stretching by Bessel and Butterworth Video Filters.

10.4 Measurements with Receivers

A set of tests was conducted using Receiver B to compare the relative contribution to pulse stretching of the receiver second IF and video filter. A mid-range value of the bandwidth ratio factor (b = 2.5) was selected so that the IF bandwidth was 2.5 times the video bandwidth. The bit rate and bandwidths were appropriately chosen for an NRZ waveform, with the video bandwidth being 200 kHz. Since Receiver B is equipped with two 500 kHz IF plug-in filters, it was possible to compare the effects of Bessel and Butterworth IF designs from the pulse-stretching viewpoint.

The results of this test are shown in Fig. 100. Trace four is the input pulse which is five microseconds long. Note that for NRZ the next pulse slot is the adjacent five microseconds time slot. The third trace shows the stretching due to the modem, video filter and wideband second IF (no IF filters) of the receiver. Comparison with trace three of Fig. 97 shows that the wideband IF introduces no pulse stretching as is to be expected from its 3 MHz bandwidth. The second trace shows the pulse output after processing through the 500 kHz linear-phase IF filter. Comparison of traces two and three indicate that while some time delay is introduced by the IF filter as seen by the later starting time of the pulse in trace two, very little additional pulse stretching is observed. Thus for a mid-range bandwidth ratio (b = 2.5) the

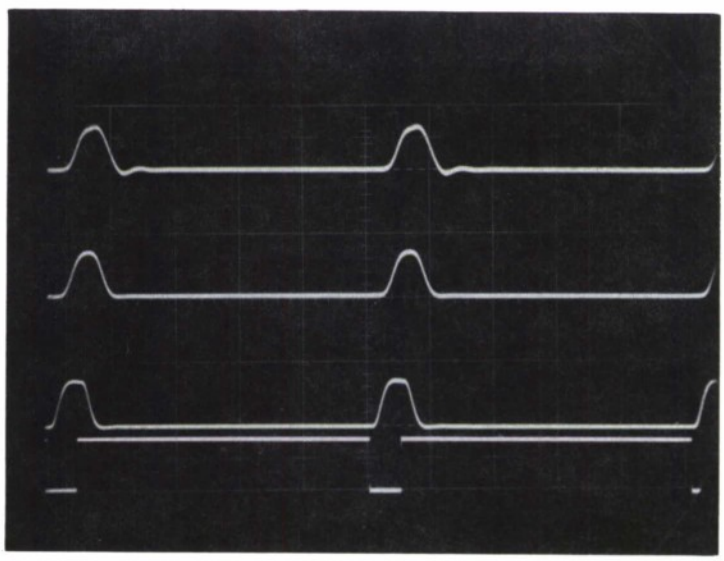

R-2521

1. Through 500 kHz Constant Amplitude IF and 200 kHz Video Filter.
2. Through 500 kHz Linear Phase IF and 200 kHz Video Filter.
3. Through Wideband IF (3 MHz) and 200 kHz Video Filter.
4. Input Pulse (T_1 = 5 μs, PRF = 20 kHz, NRZ).

Figure 100 Effects of IF Filter on Pulse Stretching for Midrange b = 2.5 with Receiver B.

video filter contributes most of the pulse stretching. The top trace shows the pulse-stretching effect of the 500 kHz constant-amplitude plug-in IF filter. Here some additional pulse stretching in the form of pulse ringing is apparent, which is attributable to ringing in the transient responses of Butterworth filters illustrated in Fig. 92. Comparison of traces one and two demonstrates the superiority of the Bessel IF filter designs for pulse modulations.

The effect of changing the bandwidth ratio b was also investigated with Receiver B. In this case the pulse stretching caused by the 500 kHz and 300 kHz linear phase plug-in IF filters was examined. The video bandwidth and pulse duration were maintained at 200 kHz and 5 microseconds respectively. The duty cycle was increased to 1/5, however, mainly for convenience. Trace four of Fig. 101 is the input pulse (NRZ) and the third trace shows the pulse stretching by the video filter. Trace two resulted from processing the modulated waveform through the 500 kHz linear-phase IF, and shows very little additional pulse stretching. The conditions here correspond to a mid-range bandwidth ratio factor of 2.5. The first trace results from processing through the 300 kHz linear-phase IF. This corresponds to a bandwidth ratio of 1.5 which is the lowest value permitted in the IRIG specifications. Here more pulse stretching is observable. This is to be expected since the IF bandwidth is closer to the video bandwidth.

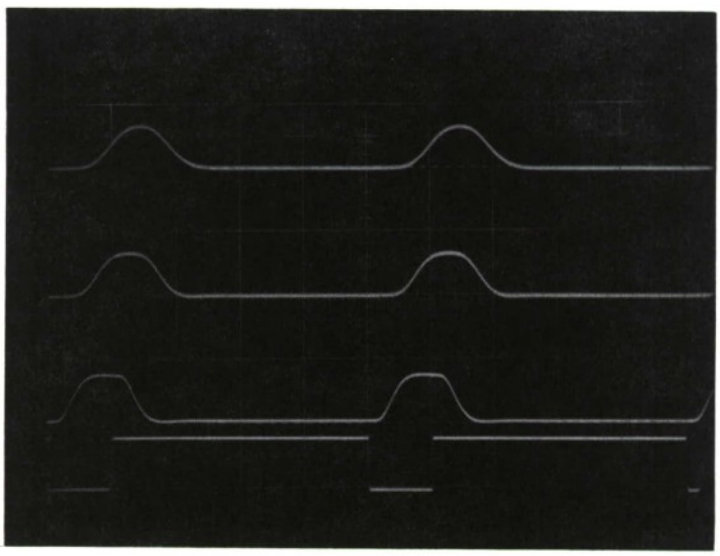

R-2522

1. Through 300 kHz Linear Phase and 200 kHz Video Filter (b = 1.5).
2. Through 500 kHz Linear Phase and 200 kHz Video Filter (b = 2.5).
3. Through Wideband IF and 200 kHz Video Filter.
4. Input Pulse (T_1 = 5 μs, PRF = 40 kHz, NRZ).

Figure 101 Effects of IF Filter on Pulse Stretching for Two Values of b with Receiver B.

A test was also conducted with Receiver B to investigate the effect of the receiver VHF RF section. Here the FM generator was a Boonton 202 J with a center frequency at 230 MHz. Tests were conducted on the RF and IF sections cascaded. As indicated previously, it is possible with Receiver B to remove the IF filters and use only the wideband amplifier. Thus, it is possible to assess the pulse stretching due to the RF section without masking from narrowband IF filters. The test results are shown in Fig. 102. Trace three is the input pulse NRZ waveform. The video bandwidth and pulse duration are maintained constant at 200 kHz and 5 microseconds respectively. The second trace shows the pulse stretching through the modem, wideband IF and video filter. Here the pulse stretching is primarily caused by the video filter. The top trace shows the pulse waveform after processing through the VHF RF, wideband IF and video filters. Comparison of traces one and two indicates no additional pulse stretching, demonstrating that the receiver RF contributes very little additional intersymbol interference.

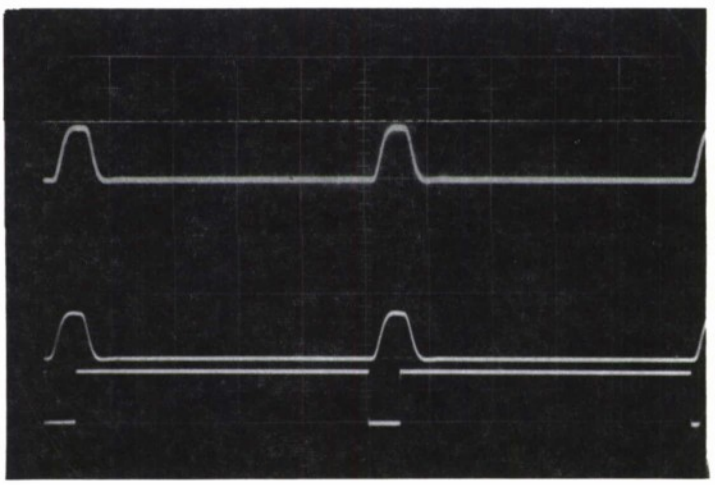

R-2523

1. Through RF and Wideband IF and 200 kHz Video.
2. Through Wideband IF and 200 kHz Video.
3. Pulse Input (T_1 = 5 μs, PRF = 20 kHz, NRZ).

Figure 102 Effect on Pulse Stretching of RF Filter (b=2.5) with Receiver B.

Similar tests to those just described were conducted with Receiver A. Receiver A is designed so that all filters have Butterworth responses. Thus TDM measurements on it, in general, demonstrated more pulse stretching. The test configuration was the same as shown in Fig. 95, using the VCO as the FM generator. The demodulator used here is the narrowband demodulator of Receiver A. The effects of the modem and video filter are illustrated in Fig. 103. Trace four is the pulse input for an NRZ waveform. Here the pulse duration is 4 microseconds corresponding to a video bandwidth (bit rate) of

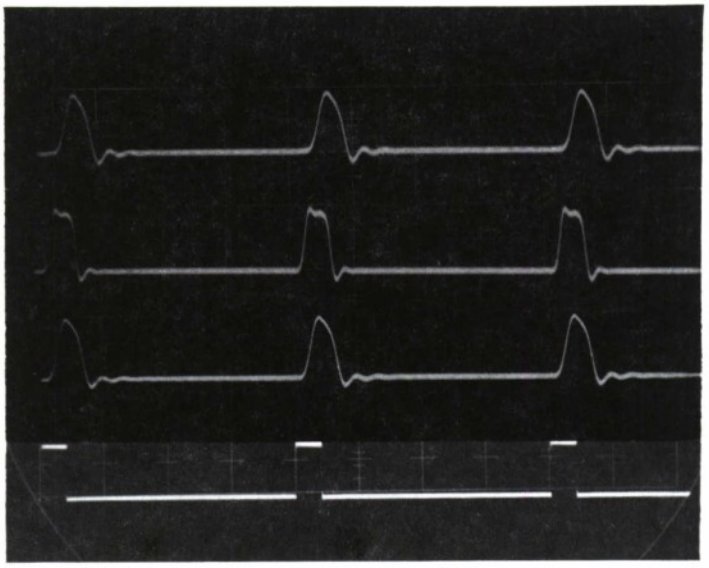

R-2513

1. Through Modem and 250 kHz Video Filter
2. Through Modem Alone.
3. Through 250 kHz Video Filter.
4. Pulse Input (T_1 = 4 μs, PRF = 25 kHz, NRZ).

Figure 103 Effects of Modem and Video Filter of Receiver A on Pulse Stretching.

250 kHz. Trace three shows the pulse stretching incurred by passing the input pulse through the video filter only. Here considerable ringing is observed which will result in intersymbol interference. The second trace shows the effects of the modem only. In this case the modems also introduce significant pulse stretching. This is primarily due to the narrowband demodulator of Receiver A. In fact, the filters in this demodulator act exactly as IF filters and their bandwidth is such that the bandwidth ratio for this trace is 2. Comparison of traces two and three indicate that the video filter still introduces more pulse stretching than this modem. The top trace shows the pulse stretching obtained using both the modem and video filter and that this combination introduces substantial pulse stretching.

The results of tests conducted on the 500 kHz Butterworth IF of Receiver A are shown in Fig. 104. The duration and video bandwidth were maintained at 4 microseconds and 250 kHz respectively. Trace three shows the NRZ input waveform. The second trace shows the pulse stretching due to the modem and video filter. The top trace shows the effects of the receiver second IF. Here the bandwidth ratio factor b = 2 which is about mid-range. The traces indicate that the IF introduces very little additional pulse stretching over that of the modem and video filter.

10.5 Measurements with the Predetection Converters and Recorder/Reproducer

The test configuration for conducting TDM tests with the recorder/reproducer is shown in Fig. 105. The simulated PCM signal obtained by pulse modulating the 10 MHz VCO is applied to the down-converter of Receiver B. The output of the down-converter (450 kHz) is then fed to the recorder/reproducer and its output applied to the direct demodulator. Several limitations existed in these recorder tests. The direct demodulator output filter is a

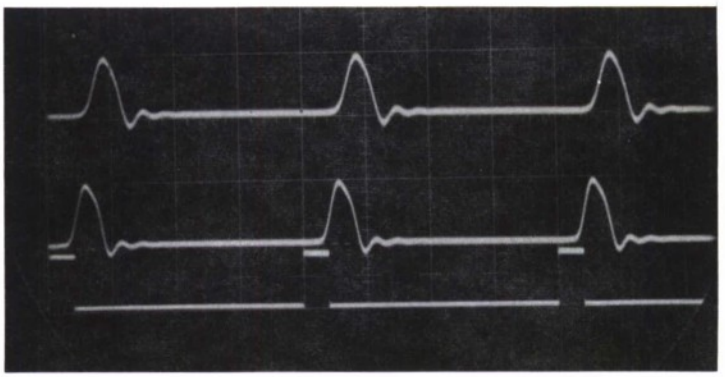

R-2514

1. Through 500 kHz Butterworth IF and 250 kHz Video Filter.
2. Through Modem and 250 kHz Video Filter.
3. Pulse Input (T_1 = 4 μs, PRF = 25 kHz, NRZ).

Figure 104 Effects of IF Filter (b = 2) of Receiver A on Pulse Stretching.

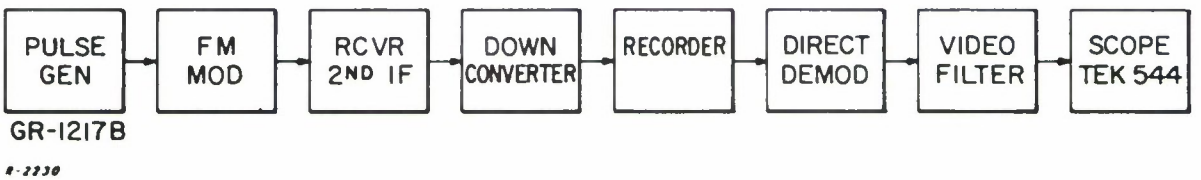

Figure 105 Block Diagram of Recorder/Reproducer TDM Test Configuration.

six-pole gaussian design with a 3 dB bandwidth of 100 kHz. For this video bandwidth the pulse duration for an RZ waveform derived from Table IX is 5 microseconds. Unfortunately only a 1 microsecond pulse was available at the time. Thus the bit rate was five times the video bandwidth rather than being equal to it. With these limitations in mind, tests were conducted on the predetection recorder.

The results obtained with the converter and recorder are shown in Fig. 106. Trace three is the input pulse. The second trace shows the effect of wideband IF of Receiver B, the down-converter/direct-demodulator and the 100 kHz video filter. Here the pulse stretching is due entirely to the video filter since the wideband IF and down-converter have bandwidths greater than 3 MHz. The top trace is the result of processing the signal out of the down-converter through the recorder/reproducer before demodulation. It can be seen that the recorder adds no noticeable pulse stretching. It should be noted that the recorder bandwidth is 2 Mc/s and thus the pulse stretching should be minimal.

A test was also conducted using the receiver second IF and the recorder. The 300 kHz linear-phase IF of Receiver B was used. This gave a bandwidth ratio of 3. The results are shown in Fig. 107. Trace

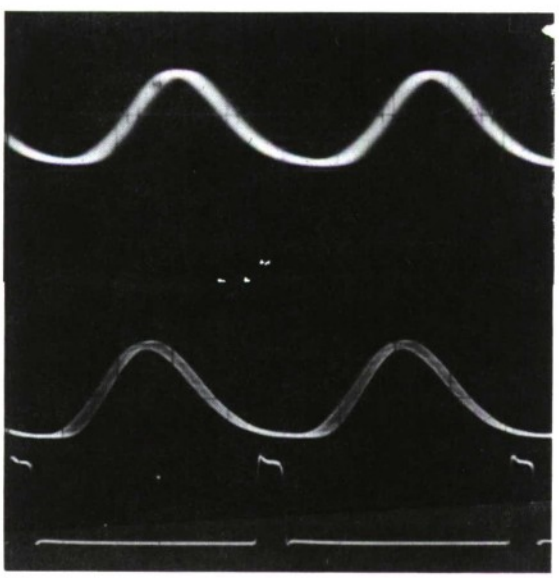

R-2515

1. Through Wideband IF and Record and 100 kHz Video Filter.
2. Through Wideband IF and 100 kHz Video Filter.
3. Input Pulse (T_1 = 1 μs, PRF = 100 kHz).

Figure 106 Effects of Down-Converter and Recorder on Pulse Stretching.

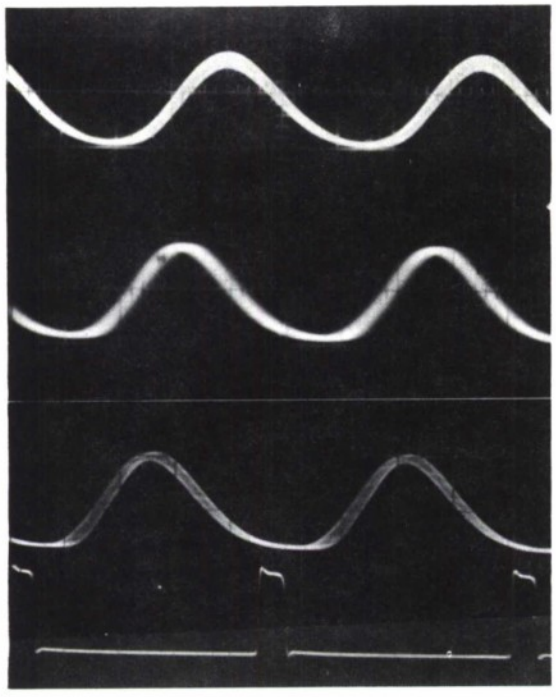

R-2516

1. Through 300 kHz Linear Phase IF, Down-Converter, Recorder, and 100 kHz Video Filter.
2. Through Wideband IF, Down-Converter, Recorder, and 100 kHz Video Filter.
3. Through Wideband IF, Down-Converter, and 100 kHz Video Filter.
4. Pulse Input (T_1 = 1 μs, PRF = 100 kHz).

Figure 107 Effects of Recorder/Reproducer and Receiver B on Pulse Stretching.

four is the pulse input with a 1 microsecond duration. The third trace is the pulse output after processing through the wideband IF, down-converter and 100 kHz video filter. The pulse stretching is due entirely to the video filter. The second trace shows the wideband IF and recorder with no noticeable increase in pulse stretching. The top trace shows the output using the 300 kHz IF and recorder. Here additional rounding is noticeable at the start of the second pulse indicating more pulse stretching. Two conclusions are evident. First, the recorder does not introduce pulse stretching whereas the receiver second IF does, and second both contribute insignificant amounts of distortion compared with the video filter. Although these tests were not conducted with proper parameter choices, it is still evident that the recorder/reproducer introduces much less intersymbol interference than either the receiver second IF or the video filter.

10.6 Conclusions

The results of the TDM tests conducted on a telemetry receiving and recording system lead to the following conclusions.

a) Bessel video filters introduce significantly less pulse stretching and hence less intersymbol interference than do Butterworth video filters.

b) For mid- and high-range values of the IF to video bandwidth ratio, the second IF filter introduces very little additional pulse stretching over that of the video filter.

c) The contribution of the second IF filter becomes more significant as this ratio is reduced to its lower limit.

d) Bessel IF filters introduce much less pulse stretching than Butterworth IF filters. Thus from the point of view of intersymbol interference, the Bessel design is always preferable in either the IF or video filters.

e) Narrowband demodulators, such as high-capture ratio types, introduce significant pulse stretching, comparable to that of the receiver second IF.

f) The Receiver RF section introduces no observable pulse stretching.

g) The predetection converters and recorders introduce no additional pulse stretching above that of the video filter.

h) In nearly all cases the principal source of intersymbol interference has been shown to be the video (premodulation) filter. Only when the receiver second IF bandwidth is at its lowest permissible value does it contribute comparable pulse distortion.

i) In all cases the intersymbol interference in TDM telemetry is determined directly by the duration of the impulse response of the filters, both premodulation and predetection, rather than by their phase characteristics.

Section XI

TRADEOFFS AND SPECIFICATIONS

11.1 Introduction

We have concentrated in Sections II through X of this report on identifying and evaluating the data degradation caused by predetection filters, and particularly by their phase characteristics. We now have effective tools to use in designing, specifying, evaluating and testing predetection filters for low data degradation. But we have not as yet indicated explicitly the tradeoffs involved between data degradation on the one hand and other filter-performance requirements on the other. We do so in the present section, and we show how these tradeoffs can be used to formulate meaningful and effective specifications.

11.2 The Nature of Specifications

In general, specifications must be:

a) Self-consistent, so that satisfying one specified criterion does not automatically prevent the satisfaction of another.

b) Attainable, either directly by known techniques, or -- if the specification is stringent enough that it has not been previously attained -- then there must be good reason to believe that it can be attained by some advanced technique.

c) Verifiable, directly or indirectly by standardizable tests.

We shall attempt to satisfy the above requirements in our proposed specification methods. But first, we need to divide specification methods into two types:

a) Performance Specifications

The desired performance characteristics, -- e.g., adjacent-channel rejection by the predetection filter -- are specified directly in terms of suitable measures of performance. No attempts are made to indicate the detailed nature of the filters; that is left to the development or design engineer who then has the flexibility to choose whatever design suits him and meet the specification.

b) Design Specifications

The specifier first determines the desired performance characteristics, then determines the corresponding design characteristics -- e.g., skirt selectivity -- that will ensure the desired performance. This type of specification generally requires accurate analytical or empirical relationships between the performance characteristics and the design characteristics.

This may not be readily available, in general, although the major results of this study supply the necessary relationships for the particular problem of phase nonlinearities.

It is frequently necessary in making design specifications to treat a system in its component parts rather than as a whole. This can lead to over-design, especially where the deficiency in the design of one subsystem can be easily compensated in the design of another. Thus, design specifications are generally less desirable than performance specifications because they depend for their effectiveness on the accuracy of the available relationships between performance and design, and because they can lead to over-design. From the viewpoint of the specifier, they require a greater effort to achieve the same end; whereas from the viewpoint of the design engineer they can restrict flexibility and resourcefulness.

Whatever the merits of the two types of specifications, it is imperative that no system should be specified both in design and in performance, because this can lead only to confusion and waste. A set of specifications should therefore contain no redundancies, whether explicit or implicit.

11.3 Specifications for Predetection Filters

The primary functions of predetection filters are:

a) to reduce the total additive noise power appearing at the demodulator input,

b) to reject interfering signals from adjacent telemetry bands, and

c) to reject undesired mixer and converter products.

The filters must perform these functions at a minimum cost in data degradation. Our objective is to show how specifications may be formulated to accomplish this end.

The functions listed as a) - c) above are best achieved by narrowing the bandwidth and sharpening the skirts of the filter, without causing undue degradation of the telemetry data. Thus, the amplitude characteristic of the filter determines the performance in terms of these functions.

The performance measure suitable for characterizing the ability of the filter to reduce additive noise is its noise bandwidth B_n, defined by

$$B_n = \frac{\int_0^\infty |H(\omega)|^2 \, d\omega}{|H(\omega_c)|^2} \quad \text{rad/sec} \tag{108}$$

where $H(\omega)$ is the transfer function of the predetection filter. The ability of the filter to reject signals in adjacent channels or undesired mixer products can be simply characterized by an attenuation factor at a given frequency. In the absence of complete knowledge as to the frequency location of undesired signals, the performance measure frequently used is the 3 dB bandwidth in conjunction with the shape factor, defined as the ratio of the frequency at the 60 dB attenuation to the frequency at 6 dB attenuation on the skirts of the amplitude characteristic. Performance specifications to ensure functions a) - c) can be drawn in terms of noise bandwidth, 3 dB bandwidth and shape factor.

On the other hand, these functions could be ensured by a variety of design specifications. The filter type (e. g., Butterworth) with complete identifying parameters and tolerances can be specified. Alternatively, the shape of the amplitude characteristic can be specified in terms of inband ripple, shape factor, asymptotic slopes (in dB/octave), or number of filter poles.

In addition, of course, the data-degrading properties of the predetection filter must be restricted by specification. We have established the I/S ratio as the appropriate measure of distortion performance in FDM telemetry. In TDM telemetry, intersymbol interference performance is readily characterized in terms of the relative area or the relative amplitude of the pulse spillover into the adjacent time slot, depending on the pulse-detection technique employed after demodulation. In the absence of complete knowledge as to the pulse-detection technique employed, or to accommodate a variety of TDM formats, then the duration of the impulse response can be used as a performance measure for TDM telemetry.

We have shown in Sections II and IV that the group-delay (or phase) characteristic of the filter determines the amount of intermodulation distortion in FDM telemetry, while in Section IX we have shown that the impulse response of the filter determines the amount of intersymbol interference in TDM telemetry. Consequently, low I/S ratio or low intersymbol interference could be ensured by a variety of design specifications. Here again, the filter type (e.g., Butterworth) with complete identifying parameters and tolerances can be specified. Alternatively, the shape of the group-delay characteristic can be specified in terms of "windows", etc. for FDM, while the detailed structure of the impulse response (as opposed to its duration) can be specified for TDM, e. g., an exponential decay constant.

Now, it is well-known that the amplitude characteristics, the group-delay (or phase) characteristic, and the impulse response of a filter are intimately related. It follows that fundamental tradeoffs exist between the various filter performance criteria, and that these tradeoffs are determined by the type of filter in question.

The general problem of specifications is fundamentally one of establishing quantitative tradeoffs between all the pertinent parameters. These tradeoffs indicate to the specifier the attainable and self-consistent performance

criteria which he may select. In the next subsection we shall present these quantitative tradeoffs for a variety of predetection filter types used in telemetry systems, and in subsequent subsections we shall indicate how these tradeoffs can be utilized in formulating performance or design specifications.

11.4 Performance Tradeoffs for Predetection Filters

We present here the attainable performance measures computed for three types of predetection filters: Butterworth filters of various orders, Bessel filters of various orders and double-tuned circuits with various coupling coefficients. The results are tabulated in Tables X, XI and XII.

The performance measures computed are:

a) the noise bandwidth B_n, as defined by Eq. (108), and normalized to the 3 dB half-bandwidth B, in rad/sec,

b) the shape factor, as defined in Subsection 11.3 above,

c) a factor representing the effect of the filter in determining the I/S ratio in FDM telemetry (see Eq. (70)), and

d) the duration T_{imp} of the filter impulse response, normalized to the 3 dB half-bandwidth B. The duration T_{imp} is defined as the time between the instant that the normalized impulse response first exceeds 0.1 and the instant that it finally dies down below 0.1. Values of BT_{imp} are read off directly from Figs. 92, 93 and 94.

The factor in c) above is presented in dB to facilitate combining it with the other two factors to determine the I/S ratio, as explained in detail in Subsection 4.3. Notice that this distortion factor is a function of the ratio of the rms frequency deviation ω_e to the filter half-bandwidth B, so a set of values for a range of ω_e/B is given in each case. As ω_e/B increases, more and more terms in the infinite sum of Eq. (70) are needed to obtain an accurate estimate of the factor in question. The computation of the power-series coefficients $\{c_i\}$ is a mathematically simple but increasingly tedious operation, so we had to content ourselves with those already presented in Tables III, IV and V. This accounts for the convergence inaccuracies indicated in Tables X-XII by asterisks.

Fortunately, most telemetry situations employ values of (ω_e/B) not in excess of 0.3, where the tabulated results are generally satisfactory. On the other hand, this factor could be more accurately computed using the Hermite-polynomials technique presented in Appendix III. The factor would then be given by $10 \log_{10} h_3^2$, and h_3 could be computed from Eq. (A3.4) using a digital computer. No convergence problems would arise in this case. In fact, we recommend that this alternate procedure be employed in the study of more advanced filter designs.

Table X

PERFORMANCE TRADEOFFS FOR
BUTTERWORTH FILTERS

			Distortion Factor, dB $10\log_{10}\left[c_3+10\,c_5\left(\frac{\omega_e}{B}\right)^2+\ldots\right]^2$				
Order n	Shape Factor	B_n/B	(ω_e/B) = 0.1	(ω_e/B) = 0.2	(ω_e/B) = 0.3	(ω_e/B) = 0.4	BT_{imp}
1	579	3.14	-10.1	-11.3	-11.2*	**	2.3
2	24.0	2.22	-7.1	-9.3	**	**	3.2
3	8.34	2.09	-8.6	-7.4	**	**	3.7
4	4.91	2.05	-8.3	-6.3	**	**	3.8
5	3.57	2.03	-7.2	-5.4	**	**	4.0
6	2.89	2.02	-6.1	-3.6	**	**	4.1

Table XI

PERFORMANCE TRADEOFFS FOR
BESSEL FILTERS

			Distortion Factor, dB $10\log_{10}\left[c_3+10\,c_5\left(\frac{\omega_e}{B}\right)^2+\ldots\right]^2$				
Order n	Shape Factor	B_n/B	(ω_e/B) = 0.1	(ω_e/B) = 0.2	(ω_e/B) = 0.3	(ω_e/B) = 0.4	BT_{imp}
1	579	3.14	-10.1	-11.3	-11.2*	**	2.30
2	29.4	2.31	-40.1	-29.5	-25.4*	-27.4*	3.09
3	10.2	2.15	-70.0	-47.2	-35.5	-23.7*	3.43
4	6.23	2.08	-99.5	-64.8	-44.1*	**	3.69
5	4.71	2.08	-131.3	-84.8	-56.5*	**	3.75
6	3.93	2.08	-163.0	-104.4	-67.5*	**	3.81

* Inaccurate due to limited number of terms available.
** Not accurate enough to cite.

Table XII

PERFORMANCE TRADEOFFS FOR DOUBLE-TUNED CIRCUITS

			Distortion Factor, dB $10\log_{10}\left[c_3+10\,c_5\left(\frac{\omega_e}{B}\right)^2+\ldots\right]^2$				
Coupling Coeff. $\underline{a}$	Shape Factor	B_n/B	(ω_e/B) = 0.1	(ω_e/B) = 0.2	(ω_e/B) = 0.3	(ω_e/B) = 0.4	BT_{imp}
0.5	28.6	2.33	-24.9	-22.9	-21.1	-17.6*	2.75
0.6	27.6	2.30	-44.6	-33.2	-24.5*	-14.9*	2.8
0.7	26.5	2.27	-21.2	-27.3	-35.5*	**	2.85
0.8	25.6	2.25	-14.5	-18.0	-25.2*	**	2.95
0.9	24.8	2.23	-10.3	-12.9	-15.3*	**	3.05
1.0	24.1	2.22	-7.1	-9.3	**	**	3.1
1.1	23.4	2.23	-4.7	-6.5	**	**	3.2
1.2	22.9	2.25	-2.7	-4.3	-3.6*	**	3.3
1.3	22.3	2.27	-1.1	-2.5	**	**	3.35
1.4	21.9	2.30	0.2	-1.1	**	**	3.45

* Inaccurate due to limited number of terms available.

** Not accurate enough to cite.

11.5 Specification of Predetection-Filter Performance

Tables X-XII can be used directly to specify filter performance. Start by determining the requirements placed on the filter by the receiving system. These requirements are usually given in terms of 3 dB bandwidth, and skirt selectivity. Compute the corresponding shape factor. Next, determine the important signal parameters. In FDM, these are the rms frequency deviation ω_e, and the video bandwidth $\hat{\omega}$. In TDM, these are the bit rate, the duty cycle, and the peak frequency deviation.

In the FDM case, compute the factor given by Eq. (69), and read the second factor representing the effect of the spectrum-shape from Fig. 34. It will usually be sufficient to consider the I/S ratio at bandedge, so use -3 dB for the second factor. Add these two factors (in dB) to the distortion factors under the appropriate (ω_e/B) in the tables. It should be possible to achieve an I/S ratio at least as good as -50 dB. Now, check in the tables to see that the desired shape factor can be achieved by the filter types capable of better than -50 dB in I/S ratio. Also, check that the resulting noise bandwidth is acceptable. If all these performance criteria are met by one or more filter types listed in the tables, then specify the corresponding numbers for: shape factor, 3 dB bandwidth, noise bandwidth, and I/S ratio. Add some margins to these numbers to allow for slight misalignments and other manufacturing imperfections.

If none of the filter types listed achieves all the performance requirements, then consider either a cascade of identical stages or a more advanced filter design such as those discussed in Section XII below. In considering cascaded stages, use Eqs. (90) and (91) and Table VI to compute the 3 dB bandwidth of each stage, then repeat the procedure described above. Use the fact that a cascade of k stages increase the I/S ratio by a factor of k^2 over that of one stage.

The above procedure will ensure that the performance specifications are both self-consistent and attainable. The measurement techniques presented in Sections II and V can be used for acceptance testing and for experimental evaluation of designs. This ensures that the specifications are verifiable by standardizable tests.

In the TDM case, compute the maximum allowable pulse-stretching from the bit rate and duty cycle. For RZ cases, choose this to be the off-time between pulses. For NRZ cases, choose it to be a fraction of the pulse width, say 20%. Multiply this time by the 3 dB half-bandwidth to obtain the maximum allowable BT_{imp}. Now, check in the tables to see that the desired shape factor can be achieved by the filter types capable of this impulse response duration. There should be no difficulty locating several types satisfying these requirements. Then specify the corresponding numbers for: shape factor, 3 dB bandwidth, noise bandwidth, and impulse-response duration. Add some margins to these numbers to allow for slight misalignments and other manufacturing imperfections.

The measurement techniques presented in Sections II and X can be used for acceptance testing and for experimental evaluation of designs. This ensures that the specifications are verifiable by standardizable tests.

11.6 Specification of Predetection-Filter Design

Although performance specifications are entirely adequate and flexible, it may still be felt desirable to constrain the cause rather than the effect through specifications. In particular, it may be desirable to specify the deviation of the group-delay (or phase) characteristic from linearity. In this section we shall present two methods to specify group-delay variations. But first we must discuss a related subject, namely, the specification of inband amplitude ripple.

It is customary to specify the inband amplitude ripple of various components in a telemetry system. These specifications are frequently quite stringent, e.g., ± 0.5 dB over most of the 3 dB bandwidth. Yet, we have been unable to find any direct dependence of data degradation on inband ripple. In fact, Bessel filters are known to have rather large variations of inband gain, and yet they can achieve very low I/S ratios because of their maximally-flat group-delay characteristics. We must conclude, therefore, that inband ripple specifications are superfluous unless amplitude-modulated signals are used. They may even be damaging if not accompanied by a consistent specification on group-delay variations. That is because in attempting to satisfy a stringent specification on inband ripple, the designer may have to sacrifice group-delay linearity or vice versa.

We have previously shown that the group-delay characteristic has no direct bearing on intersymbol interference in TDM telemetry. Thus, the purpose of specifying the group-delay characteristic would be to ensure acceptable I/S ratio in FDM telemetry.

The first method for specifying group-delay variations is the window method illustrated in Fig. 108. The variations are restricted to fall within a rectangular window of height D seconds and width equal to the 3 dB half-bandwidth. The window is restricted to the central-half of the 3 dB bandwidth because this facilitates the estimation of the power coefficients to be used in determining the distortion incurred, and because the instantaneous frequency of the input signal falls within this central-half a large percentage of the time.

To estimate the distortion incurred, we assume that the actual group-delay curve is a parabola passing through the corners of the rectangular window, as shown in Fig. 108. We compute the corresponding power coefficient c_3, and insert the result in Eq. (70). We find the distortion factor to be given by

$$(18.5 + 20 \log_{10} 2\pi \, BD) \quad \text{dB} \tag{109}$$

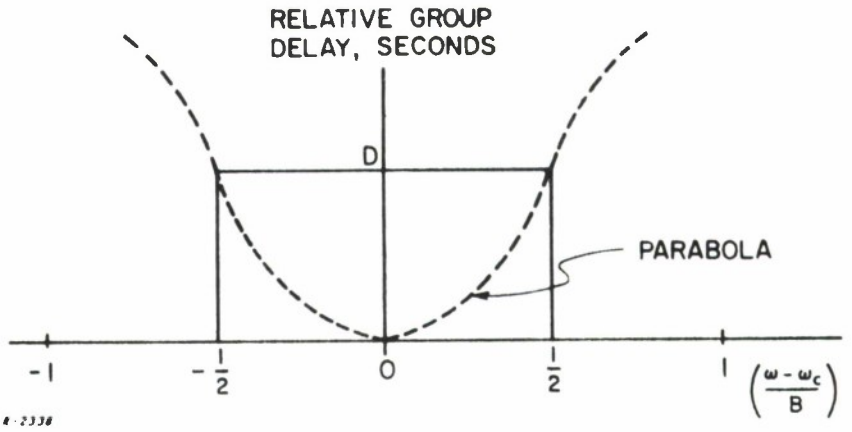

Figure 108 The Window Method for Specification of Group Delay.

The specification procedure is then similar to the one described in Subsection 11.5 above, except that instead of specifying the I/S ratio directly, we use Eq. (109) to work backwards and specify the quantity D in seconds. It should be pointed out that this procedure can yield somewhat optimistic estimates of the resultant distortion if the ratio (ω_e/B) is high, because it fails to account for nonzero power coefficients of higher order than c_3.

The second method for specifying group-delay variations is similar to the first, but is subject to less inaccuracy in the estimation of resultant distortion. The group-delay variations are restricted to fall between two of the parabolas shown in Figs. 109 or 110. To check this, the measured group delay must be normalized by multiplying it by $1/2\pi$ times and 3 dB half-bandwidth B in rad/sec, and the result plotted against the normalized frequency (ω-ω_c/B) as shown in Figs. 109 and 110. The parabolas are labeled with their corresponding distortion factors in dB, so that it is possible to make a fairly accurate estimate of the resultant distortion. The remainder of the specification procedure is similar to that described immediately above.

The group-delay measurement techniques presented in Section II can be used for acceptance testing and for experimental evaluation of designs from the group-delay viewpoint. This ensures that the specifications are verifiable by standardizable tests. In addition, these measurement techniques are extremely useful in filter alignment by the manufacturer.

11.7 Tradeoffs for Premodulation and Post-Detection Filters in TDM Telemetry

We have pointed out in Sections IX and X that intersymbol interference caused by premodulation and post-detection filters can significantly degrade the

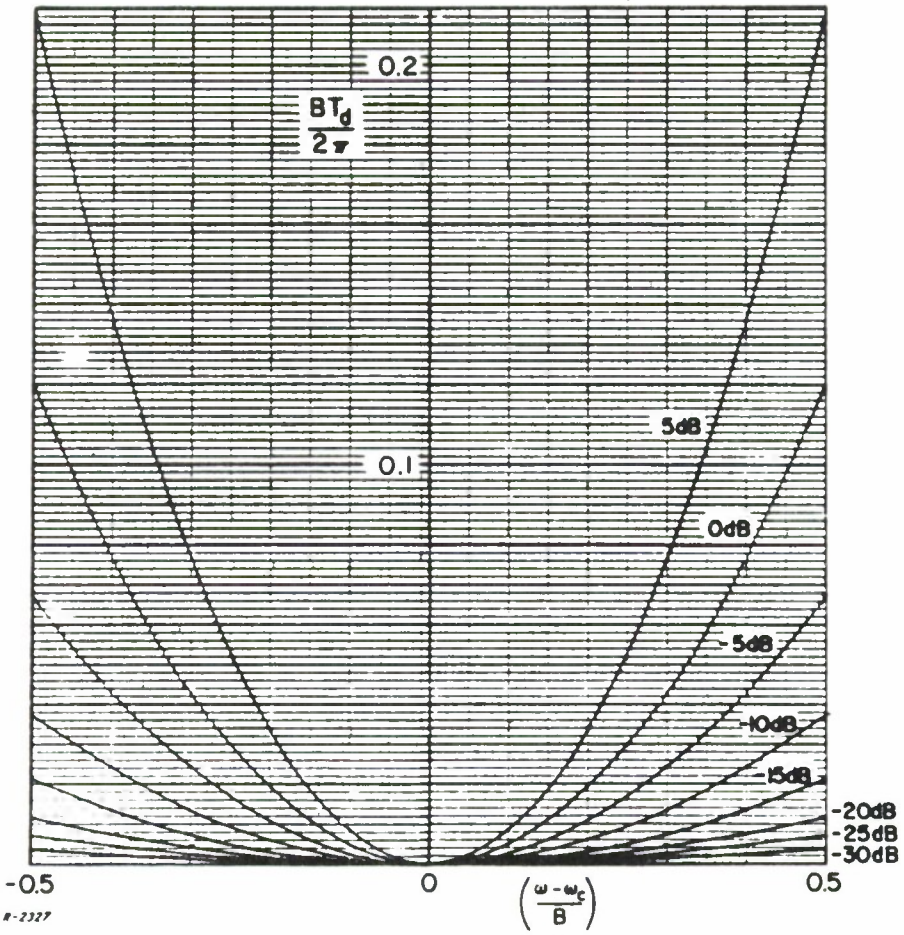

Figure 109 Nomograph for the Specification of Group Delay (High Distortion Range).

quality of TDM telemetry signals (such as PCM/FM). The compromises involved in the design of such filters are not generally understood; consequently, there is a lack of explicit standards governing their design. The existing IRIG standards are particularly vague on this point, the choices seemingly being left to equipment operators. A study effort is required to generate the necessary design information.

The premodulation filter included at the telemetry transmitter serves to narrow the video bandwidth in order to restrict the RF spectral occupancy. The design compromise is then between intersymbol interference on the one hand and RF spectral occupancy on the other. Design relationships between these two performance criteria and filter characteristics are needed. Intersymbol interference could be characterized in terms of the duration of the impulse response or similar characterizations. Spectral occupancy of RF signals must be related to frequency deviation as well as to premodulation-filter characteristics.

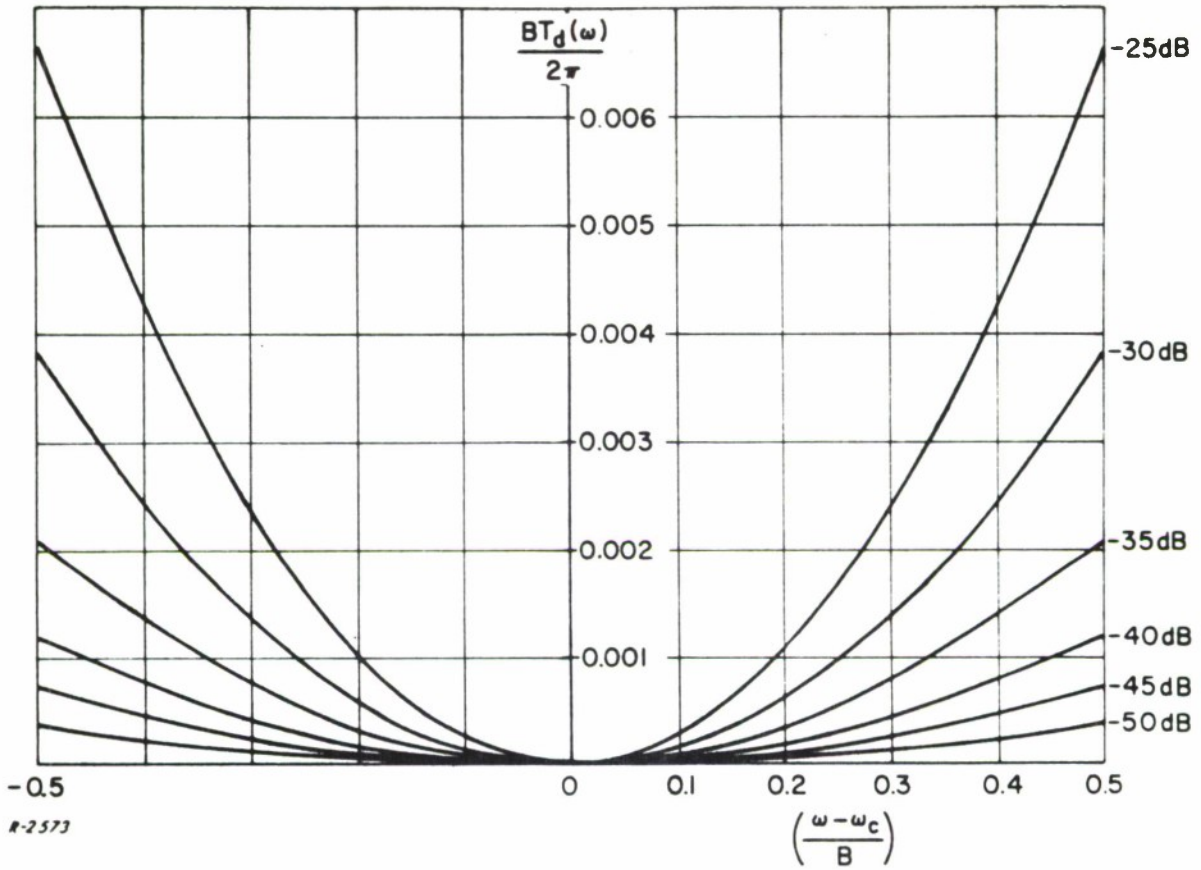

Figure 110 Nomograph for the Specification of Group Delay (Low Distortion Range).

The post-detection filter (or video filter) in the receiver serves to reduce the amount of noise fed with the digital signal from the FM (or PM) demodulator to the digital-data extractor. The noise input to this filter is thus the characteristic FM (or PM) noise. Its reduction is determined by the detailed shape of the filter amplitude response rather than simply by its noise bandwidth. The design compromise is one between intersymbol interference and reduction of FM noise.

11.8 Tradeoffs Between Multi-Signal Reception and Data Distortion

Telemetry receivers are frequently operated in the presence of more than one signal. The undesired signals may arise from sources of interfering radiation, or may simply be echoes of the desired signal caused by multipath propagation (common in airborne applications). Equipment users now frequently specify the "capture performance" of receivers, i.e., their ability to prevent the undesired signals from generating disturbances in the demodulated outputs. Good capture performance is commonly attained by using narrowband limiters consisting of amplitude limiters cascaded with narrowband filters. We have found in our laboratory tests that such high-capture-ratio demodulators introduce significant data distortion, sometimes as much distortion as that introduced by the predetection filters. Again, the design compromises between capture performance and data quality are not generally appreciated, resulting in a propensity to over-specify the capture performance at the expense of data quality.

Several mechanisms can be identified as possible causes of data distortion in high-capture-ratio demodulators. First, the narrowband filters incorporated in the limiters may cause distortion in the same way the predetection filters do (nonlinear phase, etc.). Second, these filters can introduce unwanted amplitude modulation which, in turn, introduces distortion in the demodulated output by AM-to-PM conversion in subsequent stages. Indeed, there is reason to believe that high-capture-ratio demodulators are less able to reject incidental AM at their input than standard demodulators. Such incidental AM is encountered in precisely that multi-signal environment for which capture performance is specified, so that there is likely to be a performance compromise between capture ratio and AM rejection, a compromise that determines the actual data quality in the multi-signal environment.

A study effort is required to determine the design compromises from the data quality viewpoint between multi-signal and single-signal operation. The various data-degrading mechanisms must be quantitatively identified and evaluated in terms of suitable performance characterizations. It is noteworthy that the noise-loading technique we are employing in our current study is applicable to the characterization and analysis of data quality in the multi-signal environment (especially multipath reception).

Section XII

IMPROVEMENT OF DATA QUALITY IN TELEMETRY SYSTEMS

12.1 Areas of Improvement in Receivers

It has been indicated throughout this report that a major source of data degradation in FDM telemetry systems is intermodulation distortion caused by nonlinear phase characteristics in various locations in the system. From this point of view then the data quality can be improved by reducing the phase nonlinearities of the critical system filters. Examination of several receivers has verified that the principal source of phase nonlinearity and hence data distortion is the receiver second IF filter. Thus a significant improvement in the linearity of the phase characteristic of the second IF filter will be reflected directly in an improvement in system data quality.

There are several methods by which the second IF phase linearity can be improved. Since the inband amplitude characteristic of the IF filter has been shown not to be a significant source of intermodulation distortion in telemetry situations, Bessel filters can be used to achieve the desired linear phase characteristics. Measurements with these have shown distortion to be significantly lower (12-15 dB) than a Butterworth design with the same 3 dB bandwidth. Theoretical predictions based on perfectly aligned filters indicate even more spectacular capabilities. However the use of Bessel filters necessitates a sacrifice in skirt selectivity and adjacent channel rejection. For example, a sixth-order Butterworth filter has a 2.89 shape factor while the same order Bessel filter has a shape factor of 3.93, which results in the out-of-band attenuation of the Butterworth being about 25 dB better than the Bessel filter. A compromise between the skirt selectivity and phase linearity is achievable with the Transitional Butterworth-Thomson filters (Ref. 11). These filters can be designed such that their characteristics vary between the Butterworth maximally-flat amplitude response and the Bessel maximally-flat group-delay response as the pole positions are changed. Thus, it is entirely feasible with this form of filter to select any point between the linear phase and flat amplitude designs and arrive at a compromise between these two characteristics. The resulting design trades off adjacent channel rejection for low intermodulation distortion.

A Paynter filter design (Ref. 12) could also be used for the receiver second IF. This design approximates the linear phase characteristic all across the desired band of frequency, giving a low average delay variation as compared with the Bessel design which concentrates on the near center frequency behavior. The Bessel and Paynter filters have the same relationship in phase characteristic that the Butterworth and Chebyshev filters have in amplitude characteristic. The amplitude response of the Paynter filter, however, has less amplitude variation inband and greater attenuation out of band than the

Bessel, thus providing an intermediate compromise between the desirable phase characteristic of the Bessel filter and the desirable amplitude characteristics of the Butterworth design.

The obvious drawback in the Bessel, Butterworth-Thomson and Paynter designs is the need to trade off linear phase characteristics against flat inband amplitude characteristics and high out-of-band attenuation. This is the same tradeoff encountered in most modern filter design techniques (Butterworth, Chebyshev, etc.). It is a consequence of the minimum-phase assumption which introduces an enormous simplification in the synthesis of realizable filters. The minimum-phase criterion permits the approximation of either the amplitude or phase characteristics of physically realizable filters and then specifies the other in such a way as to insure realizability. Thus, under a minimum-phase design procedure the amplitude and phase characteristics are interrelated such that simultaneous approximation of both flat amplitude and linear phase characteristics is impossible.

It is possible to simultaneously approximate a linear phase and flat amplitude filter by using a non-minimum phase design technique. One approach using such a procedure has been described by Lerner (Ref. 13) in which a passive network realization using lattice techniques is employed to derive a bandpass filter with flat inband amplitude response and a linear phase characteristic. The skirts of this filter provide at least as much out-of-band attenuation as the same order Butterworth filter for the first 50 dB. This design technique thus holds promise for satisfying both the requirements of adjacent channel rejection and low intermodulation distortion by providing filters with high skirt selectivity and low group-delay variations.

Other techniques for the design of non-minimum phase filter characteristics using the procedures of active network synthesis are under investigation. These include the application of negative impedance converters, controlled sources, and operational amplifiers in the realization of specialized filter characteristics through the independent manipulation of poles and zeroes. Kerwin and Huelsman (Ref. 14) describe such a technique in which high near-band attenuation is achieved. The active network procedures hold particular promise in that they are ideally suited to implementation with integrated circuit techniques, thus providing the additional benefit of size reduction. Networks using these techniques have been built in the range of hundreds of kHz. However, application in the frequency range of the second IF filters of telemetry receivers has not yet been achieved.

One more technique for achieving linear phase and high out-of-band rejection deserves mention. This method employs a cascade of a linear phase filter which has poor skirt selectivity and out-of-band notch filters to achieve adjacent channel rejection. In principle, this technique is similar to the well-known method of approximating the desired rectangular amplitude characteristic and then compensating the phase nonlinearities by cascading delay equalizing networks. This method is currently being investigated and it remains to be seen

if the out-of-band notches can be brought close enough to the desired bandedge to give adequate skirt selectivity without having their phase characteristics affect the inband phase linearity of the filter.

It is clear that many approaches are available for achieving filters with linear phase and high skirt selectivity. Application of these techniques to telemetry receiver designs will permit independent control of the intermodulation distortion and adjacent channel rejection characteristics which are currently interrelated in telemetry systems.

A secondary source of data degradation in telemetry receivers is the high-capture demodulator. As pointed out previously, when narrowband limiters are used to achieve high-capture performance, the filter bandwidths are generally chosen to be approximately equal to the IF bandwidth. Thus, these filters are subject to the same kind of phase nonlinearities as the second IF filters. Here, although skirt selectivity is necessary for rejecting the interfering signal, the skirts need not have as much attenuation as those of the IF filter. Thus, it might be quite acceptable to use Bessel designs for the narrowband limiters and enhance their distortion performance. It would also be possible to apply the same techniques for improving the phase linearity to the design of high-capture demodulator filters as were suggested for the second IF filters.

It would be useful to subject all of the passive and active filter types outlined here to an analysis using the Hermite Polynomial Technique (see Appendix III). This technique is a more convenient method of calculating the factor (see Eq. (70)) through which the filter phase characteristic influences the distortion level. This factor, a function of (ω_e/B), serves as a figure of merit for the filter and can be used in conjunction with other parameters such as noise bandwidth and skirt selectivity to select an optimum filter type for telemetry applications.

12.2 Areas of Improvement in Predetection Converters

Tests conducted on predetection converters for this study indicated that they could be a significant source of distortion. Several improvements in their design and use can be made in order to enhance the overall data quality. The down/up converter used here had Butterworth filters in both the down-converter and up-converter. Since adjacent channel rejection is accomplished by the second IF filter, either before or after conversion, the skirt selectivity of the down/up converter need not be extremely sharp. Thus, linear-phase (Bessel) filters could well be used here with a significant improvement in intermodulation distortion. This improvement was demonstrated by use of the down-converter/direct-demodulator which did have Bessel filters and consequently achieved low distortion.

The use of the down/up converter for predetection recording usually includes reprocessing the playback signal from the recorder through the second

IF before demodulation. This point was discussed in detail in Subsection 7.3. It should be noted that preceding and following the record process with the same IF bandwidth effectively adds 6 dB to the distortion level on the signal. This should be avoided wherever possible. In cases in which the prerecord second IF bandwidth is narrow and low record frequencies (450 kHz) are used, direct demodulation contributes less distortion than up-conversion. The distortion level is improved in this case by eliminating a second passing through the IF filter and also by eliminating the intermodulation of the up-converter LO and upper sideband, which becomes worse as the record frequency is lowered.

In addition, use of direct demodulation following the recorder will permit use of lowpass filters rather than bandpass filters to limit the spectrum. The resulting benefits of lower group delay, lower Q requirement and convenient application of active filter techniques can contribute greatly to the improvement of data quality in the predetection record process.

12.3 Areas of Improvement in Predetection Recorder/Reproducer

Measurements made with a predetection recorder demonstrated that under controlled conditions, it was not a significant source of intermodulation distortion. These conditions included a well-behaved group-delay characteristic and a high signal-to-noise ratio. The low group-delay variations are achieved by delay equalization of the recorder. The use of this or an equivalent method should be continued in order to insure low intermodulation distortion due to nonlinear phase characteristics.

The signal-to-noise ratio of the recorder is just as significant as the phase characteristic in contributing to data distortion. Continued efforts should be made to reduce the noise generated by the reproduce electronics. In addition, the bandwidth of the recorder can be tailored to the signal bandwidth by use of a selectable bandpass filter after the reproducer. In particular, it was found here that a major source of noise existed at the very low (less than 10 kHz) end of the band, which could be readily eliminated since this portion of the bandpass would seldom be occupied by the telemetry signal. A similar situation existed at the high end of the band.

12.4 Modification of Existing Receivers to Improve Data Quality

It is possible to modify existing telemetry equipment to improve the data quality. The modifications suggested below are only examples of the kind of distortion improvements that can be made to the system without adversely affecting other system parameters. Any contemplated modifications of the system should be preceded by a detailed investigation and development of the appropriate subsystems.

As an example of the kind of modifications that can be made on receivers the 500 kHz second IF filter of Receiver C will be considered. This receiver

is chosen as an example because it is currently in use at the A. F. Eastern Test Range, and because it is constructed of tubes and thus susceptible to retrofitting with the addition of a small transistorized filter package. The second IF is considered because it is the principal source of intermodulation distortion in the receiver and thus will yield the largest improvement in distortion.

As described earlier, the second IF of Receiver C is composed of a cascade of five slightly overcoupled double-tuned filters, isolated by pentode gain stages. The amplitude, group delay and distortion have been measured and the data is presented earlier in this report. For the modification described here, the form of the filter can be changed to Bessel while maintaining the same skirt attenuation. This necessitates the use of a Bessel filter with a narrower 3 dB bandwidth, but since it has been demonstrated that the amplitude characteristic does not contribute to intermodulation distortion, this introduces no adverse affects. In addition, the Bessel filter will have a lower noise bandwidth.

A detail drawing of the skirt attenuation of the receiver second IF is shown as the solid line in Fig. 111. Only that portion of the characteristic from 100 kHz offset from the center frequency (10 MHz) to 1 MHz offset is shown. This includes, however, the area of interest here. The 3 dB point is seen to be at 250 kHz and the shape factor is about 1.6. The design specification for the shape factor for this filter is 2.5 so it can be seen that the filter is well within specification.

It is of interest to see how the distortion of this filter and other types of filters which have the same skirt selectivity compare. To accomplish this a Butterworth and Bessel filter with the same skirt characteristic were designed. The dotted line in Fig. 111 is the attenuation curve for the lowest order Butterworth filter having the same out-of-band attenuation characteristics. It is for a 12^{th}-order Butterworth (Ref. 15, Chap. 4). This order filter was anticipated since the receiver IF has five double-tuned circuits (10 poles) and hence a filter of at least 10^{th}-order would be necessary. The need for 12^{th}-order comes about because of the overcoupling in the double-tuned circuits which results in higher skirt selectivity.

It can be seen that the 3 dB bandwidth of the 12^{th}-order Butterworth is identical with that of the second IF filter, in fact their characteristics are nearly identical. A computation of intermodulation distortion was made, using the phase characteristics of the 12^{th}-order Butterworth, in order to compare with the distortion predicted for a cascade of double-tuned circuits. The predicted distortion for the 12^{th}-order Butterworth at the edge of the video band ($\omega/\hat{\omega} = 1$) was -30.8 dB. The prediction for the double-tuned filter cascade in the IF of Receiver C was -32 dB. Thus there was virtually no difference in the distortion of these two different types of filters. The result of a cascade of filters having slightly lower distortion than a single filter of the same order has been observed in another test and is due to the fact that the phase nonlinearities

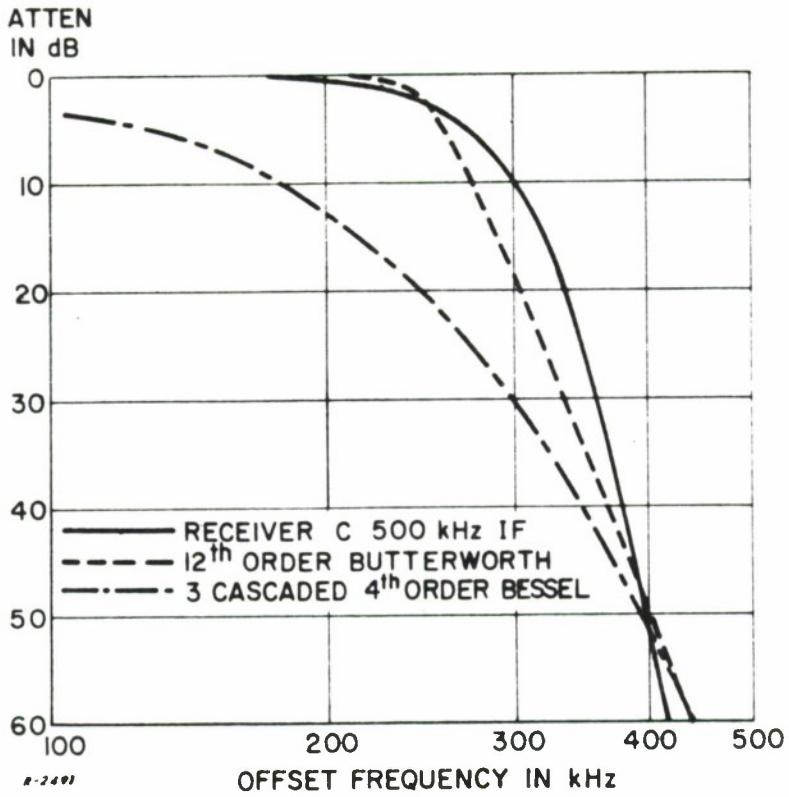

Figure 111 Skirt Selectivity for Receiver C.

of a cascade of filters are lower than those of the same order filter. However, the difference in the two cases encountered here was 1 dB or less, and this is hardly significant.

The broken line in Fig. 111 is the amplitude characteristic of a cascade of three fourth-order Bessel filters (Ref. 16). This cascade gives the same skirt attenuation as the 12^{th}-order Bessel, and in fact as the 12^{th}-order Butterworth, and is used here because distortion predictions were readily available for the fourth-order Bessel and time was not available to make distortion computations on the 12^{th}-order Bessel. Here it can be seen that the 3 dB bandwidth of the Bessel filter having the same out-of-band attenuation as a Butterworth filter, is considerably less than the Butterworth 3 dB bandwidth. In fact here it is 200 kHz as compared with 500 kHz for the Butterworth. However, as emphasized previously, the inband amplitude characteristic does not contribute to intermodulation distortion. The predicted distortion for this cascade of fourth-order Bessel filters, obtained from Table XI, is -57 dB. This is considerably less

distortion (about 25 dB) than with either of the other designs. This distortion would be even lower if a single 12th-order Bessel filter or a cascade of two sixth-order Bessel filters were used, however the relevant computations were not carried out.

The computation of distortion for both the Bessel and Butterworth filters has been made assuming perfect alignment. It should be pointed out that any misalignment would increase the distortion. In the case of the Butterworth designs where the distortion is relatively high, misalignment would not greatly alter the prediction. For the Bessel design, the low distortion is highly dependent upon alignment. However, even in tests conducted in this study on a 300 kHz Bessel filter with no attempt at alignment, the distortion was no worse than with a 500 kHz Butterworth. Thus with careful alignment, a Bessel filter can give the same adjacent channel rejection and lower distortion than a Butterworth filter and in addition, the noise bandwidth of the Bessel filter will be lower. It is thus possible to improve the distortion properties of Receiver C by replacing the narrowband second IF amplifier by a wideband (3.3 MHz) second IF amplifier which has been retrofitted to include a narrowband Bessel filter or cascade of filters.

12.5 Modification of Existing Predetection Converters to Improve Data Quality

The only simple modifications which can be made on the down/up converter are concerned with its operation in the predetection-record process. If a narrowband IF is used preceding the down-converter, then the distortion can be improved by about 6 dB by not passing the playback signal from the reproducer back through this same narrowband IF. This is readily accomplished either by direct demodulation off the reproducer output or after up-conversion. The first is more desirable in the case of low record frequencies due to the additional intermodulation distortion in the up-converter.

12.6 Modification of Existing Predetection Recorder/Reproducer to Improve Data Quality

Operational improvements can also be made with the recorder to reduce data distortion. In this case, the improvement in distortion will be derived from increasing the signal-to-noise ratio out of the recorder. This can be accomplished by inserting a controllable bandpass filter (preferably Bessel) at the reproducer output which can be used to eliminate as much of the low frequency and high frequency recorder noise as the signal bandwidth will permit. In this way the additive noise generated in the recorder can be minimized and the data quality improved.

12.7 Improving TDM Data Quality

The intersymbol interference measurements conducted for this study have demonstrated that the principal source of distortion in TDM telemetry is characterized by the impulse response of premodulation and post-detection filters. However, it has been shown that when the premodulation filters are of Bessel design, the receiver second IF amplifier does contribute pulse stretching if the IF is a Butterworth filter. Thus, improved TDM performance can be obtained by using Bessel rather than Butterworth IF filters.

12.8 Conclusions

The area in telemetry systems in which the most significant improvement in data quality can be obtained by improving the linearity of the phase characteristic is the receiver second IF. By design and specification in terms of phase linearity, or better yet group-delay variation, control of the intermodulation distortion can be gained. Evaluation of the design tradeoffs, particularly that between skirt selectivity and phase linearity, indicates that several types of filters, Butterworth-Thomson or Bessel, exist which can achieve good skirt selectivity and lower distortion. The non-minimum phase filter design procedures either with Lerner or active filters holds promise for providing both high skirt selectivity and phase linearity if the techniques described here can be extended to frequencies useful in telemetry.

In predetection converters, improvement in data quality can be obtained by using Bessel filters. In addition, operation with narrowband receiver IF's should be evaluated to ensure that unnecessary distortion is not being introduced. In predetection recorders, the SNR should be maximized to improve data quality. This can be done by adjusting the recorder bandwidth to the input signal bandwidth and eliminating unnecessary low and high frequency noise.

Section XIII

CONCLUSIONS AND RECOMMENDATIONS

13.1 Conclusions

We have studied the problem of phase nonlinearities in telemetry-receiving systems both analytically and experimentally. We divided the problem into two parts, corresponding to FDM and TDM telemetry signals.

For FDM signals, we introduced the noise-loading technique to characterize the data-degrading effects of nonlinear phase characteristics. We were able to analytically compute and to experimentally verify the distortion levels in various telemetry equipments.

For TDM signals, we showed that intersymbol interference is not directly related to phase nonlinearities, but rather to the transient responses of the receiving circuits. We established cause/effect relationships for intersymbol interference, and observed these effects experimentally.

Detailed conclusions can be found at the end of appropriate sections of this report. Suffice it to say here that the results of the study can be utilized in a variety of ways. They can clarify the cause/effect relationships so as to improve the insight of the design engineer. They supply the tools for systematic analytical design to reduce data degradation. They introduce new experimental techniques for system alignment and for the evaluation of system performance in terms of data quality. And finally, they lead to systematic techniques for system specification and acceptance testing.

13.2 Recommendations

Our primary recommendation is that the techniques, both analytical and experimental, presented in this report should be utilized to ensure data quality in all phases of telemetry system implementation. This includes system design, analysis, specification, standardization, evaluation, testing, alignment and calibration. In particular, the noise-loading technique should fill an urgent need experienced by all those concerned with telemetry systems.

Many detailed recommendations were made in the main body of the report, especially in Sections XI and XII. Methods of specification were recommended in Section XI. We emphasized the advantages of performance specifications over design specifications. In Subsections 11.7 and 11.8 we identified two areas where design tradeoffs are not generally available. A study effort in these two areas can lead to extremely useful results in improving the performance of telemetry systems.

Improvements that could be implemented in telemetry-receiving systems were presented in detail in Section XII. Some of these involved the development of some advanced types of filters for use in telemetry receivers. Others, involving the modification of existing equipment at the A. F. Eastern Test Range, are recommended for immediate consideration.

We further recommend that a laboratory development effort be initiated with the following objectives:

a) to develop and specify new predetection filter-amplifiers for low telemetry data degradation, and

b) to develop accurate and flexible data-distortion test sets for use in acceptance testing of hardware procurement in accordance with the specifications determined in a), as well as in evaluating and comparing the new designs developed in a).

The recommended approach is:

a) Development of new filter-amplifier designs applicable both to receiver IF amplifiers and to demultiplexer subcarrier filters. Data distortion will be evaluated in terms of distortion power under noise-loading conditions for FDM signals, and intersymbol interference for TDM signals. Some of the filter designs to be considered have already been discussed in Subsection 12.1 above.

b) Development of an accurate, flexible and compact distortion test set employing the noise-loading technique. This would be designed to fulfill the specific needs of telemetry equipment. It would enable testing of front ends (VHF and S-band), IF filter-amplifiers, discriminators, subcarrier filters and subcarrier discriminators. Our existing laboratory test setup -- consisting of a benchful of standard test equipment, special purpose test equipment, and breadboards -- has a residual distortion level worse than -50 dB. It is also limited in frequency deviation to about 100 kHz rms. The new test set should have residual distortion better than -60 dB for a range of rms frequency deviations from a few tens of Hz (for subcarrier tests) to 0.5 MHz (for S-band receiver tests). The large range of center frequencies required in such a test set can be covered by mixing an internally generated FM signal with one of an appropriate group of standard CW generators.

c) Development of an accurate and simple group-delay measurement set. This would be based on a simple and accurate phase-detector circuit we have developed during the current study. This circuit employs tunnel diodes as zero-crossing detectors with excellent AM rejection. The measurement set would have better than 20 ns accuracy, and automatic sweep and display capability. It would be used in acceptance testing and evaluation of predetection-filter designs from the point of view of group-delay linearity, as well as in routine filter alignment.

Section XIV

REFERENCES

1. Telemetry Standards prepared by the Telemetry Working Group of the Inter-Range Instrumentation Group of the Range Commanders' Conference; IRIG Document No. 106-60 (Revised June 1962).

2. Baghdady, E. J., Lectures on Communication System Theory, McGraw-Hill Book Co., Inc., New York, 1961.

3. Papoulis, A., The Fourier Integral and Its Applications, McGraw-Hill Book Co., Inc., New York, 1962.

4. Weinberg, L., Network Analysis and Synthesis, McGraw-Hill Book Co., Inc., New York, 1962.

5. Orchard, H. J., "The Phase and Envelope Delay of Butterworth and Tehebycheff Filters," IRE Trans. on Circuit Theory, Vol. CT-7, No. 2, pp. 180-181, June 1960.

6. Storch, L., "Synthesis of Constant-Time-Delay Ladder Networks Using Bessel Polynomials," Proc. IRE, Vol. 42, No. 11, pp. 1666-1675, November 1954.

7. Seely, S., Radio Electronics, McGraw-Hill Book Co., Inc., New York, 1956.

8. Starr, J., "Envelope Delay in a Tape Recorder System," Proc. International Telemetry Conference, Vol. I, pp. 595-612, May 1965.

9. Thomson, W. E., "The Response of a Non-Linear System to Random Noise," IEE Monograph, No. 106R, September 1954.

10. Henderson, K. W. and W. H. Kautz, "Transient Response of Conventional Filters," IRE Trans. on Circuit Theory, Vol. CT-5, No. 4, pp. 333-347, December 1958.

11. Peerless, Y. and T. Murakami, "Analysis and Synthesis of Transitional Butterworth-Thomson Filters and Bandpass Amplifiers," RCA Review, pp. 60-94, March 1957.

12. Hansen, P. D., "New Approaches to the Design of Active Filters," The Lightening Empiricist, Vol. 13, Nos. 1 and 2, pp. 3-16, July 1965.

13. Lerner, R. M., "Bandpass Filters with Linear Phase," Proc. IEEE, Vol. 52, pp. 249-268, March 1964.

14. Kerwin, W. J. and L. P. Huelsman, "The Design of High Performance Active R-C Bandpass Filters," IEEE International Convention Record, Vol. 14, Part 10, pp. 74-80, March 1966.

15. Filters, Theory and Practice, White Electromagnetics Inc., Rockville, Maryland, 1963.

16. Thomson, W. E., "Networks with Maximally Flat Delay," Wireless Engineer, Vol. 29, pp. 256-263, October 1952.

APPENDIX I

DERIVATION OF THE QUASI-STATIONARY TRANSFER RELATION

We wish to derive Eq. (41) from the general transfer relation in Eq. (36). Inserting Eq. (40) in Eq. (36), utilizing the trigonometric identities for the sine and cosine of the difference of two angles, and then dividing numerator and denominator by $\cos \phi(t)$ yields

$$\tan \theta\,(t) = \frac{\left[\tan\phi(t) \int h_p(\tau) \cos(\tau\dot{\phi}(t))d\tau - \int h_p(\tau) \sin(\tau\dot{\phi}(t))\, d\tau \right.}{\left. - \int h_q(\tau) \cos(\tau\dot{\phi}(t))\, d\tau - \tan\phi(t) \int h_q(\tau) \sin(\tau\dot{\phi}(t))\, d\tau \right]}$$

$$\frac{\left[\int h_p(\tau) \cos(\tau\dot{\phi}(t))\, d\tau + \tan\phi(t) \int h_p(\tau) \sin(\tau\dot{\phi}(t))\, d\tau \right.}{\left. + \tan\phi(t) \int h_q(\tau) \cos(\tau\dot{\phi}(t)) - \int h_q(\tau) \sin(\tau\dot{\phi}(t))\, d\tau \right]} \tag{AI.1}$$

Now, recognize the following Fourier transforms:

$$\mathrm{Re}\left[H_p(\dot{\phi})\right] = \int h_p(\tau) \cos(\tau\dot{\phi})\, d\tau \tag{AI.2}$$

$$\mathrm{Im}\left[H_p(\dot{\phi})\right] = -\int h_p(\tau) \sin(\tau\dot{\phi})\, d\tau \tag{AI.3}$$

$$\mathrm{Re}\left[H_q(\dot{\phi})\right] = \int h_q(\tau) \cos(\tau\dot{\phi})\, d\tau \tag{AI.4}$$

$$\mathrm{Im}\left[H_q(\dot{\phi})\right] = -\int h_q(\tau) \sin(\tau\dot{\phi})\, d\tau \tag{AI.5}$$

Substituting from Eqs. (AI.2) - (AI.5) into (AI.1), and dividing numerator and denominator by $\left\{\mathrm{Re}\left[H_p(\dot{\phi})\right] + \mathrm{Im}\left[H_q(\dot{\phi})\right]\right\}$ we get

$$\tan\theta(t) = \frac{\dfrac{\mathrm{Im}\left[H_p(\dot{\phi})\right] - \mathrm{Re}\left[H_q(\dot{\phi})\right]}{\mathrm{Re}\left[H_p(\dot{\phi})\right] + \mathrm{Im}\left[H_q(\dot{\phi})\right]} + \tan\phi(t)}{1 - \dfrac{\mathrm{Im}\left[H_p(\dot{\phi})\right] - \mathrm{Re}\left[H_q(\dot{\phi})\right]}{\mathrm{Re}\left[H_p(\dot{\phi})\right] + \mathrm{Im}\left[H_q(\dot{\phi})\right]} \cdot \tan\phi(t)} \tag{AI.6}$$

The similarity of Eq. (AI-6) to the trigonometric identity

$$\tan(\alpha + \beta) = \frac{\tan\alpha + \tan\beta}{1 - \tan\alpha\tan\beta} \tag{AI. 7}$$

is exploited to conclude that

$$\theta(t) = \arctan \frac{\mathrm{Im}\left[H_p(\dot{\phi})\right] - \mathrm{Re}\left[H_q(\dot{\phi})\right]}{\mathrm{Re}\left[H_p(\dot{\phi})\right] + \mathrm{Im}\left[H_q(\dot{\phi})\right]} + \phi(t) \tag{AI. 8}$$

With the aid of Eqs. (29) and (30) we can write

$$\mathrm{Im}\left[H_p(\dot{\phi})\right] - \mathrm{Re}\left[H_q(\dot{\phi})\right] = \mathrm{Im}\left[H_1(\dot{\phi} + \omega_c)\right] \tag{AI. 9}$$

$$\mathrm{Re}\left[H_p(\dot{\phi})\right] + \mathrm{Im}\left[H_q(\dot{\phi})\right] = \mathrm{Re}\left[H_1(\dot{\phi} + \omega_c)\right] \tag{AI. 10}$$

Therefore

$$\theta(t) = \arctan \frac{\mathrm{Im}\left[H_1(\dot{\phi} + \omega_c)\right]}{\mathrm{Re}\left[H_1(\dot{\phi} + \omega_c)\right]} + \phi(t) \tag{AI. 11}$$

The arc tan is immediately recognized to be the phase characteristic $\Phi\left[\dot{\phi} + \omega_c\right]$, and use of Eq. (22) finally yields the desired Eq. (41).

APPENDIX II

DERIVATION OF EQUATION (52)

In this Appendix we fill in the steps omitted in the derivation of Eq. (52) presented in the main test. To apply Eq. (49) to the transfer relation of Eq. (47) we must write out the first few derivatives of $\sin\phi(t)$ and $\cos\phi(t)$. These are

$$\frac{d}{dt}\left[\sin\phi(t)\right] = \phi' \cos\phi \tag{A2.1}$$

$$\frac{d^2}{dt^2}\left[\sin\phi(t)\right] = \phi'' \cos\phi - \phi'^2 \sin\phi \tag{A2.2}$$

$$\frac{d^3}{dt^3}\left[\sin\phi(t)\right] = \left(\phi^{(3)} - \phi'^3\right)\cos\phi - 3\phi'\phi'' \sin\phi \tag{A2.3}$$

$$\frac{d^4}{dt^4}\left[\sin\phi(t)\right] = \left(\phi^{(4)} - 6\phi'^2\phi''\right)\cos\phi + \left(\phi'^4 - 4\phi'\phi^{(3)} - 3\phi''^2\right)\sin\phi \tag{A2.4}$$

$$\frac{d^5}{dt^5}\left[\sin\phi(t)\right] = \left(\phi^{(5)} - 15\phi'\phi''^2 - 10\phi'^2\phi^{(3)} + \phi'^5\right)\cos\phi$$

$$- 5\left(-2\phi'^3\phi'' + \phi'\phi^{(4)} + 2\phi''\phi^{(3)}\right)\sin\phi \tag{A2.5}$$

and

$$\frac{d}{dt}\left[\cos\phi(t)\right] = -\phi' \sin\phi \tag{A2.6}$$

$$\frac{d^2}{dt^2}\left[\cos\phi(t)\right] = -\phi'' \sin\phi - \phi'^2 \cos\phi \tag{A2.7}$$

$$\frac{d^3}{dt^3}\left[\cos\phi(t)\right] = \left(\phi'^3 - \phi^{(3)}\right)\sin\phi - 3\phi'\phi'' \cos\phi \tag{A2.8}$$

$$\frac{d^4}{dt^4}[\cos\phi(t)] = \left(6\phi'^2\phi'' - \phi^{(4)}\right)\sin\phi + \left(\phi'^4 - 4\phi'\phi^{(3)} - 3\phi''^2\right)\cos\phi \tag{A2.9}$$

$$\frac{d^5}{dt^5}[\cos\phi(t)] = \left(-\phi^{(5)} + 10\phi'^2\phi^{(3)} + 15\phi'\phi''^2 - \phi'^5\right)\sin\phi$$

$$+ 5\left(-\phi'\phi^{(4)} - 2\phi''\phi^{(3)} + 2\phi'^3\phi''\right)\cos\phi \tag{A2.10}$$

Substitution of Eqs. (A2.1) through (A2.5) into Eq. (49) gives for the convolution with $\sin\phi(t)$:

$$h_p(t) \otimes \sin\phi(t) = \left[a_o - \frac{a_2}{B^2}\phi'^2 - 3\frac{a_3}{B^3}\phi'\phi'' + \frac{a_4}{B^4}\left(\phi'^4 - 4\phi'\phi^{(3)} - 3\phi''^2\right)\right.$$

$$\left. - 5\frac{a_5}{B^5}\left(-2\phi'^3\phi'' + \phi'\phi^{(4)} + 2\phi''\phi^{(3)}\right)\right]\sin\phi$$

$$+\left[\frac{a_1}{B}\phi' + \frac{a_2}{B^2}\phi'' + \frac{a_3}{B^3}\left(\phi^{(3)} - \phi'^3\right) + \frac{a_4}{B^4}\left(\phi^{(4)} - 6\phi'^2\phi''\right)\right.$$

$$\left. + \frac{a_5}{B^5}\left(\phi^{(5)} - 15\phi'\phi''^2 - 10\phi'^2\phi^{(3)} + \phi'^5\right)\right]\cos\phi \tag{A2.11}$$

We recognize the series for the real and imaginary parts of the transfer function with $\phi(t)$ as argument

$$R[\phi'(t)] = a_o - \frac{a_2}{B^2}\phi'^2 + \frac{a_4}{B^4}\phi'^4 - \ldots \tag{A2.12}$$

$$X[\phi'(t)] = \frac{a_1}{B}\phi' - \frac{a_3}{B^3}\phi'^3 + \frac{a_5}{B^5}\phi'^5 - \ldots \tag{A2.13}$$

and the additional terms defined in Eqs. (50) and (51). Recognizing these we may write (A2.11) as

$$h_p(t) \otimes \sin\phi(t) = \{R[\phi'(t)] + G(t)\} \sin\phi(t) + \{X[\phi'(t)] + F(t)\} \cos\phi(t) \tag{A2.14}$$

Similarly we can use Eqs. (A2.6) – (A2.10) to write the denominator of Eq. (47) as

$$h_p(t) \otimes \cos\phi(t) = -\{X[\phi'(t)] + F(t)\} \sin\phi(t) + \{R[\phi'(t)] + G(t)\} \cos\phi(t) \tag{A2.15}$$

We have shown that for the first few terms the coefficient of $\sin\phi(t)$ in (A2.14) is equal to the coefficient of $\cos\phi(t)$ in (A2.15) and the coefficient of $\cos\phi(t)$ in (A2.14) is equal to the negative of the coefficient of $\sin\phi(t)$ in (A2.15). It can be shown that this property is general and holds for higher-order terms as well.

If we insert Eq. (A2.14) and Eq. (A2.15) into (47) we have

$$\phi(t) = \tan^{-1} \frac{\{R[\phi'(t)] + G(t)\} \sin\phi(t) + \{X[\phi'(t)] + F(t)\} \cos\phi(t)}{-\{X[\phi'(t)] + F(t)\} \sin\phi(t) + \{R[\phi'(t)] + G(t)\} \cos\phi(t)} \tag{A2.16}$$

To obtain Eq. (52) we simply divide numerator and denominator in the right-hand side of (A2.16) by $\{R[\phi'(t)] + G(t)\} \cos\phi(t)$.

APPENDIX III

DISTORTION SPECTRUM: HERMITE-POLYNOMIALS TECHNIQUE

The power-density spectrum of the intermodulation distortion may be computed with the aid of the Hermite-polynomials technique due to Thompson (Ref. 9). This technique has certain advantages which we discuss below over the power-series technique. The same procedure as that of Section 4.2 is used here, except that the PM distortion term of Eq. (41) is represented by a series of Hermite polynomials in x(t):

$$\Phi[\omega_e x(t) + \omega_c] = \sum_{i=0}^{\infty} h_i H_i[x(t)] \tag{A3.1}$$

The Hermite polynomials are given generally by

$$e^{-x^2/2} H_i(x) = (-1)^i \frac{d^i}{d_x^i} e^{-x^2/2} \tag{A3.2}$$

The first few polynomials are easily seen to be

$$\begin{aligned} H_0(x) &= 1 \\ H_1(x) &= x \\ H_2(x) &= x^2 - 1 \\ H_3(x) &= x^3 - 3x \\ &\vdots \end{aligned} \tag{A3.3}$$

The corresponding Hermite coefficients h_i of Eq. (A3.1) are well-known to be

$$h_i = \frac{1}{i!\sqrt{2\pi}} \int_{-\infty}^{\infty} \Phi[\omega_e x + \omega_c] e^{-x^2/2} H_i(x)\, dx \tag{A3.4}$$

Now, Thompson (Ref. 9) has shown that for gaussian inputs

$$R_\theta(\tau) = \sum_{n=0}^{\infty} n!\, h_n^2 R_x^n(\tau) \tag{A3.5}$$

Again, we ignore the zero- and first-order terms since they do not represent intermodulation distortion. Applying the Fourier transformation of Eq. (62) to Eq. (A3.5) yields the PM distortion spectrum

$$I_\theta(\nu) = \sum_{n=2}^{\infty} n!\, h_n^2\, S_x^{(n)}(\nu) \tag{A3.6}$$

Finally, we use Eq. (57) and divide by $S_x(\nu)$ to obtain the I/S ratio as a function of normalized video frequency

$$\frac{I_y(\nu)}{S_x(\nu)} = \left(\frac{\hat{\omega}\nu}{\omega_e}\right)^2 \sum_{n=2}^{\infty} n!\, h_n^2\, \frac{S_x^{(n)}(\nu)}{S_x(\nu)} \tag{A3.7}$$

It is instructive to write out a few distortion terms from Eq. (A3.7)

$$\begin{aligned} I_y(\nu) = {} & 2!\left(\frac{\hat{\omega}\nu}{\omega_e}\right)^2 h_2^2\, S_x^{(2)}(\nu) \\ & + 3!\left(\frac{\hat{\omega}\nu}{\omega_e}\right)^2 h_3^2\, S_x^{(3)}(\nu) \\ & + 4!\left(\frac{\hat{\omega}\nu}{\omega_e}\right)^2 h_4^2\, S_x^{(4)}(\nu) \\ & + \ldots . \end{aligned} \tag{A3.8}$$

Comparison of Eq. (A3.8) with Eq. (66) reveals the simplification of the final result achieved by the Hermite-polynomials technique. In place of the infinite sum of power coefficients appearing in each term of Eq. (66), there is now in Eq. (A3.8) a single Hermite coefficient determining the distortion-power level of a given order. Note that this coefficient is implicitly a function of ω_e/B. Thus each term in the series of Hermite polynomials Eq. (A3.1) is associated with an intermodulation-distortion product of a given order.

If the predetection-filter phase characteristic $\Phi(\omega)$ is available in the form of an analytical expression, it is relatively easy to compute the power-series coefficients c_i. The computation of the Hermite coefficients h_i from Eq. (A3.4) may prove a more difficult matter. On the other hand, if $\Phi(\omega)$ is available in empirical form, say as a graph of direct measurements, then numerical techniques can readily be applied to accurately compute h_i from Eq. (A3.4). Numerical techniques for computing power-series coefficients are subject to significant approximation errors. Thus, the Hermite-polynomials technique is particularly suited to the processing of experimental data.

APPENDIX IV

DISTORTION DUE TO MODULATOR-DEMODULATOR NONLINEARITIES

In laboratory measurements we have observed a "noise floor" consisting primarily of intermodulation distortion caused by nonlinearities in the modulator and demodulator. When making measurements of the intermodulation distortion caused by a predetection filter, correction must be made to remove the effect of the distortion due to the modem. In making this correction, one faces the question of whether or not distortion waveforms from the two sources are correlated. If these waveforms were exactly correlated, voltage addition would take place. If, as we shall show in this appendix, the waveforms are completely uncorrelated, power addition occurs. Before proving this we characterize the intermodulation distortion spectrum of a non-ideal modem.

The modem configuration is shown in Fig. A4.1 where the input "frequency" is v(t), the actual transmitted frequency (a replica of v(t)) is $\dot{\phi}(t)$, and the output "frequency"(a replica of $\dot{\phi}(t)$) is w(t). It is reasonable to assume that both the VCO and the discriminator operate without memory, so that we may write the output of each as a power series in the input

$$\dot{\phi}(t) = e_1 v(t) + e_2 v^2(t) + e_3 v^3(t) + \ldots \qquad \text{(A4.1)}$$

and

$$w(t) = f_1 \dot{\phi}(t) + f_2 \dot{\phi}^2(t) + f_3 \dot{\phi}^3(t) + \ldots \qquad \text{(A4.2)}$$

These two series represent the static characteristics of the VCO and discriminator respectively. By combining (A4.1) and (A4.2) we may write a series for the overall characteristic of the modem

$$w(t) = g_1 v(t) + g_2 v^2(t) + g_3 v^3(t) + \ldots \qquad \text{(A4.3)}$$

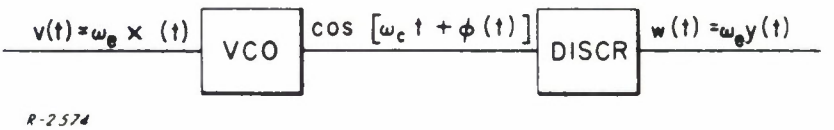

Figure A4.1 Modem Configuration.

where the coefficients g_i can be written in terms of the e's and f's as

$$g_1 = e_1 f_1 \tag{A4.4}$$

$$g_2 = e_2 f_1 + e_1^2 f_2 \tag{A4.5}$$

$$g_3 = e_3 f_1 + 2e_1 e_2 f_2 + e_1^3 f_3 \tag{A4.6}$$

etc.

In practice, the w(t) vs v(t) characteristic can be measured to obtain the g's, or the individual characteristics can be measured to obtain the e's and f's which can then be used to calculate the g's.

From Eq. (A4.3) we may write the transfer relation in terms of unity-mean-square variables x(t) and y(t) as

$$y(t) = \frac{1}{\omega_e} \sum_{i=1}^{\infty} g_i [\omega_e x(t)]^i \tag{A4.7}$$

Applying Thompson's result (Ref. 9) exactly as we did in Section 4.2 we find the autocorrelation of the output is given by

$$R_y(\tau) = \frac{1}{\omega_e^2} \sum_{n=0}^{\infty} n!\, R_x^n(\tau) \left[\sum_{j=0}^{\infty} \frac{(n+2j)!}{2^j j!\, n!}\, g_{n+2j}\, \omega_e^{n+2j} \right]^2 \tag{A4.8}$$

As before this may be transformed to give the distortion spectrum

$$I_y(\nu) = \frac{1}{\omega_e^2} \sum_{n=2}^{\infty} n!\, S_x^{(n)}(\nu) \left[\sum_{j=0}^{\infty} \frac{(n+2j)!}{2^j j!\, n!}\, g_{n+2j}\, \omega_e^{n+2j} \right]^2 \tag{A4.9}$$

We leave the result in this form rather than attempting to single out the dominant terms because it is not clear which terms will dominate in all cases.

Now we proceed to the question of the correlation between the intermodulation due to the modem and that due to the predetection filter. The system configuration is shown in Fig. A4.2. If the filter is ideal (no distortion), Eq. (A4.3) holds

$$w(t) = \sum_{n=1}^{\infty} g_n v^n(t) = v(t) + \sum_{n=2}^{\infty} g_n v^n(t) \tag{A4.10}$$

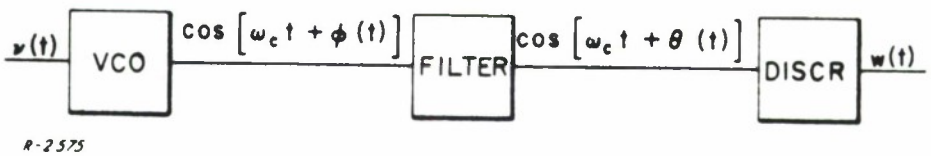

Figure A4.2 Modem and Predetection Filter.

On the other hand, if the modem is ideal and if the quasi-stationary condition holds for the filter, we have

$$\theta(t) = \phi(t) + \sum_{m=1}^{\infty} \frac{c_m}{B^m} \dot{\phi}^m(t) \qquad \text{(A4.11)}$$

Where the c's are the filter phase coefficients used throughout this report. Differentiating with respect to time yields

$$\dot{\theta}(t) = \dot{\phi}(t) + \sum_{m=1}^{\infty} \frac{mc_m}{B^m} \dot{\phi}^{m-1}(t)\, \ddot{\phi}(t) \qquad \text{(A4.12)}$$

Recognizing that $\dot{\phi}(t) = v(t)$ and $\dot{\theta}(t) = w(t)$ (we are assuming ideal VCO and discriminator) we can write this as

$$w(t) = v(t) + \dot{v}(t) \sum_{m=1}^{\infty} \frac{mc_m}{B^m} v^{m-1}(t) \qquad \text{(A4.13)}$$

Equations (A4.10) and (A4. 13) represent the distortion in the two cases of ideal filter and ideal modem.

When neither the modem nor the filter is ideal, and when the distortion is low, it is readily shown that the total distortion is given by the sum of the distortions in (A4.10) and (A4.13). That is,

$$w(t) = v(t) + \sum_{n=2}^{\infty} g_n v^n(t) + \dot{v}(t) \sum_{m=1}^{\infty} \frac{mc_m}{B^m} v^{m-1}(t) \qquad \text{(A4.14)}$$

This ignores "second-order" distortions such as, for example, the distortion arising in the discriminator and acting upon the distortion waveform produced by the filter. However, in the ordinary situation where "first-order" distortions are at least 20 dB below the signal level, "second-order" distortions will be at least 40 dB below signal level and can be neglected.

If we define new variables r(t) and s(t) for the distortion waveforms

$$r(t) = \sum_{n=2}^{\infty} g_n v^n(t) \tag{A4.15}$$

$$s(t) = \dot{v}(t) \sum_{m=1}^{\infty} \frac{mc_m}{B^m} v^{m-1}(t) \tag{A4.16}$$

then the total distortion is r(t) + s(t). To investigate the correlation between the components, we must form the autocorrelation of the total distortion, given by

$$\overline{[r(t)+s(t)]\,[r(t+\tau)+s(t+\tau)]} = \overline{r(t)\,r(t+\tau)} + \overline{r(t)\,s(t+\tau)} + \overline{s(t)\,r(t+\tau)} + \overline{s(t)\,s(t+\tau)} \tag{A4.17}$$

We first observe that the first and last terms are the autocorrelations of the modem distortion alone and the filter distortion alone. When transformed, they give the distortion spectra calculated in (A4.9) and (67) respectively. Therefore, to show that the two distortions are uncorrelated (and hence their powers add) we must show that the sum of the second and third terms of Eq. (A4.17) is zero. These terms are given by

$$\overline{r(t)\,s(t+\tau)} = \sum_m \sum_n \frac{mc_m g_n}{B^m} \overline{\dot{v}(t+\tau)\, v^{m-1}(t+\tau)\, v^n(t)} \tag{A4.18}$$

$$\overline{s(t)\,r(t+\tau)} = \sum_m \sum_n \frac{mc_m g_n}{B^m} \overline{\dot{v}(t)\, v^{m-1}(t)\, v^n(t+\tau)} \tag{A4.19}$$

We will establish that their sum is zero by showing that, for any m and n,

$$\overline{\dot{v}(t+\tau)\, v^{m-1}(t+\tau)\, v^n(t)} = -\overline{\dot{v}(t)\, v^{m-1}(t)\, v^n(t+\tau)} \tag{A4.20}$$

First recall that for $x_1, x_2, \ldots, x_k$ zero-mean gaussian random variables

$$\overline{x_1, x_2, \ldots, x_k} = \begin{cases} \sum \prod \overline{x_i x_j} & k \text{ even} \\ 0 & k \text{ odd} \end{cases} \tag{A4.21}$$

where the $\sum \prod$ denotes the sum over all distinguishable products of pairs of x's. For example

$$\overline{x_1 x_2 x_3 x_4} = \overline{x_1 x_2} \cdot \overline{x_3 x_4} + \overline{x_1 x_3} \cdot \overline{x_2 x_4} + \overline{x_1 x_4} \cdot \overline{x_2 x_3} \tag{A4.22}$$

The number of terms will in general be

$$N = k! \Big/ \frac{k}{2}!\, 2^{k/2} \tag{A4.23}$$

Note that each x_i appears once in every term.

Applying the above result to Eq. (A4.20) we can write (with the noise-loading technique v(t) and $\dot{v}(t)$ are gaussian random processes) the left-hand side as

$$\overline{\dot{v}(t+\tau)\, v^{m-1}(t+\tau)\, v^{n}(t+\tau)} = \sum_{j=1}^{N} \left\{ \begin{array}{c} \overline{\dot{v}(t+\tau)\, v(t+\tau)} \\ \text{or} \\ \overline{\dot{v}(t+\tau)\, v(t)} \end{array} \right\} \alpha_j(\tau) \tag{A4.24}$$

On the other hand, if we apply (A4.21) to the expectation on the right-hand side of Eq. (A4.19) we find

$$\overline{\dot{v}(t)\, v^{m-1}(t)\, v^{n}(t+\tau)} = \sum_{j=1}^{N} \left\{ \begin{array}{c} \overline{\dot{v}(t)\, v(t)} \\ \text{or} \\ \overline{\dot{v}(t)\, v(t+\tau)} \end{array} \right\} \beta_j(\tau) \tag{A4.25}$$

In both cases the number of terms N is

$$N = \frac{(m+n)!}{\left(\frac{m+n}{2}\right)!\, 2^{\frac{m+n}{2}}} \tag{A4.26}$$

If we number terms the same way in Eqs. (A4.24) and (A4.25) we can see that

$$\alpha_j(\tau) = \beta_j(-\tau) \tag{A4.27}$$

Because the left-hand sides of the equations are the same expectation with t and $(t+\tau)$ interchanged. Furthermore, $\alpha_j(\tau)$ and $\beta_j(\tau)$ are both of the form

$$\overline{v(t)\, v(t)}^{u} \cdot \overline{v(t+\tau)\, v(t)}^{v} \cdot \overline{v(t)\, v(t+\tau)}^{w}, \quad 2(u+v+w) = m+n-2 \tag{A4.28}$$

The derivative of v(t) does not appear because we have factored it out in Eqs. (A4.24) and (A4.25). This form is an even function of τ, so we have

$$\alpha_j(\tau) = \alpha_j(-\tau) \tag{A4.29}$$

and

$$\beta_j(\tau) = \beta_j(-\tau) \tag{A4.30}$$

Combining this with (A4.27) we have

$$\alpha_j(\tau) = \beta_j(\tau) \tag{A4.31}$$

Now we recall another result from the theory of gaussian processes, namely

$$\overline{v(t)\,\dot{v}(t+\tau)} = \frac{d}{d\tau}\,\overline{v(t)\,v(t+\tau)} \tag{A4.32}$$

Since $\overline{v(t)\,v(t+\tau)}$ is an even function of τ this implies that $\overline{v(t)\,\dot{v}(t+\tau)}$ is an odd function of τ; that is

$$\overline{v(t)\,\dot{v}(t+\tau)} = -\,\overline{v(t+\tau)\,\dot{v}(t)} \tag{A4.33}$$

Combining (A4.33) and (A4.31) we see that each term on the right-hand side of (A4.24) is the negative of the corresponding term on the right-hand side of (A4.25). Therefore Eq. (A4.20) is proven, and we have established that modem distortion and filter distortion are uncorrelated.

APPENDIX V

USE OF THE LOWPASS PROTOTYPE IN TDM

In Section 9.1 we expressed the phase output $\theta(t)$ in terms of equivalent lowpass filters $h_p(t)$ and $h_q(t)$. These equivalents are obtained from the original bandpass filter $h(t)$ by shifting operations in the frequency domain (see Section 3.2). In filter synthesis problems it is more convenient to work with the "lowpass prototype" of $h(t)$, which we will denote by $f(t)$. $f(t)$ is defined through the Laplace transforms

$$H(s) = F\left(s + \frac{\omega_o^2}{s}\right) \tag{A5.1}$$

The convenience of this definition results from the fact that a lowpass filter design may be converted to a bandpass design centered at frequency ω_o by the simple insertion of appropriate inductances in parallel with the existing capacitances and appropriate capacitances in series with the existing inductances in the lowpass filter design (Ref. 4).

To obtain a relationship between $h(t)$ and $f(t)$ from (A5.1), we must follow a rather indirect approach. First, we note that the Taylor series expansion for $H(s)$ about an arbitrary point, s_o, is

$$H(s) = H(s_o) + \frac{(s - s_o)}{1!} H'(s_o) + \frac{(s - s_o)^2}{2!} H''(s_o) + \ldots \tag{A5.2}$$

Choosing $s_o = j\omega_o$ we may calculate the coefficients of the leading term by reference to Eq. (A5.1) as

$$H(s_o) = F(0) \tag{A5.3}$$

$$H'(s_o) = 2F'(0) \tag{A5.4}$$

$$H''(s_o) = 4F(0) + \frac{2j}{\omega_o} F'(0) \tag{A5.5}$$

So, we have the following series for $H(s)$:

$$H(s) = F(0) + 2(s - j\omega_o) F'(0) + (s - j\omega_o)^2 \left[2F''(0) + \frac{j}{\omega_o} F'(0)\right] + \ldots \tag{A5.6}$$

This is not the desired result because it does not yield an explicit relation between h(t) and f(t), so we turn our attention to the Maclaurin series for F(s):

$$F(s) = F(0) + \frac{s}{1!} F'(0) + \frac{s^2}{2!} F''(0) + \ldots \tag{A5.7}$$

Replacing s with $(s - j\omega_o)$ we obtain

$$F(s - j\omega_o) = F(0) + \frac{(s - j\omega_o)}{1!} F'(0) + \frac{(s - j\omega_o)^2}{2!} F''(0) + \ldots \tag{A5.8}$$

We notice that both Eqs. (A5.6) and (A5.8) are series in powers of $(s - j\omega_o)$, so we may subtract Eq. (A5.8) from Eq. (A5.6) by subtracting coefficients of equal powers of $(s - j\omega_o)$:

$$H(s) = F(s - j\omega_o) + (s - j\omega_o) F'(0) + \frac{(s - j\omega_o)^2}{2!} \left[3F''(0) + \frac{2j}{\omega_o} F'(0)\right] + \ldots \tag{A5.9}$$

We now have a relationship which we can readily transform to yield an explicit relation between h(t) and f(t):

$$h(t) = e^{j\omega_o t} \left\{f(t) + F'(0)\,\delta'(t) + \frac{1}{2!}\left[3F''(0) + \frac{2j}{\omega_o} F'(0)\right] \delta''(t) + \ldots\right\} \tag{A5.10}$$

Now, if we write $F(j\omega)$ in terms of its real and imaginary parts as

$$F(j\omega) = R(j\omega) + jX(j\omega) \tag{A5.11}$$

we know that $R(j\omega)$ is an even function while $X(j\omega)$ is an odd function of $(j\omega)$. Thus, we note that

$$F'(0) = jX'(0) \text{ and } F''(0) = R''(0) \tag{A5.12}$$

Furthermore, we know that h(t) is a real function and hence we may disregard the imaginary terms in the series (A5.10). This yields,

$$h(t) = \left\{f(t) + \frac{1}{2}\left[3R''(0) - \frac{2}{\omega_o} X'(0)\right] \delta''(t) + \ldots\right\} \cos \omega_o t - \left\{X'(0)\,\delta'(t) + \ldots\right\} \sin \omega_o t \tag{A5.13}$$

This is the desired relationship between h(t) and f(t). It is analogous to the relationship

$$h(t) = 2h_p(t) \cos \omega_o t + 2h_q(t) \sin \omega_o t \qquad \text{(A5.14)}$$

which was used in deriving Eq. (95). Using Eq. (A5.13) instead of Eq. (A5.14) an alternate form of Eq. (95) may be written which involves f(t) rather than $h_p(t)$ and $h_q(t)$. Furthermore, by using the same series expansions for the trignonmetric function which were used to obtain Eq. (96), we may again obtain a series of the form

$$\theta(t) = \theta_1(t) + \theta_2(t) + \theta_3(t) + \ldots \qquad \text{(A5.15)}$$

The first three terms of the series are found to be:

$$\theta_1(t) = \frac{1}{2} \int f(\tau)\, \phi(t-\tau)\, d\tau + \frac{1}{4}\left[3R''(0) - \frac{2}{\omega_o} X'(0)\right] \phi''(t) + \ldots \qquad \text{(A5.16)}$$

$$\theta_2(t) = -\frac{1}{2} X'(0)\, \phi(t)\, \phi'(t) + \frac{1}{4} X'(0)\, \phi'(t) \int f(\tau)\, \phi(t-\tau)\, d\tau$$

$$+ \frac{1}{8} X'(0)\left[3R''(0) - \frac{2}{\omega_o} X'(0)\right] \phi'(t)\, \phi''(t) \qquad \text{(A5.17)}$$

and

$$\theta_3(t) = -\frac{1}{12} \int f(\tau)\, \phi^3(t-\tau)\, d\tau + \frac{1}{4}\, \theta_1(t) \int f(\tau)\, \phi^2(t-\tau)\, d\tau$$

$$- \frac{1}{4}\, \theta_1(t) \int^2 f(\tau)\, \phi(t-\tau)\, d\tau + \frac{1}{12} R(0)\, \theta_1^{\,3}(t)$$

$$+ \frac{1}{24}\left[3R''(0) - \frac{2}{\omega_o} X'(0)\right]\left[3\phi^2(t) - 6\phi(t)\, \theta_1(t) + 3\theta_1^{\,2}(t)\right] \phi'(t) \qquad \text{(A5.18)}$$

Since we are primarily concerned with intersymbol interference, we are interested in the output waveform outside the nominal time slot of the input pulse. Consequently, we may discard all terms in Eqs. (A5.16) – (A5.18) which contain $\phi(t)$ or one of its derivatives as a factor, resulting in the simplified relations which are valid outside the nominal time slot of the input pulse:

$$\theta_1(t) = \frac{1}{2} \int f(\tau)\, \phi(t-\tau)\, d\tau \qquad \text{(A5.19)}$$

$$\theta_2(t) = 0 \tag{A5.20}$$

$$\theta_3(t) = -\frac{1}{12}\int f(\tau)\,\phi^3(t-\tau)\,d\tau + \frac{1}{4}\theta_1(t)\int f(\tau)\,\phi^2(t-\tau)\,d\tau$$

$$-\frac{1}{4}\theta_1^{\,2}(t)\int f(\tau)\,\phi(t-\tau)\,d\tau + \frac{1}{12}R(0)\,\theta_1^{\,3}(t)$$

$$= -\frac{1}{12}\int f(\tau)\,\{\phi(t-\tau) - \theta_1(t)\}^3\,d\tau \tag{A5.21}$$

Equation (A5.19) is identical with Eq. (96) when $h_p(t)$ is replaced by $f(t)/2$ and $h_q(t)$ is set equal to zero. Therefore, it is clear that for calculations pertaining to the period of time after termination of the input pulse, either the lowpass equivalent $h_p(t)$ or the lowpass prototype $f(t)$ may be used interchangeably. This applies in particular to the considerations developed in Section 9.2 to show that the duration of the output is directly related to the duration of the impulse response $h_p(t)$.

Security Classification

DOCUMENT CONTROL DATA - R&D

(Security classification of title, body of abstract and indexing annotation must be entered when the overall report is classified)

1. ORIGINATING ACTIVITY (Corporate author) ADCOM, Inc. 808 Memorial Drive Cambridge, Mass. 02139	2a. REPORT SECURITY CLASSIFICATION Unclassified 2b. GROUP

3. REPORT TITLE

Study of Telemetry Receiver and Recorder Phase Linearity Problems

4. DESCRIPTIVE NOTES (Type of report and inclusive dates)

Final Report Aug 1965 - May 1966

5. AUTHOR(S) (Last name, first name, initial)

Ghais, Ahmad F. Boardman, Charles J.
Ferrari, Eugene J.

6. REPORT DATE	7a. TOTAL NO. OF PAGES	7b. NO. OF REFS
August 1966	194	16

8a. CONTRACT OR GRANT NO.	9a. ORIGINATOR'S REPORT NUMBER(S)
AF19(628)5655 b. PROJECT NO.	G-71-F
c.	9b. OTHER REPORT NO(S) (Any other numbers that may be assigned this report)
d.	ESD-TR-66-409

10. AVAILABILITY/LIMITATION NOTICES

Distribution of this Document is unlimited.

11. SUPPLEMENTARY NOTES	12. SPONSORING MILITARY ACTIVITY
	Electronic Systems Division L. G. Hanscom Field, Bedford, Mass

13. ABSTRACT

The problem of phase nonlinearities in telemetry-receiving systems is studied. The principal data-degrading effect is shown to be intermodulation distortion of FDM telemetry signals. Another form of data degradation, namely intersymbol interference in TDM telemetry signals, is found not to be related directly to phase non-linearities, but rather to the transient response of the receiving system.

The noise-loading technique is introduced as an effective means of characterizing, analyzing and measuring intermodulation distortion. Analy tical results are established relating the amount of intermodulation distortion to signal and receiving-system parameters. These relationships are verified experimentally using typical telemetry receivers, converters and recorders. Some other sources of data degradation are also identified and evaluated.

The study results are used to establish quantitative tradeoffs between the performance parameters of receiving systems. These tradeoffs are then used in formulating methods of specification for low data degradation. Improvements that can be implemented in existing and future systems are discussed, and it is recommended that study and development efforts should be undertaken to improve data quality.

DD FORM 1 JAN 64 1473

Security Classification

14. KEY WORDS	LINK A		LINK B		LINK C	
	ROLE	WT	ROLE	WT	ROLE	WT
Telemetry, FDM						
_____, TDM						
Phase (non) linearity						
Telemetry-Data Degradation						
Distortion, Intermodulation						
Interference, Intersymbol						
Telemetry Receivers						
_____ Converters						
Recorder, Predetection						
Filter, Predetection						
Noise-loading technique						
Quasi-stationary response						

INSTRUCTIONS

1. ORIGINATING ACTIVITY: Enter the name and address of the contractor, subcontractor, grantee, Department of Defense activity or other organization *(corporate author)* issuing the report.

2*a*. REPORT SECURITY CLASSIFICATION: Enter the overall security classification of the report. Indicate whether "Restricted Data" is included. Marking is to be in accordance with appropriate security regulations.

2*b*. GROUP: Automatic downgrading is specified in DoD Directive 5200.10 and Armed Forces Industrial Manual. Enter the group number. Also, when applicable, show that optional markings have been used for Group 3 and Group 4 as authorized.

3. REPORT TITLE: Enter the complete report title in all capital letters. Titles in all cases should be unclassified. If a meaningful title cannot be selected without classification, show title classification in all capitals in parenthesis immediately following the title.

4. DESCRIPTIVE NOTES: If appropriate, enter the type of report, e.g., interim, progress, summary, annual, or final. Give the inclusive dates when a specific reporting period is covered.

5. AUTHOR(S): Enter the name(s) of author(s) as shown on or in the report. Enter last name, first name, middle initial. If military, show rank and branch of service. The name of the principal author is an absolute minimum requirement.

6. REPORT DATE: Enter the date of the report as day, month, year; or month, year. If more than one date appears on the report, use date of publication.

7*a*. TOTAL NUMBER OF PAGES: The total page count should follow normal pagination procedures, i.e., enter the number of pages containing information.

7*b*. NUMBER OF REFERENCES: Enter the total number of references cited in the report.

8*a*. CONTRACT OR GRANT NUMBER: If appropriate, enter the applicable number of the contract or grant under which the report was written.

8*b*, 8*c*, & 8*d*. PROJECT NUMBER: Enter the appropriate military department identification, such as project number, subproject number, system numbers, task number, etc.

9*a*. ORIGINATOR'S REPORT NUMBER(S): Enter the official report number by which the document will be identified and controlled by the originating activity. This number must be unique to this report.

9*b*. OTHER REPORT NUMBER(S): If the report has been assigned any other report numbers *(either by the originator or by the sponsor)*, also enter this number(s).

10. AVAILABILITY/LIMITATION NOTICES: Enter any limitations on further dissemination of the report, other than those imposed by security classification, using standard statements such as:

(1) "Qualified requesters may obtain copies of this report from DDC."

(2) "Foreign announcement and dissemination of this report by DDC is not authorized."

(3) "U. S. Government agencies may obtain copies of this report directly from DDC. Other qualified DDC users shall request through _____."

(4) "U. S. military agencies may obtain copies of this report directly from DDC. Other qualified users shall request through _____."

(5) "All distribution of this report is controlled. Qualified DDC users shall request through _____."

If the report has been furnished to the Office of Technical Services, Department of Commerce, for sale to the public, indicate this fact and enter the price, if known.

11. SUPPLEMENTARY NOTES: Use for additional explanatory notes.

12. SPONSORING MILITARY ACTIVITY: Enter the name of the departmental project office or laboratory sponsoring *(paying for)* the research and development. Include address.

13. ABSTRACT: Enter an abstract giving a brief and factual summary of the document indicative of the report, even though it may also appear elsewhere in the body of the technical report. If additional space is required, a continuation sheet shall be attached.

It is highly desirable that the abstract of classified reports be unclassified. Each paragraph of the abstract shall end with an indication of the military security classification of the information in the paragraph, represented as *(TS)*, *(S)*, *(C)*, or *(U)*.

There is no limitation on the length of the abstract. However, the suggested length is from 150 to 225 words.

14. KEY WORDS: Key words are technically meaningful terms or short phrases that characterize a report and may be used as index entries for cataloging the report. Key words must be selected so that no security classification is required. Identifiers, such as equipment model designation, trade name, military project code name, geographic location, may be used as key words but will be followed by an indication of technical context. The assignment of links, rules, and weights is optional.

ESD TR 66-409

Errata

At the end of Section 1.3 on Page 6 of Referenced report, insert the following paragraph:

> Sections III and IV are based in part on prior work performed by ADCOM, Inc. with the support of the NASA Goddard Space Flight Center, Advanced Development Division. This work is documented in the Final Report of Task II on Contract NAS 5-9742 to be published in the fall of 1966.

DEPARTMENT OF THE AIR FORCE
HEADQUARTERS ELECTRONIC SYSTEMS DIVISION (AFSC)
LAURENCE G. HANSCOM FIELD, BEDFORD, MASSACHUSETTS 01731

REPLY TO ATTN OF: ESE(Mr. O'Brien/5322) 18 July 1966

SUBJECT: Release of Technical Document

TO: ESTIP

Identification: ESD-TR-66-409 and ESD-TR-66-408, Vol I & II

ESE has no objection to release of the above-cited document to the Clearinghouse for Scientific and Technical Information.

JOHN T. O'BRIEN
Chief, Public Information Division
Information Office

2 Atch
n/c